Low-Level Birefringence Measurement Methods Applied to The Characterization of Optical Fibers and Interconnects

A Thesis
Presented to
The Academic Faculty

by

Carole C. Montarou

In Partial Fulfillment
of the Requirements for the Degree
Doctor of Philosophy

School of Electrical and Computer Engineering
Georgia Institute of Technology
April 2005

Low-Level Birefringence Measurement Methods Applied to The Characterization of Optical Fibers and Interconnects

Approved by:

Professor Thomas K. Gaylord, Advisor
School of ECE
Georgia Institute of Technology

Professor Gee-Kung Chang
School of ECE
Georgia Institute of Technology

Professor John A. Buck
School of ECE
Georgia Institute of Technology

Professor Phillip N. First
School of Physics
Georgia Institute of Technology

Professor Glenn S. Smith
School of ECE
Georgia Institute of Technology

Date Approved: March 28, 2005

A mon grand-père,

Arsène Montarou

ACKNOWLEDGEMENTS

Now that I have reached the end of my Ph.D, it is first almost difficult to believe it and I cannot help but thinking of all the people who made this adventure possible.

First, I would like to express my deepest gratitude to Distinguished Prof. Thomas Gaylord who has been so patient, encouraging, supportive, and a great source of inspiration. His passion for optics and science in general is simply contagious. He is truthfully an exceptional person and an example for all. I have learned so much from him at so many different levels either scientifically or professionally. Most of all, I think I owe him millions of thanks for setting goals for me that I never thought I was capable of reaching. Looking back, I am so fortunate that he believed I could succeed in my graduate studies when I had almost given up. If it were not for him, I probably would not have stayed in graduate school.

I also would like to thank the member of my Ph.D. committee Prof. John Buck, Prof. Gee-Kung Chang, Prof. Phillip First, and Prof. Glenn Smith. Their careful reading of my thesis as well as their questions and comments were greatly appreciated.

Working in the optics laboratory at Georgia Tech means working with a group of fantastic people. Thank you to Brent Bachim, Dr. Muhannad Bakir, Mohammad Braiwish, Dr. Don Davis, Dr. Dan Guthrie, Prof. Elias Glytsis and his wife Dr. Dimitra Glytsis, Greg Kilby, Jon Maikisch, Dr. Antony Mule, Femi Ogunsola, Justin Stay, Dr. Greg VanWiggeren, Dr. Ricardo Villalaz, Dr. David Walker, Dr. Shun-Der Wu and his wife Eva Hsu. Besides being a group of bright and talented people from whom I learned so much, this research group is certainly one of the most enjoyable and interesting ones I know. We all come from different countries, different cultures, different backgrounds having very different opinions which we always shared openly. I cannot think of a subject from cooking to politics that we did not discuss or debate very passionately at times. However different all of our opinions were, we always maintained harmonious working relationships without taking anything personally or at least not that I know of! I feel so blessed I did my Ph.D. research among such

outstanding individuals. Creativity stems from this kind of environment. I have a profound respect and admiration for all of them.

Special thanks to Brent Bachim for providing me with long-period fiber gratings and to always have answers to my numerous questions. Thanks to Dr. Muhannad Bakir for providing me with polymer pillars.

I also would like to thank Prof. William Wepfer for making it possible for me to start graduate school at Georgia Tech.

Thanks to Mike Ludden who always ran to the rescue when I had problems with the Olympus microscope. His help and expertise were priceless.

The people in my personal life were just as supportive. I first want to thank my parents Alain and Claudette for never setting any limits on what I could do and for encouraging me in everything I wanted to accomplish. I have always been pushed to do the best I could. Thanks to my sister Cécile whose friendship and love I cherish a lot.

Special thanks to Annie Lemoine, Daniel Lemoine, Valentin Lemoine, Benjamin Lemoine, Mickaël Lemoine, Elise Lemoine, and the most recent addition to the family, Camille Lemoine. I am most grateful for their friendship and their support. I thank specially Mickaël, "Mimi" who was the reason I came to the United States for the first time ten years ago and started my American journey. This drastically affected the course of my life to say the least. Dear Marie-Thérèse, wherever you are, I want to thank you for trusting me and introducing me to your family.

I want to thank all the friends I have and had in Atlanta over the years with whom I shared precious personal moments. Thanks to Andrea, Daphne, Diego, Eduardo and Sandra, Guinka, Julia, Penelope, the Simoes Family to name just a few. All of them have contributed to make my life in Atlanta feel like home. Thank you for never making me feel alone.

Last, I want to send my warmest thoughts and prayers to my grand-father, Arsène Montarou who, at this time, is fighting the biggest battle of his life with the greatest dignity and strength. My grand-mother Genevève Montarou is equally brave in supporting her spouse in a difficult ordeal. No matter how strong the pain, no matter the outcome,

they astonish me yet again showing nothing but smiles, laughters, and humor. It is truly unbelievable to be so strong and so positive in face of the inevitable. This, I will always remember and carry with me everywhere I go, because there are no other people I know more alive and living. Thanks to both of you for this formidable gift!

CAROLE C. MONTAROU

Georgia Institute of Technology

April 2005

TABLE OF CONTENTS

LIST OF TABLES

LIST OF FIGURES

SUMMARY

Birefringence measurements are of great importance in a plethora of applications spanning from biology to optical communications. Birefringence measurements of nerve-fiber layers have emerged as an important diagnostic technique for early detection of glaucoma. Stress-induced birefringence in optical devices affects their performances by causing Polarization-Mode Dispersion (PMD) and Polarization-Dependent Loss (PDL). Stress-relaxation constitutes a key phenomenon governing the fabrication of some optical devices such as Long-Period Fiber Gratings (LPFGs). This drives the need to develop accurate optical instrumentation techniques to evaluate form and stress-induced birefringence in optical devices and biological cells. This thesis deals with the analysis, development, and implementation of new techniques for measuring optical retardation. These techniques are used for the measurements of the retardations resulting from stress-induced birefringence in optical fibers and interconnects.

The detailed analysis of two existing retardation measurement techniques, the Sénarmont and the Brace-Köhler techniques, is first performed. The transmittance by the optical system is derived using Jones calculus and is expressed as a function of the orientation of the various optical elements. The applicability ranges, the resolutions, and the accuracies are determined for both techniques and their limitations are identified.

This thesis further presents a new retardation measurement technique, the Two-Waveplate Compensator (TWC) method, consisting of rotating a compensator waveplate of known retardation to obtain a linearly polarized output when a birefringent sample is observed at 45 *deg* from extinction. Rotating an analyzer allows a null of intensity to be measured instead of a minimum of intensity as is the case with the Brace-Köhler technique. The expression for producing a linearly polarized output is derived without approximation as a function of the individual waveplate retardations. The applicability range, the resolution, and the accuracy of the TWC technique are determined. The new Automated Two-Waveplate-Compensator

(ATWC) is presented for the full-field evaluation of the retardation angle and magnitude. The new Phase-Stepping Two-Waveplate Retarder (PSTWR) is also presented which enables the measurement of the retardation angle and magnitude by recording intensities for various orientations of the compensator. The transmittance expression is used to derive the systems of equations necessary to compute the retardation angle and magnitude with 2, 3, and N compensator angles.

Having introduced techniques for use in monochromatic light, the new Colorimetry-Based Retardation Measurement (CBRM) method is presented for use in white-light. The white-light interference colors are calibrated to the retardations using a polarization microscope and a spectrophotometer. After calibration, the retardation of a sample can be quantified immediately by simply measuring the white-light interference color that it produces. The usefulness of the CBRM method is experimentally verified using various test waveplates.

The accuracies of these various retardation measurement techniques are evaluated for single-point measurement using an experimental configuration consisting of two polarizers and two waveplates. The retardation resulting from the stress-induced birefringence in optical devices is very small usually less than 5 nm. Crossed zero-order half-waveplates and crossed zero-order quarter-waveplates are therefore used to generate the needed small retardations and to compare the Sénarmont, Brace-Köhler, and TWC techniques. Each technique is also implemented for two-dimensional retardation measurements using a polarization microscope. Experimental and image processing procedures are presented. The accuracies of the Sénarmont, Brace-Köhler, and TWC techniques are evaluated for two-dimensional measurements.

Finally, the Brace-Köhler and TWC techniques are applied to the characterization of various optical fibers and optical interconnects. The transmittances calculated from the retardation measurements are compared to the intensity of the crossed-polarizers images to assess the accuracies and sensitivities of the techniques. An algorithm based on Fourier theory is presented to compute the inverse Abel transform relating the residual stress profile to the retardation measurements. The stress-induced birefringence is measured in polymer

pillar interconnects, single-mode fibers, and long-period fiber gratings.

CHAPTER 1

RETARDATION MEASUREMENTS

1.1 Introduction

The polarization of the light transmitted through a medium conveys information about the transmitting medium. This information is vital, for example, in the case of a bee whose retinotopic vision allows it to learn and recognize the state of partial polarization of the skylight depending on the sun's position and therefore allowing the bee to assess and communicate the locations of vital resources [1–3]. When light travels through anisotropic media, its polarization state is modified due to natural and/or induced birefringence whose magnitude and orientation is often directly related to characteristics of devices or of living cells. Knowing the polarization state of the light incident upon a sample, the detection and analysis of the polarization state of the transmitted light allow the determination of the sample's birefringence distribution. This motivates the need for developing quantitative techniques which enable the accurate measurement of the retardation magnitude and fast/slow axis orientations leading to the determination of sample's physical properties.

In crystallography, growth-induced birefringence arises from lattice mismatch in rare-earth garnets grown from the melt. This is an undesirable attribute for crystals that are to be used as substrates for magnetic devices or laser host crystals. This motivates the need for measuring and monitoring the growth-induced birefringence [4–6].

In fluid mechanics, using a differential interference polarization interferometer, white light interference colors are produced due to refractive index variations in a two-dimensional flow. Analysis of the white light interference colors leads to the quantitative determination of the fluid temperature and density gradient [7].

In biology, birefringence imaging has become a powerful tool for the dynamic observation of the growth cones of developing neurites and of the bundled microtubules in living cells. Birefringence imaging using polarization interference microscopy reveals details about the

cell structure during the various stages of a transformation [8, 9]. More recently, birefringence has been related to the retinal nerve fiber layer in the human eye and its measurement can be used for early detection of glaucoma [10].

In thin films, the reflection or transmission of polarized light introduces a phase-shift whose accurate measurement allows the determination of the film thickness, refractive index, and extinction coefficient [11].

In transparent materials such as glass and plastic, birefringence is induced by residual stress. Using the stress-optic effect, stress-induced birefringence measurements are used for quality control and quality enhancement by monitoring the amount of stress in selected locations [12, 13].

Residual stress also significantly impacts the lifetime, reliability, and failure modes of micromachined and microelectronic devices. High levels of residual stress may lead to cracking and delamination in thin films and interconnects, thus motivating the need for measuring and controlling the level of stress in those devices [14]. In technologies such as Micro Electrical Mechanical Systems (MEMS), parameters such as mirror curvature may be controlled by adjusting the amount of residual stress in electropated nickel films adding one more degree of freedom to the system [15].

In optical communications, residual stress affects the performance of optical fibers and planar waveguides. For example, residual stress determines the amount of Polarization Mode Dispersion (PMD) in optical fibers [16–18]. Stress-induced birefringence measurements in optical fibers delineate the roles of thermal and mechanical stress [19–23]. These measurements also allow the influence of OH impurity on the total residual stress to be quantified [24]. They also allow the residual stress to be related to the refractive index change [25–27]. Stress-induced birefringence measurements are needed to understand the mechanisms of stress relaxation occuring during the fabrication of long-period fiber gratings using CO_2 laser irradiation [28–30]. Stress-induced birefringence measurements are also essential in the design of polarization-maintaining optical fibers and waveguides which can lead to the fabrication of fiber gyroscopes, polarization-maintaining fiber amplifiers, PMD emulators and compensators [31], and polarization-insensitive arrayed waveguide gratings

routers [18].

Several techniques have been developed to measure retardation magnitude and orientation. Photoelastic measurements involve the use of circular polariscopes, i.e. polarizers and quarter waveplates, together with intensity measurements to retrieve the retardation magnitude of a sample [32]. The use of quarter waveplates affects the accuracy of the technique especially when it is used in white light [33]. Based on the photoelasticity principle, Spectral Content Analysis (SCA) uses a circular polariscope and a CCD camera in white-light to allow full-field retardation measurements [12, 13]. This technique is also subject to error due to the use of quarter waveplates and only takes into account a finite number of wavelengths of the transmitted light discriminating most of the optical signal. Further, these techniques can not detect low-level birefringence such as that present in optical fibers and waveguides.

Recently, photoelastic modulators have been used to modulate the polarization state of the light traveling through an optical system composed of polarizers and the sample under investigation. It has been shown that the frequency demodulation of the transmitted optical signal leads to accurate measurements of the low-level retardation magnitude and fast/slow axis orientations of the sample [34, 35]. This technique however possesses a low spatial resolution on the order of a millimeter which renders impossible the profiling of devices such as optical fibers and waveguides.

In biology, polarization microscopy has proven to be very effective in detecting low-level birefringence in living cells [36, 37]. The use of compensators allows the detection of low-level birefringence [36]. More recently, a new liquid-crystal-based compensator has been added to a polarization microscope to allow the detection of low-level retardation magnitude and fast/slow axis orientations in living cells [38]. A finite number of sample images are recorded for various birefringence settings of the compensator. For each pixel, the various intensities recorded allow a system of intensity equations to be solved for the two unknowns corresponding to the retardation magnitude and fast/slow axis orientations of the sample. The technique relies, however, on the accurate measurement of the light intensity and the compensator used is not a conventional, simple, commercially available compensator.

Another well-known technique to measure low-level birefringence is based on the Brace-Köhler compensator. The method consists of finding a minimum of intensity by rotating a compensator plate when a sample is observed between crossed polarizers. The measured compensator angle relative to the compensator extinction orientation when no sample is in the light path allows the determination of the unknown retardation [39, 40]. The technique however uses a small-retardation approximation and an intensity minimum is found rather than complete extinction. This may adversely affect the accuracy of the measurement. Furthermore, the Brace-Köhler compensator technique assumes that the sample retardation orientation is known.

When using monochromatic light for low-level retardation measurements, there is a need for a method based on finding a null of intensity which is more accurately measurable than a light intensity minimum or the absolute light intensity. When using white-light, there is also a need for a method using commercially available equipment and measuring the color of the transmitted light as opposed to measuring the response at only a finite number of wavelengths.

1.2 Retardation Measurement Techniques

1.2.1 Compensators

Several compensators are available to quantify retardation including the Berek compensator, the Sénarmont compensator, and the Brace-Köhler compensator. As the name indicates, measuring retardation by compensation consists of rotating a waveplate of known retardation so that it compensates for the retardation produced by a sample. In this research, the primary focus is on the Brace-Köhler and Sénarmont compensator techniques.

The Sénarmont compensator technique uses a quarter waveplate and monochromatic light. The sample is oriented at 45 degrees from extinction between crossed polarizers. A quarter waveplate, i.e., the Sénarmont compensator, is inserted so its slow axis is parallel to the polarizer transmission direction. In this configuration, elliptically polarized light exiting the sample is converted to linearly polarized light. The angular inclination of the linearly polarized output is exactly half of the total phase retardation introduced by the

sample. Rotating the analyzer until extinction allows the determination of the sample retardation [39, 40]. The Sénarmont compensator technique can measure retardations up to 1 λ. It has been recently used in optical communications to measure the residual stress profile of optical fibers [16, 30, 31, 41].

The Brace-Köhler compensator technique uses a mica waveplate of known low retardation and is commonly used to measure birefringence in low-strain glasses and inorganic crystals [6, 40]. Typical commercial values of compensator retardations are $\lambda/10$ or $\lambda/30$. The sample is oriented at 45 degrees from extinction between crossed polarizers. The mica plate is inserted into the light path so its slow axis is first parallel to the polarizer transmission direction. The mica plate is then rotated until an intensity minimum is observed. Using a small retardation approximation, the angle deviation of the mica plate from its extinction position allows the calculation of the sample retardation. In contrast to the Sénarmont compensator, it does not produce complete extinction but only minimizes the intensity transmitted through the polarizer-sample-compensator-analyzer configuration.

Neither of the above techniques has been evaluated in terms of accuracy and resolution when applied to the measurement of low-level retardations such as those present in optical fibers and interconnects. The Sénarmont technique has proven effective to measure retardations up to 1λ. However, this technique is not generally suitable for low retardations as its accuracy decreases with retardation. The Brace-Köhler technique is more suitable for low retardations however finding a minimum of intensity is not as accurate as finding a complete extinction. Further, the small-retardation approximation used in this technique may also affect its accuracy.

1.2.2 Photoelasticity

Photoelasticity may be applied in a plane or circular polariscope to measure retardation. In a plane polariscope, the sample is placed between crossed or parallel polarizers and is thus illuminated by linearly polarized light whereas in a circular polariscope quarter waveplates are added before and after the sample so it is illuminated with circularly polarized light. The theoretical expressions of the intensity transmitted through such polariscopes are known as

a function of the sample retardation magnitude and fast/slow axis orientations. Measuring the transmitted intensity allows the determination of the sample retardation [32, 33]. The accuracy of the method depends on the accuracy with which the transmitted intensity can be measured. When using circular polariscopes, the measurement is subject to errors due to the quarter waveplates especially when it is done in white light [33, 42].

Phase-stepping photoelasticity is an expansion of the conventional photoelasticity methods. It uses non-conventional polariscopes which are a combination of plane and circular polariscopes. The retardation magnitude and fast/slow axis orientations of a sample are measured by recording a number of transmitted intensities for various relative orientations of the optical elements in the polariscope [32, 42].

The several photoelastic methods have also been implemented for measuring retardations when polariscopes are illuminated with white-light. White-light interference colors are produced when a sample exhibiting birefringence is observed between crossed or parallel polarizers. One given retardation produces one unique color. Spectral Content Analysis (SCA) uses a spectrophotometer to measure a finite number of wavelengths in the transmitted light. The retardation is determined by associating the measured spectrum with the theoretical spectral signature characteristic of the retardation producing it [12, 13, 43]. Measuring only a finite number of wavelengths in the transmitted light does not utilize most of the optical signal. This can be overcome if the complete color is measured. Other methods are based on RGB measurements. A truth table is created relating known values of retardation to RGB values. Sample retardations are then determined by measuring the resulting RGB values and associating them with a retardation by referring to the calibration table [44–46].

1.2.3 Photoelastic Modulators

Photoelastic modulators have been used to measure retardation magnitude and fast/slow axis orientations. A photoelastic modulator made of a transparent material and a piezoelectric transducer allows the modulation of the polarization state of an optical signal incident upon a sample of unknown retardation placed between crossed polarizers. The transmitted

intensity can then be expressed as a Fourier series in time whose various harmonics are multiples of the modulating frequency. The coefficients weighting the various harmonics are functions of the sample retardation magnitude and can be determined using a lock-in amplifier. In a first configuration, the sample fast/slow axis orientations are assumed to be known and using one photoelastic modulator allows the measurement of the sample retardation magnitude [34].

The instrument sensitivity was increased by changing the orientation of the sample and the analyzer. Instead of the sample birefringent axis being parallel to the first polarizer transmission direction, and the analyzer polarization transmission direction being perpendicular to that of the polarizer, sample and analyzer are rotated 45 degrees in this second configuration. It has been shown that the first harmonic of the transmitted optical signal is directly proportional to the sample retardation magnitude and that it carries most of the transmitted signal in this new configuration . This ultimately increases the instrument sensitivity [47, 48].

The instrument was further improved by adding the capability to measure the fast/slow axis orientations. This was accomplished by making two measurements corresponding to two different orientations of the analyzer. This allows a system of equations to be solved for the sample retardation magnitude and fast/slow axis orientations [35,49]. The configuration can incorporate two detecting arms whose analyzer orientations are the two orientations needed to determine the retardation magnitude and orientation. Another configuration was developed with two photoelastic modulators and only one detecting arm. Having the photoelastic modulators slow axes oriented at 45 degrees from each other allows the measurement of the sample retardation magnitude and orientation [50, 51].

The main limitation of the photoelastic-modulator-based retardation measurement technique is the low spatial resolution. The sample is illuminated with a light beam of diameter on the order of one millimeter and no image is formed. It can therefore only measure at a single-point requiring scanning for two-dimensional profiling. The beam diameter is much too large to enable the instrument to measure the two-dimensional distribution of retardation in samples that are only several hundreds microns wide such as optical fibers and

optical interconnects.

1.2.4 Polarization Microscopy

The presence of very weak birefringence in biological cells has been a primary motivation behind the use and enhancement of polarization microscopy in detecting low-level birefringence. In polarization microscopy, the sample is illuminated with polarized light by placing a polarizer before the condensing lens of the microscope. If birefringence is present in the sample, this linearly polarized light is split into two orthogonally polarized beams traveling through the sample with different refractive indices [40]. The resulting optical path difference introduces a phase-shift between the polarizations. By placing a second polarizer after the objective lens, the intensities in the image become a function of the magnitude of the phase-shift and of the orientation of the birefringent axis of the sample. To improve the sensitivity to birefringence in the polarization microscope, its contrast can be enhanced by using a bright source, increasing the extinction ratio of the polarizers, using strain-free lenses, and using low numerical aperture lenses. All of these improvements cause the contrast between the birefringent object and background to be increased [36]. Swann *et al.* [36] have developed a photographic retardation measurement method. The density of the photographic film is calibrated for various retardations. The calibration curves are used to determine unknown retardation by inspecting the density of a film exposed to the image of a sample. This method, however, suffers from a very low resolution and necessitates long exposure times.

A revolving tilted compensator known as a Berek compensator has been used to measure weak birefringence. As the tilted compensator is rotated, elliptically polarized light is produced whose varying ellipticity modulates the transmitted intensity. The intensity maxima correspond to orientations of the compensator for which its birefringent axis is at 45 degrees from the polarizer transmission axis. For zero birefringence, these intensity maxima have equal magnitudes whereas local intensity maxima and global intensity maxima are observed when a birefringent object is inserted into the light path. Using calibration and measuring the ratio of the local maxima to the global maxima has proven efficient in measuring weak

birefringences [37].

The Brace-Köhler compensator is another well-know technique used to measure birefringence in biological samples [39, 40]. Its principle of operation has been explained in Sec. 1.2.1 and will be analyzed thoroughly in this research. The rotating dial of the compensator has been connected to a digital display to facilitate the reading of the angle when looking for the intensity minimum. The configuration allows the digitally read angle to be converted directly into retardation [52].

More recently, Oldenbourg *et al.* [38] incorporated electro-optical modulators to act as a universal compensator in a polarization microscope. In this new configuration, the sample is illuminated with circularly polarized light and two liquid crystal devices are used as variable linear retarders by adjusting the applied voltage. Similar to phase-stepping interferometry, it has been shown that by setting the liquid crystal modulators to four different biases, four sample images are recorded and the four intensity distributions allow a system of equations to be solved for the retardation magnitude and fast/slow axis orientations of the sample at each point of the field of view, and for the resulting linear retarder retardation magnitude and fast/slow axis orientations produced by the liquid crystal devices compensating for the sample retardation at each point of the field of view. The technique has been applied to image the birefringence magnitude and orientation in growth cones of developing neurites and microtubules of living cells [8, 9]. Several algorithms using various numbers of recorded images have been presented to increase the speed, sensitivity, and accuracy of the instrument [53].

This technique relies however on measuring accurately the light intensity transmitted through the optical system and may not be as accurate as detecting a null of intensity. Furthermore, the universal compensator used is not a conventional, simple compensator provided with a polarization microscope. This motivates the need for new retardation measurement techniques using conventional equipment and detecting a null of intensity instead.

1.3 Research Objectives

The objectives of this research are the analysis, implementation, and comparison of new retardation measurement techniques for single-point and full-field retardation evaluation for use in monochromatic light and white light. These techniques will be applied to the retardation measurement of optical retarders, optical fibers and optical interconnects. The main contribitions of this thesis work are organized as follows:

1. The Sénarmont and Brace-Köhler techniques are theoretically analyzed in terms of their accuracies, resolutions and applicability ranges. The transmitted intensities as a function of analyzer and compensator angles are derived using Jones calculus. The main limitations of these techniques are determined for accurate measurements of large and small retardations.

2. The new Two-Waveplate Compensator (TWC) technique is developed for use with monochromatic light. It is based on rotating a waveplate of known retardation to produce linearly polarized light when a sample is placed between polarizers. Extinction is obtained by rotating the analyzer so it is perpendicular to the polarization direction. The accuracy, resolution and applicability range of the TWC are theoretically determined. The condition for linearly polarized transmitted light is expressed as a function of sample and compensator retardations without approximation. The TWC is shown to be more accurate than the Brace-Köhler and Sénarmont techniques.

3. The Phase-Stepping Two-Waveplate Retarder (PSTWR) is also developed for use with monochromatic light. In this technique, a sample and a waveplate of known retardation are placed between crossed polarizers. Biases are introduced by rotating the waveplate to various orientations and by measuring the corresponding transmitted intensities. This allows a system of intensity equations to be solved for the sample retardation magnitude and orientation. By taking a large number of measurements, the PSTWR is shown to be a high-accuracy retardation measurement technique.

4. A Colorimetry Based Retardation Measurement (CBRM) technique is developed for

use with white-light. It is based on the accurate measurement of the white-light interference colors produced for various values of birefringence. It uses a polarization microscope and a photospectrometer. A calibration color/retardation database is created by measuring the color corresponding to each retardation. This database is used to determine a sample's retardation by measuring the white-light color produced when it is observed with a polarization microscope between crossed polarizers. The CBRM is tested on a variety of retarders and its accuracy and resolution are evaluated.

5. The Sénarmont, Brace-Köhler, and TWC techniques are implemented for single-point retardation measurements. Small retardations are produced by crossing half-waveplates and quarter-waveplates designed for closely spaced wavelengths. The accuracy of each technique is determined from a large number of measurements.

6. The Sénarmont, Brace-Köhler, and TWC are implemented for full-field retardation measurements using a polarization microscope. The techniques' accuracies are evaluated for two-dimensional retardation measurements.

7. The Brace-Köhler and TWC techniques are applied to a variety of optical fibers and polymer waveguides. The axial residual stress profile is determined in single-mode fibers, long-period fiber gratings and polymer pillar interconnects from the retardation measurements.

CHAPTER 2

BIREFRINGENCE IN OPTICAL DEVICES

2.1 Stress-Induced Birefringence

2.1.1 Photoelastic Effect

When subject to a mechanical stress, transparent materials such as glass and plastic, become birefringent. This is known as the photoelastic effect and is the basis of experimental techniques to determine the stress distribution in transparent materials. In Fig. 2.1, a compressive stress σ_y is applied to a glass plate in the y-direction. When a light beam propagating along the x-direction passes through the plate, it is decomposed into two waves that are respectively polarized along the y-axis, parallel to the applied stress direction, and along the z-axis, perpendicular to the applied stress direction. Each wave travels with a different refractive index, respectively, n_y and n_z. It has been empirically shown that the birefringence $n_z - n_y$ is proportional to the stress applied [54–56],

$$n_z - n_y = C\sigma_y, \tag{2.1}$$

where C is the stress-optic coefficient of the material expressed in $nm/cm/MPa$. Knowing the stress-optic coefficient of the material and measuring the birefringence allow the determination of the stress applied to the material.

2.1.2 Photoelastic Effect in Silica Glass

Silica glasses are the principal material involved in the fabrication of optical fibers, planar lightwave circuits, and microlithographic optical tools. Their main advantages are high transmission, high index homogeneity, and low absorption loss [57, 58]. Birefringence is induced in fused silica when stress is applied to the material due to the photoelastic effect. Understanding the wavelength and material composition dependence of the birefringence is crucial to control the quality and performances of optical devices made of silica. The stress-optic coefficient of fused silica as a function of wavelength was measured in Reference 57

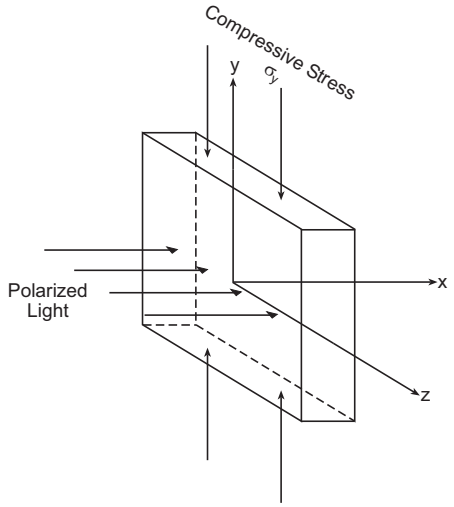

Figure 2.1: Photoelastic effect in transparent materials. The material is subject to a compressive stress σ_y. Polarized light incident upon the material is decomposed into two orthogonal polarizations along the y and z axes. Birefringence is induced between the two polarizations which propagate with two different refractive indices n_y and n_z respectively.

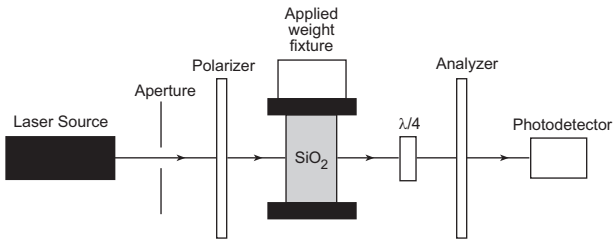

Figure 2.2: Measurement of the stress-optic coefficient of fused silica. The sample is placed between crossed polarizers. A load is applied to the sample to produce a uniaxial compressive stress. The resulting retardation is measured using the Sénarmont compensator method [57].

Table 2.1: Stress-optic coefficient of fused silica at various wavelengths [57].

Wavelength (nm)	Stress-Optic Coefficient ($nm/cm/MPa$)
633	35±1
248	42±1
193	51±1

using the experimental configuration shown in Fig. 2.2. An air-driven piston shaft applied various stresses to the sample of SiO_2. The resulting birefringence was measured by rotating the analyzer until extinction applying the Sénarmont compensator method. The stress-optic coefficient was computed by calculating the slope of the linear fit describing the variations of the birefringence as a function of the applied stress. The stress-optic coefficient was measured at wavelengths equal to 193 nm, 248 nm and 633 nm. The measured stress-optic coefficients are indicated in Table 2.1.

Stress-induced birefringence arises during the fabrication of optical devices made of silica due to thermal and mechanical stresses. This stress-induced birefringence affects the transmission characteristics of optical waveguides causing unwanted polarization-dependent loss and polarization-mode dispersion. It also affects the optical elements such as lenses used in microlithographic applications causing distortion of projected wave front thereby degrading the image being patterned on a silicon wafer.

2.1.3 Residual Stress

Residual stresses in optical waveguide materials are the combination of thermal and mechanical stresses. The thermal stress is caused by thermal expansion mismatch between constituent materials. The mechanical stress is caused by the forces applied during the fabrication process [19] and structural asymmetry in the device [17, 59, 60]. Consequently, birefringence is induced through the photoelastic effect. This section describes the origins of thermal and mechanical stresses.

2.1.3.1 Thermal Stress

Optical fibers are drawn from cylindrical preforms made by chemical vapor deposition process [58]. In an optical fiber, the thermal stress results from the thermal expansion coefficient mismatch between the core and the cladding materials [22, 23]. The materials composing the core and cladding layers being different, their responses to temperature increase during fabrication differ and stresses develop. These stresses remain after cooling of the optical fiber to room temperature.

The need for a given refractive index profile requires different dopant concentrations in the core and the cladding which can worsen the expansion coefficient mismatch [20] in optical fibers. As the optical fiber is drawn and cools down, the set temperature is different along the radius of a cross-section of the fiber. As a result, certain areas solidify while others remain fluid causing stresses to develop.

Similar effects occur during the fabrication of fused silica-based planar optical waveguides. The thermal stresses originate from the bonding of layers made of different materials creating thermal expansion coefficient gradients. When a silicon substrate is used, the annealing of the upper glass layer strains the glass due to the thermal expansion coefficient difference between the silicon substrate and the fused silica waveguide [17, 59, 61–64].

2.1.3.2 Mechanical Stress

In addition to thermal stress, a second kind of stress arises from the pulling tension with which an optical fiber is drawn out of the melting preform [23, 65, 66]. When high pulling tensions are used, a significant amount of the stress remains in the optical fiber. Asymmetric tensile stresses in the core and the cladding during the pulling process will also be frozen in the optical fiber. For higher production quantities, fibers are drawn at higher speeds using larger pulling tensions. It has been shown that pulling optical fibers with high tensions increases the mechanical stress by introducing more OH impurities in the silica glass [24].

The fabrication processes of silica-based wave-guides on silicon substrates also cause mechanical stress in planar lightwave circuits [67–69]. An overcladding made by Flame

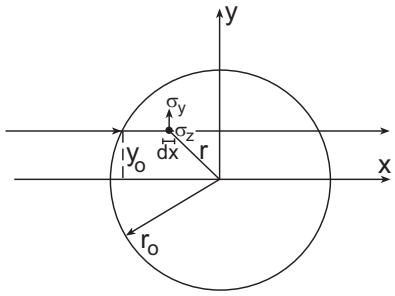

Figure 2.3: Polarized light is incident on an optical fiber. The radius of the optical fiber is r_o. Light propagates along the x direction perpendicular to the fiber axis. The residual stress components along the directions y and z are σ_y and σ_z respectively. The residual stress induces birefringence and the incident light is decomposed into two orthogonal polarizations along the y and z axes.

Hydrolysis Deposition (FHD) has been described to eliminate the stress-induced birefringence of a planar waveguide [70]. The material's mechanical and elastic properties such as the Young's modulus and Poisson ratio mismatch between layers of the waveguiding device produce strains which also results into mechanical stress [17, 59, 61].

Furthermore, structural asymmetry in the waveguide design affects the strain distribution [71]. Geometrical parameters such as thickness ratio and width ratio between layers can be tailored to even the strain distribution and decrease the mechanical stress [17, 18, 59, 61, 72].

An undercladding ridge or a stress-relief groove can be added to decrease the stress originating from structural asymmetry [60, 62]. The stress-induced birefringence can be reduced in a deep-ridge waveguide structure by incorporating a grating-loaded overcladding layer [73]. Structural birefringence can be completely eliminated in a deep-ridge vertical-groove structure which consists of a ridge waveguide surrounded by stress-relief vertical grooves separated by a fixed period [74].

2.1.3.3 Stress-Induced Birefringence in Optical Interconnects

As shown in Sec. 2.1.2, fused silica becomes uniaxially birefringent when stresses are applied. The photoelastic effect can be used to evaluate the residual stress present in optical fibers and waveguides through birefringence measurements. Considering the cross-section of an optical fiber in Fig. 2.3, light is incident perpendicularly to the fiber axis. It has been shown

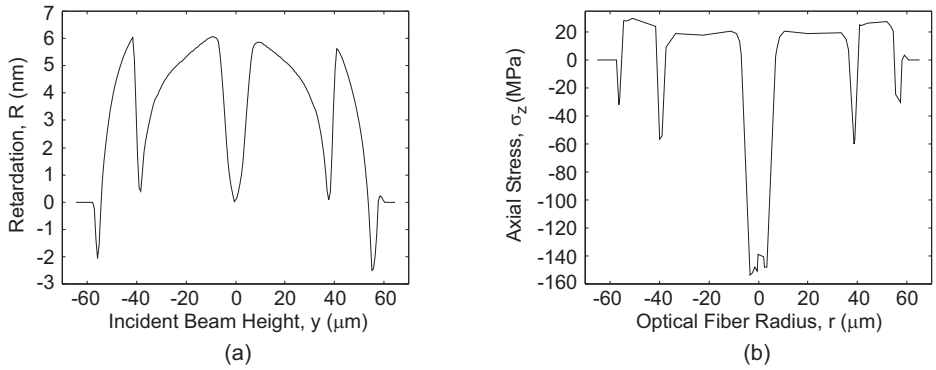

Figure 2.4: (a) Retardation for a beam incident perpendicularly to the fiber axis. The retardation is calculated using Eq. (2.2) (b) Residual stress in an optical fiber that has been drawn with a force of 3.48 N [28].

that the retardation $R(y)$ of a beam incident on the fiber at y is given by [16, 20]

$$R(y) = 2C \int_y^{r_o} \sigma_z(r) \frac{rdr}{\sqrt{r^2 - y^2}}, \tag{2.2}$$

with C stress-optic coefficient of fused-silica, r_o radius of the optical fiber, y vertical coordinate of the incident beam, $\sigma_z(r)$ axial stress. It is assumed that the beam is not deflected upon its passage through the optical fiber. Using an inverse Abel transform, the axial stress $\sigma_z(r)$ is computed by

$$\sigma_z(r) = -\frac{1}{\pi C} \int_r^{r_o} \frac{dR(y)/dy}{\sqrt{y^2 - r^2}} dy. \tag{2.3}$$

Measuring the retardation along the cross-section of an optical fiber allows the determination of the axial stress profile using Eq. (2.3). Figures 2.4(a) and 2.4(b) give an example of how the residual stress is calculated using the retardation profile in Eq. (2.3). Figure 2.4(a) represents the measured retardation profile of an optical fiber that has been drawn with a force of 3.48 N [28]. Figure 2.4(b) represents the calculated axial residual stress using Eq. (2.3). Inversely, the retardation profile can be retrieved using Eq. (2.2).

2.2 Stress-Induced Birefringence Effects

Built-in stresses in optical fibers and waveguides significantly impact their transmission characteristics, quality, and reliability. Built-in stresses cause refractive index profile distortion and stress-induced birefringence leads to Polarization-Mode Dispersion (PMD) and

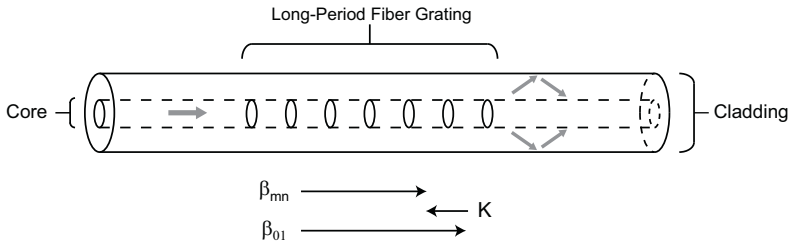

Figure 2.5: Light coupling between a core-guided mode to a cladding-guided mode in a LPFG. The phases of the two modes are matched due to the grating. β_{01} is the propagation constant of the LP_{01} core-guided mode and β_{mn} the propagation constant of the LP_{mn} cladding-guided mode. K is the grating vector.

Polarization-Dependent Loss (PDL) [65]. This section describes some of the effects of residual stress and stress-induced birefringence on optical fibers and wave-guides.

2.2.1 Optical Fibers

Residual stress in optical fibers affects both their mechanical and transmission properties. The quality and reliability of an optical fiber is mostly determined by its surface crack growth which depends on the residual stress state. A microcrack at the surface of the fiber tends to propagate under tensile stress while it tends to be contained under compressive stress [65]. The wave-guiding properties of an optical fiber are mostly determined by its refractive index profile which can be perturbed by residual stress. Polarization-Mode Dispersion (PMD) which results into a differential group delay between two polarizations has been partly linked to residual stress and may degrade the optical fiber performances [19, 65, 75].

Fiber gratings are of great importance in optical fiber communications as they are used to fabricate band-rejection filters, gain equalizers, and dispersion compensation devices [76,77]. Long-period Fiber Gratings (LPFGs), for example, couple the light from a core-guided mode to a cladding-guided mode due to the presence of a periodic refractive index change along the axis of the optical fiber. The coupling between the two modes of a LPFG is represented in Fig. 2.5. An example of the spectrum of the light transmitted by a LPFG is represented in Fig. 2.6.

In recent years, LPFGs have been fabricated using CO_2 laser pulses to modify periodically the refractive index profile along the axis of an optical fiber [76–78]. These gratings

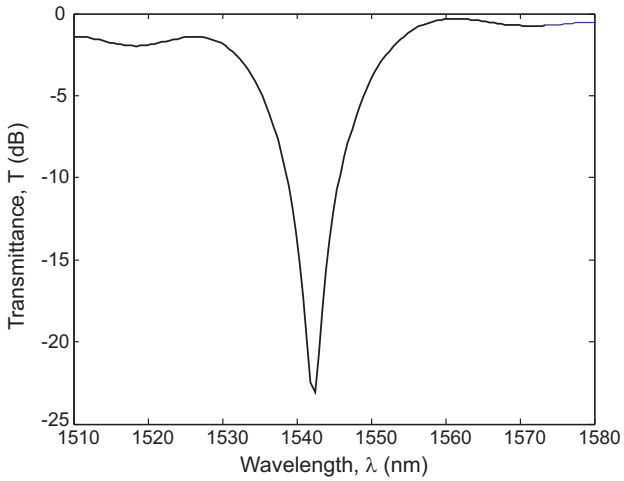

Figure 2.6: Spectral transmittance of a LPFG [76, 77].

have proven to be more stable than those fabricated using UV-exposure. The refractive index changes induced by the CO_2 laser irradiations are directly related to the amount of residual stress in the optical fiber [21, 28, 29]. The index change is produced by a relaxation of the built-in stress.

More recently, a detailed analysis of the effects of birefringence on the spectral transmittance of CO_2-laser-induced LPFGs has been presented [78]. An important effect caused by birefringence in fiber gratings is Polarization-Dependent Loss (PDL). Due to the azimuthally asymmetric refractive index profile in LPFGs, the transmittance of the grating may be polarization dependent in which case the transmission and the resonant wavelength will vary with polarization. PDL negatively affects the performances of LPFGs used as gain-flattening filters in erbium-doped fiber amplifiers for example.

Refractive index asymmetry due to photo-induced birefringence in Bragg gratings leads to Polarization-Mode Dispersion (PMD) which introduces a differential group delay between different polarizations. The photo-induced birefringence can also give rise to Polarization-Dependent Loss (PDL) at certain wavelengths. The refractive index asymmetry is caused by the fact that the fiber is UV-exposed on one side only. A more uniform index change can be obtained by exposing the fiber a second time on the other side at 180 *deg* from the first exposure [27].

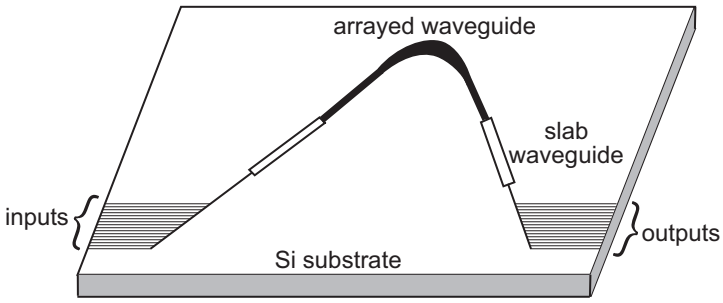

Figure 2.7: Arrayed Waveguide Grating (AWG) multiplexer on silicon substrate [60].

2.2.2 Lightwave Devices

Silica-based Planar Lightwave Circuit (PLC) devices have been widely used in optical communication networks as splitter/combiners, spatial switches, couplers, and multi/demultiplexers [60, 79]. Among the many advantages of PLCs are low propagation loss, long-term stability and low-loss coupling to optical fibers. More recently, wafer level optical input-output interconnections have been demonstrated using Sea of Polymer Pillars (SoPPs) [80–82]. The coefficient of thermal expansion mismatch between the optical devices materials and the silicon substrate they are fabricated on gives rise to stress asymmetry. This induces birefringence that renders optical devices polarization sensitive.

This constitutes a major issue in Arrayed Waveguide Gratings (AWGs) for example in which the effective refractive index is polarization-dependent because of the stress-induced birefringence resulting in a polarization-dependent wavelength shift in the transmission spectrum of the AWG [83–86]. A diagram of an AWG multiplexer is shown in Fig. 2.7. An AWG is composed of input/output waveguides, two slab waveguides and an arrayed waveguide. The transmission spectrum of an AWG differs for TE and TM polarized light because of the stress-induced birefringence. The wavelength shift of the transmission spectrum peak between both polarizations in Reference 60 is calculated to be $\sim$0.11 nm. The PDL is 1.64 dB.

In the arrayed waveguide grating, the thermal expansion mismatch between the core and the overcladding on one hand, and between the core and the silicon substrate on the other hand gives rise to compressive stress in the horizontal and vertical direction in the core leading to birefringence. The stress asymmetry can be controlled by adding

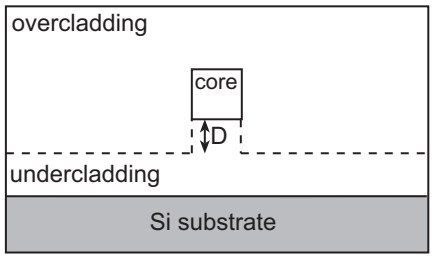

Figure 2.8: Undercladding ridge structure in an arrayed-waveguide to reduce stress-induced birefringence effects [60].

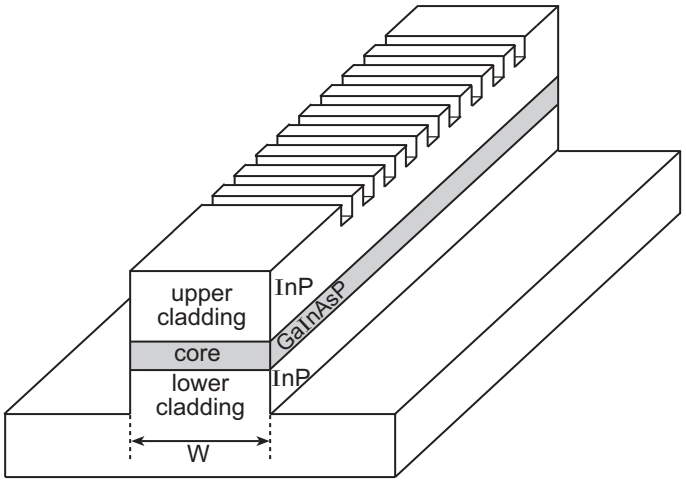

Figure 2.9: Deep-ridge distributed feedback waveguide [73].

an undercladding ridge under the core of the arrayed waveguide as shown in Fig. 2.8. The height D of the undercladding ridge in Fig. 2.8 can be adjusted so as to render the AWG polarization-insensitive. Kasahara *et al.* demonstrated a polarization-insensitive 16-channel AWG with 100 GHz channel spacing by incorporating a 3 μm heigh undercladding ridge [60].

All-optical switching operations which do not require optical-electrical/electrical-optical conversion can be achieved combining the optical Kerr effect and the Distributed Feedback (DFB) mechanism in nonlinear media. The devices thus developed exhibit however strong structural birefringence and therefore are polarization-sensitive. Polarization-insensitivity is needed for use in optical communications networks. A deep-ridge waveguide structure shown in Fig. 2.9 has proven to be effective in reducing polarization sensitivity in DFB waveguide [73]. The device was fabricated using a 300 nm thick InP upper cladding layer

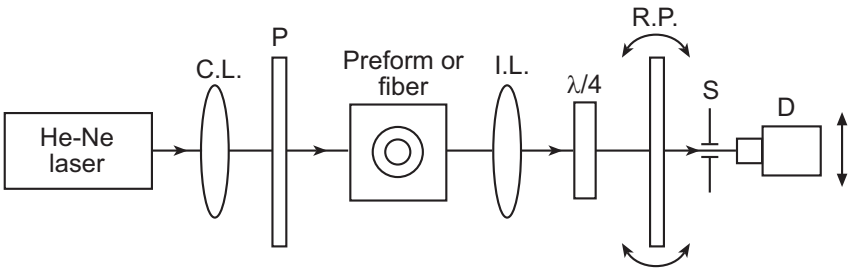

Figure 2.10: Stress-induced birefringence measurements in optical fibers and preforms using Sénarmont technique [16]. C.L., cylindrical lens; P, polarizer; I.L., imaging lens; $\lambda/4$, quarter-waveplate; R.P., rotating polarizer; S, slit; D, detector.

and a 450 nm thick GaInAsP guiding layer. The grating periodicity was set equal to 235 nm to operate at a wavelength of 1.55 μm. When the incident light spectrum is located into the stopband of the DFB region, the light is reflected. When the incident light contains wavelengths that can be pumped in the DFB region, the refractive index is modified due to the Kerr effect. The Bragg condition is no longer satisfied and the light is transmitted. Birefringence effects can be controlled by proper design of the width of the ridge waveguide. Polarization insensitivity was achieved for a waveguide width W equal to 1.1 μm.

2.3 Stress-Induced Birefringence Measurement

2.3.1 Single-Point Measurements Using Sénarmont Technique

Several methods have been developed for the measurement of stress-induced birefringence in optical fibers and preforms. Chu *et al.* measured residual stress in optical fibers and preforms using the experimental configuration shown in Fig. 2.10 [16]. The fiber is placed in index matching oil and its axis is oriented at 45 *deg* from extinction between crossed polarizers. A quarter-waveplate is inserted into the light path following the fiber with its fast and slow axes parallel to the polarizers transmission directions. A single beam of light is focused onto the optical fiber and imaged on a photodetector.

This is the well-known configuration of the Sénarmont technique [39, 40]. The light transmitted by the optical fiber is elliptically polarized with its polarization ellipse semi-axes coinciding with the crossed polarizers transmission directions and the quarter-waveplate fast and slow axes. The light incident onto the quarter-waveplate is subsequently decomposed

into two vibrations with amplitudes proportional to the polarization ellipse semi-axes and having a phase-difference of $\pi/2$. Another $\pi/2$ phase-difference is added or subtracted by the quarter-waveplate which produces a linearly polarized output whose orientation depends on the ratio of the polarization ellipse semi-axes of the light transmitted by the fiber. This ratio is directly related to the phase-shift introduced by the optical fiber. Rotating the analyzer so as to be perpendicular to the transmitted linearly polarized light therefore producing extinction allows the determination of the polarization orientation and of phase-shift undergone in the optical fiber. In fact, it can easily be shown that the analyzer angle θ_A producing extinction is simply related to the fiber phase-shift ϕ_f by

$$\phi_f = 2\theta_A. \tag{2.4}$$

The retardation R is given by

$$R = \frac{\theta_A}{\pi}\lambda, \tag{2.5}$$

where λ is the wavelength of the light source. In the experiment shown in Fig. 2.10, the sliding slit and photodetector are translated vertically to measure the retardation along the cross-section of the optical fiber point by point. The axial residual stress is computed using Eq. (2.3).

A similar experimental configuration such as that in Fig. 2.10 was used to study the amount of residual stress in optical fibers and preforms as a function of the dopants concentration and the drawing force [87, 88]. In this work, however, the sample was vertically translated instead of the photodetector.

The above technique suffers, however, from a limited spatial resolution because of the finite size of the single-beam illumination. Scanning is needed to obtain the complete birefringence profile which requires time and continuous realignment of the optical elements instead of making one single measurement for the entire sample. The scanning may also lead to inaccuracies because of uncertainties or errors in the vertical translation of either the detector [16] or the sample itself [87, 88]. Further, the Sénarmont technique is known to be accurate for retardations up to 1λ. However, its accuracy decreases with retardation which renders the Sénarmont technique unsuitable for measuring exceedingly small retardations

such as those produced by transversely illuminated optical fibers and waveguides [40].

2.3.2 Full-Field Measurements Using Polarization Microscopy

A polarization microscope equipped with a half-shade device allows the measurement of the residual stress profile in optical fibers without scanning the sample or the detector and achieving high spatial resolution [89]. A half-shade device consists of a linear polarizer and a half-waveplate placed before the condensing lens of the microscope. The polarizer transmission direction is oriented at what is defined as the half-shade angle so that the light focused onto the sample by the condenser is composed of two orthogonal polarizations. An interference image is formed after transmission through an analyzer. In a polarization microscope, the intensity variations in the image depend on the phase-difference variations in the sample caused by birefringence. The half-shade device divides the field-of-view into two regions with different background intensities producing two complementary images of the fiber with unequal intensity variations.

In the technique presented in Reference 89, two different intensity profiles are subtracted in the image on either side of the half-shade boundary along the axis of the optical fiber . The fiber birefringence is shown to be proportional to the intensity difference between those profiles under a small angle approximation.

Even though this method has proven successful in measuring birefringence in optical fibers, it does not take into account the variations along its axis. The intensities used in computing the birefringence are taken at two different locations which are not closely spaced. This renders impossible the birefringence profiling at any given cross-section of the fiber. In fact this technique computes an averaged birefringence between the two different axial positions at which the intensities are recorded on either side of the half-shade boundary. The small angle approximation also affects the accuracy of this technique.

Another possible experimental configuration to measure two-dimensional birefringence is shown in Fig. 2.11 [30, 31, 41, 90]. An inverted microscope is illuminated by a He-Ne laser followed by a diffuser to eliminate the speckle effect. A rotating polarizer and a quarter-waveplate with its fast and slow axes parallel to the crossed polarizers transmission

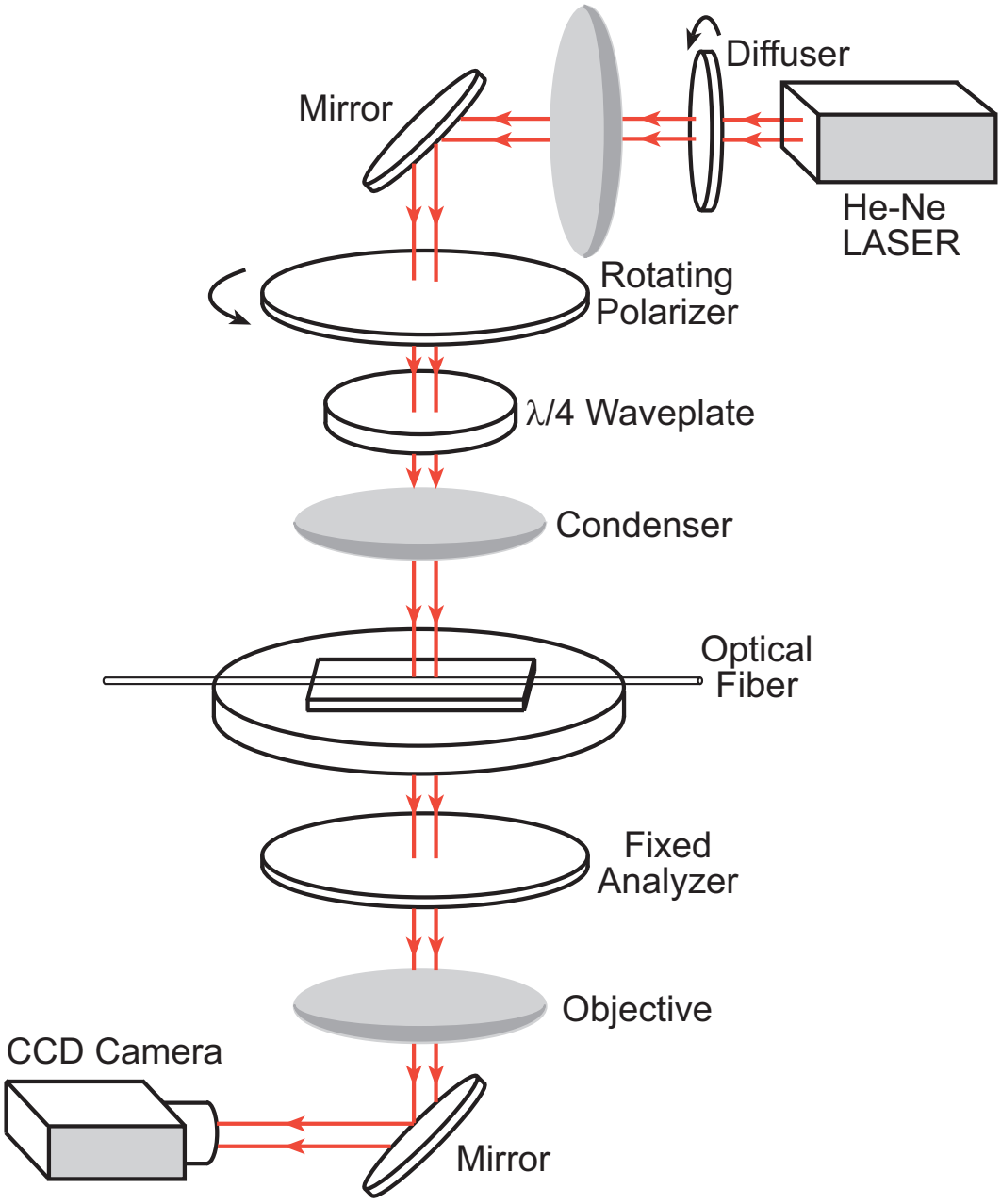

Figure 2.11: Two-dimensional birefringence measurement of optical fibers with polarization microscopy [30].

directions are inserted just before the condensing lens. The fiber is placed on the microscope stage with its axis at 45 *deg* from the analyzer transmission direction. The light is transmitted by the analyzer and an image is projected on a CCD camera after passing through the objective lens [30].

Studying the successive polarization states of the light on the Poincaré sphere, it was shown that by rotating the first polarizer, an elliptically polarized input can be generated which combined with the phase-shift introduced by the optical fiber produces a minimum of intensity after transmission by the analyzer. At that minimum, the relationship between the phase-shift Φ in the fiber and the angle η between the polarizer transmission direction and the fiber axis is

$$\Phi = \frac{\pi}{2} - 2\eta. \tag{2.6}$$

Measuring the angle η producing minimum intensity and using Eq. 2.6 allows the determination of the retardation and the retrieval of the axial residual stress profile in any cross-section of the optical fiber [30, 31, 41, 90].

In spite of the quarter waveplate being placed before the sample instead of after the sample, this technique bears similarities with the Sénarmont method. The analysis of the method presented in Reference 30 is done in terms of output intensity instead of the polarization of the light incident on the analyzer at minimum. It is worthwhile to study this polarization to determine if it is indeed a method identical to the Sénarmont technique.

The electric field is represented by a Jones vector expressed in the different systems of axes shown in Fig. 2.12. Using Jones calculus, the phasor $\vec{\mathcal{E}}_F$ transmitted by the optical fiber in the fiber system is given by,

$$\vec{\mathcal{E}}_F = T(\Phi)R(45^o)T(\frac{\pi}{2})R(-\theta)\begin{pmatrix}1\\0\end{pmatrix}, \tag{2.7}$$

where $R(45^o)$ and $R(-\theta)$ are rotation matrices of angles equal respectively to 45^o and $-\theta$, $T(\Phi)$ and $T(\frac{\pi}{2})$ are Jones transmission matrices of phase-shifts equal respectively to Φ and $\frac{\pi}{2}$. Similarly, the transmitted phasor $\vec{\mathcal{E}}_A$ in the analyzer system is given by

$$\vec{\mathcal{E}}_A = R(45^o)T(\Phi)R(45^o)T(\frac{\pi}{2})R(-\theta)\begin{pmatrix}1\\0\end{pmatrix}. \tag{2.8}$$

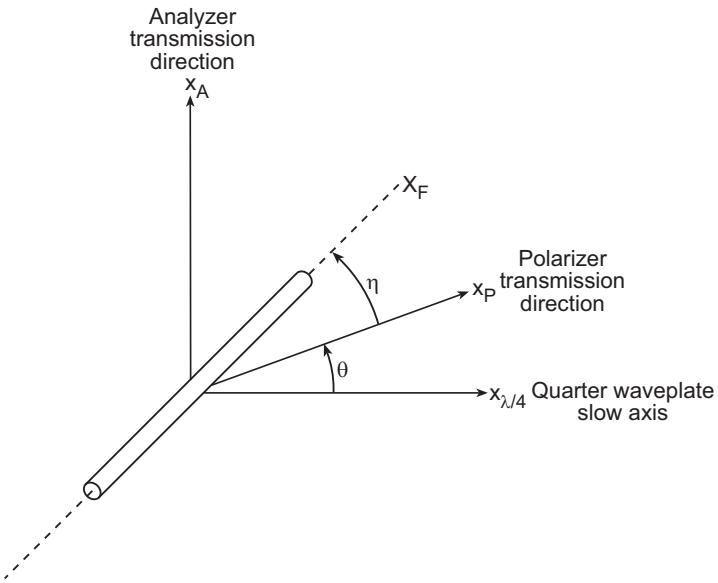

Figure 2.12: System of axes for the optical elements in Fig. 2.11. $x_{\lambda/4}$, quarter-waveplate slow axis; x_P, polarizer transmission direction; x_A, analyzer transmission direction; θ, angle between polarizer transmission direction and fiber axis; η, angle between polarizer transmission direction and fiber axis.

Carrying out the matrix multiplications,

$$\vec{\mathcal{E}}_F = \frac{1}{\sqrt{2}} \begin{pmatrix} e^{j\theta} \\ -e^{j(\Phi-\theta)} \end{pmatrix}, \tag{2.9}$$

$$\vec{\mathcal{E}}_A = \begin{pmatrix} -je^{j\frac{\Phi}{2}} \sin(\frac{\Phi}{2}) \\ -e^{j\frac{\Phi}{2}} \cos(\frac{\Phi}{2}) \end{pmatrix}. \tag{2.10}$$

The intensity I_A transmitted by the analyzer is derived

$$I_A = \mathcal{E}_{Ax}\mathcal{E}^*_{Ax}, \tag{2.11}$$

$$= \sin^2(\frac{\Phi}{2} - \theta), \tag{2.12}$$

with $\mathcal{E}_{Ax}$ the component of the Jones vector $\vec{\mathcal{E}}_A$ along the transmission direction of the analyzer x_A. Equation (2.12) is equal to zero when

$$2\theta = \Phi, \tag{2.13}$$

in which case extinction is obtained. When Eq. (2.13) is satisfied, the phase-shift between the two components of the Jones vector $\vec{\mathcal{E}}_F$ is equal to zero and the light is linearly polarized. Equation (2.13) is equivalent to the Sénarmont technique formula Eq. (2.4) introduced

earlier. Even though the angle θ between the quarter-waveplate slow axis and the polarizer transmission direction is considered for this analysis, substituting $\theta = \frac{\pi}{4} - \eta$ into Eq. (2.13) leads to Eq. (2.6) used in the method developed in Reference 30. The method presented in Reference 30 is thereby identical to the Sénarmont technique and bears the same disadvantages outlined in Sec. 2.3.1 to measure exceedingly small retardations such as those present in optical fibers.

2.4 Motivation

Birefringence is induced in optical devices due to the presence of residual stress through the photoelastic effect. Stress-induced birefringence may be detrimental to the quality, reliability, and performance of optical fibers and interconnects. This motivates the need to measure and control the amount of stress-induced birefringence. The accuracy of the currently available techniques to measure birefringence and stress in optical fibers does not seem suitable for the measurement of small retardations produced by transversely illuminated optical fibers.

New birefringence measurement techniques need to be developed to accurately measure stress-induced birefringence. The accuracies of these new techniques need to be determined and compared to those of the existing available techniques. These high-accuracy birefringence measurement methods may then be used to evaluate the tolerable amount of stress-induced birefringence in optical fibers and interconnects in terms of their performance and reliability. Having determined the tolerable birefringence levels, these birefringence measurement techniques can be used during and after the manufacturing process to assess the usability of optical devices.

In this thesis, the existing Brace-Köhler technique and the new Two-Waveplate-Compensator (TWC) technique are investigated for the accurate measurement of stress-induced birefringence and residual stress in optical fibers and interconnects. Their accuracies are evaluated for single-point and full-field retardation measurements.

CHAPTER 3

COMPENSATION TECHNIQUES

Compensation techniques consist of using a waveplate of known retardation to compensate or minimize the retardation produced by a sample of unknown retardation placed between crossed polarizers. The optical elements composing a two-waveplate system are shown in Fig. 3.1.

With the Sénarmont technique, the unknown retardation is oriented at 45 *deg* from extinction and followed by a quarter-waveplate whose fast or slow axis is parallel to the polarizer transmission direction. In this configuration, the light transmitted by the quarter waveplate is linearly polarized and the polarization angle is directly related to the phase retardation of the unknown waveplate. Rotating the analyzer until extinction occurs allows the determination of the unknown retardation.

The Brace-Köhler technique is usually used to measure low-level retardations. A mica waveplate of known small retardation is rotated to minimize the phase-shift produced by the unknown waveplate at 45 *deg* from extinction. A small retardation approximation allows the determination of the unknown retardation. In this chapter, both techniques will be studied in terms of their applicability range, resolution, and accuracy.

3.1 Sénarmont Compensator

3.1.1 Two-Waveplate System Analysis

The Sénarmont compensator technique is a well-known technique to measure retardations from 0 to λ. The experimental configuration of the Sénarmont technique is represented in Fig. 3.2. The unknown retardation, Sample in Fig. 3.2, is oriented at 45 *deg* from extinction. Waveplate 2 is a quarter-waveplate oriented at extinction, i.e., its slow axis is parallel to the polarizer transmission direction. The polarizers are first crossed. Jones calculus is used to analyze the polarization and intensity of the light transmitted through the optical system [3].

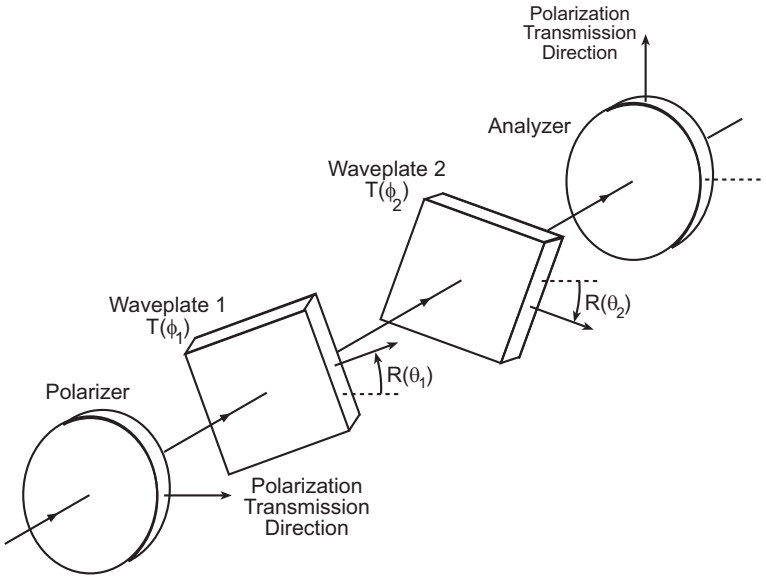

Figure 3.1: Waveplate 1 and Waveplate 2 with retardations equal ϕ_1 and ϕ_2 are placed between crossed polarizers. Waveplate 1 and Waveplate 2 slow axis angles with respect to the first polarizer transmission direction are θ_1 and θ_2 respectively. The Jones rotation matrices are $\mathrm{R}(\theta_1)$ and $\mathrm{R}(\theta_2)$ respectively and the Jones transmission matrices, $\mathrm{T}(\phi_1)$ and $\mathrm{T}(\phi_2)$.

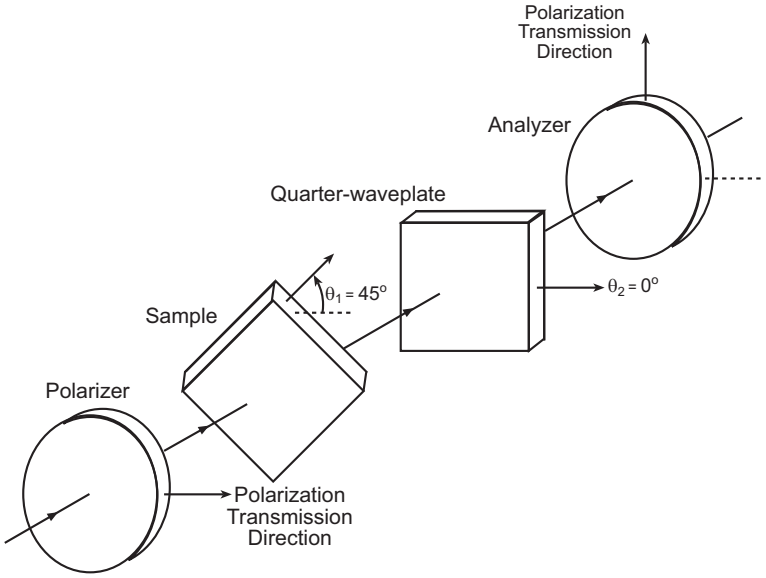

Figure 3.2: Two-waveplate configuration of the Sénarmont technique. The sample is at 45^o from extinction followed by a quarter-waveplate at extinction.

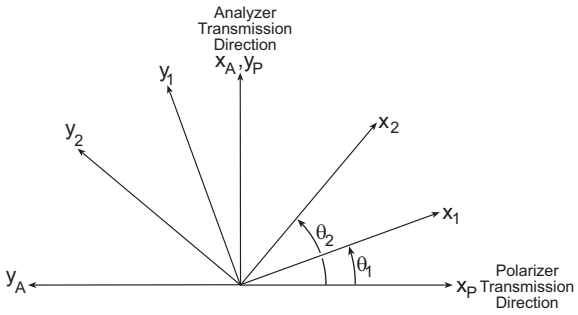

Figure 3.3: The axes x_P and x_A are the polarization transmission directions of the polarizer and analyzer. The waveplates slow axes are x_1 and x_2, their fast axes are y_1 and y_2. The waveplates slow axes angles with respect to the polarizer transmission direction x_P are θ_1 and θ_2.

The Jones transmission matrices of Waveplate 1 and Waveplate 2 are respectively $T(\phi_1)$ and $T(\phi_2)$ in Fig. 3.1, and the Jones rotation matrices corresponding to the angle between the polarizer transmission direction and the slow axes of Waveplate 1 and Waveplate 2 are $R(\theta_1)$ and $R(\theta_2)$. The different systems of axes for each optical element are represented in Fig. 3.3. The polarization transmission directions of the polarizer and the analyzer are respectively x_P and x_A whereas the slow axes of the waveplates of phase-shift ϕ_1 and ϕ_2 are respectively x_1 and x_2 in Fig. 3.3. Throughout this analysis, the Jones transmission matrix $T(\phi)$ of an optical element producing a phase-shift ϕ is defined as

$$T(\phi) = \begin{pmatrix} 1 & 0 \\ 0 & e^{j\phi} \end{pmatrix}, \tag{3.1}$$

and the rotation matrix $R(\theta)$ for a rotation of angle θ is

$$R(\theta) = \begin{pmatrix} \cos\theta & \sin\theta \\ -\sin\theta & \cos\theta \end{pmatrix}. \tag{3.2}$$

The Jones vector $\vec{\mathcal{E}}_1$ characteristic of the electric field transmitted by Waveplate 1 and defined in the polarizer system of axes x_P and y_P is

$$\vec{\mathcal{E}}_1 = R(-\theta_1)T(\phi_1)R(\theta_1)\begin{pmatrix} 1 \\ 0 \end{pmatrix}. \tag{3.3}$$

The two-waveplate configuration of the Sénarmont technique is represented in Fig. 3.2. Substituting $\theta_1 = 45^o$ and carrying out the matrix multiplication leads to

$$\vec{\mathcal{E}}_1 = \begin{pmatrix} \frac{1}{2} + \frac{1}{2}e^{j\phi_1} \\ \frac{1}{2} - \frac{1}{2}e^{j\phi_1} \end{pmatrix}. \tag{3.4}$$

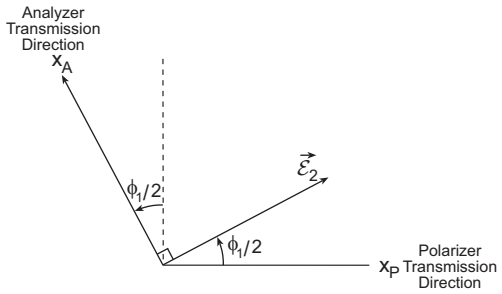

Figure 3.4: Analyzer position producing extinction with the Sénarmont method. $\vec{\mathcal{E}}_2$ is the Jones vector representing the electric field transmitted by the quarter-waveplate. The electric field polarization angle relative to the polarizer transmission direction is exactly equal to half the phase-shift produced by Waveplate 1. The Analyzer must be rotated by an angle $\phi_1/2$ to produce extinction.

Factoring out $e^{j\frac{\phi_1}{2}}$ and using the complex forms of the sine and cosine functions gives

$$\vec{\mathcal{E}}_1 = e^{j\frac{\phi_1}{2}} \begin{pmatrix} \cos\dfrac{\phi_1}{2} \\ -j\sin\dfrac{\phi_1}{2} \end{pmatrix}. \tag{3.5}$$

The Jones vector $\vec{\mathcal{E}}_2$ of the electric field transmitted by Waveplate 2 and defined in the polarizer system of axes is obtained by multiplying $\vec{\mathcal{E}}_1$ with the Jones transmission matrix $T(\phi_2)$ and is

$$\vec{\mathcal{E}}_2 = T(\phi_2)\vec{\mathcal{E}}_1. \tag{3.6}$$

In the case of the Sénarmont technique, Waveplate 2 is a quarter-waveplate. Substituting $\phi_2 = \pi/2$ in the above equation, $\vec{\mathcal{E}}_2$ becomes

$$\vec{\mathcal{E}}_2 = \begin{pmatrix} 1 & 0 \\ 0 & e^{j\frac{\pi}{2}} \end{pmatrix} e^{j\frac{\phi_1}{2}} \begin{pmatrix} \cos\dfrac{\phi_1}{2} \\ -j\sin\dfrac{\phi_1}{2} \end{pmatrix}. \tag{3.7}$$

Carrying out the matrix multiplication and substituting $j = e^{j\pi/2}$, the Jones vector of the electric field transmitted by Waveplate 2 is

$$\vec{\mathcal{E}}_2 = e^{j\frac{\phi_1}{2}} \begin{pmatrix} \cos\dfrac{\phi_1}{2} \\ \sin\dfrac{\phi_1}{2} \end{pmatrix}. \tag{3.8}$$

The configuration producing extinction of the light transmitted by the quarter-waveplate is represented in Fig. 3.4. According to Eq. (3.8), the electric field transmitted by the quarter-waveplate is at an angle equal to $\frac{\phi_1}{2}$ from the polarizer transmission direction as is shown in Fig. 3.4. The analyzer must be rotated by the same amount to be perpendicular to

the electric field. The analyzer angle producing extinction is exactly equal to half the phase-shift ϕ_1 produced by the sample Waveplate 1. This is the basis for the Sénarmont method. Assuming ξ is the analyzer angle producing extinction, it is related to the phase-shift ϕ_1 of Waveplate 1 by

$$\phi_1 = 2\xi. \tag{3.9}$$

The corresponding retardation R_1 is thus

$$R_1 = \frac{\phi_1}{2\pi}\lambda \tag{3.10}$$

$$R_1 = \frac{\xi}{\pi}\lambda, \tag{3.11}$$

where λ is the wavelength. Equation (3.11) is valid when the sample retardation is less than one wavelength which corresponds to zero-order retardation. The sample retardation may be greater than one wavelength and Eq. (3.11) can be generalized for any given order of retardation and is

$$R_1 = (n + \frac{\xi}{\pi})\lambda, \tag{3.12}$$

with n, an integer associated with the retardation order. For retardations between 0 and λ, n is equal to 0. For retardations between λ and 2λ, n is equal to 1 and so on. The retardation order can be determined by observing the white-light interference color [40].

3.1.2 Applicability Range

The applicability range of the Sénarmont compensator technique is defined by Eq. (3.12). The analyzer angle producing extinction for samples retardations ranging from 0 to 4λ is represented in Fig. 3.5. Since the analyzer angle producing extinction is half the phase-shift of the sample (Waveplate 1), it only needs to be rotated over a total angular range of 180 *deg* as the retardation increases to a full wavelength. The analyzer angle does not however allow the determination of the retardation order. Retardations separated by exactly a full-wavelength produce equal phase-shifts and when using the Sénarmont technique, the measured analyzer angles are also equal. This is seen in Fig 3.5 where the analyzer angle varies periodically from 0 to 180 *deg* as the sample retardation increases from 0 to 4λ.

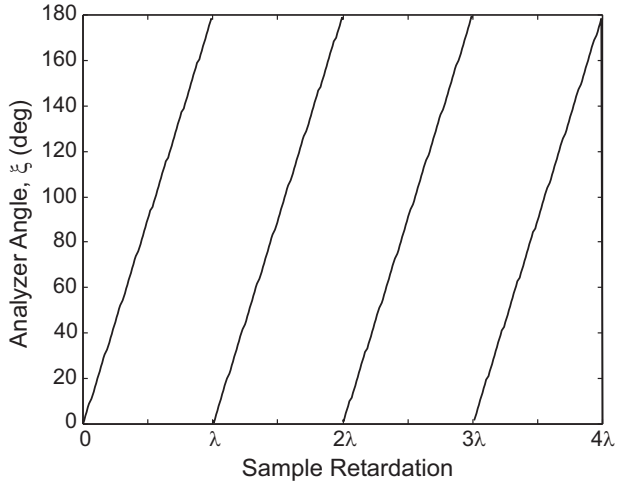

Figure 3.5: Analyzer angle producing extinction in the Sénarmont compensator technique for samples of retardation ranging from 0 to 4λ.

A white-light interference color chart such as that in Fig. 3.6 can be used to determine the retardation order [40].

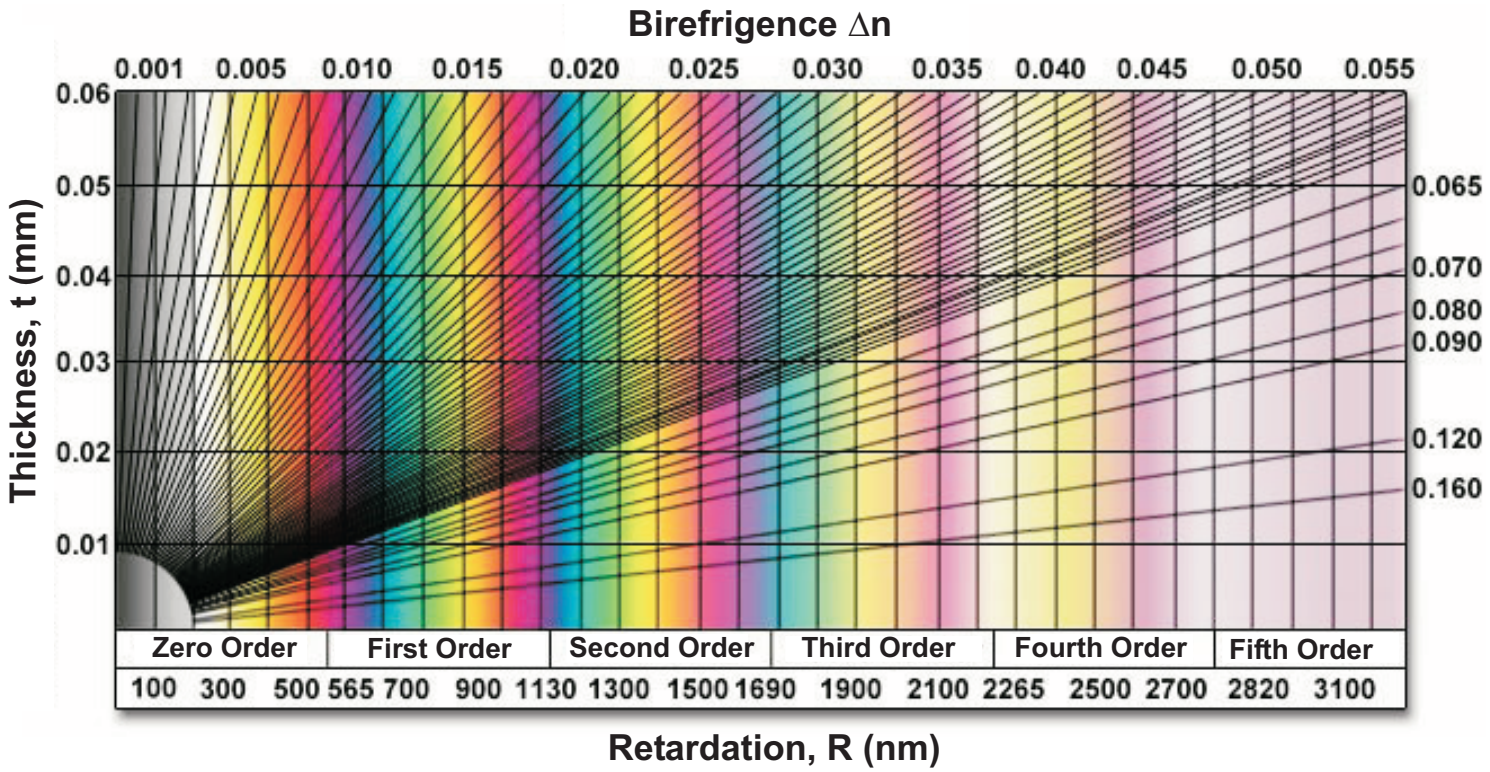

Figure 3.6: White-light interference color chart. The colors are shown for retardations R from 0 to 3300 nm. The corresponding thickness t (vertical axis) and the birefringence Δn (diagonal lines) are also indicated.

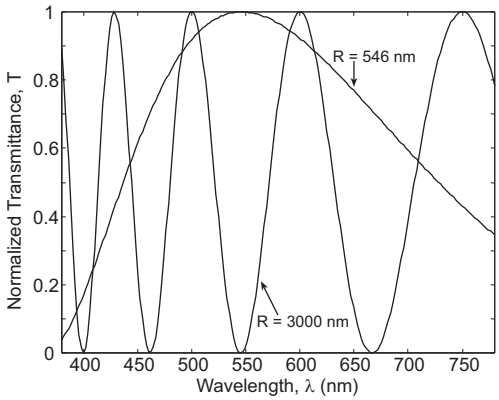

Figure 3.7: Transmittance between crossed polarizers for retardations $R = 546\ nm$ and $R = 3000\ nm$.

This color chart allows the determination of the white-light interference colors produced by increasing retardations R. The retardation is related to the thickness t and the birefringence Δn by

$$R = t\Delta n, \tag{3.13}$$

where R and t are expressed in the same length units and Δn is the difference between the ordinary and extraordinary refractive indices of the birefringent material. The color chart in Fig. 3.6 indicates the thickness t and the birefringence Δn on the vertical axis and the diagonal lines corresponding to the retardation values along the horizontal axis.

The zero-order retardation is usually delimited by the e-line, i.e., $R = 546\ nm$. When a sample is observed between crossed polarizers in white-light, the interference color produced is first compared to the color chart and allows the determination of the retardation order. The Sénarmont compensator measurement is then made with a polarization microscope for example by inserting an interference filter whose transmittance is centered at 546 nm (green line) in front of the light source. Having previously determined the retardation order n, Eq. (3.12) is used to determine the retardation by substituting $\lambda = 546\ nm$.

As the retardation increases, the white-light interference colors become more and more washed out which renders difficult the determination of the retardation order. The normalized transmittance T between crossed polarizers is given by,

$$T = \cos^2\Big(\frac{R}{\lambda}\pi\Big). \tag{3.14}$$

Table 3.1: Resolution ΔR of the Sénarmont technique for various angular resolutions $\Delta\xi$ for $\lambda = 546\ nm$.

$\Delta\xi$ (deg)	ΔR (nm)
1	3
0.1	0.3
0.01	0.03
0.001	0.003
0.0001	0.0003

The transmittance for retardations $R = 546\ nm$ and $R = 3000\ nm$ is plotted as a function of wavelength in Fig 3.7. The transmittance for $R = 546\ nm$ is seen as a bright purple on the color chart and corresponds to the first-order fringe. The transmittance for $R = 3000\ nm$ is seen as a very washed out pink on the color chart and is in the fifth-order retardation area. As the retardation increases, the transmittance oscillates more as a function of wavelength and the color of the transmitted light appears almost white. Considering that it is difficult to determine the retardation order beyond the fourth order, the Sénarmont compensator technique is thus applicable for retardations ranging from 0 to 5λ using the white-light interference color chart and Eq. (3.12).

3.1.3 Resolution

The resolution is defined by the smallest retardation difference measurable with the Sénarmont compensator technique. This is calculated using the relationship between the phase-shift due to the sample and the analyzer angle producing extinction in Eq. (3.9). Considering a phase-shift change $\Delta\phi$ produced by a retardation change ΔR in a sample, the corresponding analyzer angular change $\Delta\xi$ is

$$\Delta\xi = \frac{\Delta\phi}{2}. \tag{3.15}$$

The smallest measurable retardation difference is thus directly related to the angular resolution of the rotation mount in which the analyzer is placed. The resolution of the Sénarmont technique is calculated for $\lambda = 546\ nm$ in Table 3.1 for different angular resolutions $\Delta\xi$. The Sénarmont technique can achieve a very good resolution provided the analyzer can be

rotated in sufficiently small angular increments.

3.1.4 Error Analysis

The main parameters in the optical system of the Sénarmont technique governing the measurement accuracy are the retardation and orientation of the quarter-waveplate [91]. In theory, it is assumed that a perfect quarter-waveplate is used and that its fast or slow axis is exactly oriented parallel to the polarizer transmission direction. In reality, this is often not the case and even though the retardation error and misalignment may be very small, this impacts drastically the retardation measurement of the sample.

When the quarter-waveplate retardation and orientation are incorrect, the light transmitted is elliptically polarized instead of linearly polarized. Rotating the analyzer as is usually done with the Sénarmont technique produces a minimum of intensity when its transmission direction is perpendicular to the minor axis of the ellipse of polarization. The difference between the inclination of the minor axis of the ellipse and the linearly polarized output produced with ideal conditions is used to compute the measurement error for a given sample's retardation. The relative error is represented in color plots as a function of quarter-waveplate error and misalignment.

The relative measurement error is calculated in Figs. 3.8(a) and 3.8(b) for two samples' retardations respectively equal to 200 nm and 100 nm. A wavelength of 546 nm is used for this calculation corresponding to the center wavelength of a narrow-band interference filter commonly used with a Olympus polarization microscope for measuring retardations with the Sénarmont technique. For a maximum quarter-waveplate error of 5 nm and a maximum misalignment of 3 deg, the maximum error for a sample with a retardation of 200 nm is 4.5% which corresponds to 9 nm. The relative measurement error doubles for a sample with a retardation of 100 nm with maximum error increasing to 9% which also corresponds to 9 nm. The absolute measured retardation deviation remains approximately the same for both samples' retardations over the same range of quarter-waveplate error and misalignment. The relative measurement error thereby increases as the sample's retardation decreases.

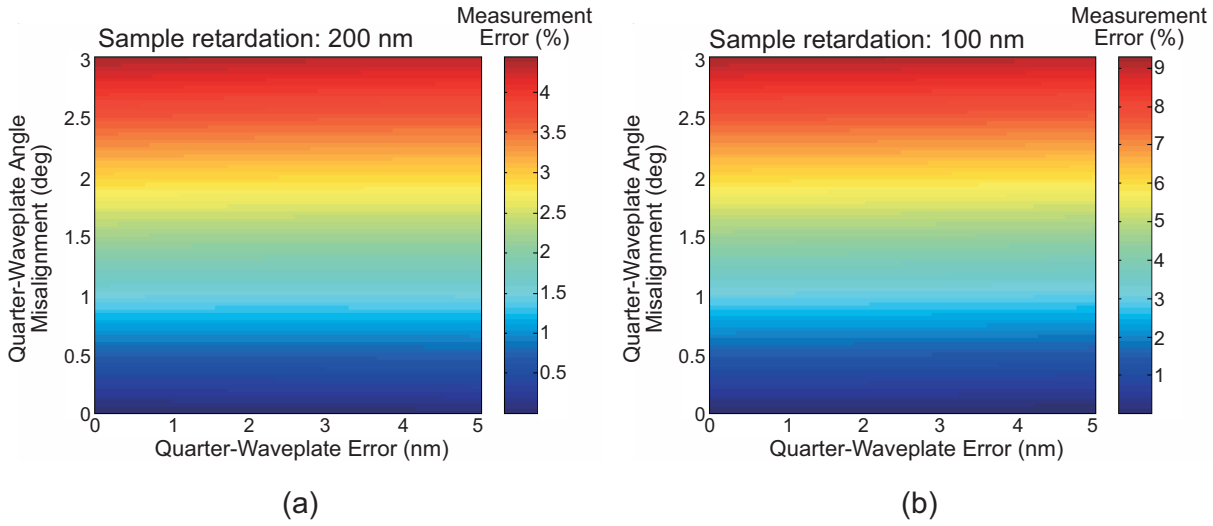

Figure 3.8: Measurement error of the Sénarmont technique as a function of quarter-waveplate error and misalignment at a wavelength of 546 nm. (a) The sample's retardation is equal to 200 nm (b) The sample's retardation is equal to 100 nm.

This makes the Sénarmont technique unsuitable for measuring the exceedingly small retardations produced by optical devices. The relative measurement error as a function of quarter-waveplate error and misalignment is also calculated for samples' retardations equal to 20 and 10 nm in Figs. 3.9(a) and 3.9(b).

As the sample's retardation decreases, the measurement accuracy is more sensitive to the quarter-waveplate error but mostly to its misalignment. The maximum error produced for a sample of retardation 20 nm in Fig. 3.9(a) is about 30% for a misalignment of 2 deg. This corresponds to an absolute retardation deviation of 6 nm. This becomes worse with a sample of retardation equal to 10 nm in Fig. 3.9(b) with the maximum error reaching 30% corresponding to a deviation of 3 nm for a quarter-waveplate misalignment of only 1 deg.

This high sensitivity to the quarter-waveplate misalignment renders the accuracy of the Sénarmont technique extremely low for very small samples' retardations. This will also be demonstrated experimentally in this research.

3.2 Brace-Köhler Compensator

The Brace-Köhler compensator retardation measurement method, also known as the elliptic compensator method, consists in finding a minimum of intensity by rotating a compensator

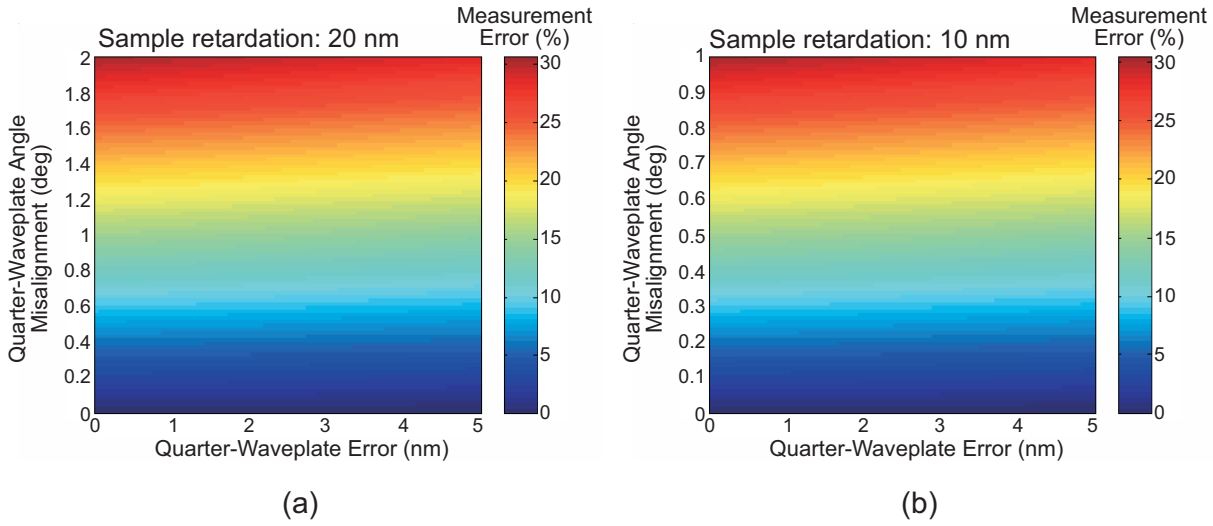

Figure 3.9: Measurement error of the Sénarmont technique as a function of quarter-waveplate error and misalignment at a wavelength of 546 nm. (a) The sample's retardation is equal to 20 nm (b) The sample's retardation is equal to 10 nm.

waveplate in order to determine a sample retardation. The two waveplates are placed between crossed polarizers. With the sample at 45 deg from extinction, the compensator angle producing a minimum and measured from the compensator extinction position allows the calculation of the sample retardation R_S [39],

$$R_S = -R_C \sin(2\theta_C), \tag{3.16}$$

with R_C the compensator retardation, and θ_C the compensator angle. Equation (3.16) is only valid if the compensator retardation is greater than the sample retardation. When the sample retardation is greater, the role of both waveplates are inverted and the sample is rotated until an intensity minimum is obtained in which case the sample retardation is computed using,

$$R_S = -\frac{R_C}{\sin(2\theta_S)}, \tag{3.17}$$

3.2.1 Two-Waveplate System Analysis

The analysis and the understanding of the working principle of the Brace-Köhler compensator necessitates the development of a numerical tool to calculate the light intensity transmitted through the optical system. The optical elements to be considered in the

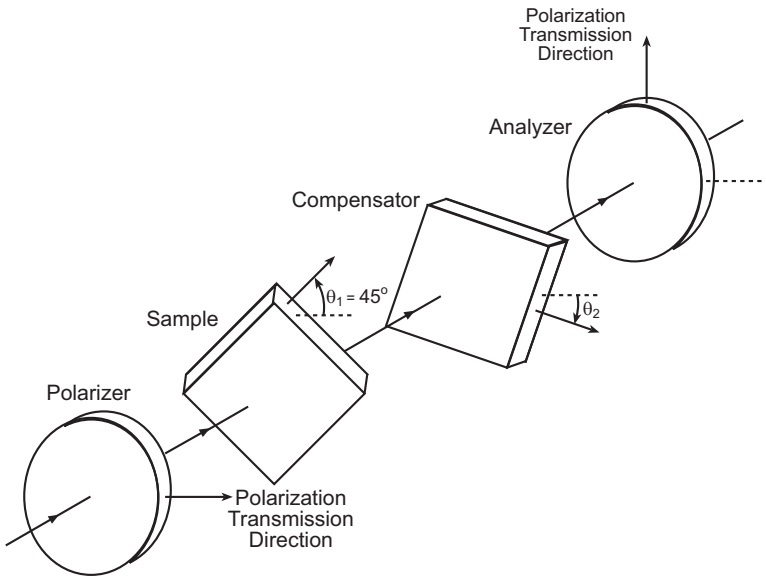

Figure 3.10: Two-waveplate configuration of the Brace-Köhler technique. The sample is at 45^o from extinction followed by a compensator of known retardation. The compensator is rotated in order to obtain a minimum of intensity between crossed polarizers.

Brace-Köhler compensator case are represented in Fig. 3.10. Two waveplates producing respectively phase-shifts ϕ_1 and ϕ_2 are placed between crossed polarizers. The orientations of their slow axes relative to the polarizer transmission direction are respectively θ_1 and θ_2. Jones calculus is also used to determine the output intensity [3].

The output light intensity is computed by calculating first the Jones vector $\vec{\mathcal{E}}_A$ in the system of the analyzer after traveling through the optical system

$$\vec{\mathcal{E}}_A = R(\frac{\pi}{2} - \theta_2)T(\phi_2)R(\theta_2 - \theta_1)T(\phi_1)R(\theta_1)\begin{pmatrix}1\\0\end{pmatrix}, \tag{3.18}$$

with rotation matrices $R(\theta_1)$, $R(\theta_2-\theta_1)$ and $R(\pi/2-\theta_2)$ representing respectively rotations of angle θ_1, $\theta_2 - \theta_1$, and $\pi/2 - \theta_2$, transmission matrices $T(\phi_1)$ and $T(\phi_2)$ representing transmission through the waveplates of phase-shifts ϕ_1 and ϕ_2. Normalizing the Jones vector exiting the first polarizer, the Jones vector $\vec{\mathcal{E}}_A$ exiting the analyzer is given by

$$\begin{aligned}\vec{\mathcal{E}}_A \;=\; & \begin{pmatrix}\sin\theta_2 & \cos\theta_2\\ -\cos\theta_2 & \sin\theta_2\end{pmatrix}\begin{pmatrix}1 & 0\\ 0 & \exp^{j\phi_2}\end{pmatrix}\begin{pmatrix}\cos(\theta_2-\theta_1) & \sin(\theta_2-\theta_1)\\ -\sin(\theta_2-\theta_1) & \cos(\theta_2-\theta_1)\end{pmatrix}\\ & \begin{pmatrix}1 & 0\\ 0 & e^{j\phi_1}\end{pmatrix}\begin{pmatrix}\cos\theta_1 & \sin\theta_1\\ -\sin\theta_1 & \cos\theta_1\end{pmatrix}\begin{pmatrix}1\\0\end{pmatrix}.\end{aligned} \tag{3.19}$$

Performing the matrix multiplication gives

$$\vec{\mathcal{E}}_A = \begin{pmatrix} \sin\theta_2\cos\theta_1\cos(\theta_2-\theta_1) - \sin\theta_2\sin\theta_1\sin(\theta_2-\theta_1)e^{j\phi_1} \\ -\cos\theta_2\cos\theta_1\sin(\theta_2-\theta_1)e^{j\phi_2} - \cos\theta_2\sin\theta_1\cos(\theta_2-\theta_1)e^{j(\phi_1+\phi_2)} \\ \\ -\cos\theta_2\cos\theta_1\cos(\theta_2-\theta_1) + \cos\theta_2\sin\theta_1\sin(\theta_2-\theta_1)e^{j\phi_1} \\ -\sin\theta_2\cos\theta_1\sin(\theta_2-\theta_1)e^{j\phi_2} - \sin\theta_2\sin\theta_1\cos(\theta_2-\theta_1)e^{j(\phi_1+\phi_2)} \end{pmatrix}. \quad (3.20)$$

The component of the Jones vector corresponding to the analyzer transmission direction is the component along the x_A axis of the analyzer system according to the convention defined in Fig (3.3). The intensity I_A transmitted through the analyzer can thus be computed and is given by

$$\begin{aligned} I_A &= \mathcal{E}_{A_x}.\mathcal{E}^*_{A_x} \\ &= \sin^2\theta_2\{\cos^2\theta_2\cos^2\frac{\phi_1}{2} + \cos^2(2\theta_1-\theta_2)\sin^2\frac{\phi_1}{2}\} \\ &\quad + \cos^2\theta_2\{\sin^2\theta_2\cos^2\frac{\phi_1}{2} + \sin^2(2\theta_1-\theta_2)\sin^2\frac{\phi_1}{2}\} \\ &\quad -\frac{1}{2}\sin 2\theta_2\{\sin 2\theta_2\cos^2\frac{\phi_1}{2}\cos\phi_2 - \sin(4\theta_1-2\theta_2)\cos\phi_2\sin^2\frac{\phi_1}{2} \\ &\quad\quad - \sin 2\theta_1\sin\phi_1\sin\phi_2\}. \quad (3.21) \end{aligned}$$

The above expression represents the intensity transmitted through an optical system composed of two waveplates arbitrarily oriented and placed between crossed polarizers. Having normalized the Jones vector characteristic of the electric field transmitted through the first polarizer, Eq. (3.21) allows the computation of the intensity transmitted through the optical elements relative to that exiting the first polarizer.

In the particular case of the Brace-Köhler compensator, the fixed waveplate is oriented at 45 *deg* from extinction. Assuming the fixed waveplate produces the phase-shift ϕ_1 in Fig. 3.10 and the rotating waveplate produces the phase-shift ϕ_2, the relative intensity I_{BK} transmitted in the case of the Brace-Köhler compensator can be computed by substituting θ_1 equal $\pi/4$ into Eq. (3.21)

$$\begin{aligned} I_{BK} &= I_A(\theta_1 = \frac{\pi}{4}) \\ &= 2\sin^2\theta_2\cos^2\theta_2\cos^2\frac{\phi_1}{2} + \sin^2\frac{\phi_1}{2}\{\sin^4\theta_2 + \cos^4\theta_2\} \end{aligned}$$

$$-\frac{1}{2}\sin 2\theta_2\{\sin 2\theta_2 \cos^2\frac{\phi_1}{2}\cos\phi_2 - \sin 2\theta_2 \cos\phi_2 \sin^2\frac{\phi_1}{2} - \sin\phi_1 \sin\phi_2\}. \quad (3.22)$$

Using trigonometric identities, Eq. (3.22) can be simplified to

$$I_{BK\perp} = \sin^2 2\theta_2 \cos\phi_1 \sin^2\frac{\phi_2}{2} + \frac{1}{2}\sin 2\theta_2 \sin\phi_1 \sin\phi_2 + \sin^2\frac{\phi_1}{2}, \quad (3.23)$$

where the subscript $\perp$ indicates that the polarizers are crossed. A similar approach allows the derivation of the intensity between parallel polarizers by considering the Jones vector component along the y_A axis of the analyzer system

$$I_{BK\parallel} = -\sin^2 2\theta_2 \cos\phi_1 \sin^2\frac{\phi_2}{2} - \frac{1}{2}\sin 2\theta_2 \sin\phi_1 \sin\phi_2 + \cos^2\frac{\phi_1}{2}. \quad (3.24)$$

Assuming no reflection or absorption of the optical system, both intensities satisfy

$$I_{BK\perp} + I_{BK\parallel} = 1 \quad (3.25)$$

The Brace-Köhler compensator retardation measurement method assumes that the retardations of the sample and the compensator are small [39]. Under the small retardation approximation, Eq. (3.23) leads to the following intensity

$$I_{APX} = \left(\frac{\phi_1}{2} + \frac{\phi_2}{2}\sin 2\theta_2\right)^2, \quad (3.26)$$

with I_{APX} representing the transmitted intensity under the small retardation approximation. Under this approximation, a null of intensity is obtained when

$$\begin{aligned} \frac{\phi_1}{2} + \frac{\phi_2}{2}\sin 2\theta_2 &= 0 \\ \phi_1 &= -\phi_2 \sin 2\theta_2. \end{aligned} \quad (3.27)$$

Note that Eq. (3.27) is valid only if $\phi_1 \leqslant \phi_2$, i.e., the retardation of the fixed waveplate is less than or equal to the retardation of the rotating waveplate. When the sample retardation is less than or equal to the compensator retardation, the sample waveplate is fixed at 45 *deg* from extinction and the compensator waveplate is rotated [39]. The phase-shift ϕ_1 produced by the sample is then given by Eq. (3.27). When the sample retardation is greater than the compensator retardation, the compensator waveplate is fixed at 45 *deg* from extinction and

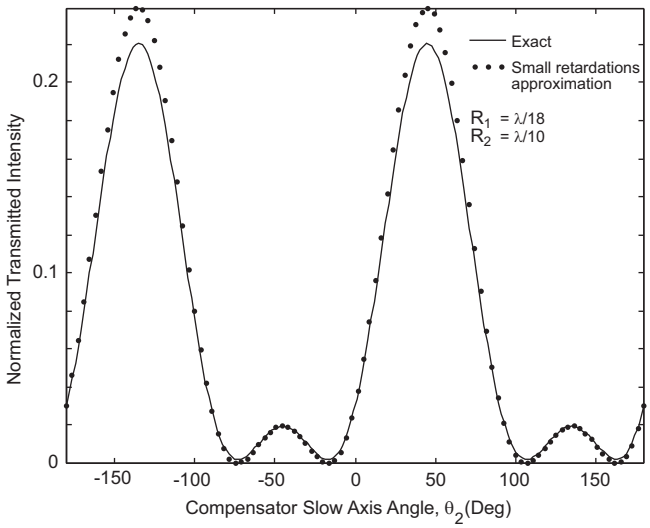

Figure 3.11: In a two-waveplate system, the first sample of retardation $R_1 = \lambda/18$ is at 45 *deg* from extinction and the compensator of retardation $R_2 = \lambda/10$ is rotated. The intensity is plotted as a function of the compensator slow axis angle θ_2. The solid line represents the exact intensity, the dotted line represents the intensity calculated using a small retardation approximation.

the sample waveplate is rotated. The phase shift ϕ_2 produced by the sample is then given by

$$\phi_2 = -\frac{\phi_1}{\sin 2\theta_2}. \tag{3.28}$$

The transmitted intensities calculated using Eq. (3.23) and Eq. (3.26) are plotted in Fig. 3.11. The compensator phase-shift ϕ_2 corresponds to $\lambda/10$ as it is the value of a commercially available Brace-Köhler compensator manufactured by Olympus. The sample phase-shift ϕ_1 is arbitrarily chosen to correspond to $\lambda/18$. The intensity minima produced when the compensator is rotated are not nulls of intensity. The reason complete extinction can not be produced with the Brace-Köhler compensator can be understood by determining the successive polarization states of the light in the two-waveplate system of Fig. 3.11. It will be seen later how the compensator angle producing minimum of intensity is calculated analytically. The successive polarization states when the compensator waveplate is rotated to produce an intensity minimum are shown in Fig. 3.12. These polarization states have been determined using the waveplates retardation values of Fig. 3.11. After traveling through the sample, the light is elliptically polarized and the principal axes of the ellipse traced by the

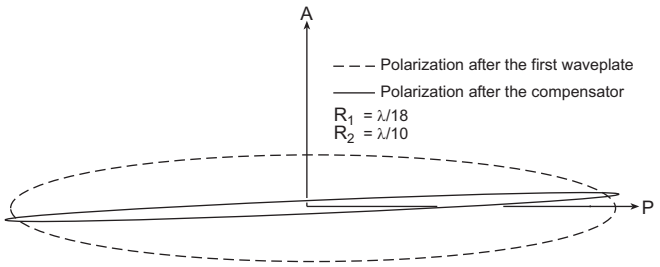

Figure 3.12: Polarization resulting from a sample of retardation $R_1 = \lambda/18$ and a compensator of retardation $R_2 = \lambda/10$ placed between crossed polarizers. The polarizer and analyzer transmission directions are P and A. The sample is at 45 *deg* from extinction and the compensator slow axis angle with respect to P is $\theta_2 = -17.03^o$. In this configuration, the intensity transmitted through the analyzer is minimum.

electric field coincide with the polarization transmission directions of the crossed polarizers. This ellipse of polarization is represented by the dashed line in Fig. 3.12. The compensator angle necessary to obtain a minimum of intensity along the transmission direction of the analyzer for $R_1 = \lambda/18$ and $R_2 = \lambda/10$ is equal to -17.03 *deg*. The electric field exiting the compensator is calculated using Jones calculus and the corresponding ellipse of polarization is shown as a solid line in Fig. 3.12. The electric field exiting the compensator is elliptically polarized. The major axis of the ellipse traced by the electric field incident upon the analyzer makes an angle equal to 2.4 *deg* with respect to the polarizer transmission direction. In the Brace-Köhler configuration, the minimum of intensity obtained by rotating the compensator plate corresponds to the case in which the ellipse traced by the electric field transmitted by the two waveplates produces the smallest component along the analyzer transmission direction.

3.2.2 Brace-Köhler Method Analysis

Further analysis is needed to understand the conditions that govern the existence and location of the intensity minima observed as the compensator is rotated. The first and second derivatives of the intensity as a function of the rotating waveplate orientation θ_2 are obtained from Eq. (3.23) as

$$\frac{\partial I_{BK}}{\partial \theta_2} = \cos 2\theta_2 \{2 \sin 2\theta_2 \cos \phi_1 (1 - \cos \phi_2) + \sin \phi_1 \sin \phi_2\}, \tag{3.29}$$

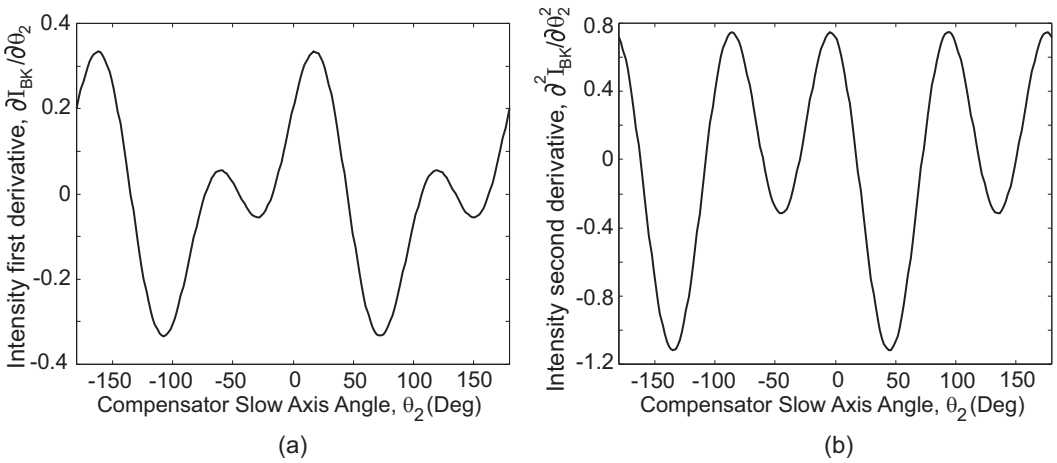

Figure 3.13: (a) First derivative with respect to θ_2 of the transmitted intensity in Fig. 3.11. $R_1 = \lambda/18$ and $R_2 = \lambda/10$. (b) Second derivative with respect to θ_2 of the transmitted intensity in Fig. 3.11.

and

$$\frac{\partial^2 I_{BK}}{\partial\theta_2^2} = 8\cos\phi_1 \sin^2\frac{\phi_2}{2} - 16\sin^2 2\theta_2 \cos\phi_1 \sin^2\frac{\phi_2}{2} - 2\sin 2\theta_2 \sin\phi_1 \sin\phi_2. \quad (3.30)$$

The first and second derivatives of the intensity I_{BK} represented in Fig. 3.11 are plotted in Fig. 3.13. The locations of the extrema of intensity are given by Eq. (3.29) when

$$0 = \cos 2\theta_2\{2\sin 2\theta_2 \cos\phi_1(1-\cos\phi_2) + \sin\phi_1 \sin\phi_2\}. \quad (3.31)$$

There is a first group of intensity extrema which occur for $\cos\theta_2 = 0$, i.e., $\theta_2 = (2n+1)\times 45$ *deg* where n is an integer. For the case represented in Fig. 3.11, these correspond to the global and local intensity maxima observed at -135, -45, $+45$ and, $+135$ *deg*. These maxima positions are also seen in Fig. 3.13(a) of the first intensity derivative. These intensity extrema, whether they are minima or maxima, are "non-retardation-based" extrema as they are always observed for $\theta_2 = (2n+1)\times 45$ *deg* independently of the phase-shifts values ϕ_1 and ϕ_2. As a consequence, finding the rotating waveplate angle for which they occur does not bring any quantitative information about the waveplates retardations. Substituting θ_2 equal 45 and -45 *deg* in Eq. (3.23), the normalized transmitted intensities of the non-retardation-based extrema are given as a function of ϕ_1 and ϕ_2 by

$$I_{NRB1}(\theta_2 = +45^o) = \sin^2(\frac{\phi_1+\phi_2}{2}) \quad (3.32)$$

$$I_{NRB2}(\theta_2 = -45^o) = \sin^2(\frac{\phi_1-\phi_2}{2}). \quad (3.33)$$

The second group of intensity extrema occur for the second factor in Eq. (3.29) equal to zero. The analytical expression of the necessary rotating waveplate angle θ_2 to produce these intensity extrema is given by

$$\sin 2\theta_2 = \frac{\sin\phi_1 \sin\phi_2}{2\cos\phi_1(\cos\phi_2 - 1)}. \tag{3.34}$$

Unlike the non-retardation-based extrema, this second group of extrema occur only if

$$\left| \frac{\sin\phi_1 \sin\phi_2}{2\cos\phi_1(\cos\phi_2 - 1)} \right| \leqslant 1. \tag{3.35}$$

Provided that the phase-shifts ϕ_1 and ϕ_2 satisfy Eq. (3.35), four "retardation-based" intensity extrema occur as the rotating plate is rotated from 0 to 360 *deg* and their angular orientations are given by

$$\sin\{2\theta_2\} = \sin\{2(\theta_2 + 180^o)\} = \sin\{2(90^o - \theta_2)\} = \sin\{2(-90^o - \theta_2)\}. \tag{3.36}$$

In the case represented in Fig. 3.11, these extrema are intensity minima and occur for θ_2 equal to -72.97, -17.03, 107.03, and 162.97 *deg*. The angle θ_2 for which they are observed is a function of the phase-shifts values ϕ_1 and ϕ_2. As a consequence, varying the angle θ_2 until these retardation-based extrema are observed and knowing one waveplate phase-shift ϕ_1 or ϕ_2 allows the determination of the other waveplate phase-shift respectively ϕ_2 or ϕ_1 using Eq. (3.34). It can be shown that for small retardations, Eq. (3.34) leads to the small retardation approximation formulas Eqs. (3.16) and (3.17). Equation (3.34) provides an exact formula for the calculation of the unknown retardation when using the Brace-Köhler compensator technique without restricting it to small retardations. It can therefore not only lead to more accurate retardation measurements, but also extend the range of compensator and sample retardations over which the Brace-Köhler compensator technique is applicable. Substituting Eq. (3.34) into Eq. (3.23), the normalized intensity of the retardation-based extrema can be computed as a function of ϕ_1 and ϕ_2 and is

$$I_{RB} = \sin^2\frac{\phi_1}{2} - \frac{\sin^2\phi_1 \sin^2\phi_2}{16\cos\phi_1 \sin^2(\phi_2/2)}. \tag{3.37}$$

If the intensity of the retardation-based extrema is greater than that of the non-retardation-based extrema, global intensity maxima are observed whenever θ_2 satisfies Eq. (3.34) and

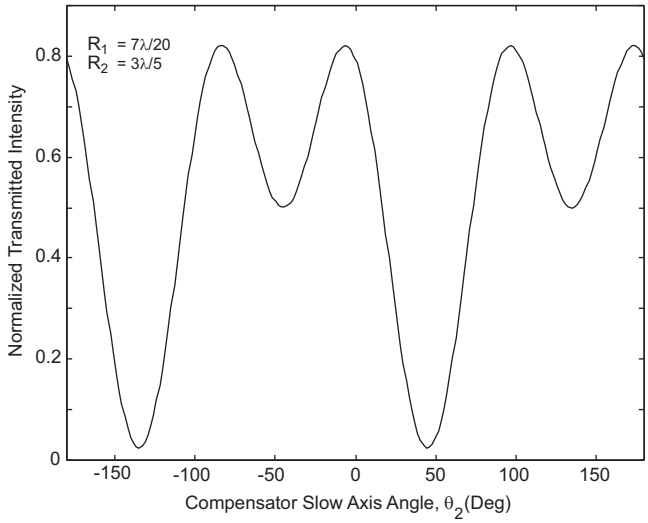

Figure 3.14: Normalized transmitted intensity of a sample of retardation $R_1 = 7\lambda/20$ and a compensator of retardation $R_2 = 3\lambda/5$ placed between crossed polarizers. The sample is at 45 *deg* from extinction and the compensator is rotated. The retardation-based extrema satisfying Eq. (3.34) are global maxima.

local and global minima are observed for $\theta_2 = (2n+1) \times 45\ deg$. This is illustrated in Fig. 3.14 for which the fixed waveplate retardation $R_1 = 7\lambda/20$ and the rotating waveplate retardation $R_2 = 3\lambda/5$. The retardation-based extrema are maxima and occur for θ_2 equal to -83.54, -6.46, 96.46, and 173.54 *deg*. For these retardations, the Brace-Köhler compensator technique is inapplicable since the intensity minima are non-retardation-based extrema.

3.2.3 Method Applicability

The applicability range of the Brace-Köhler compensator technique needs to be defined and expressed in terms of sample and compensator retardations. The applicability condition of the technique can be stated simply: for any given pair of sample and compensator retardations, retardation-based minima must exist when one or the other plate is rotated. This can be expressed as three mathematical inequalities

$$\left| \frac{\sin\phi_1 \sin\phi_2}{2\cos\phi_1(\cos\phi_2 - 1)} \right| \leqslant 1, \tag{3.38}$$

$$\sin^2\frac{\phi_1}{2} - \frac{\sin^2\phi_1 \sin^2\phi_2}{16\cos\phi_1 \sin^2(\phi_2/2)} \leqslant \sin^2(\frac{\phi_1+\phi_2}{2}) \tag{3.39}$$

$$\sin^2\frac{\phi_1}{2} - \frac{\sin^2\phi_1\sin^2\phi_2}{16\cos\phi_1\sin^2(\phi_2/2)} \quad \leqslant \quad \sin^2(\frac{\phi_1-\phi_2}{2}) \tag{3.40}$$

The first inequality represents the condition for the existence of retardation-based intensity extrema. The two other inequalities are the condition for these retardation-based intensity extrema to be global minima, i.e., the retardation-based intensity extrema are less than the non-retardation-based intensity extrema. If either of these conditions is not satisfied, no minima of intensity satisfying Eq. (3.34) can be found by either rotating the compensator or rotating the sample and thus the Brace-Köhler compensator method can not be applied. The three inequalities (3.38), (3.39), and (3.40) constrain the value of the magnitude of the retardation-based minima. It can be shown that if Eq. (3.38) is not satisfied, the transmitted intensity calculated using Eq. (3.37) is negative. Further, it can also be shown that if Eq. (3.39) is satisfied, Eq. (3.40) is also satisfied. This means that if the retardation-based extrema is less than either of the non-retardation-based extrema, it is in fact less than both of the non-retardation-based extrema. The condition of existence of the retardation-based minima can be expressed as one unique mathematical inequality by constraining their magnitude to be greater than zero and less than the non-retardation-based intensity extrema, namely

$$0 \leqslant \sin^2\frac{\phi_1}{2} - \frac{\sin^2\phi_1\sin^2\phi_2}{16\cos\phi_1\sin^2(\phi_2/2)} \leqslant \sin^2(\frac{\phi_1+\phi_2}{2}). \tag{3.41}$$

This condition is represented in Fig. 3.15 as a function of sample and compensator retardations ranging from 0 to λ. It represents the normalized transmitted intensity of the retardation-based minima for any given pair of sample and compensator retardations. The white region represents sample and compensator retardations for which the Brace-Köhler compensator technique cannot be applied to measure the sample retardation.

As was shown earlier in Fig. 3.14, retardation-based maxima may occur instead of minima. According to Eq. (3.25), whenever retardation-based maxima occur between crossed polarizers, then non-retardation-based minima occur between parallel polarizers and conversely. As a result, the Brace-Köhler compensator applicability range may be increased by simply introducing the possibility of making the measurement between parallel polarizers.

The expressions for the retardation-based and non-retardation-based extrema between

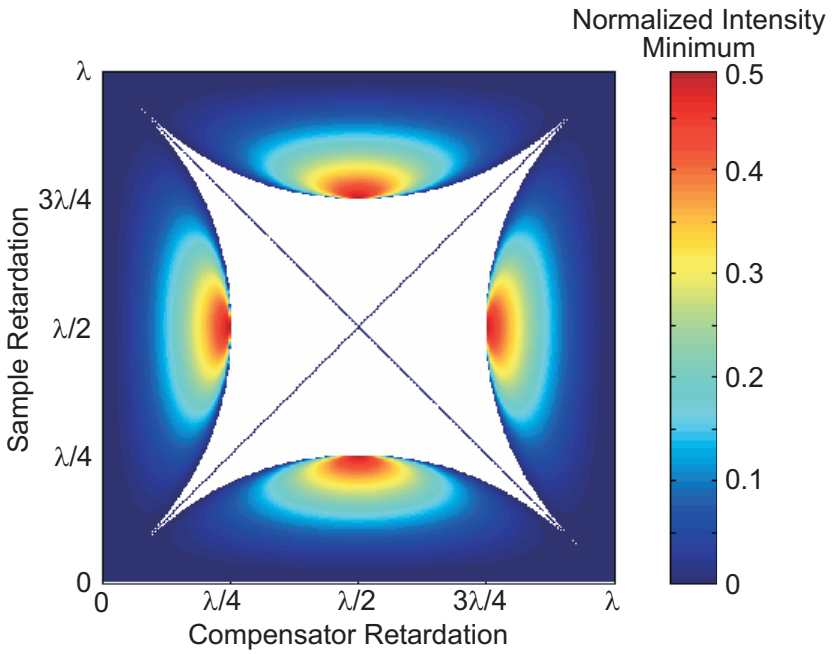

Figure 3.15: Normalized intensity minima for the Brace-Köhler technique illustrating its applicability range between crossed polarizers. The retardation-based intensity minima are calculated for sample and compensator retardations ranging from 0 to λ. It is assumed that the waveplates are between crossed polarizers. The white region represents retardations for which there are no retardation-based minima.

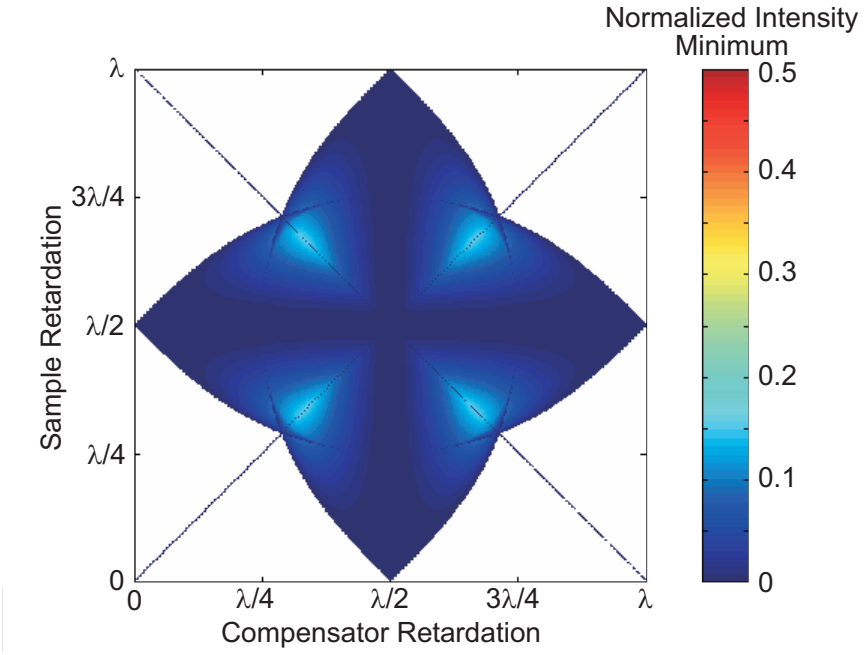

Figure 3.16: Normalized intensity minima for the Brace-Köhler technique illustrating its applicability range between parallel polarizers. The retardation-based intensity minima are calculated for sample and compensator retardations ranging from 0 to λ. It is assumed that the waveplates are between parallel polarizers. The white region represents retardations for which there are no retardation-based minima.

parallel polarizers are derived using Eqs. (3.25), (3.32), (3.33), and (3.37) and are

$$I_{NRB1\parallel} = \cos^2\Big(\frac{\phi_1+\phi_2}{2}\Big), \tag{3.42}$$

$$I_{NRB2\parallel} = \cos^2\Big(\frac{\phi_1-\phi_2}{2}\Big), \tag{3.43}$$

$$I_{RB\parallel} = \cos^2\frac{\phi_1}{2} + \frac{\sin^2\phi_1\sin^2\phi_2}{16\cos\phi_1\sin^2(\phi_2/2)}. \tag{3.44}$$

Similar to the case between crossed polarizers, retardation-based minima between parallel polarizers exist whenever the inequality

$$0 \leqslant \cos^2\frac{\phi_1}{2} + \frac{\sin^2\phi_1\sin^2\phi_2}{16\cos\phi_1\sin^2(\phi_2/2)} \leqslant \cos^2(\frac{\phi_1+\phi_2}{2}) \tag{3.45}$$

is satisfied. The magnitude of the retardation-based minima between parallel polarizers is represented in Fig. 3.16 as a function of the sample and compensator retardations. The white region represents sample and compensator retardations for which the Brace-Köhler compensator technique cannot be applied between parallel polarizers.

By superimposing Figs. 3.15 and 3.16, sample and compensator retardations for which

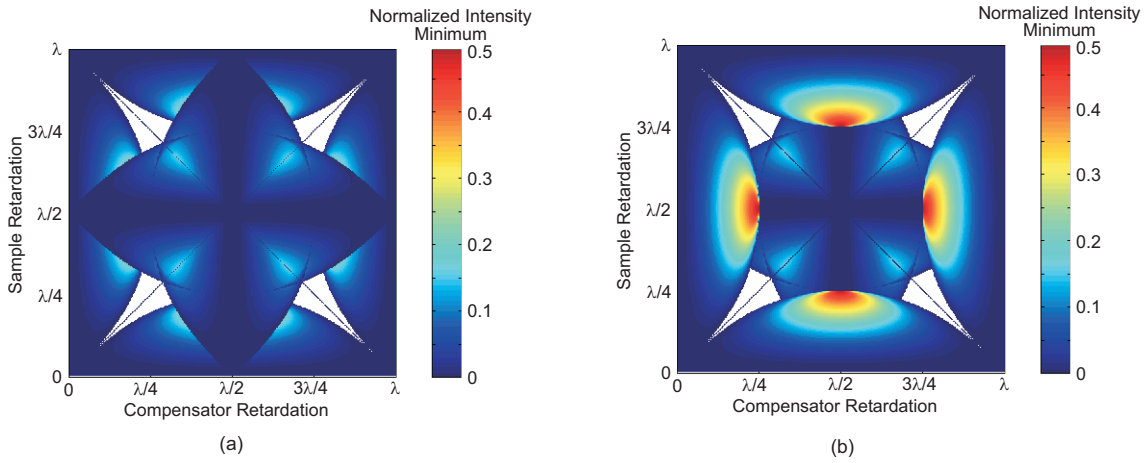

Figure 3.17: Retardation-based minima between crossed and parallel polarizers. (a) Retardation-based minima between parallel polarizers are superimposed onto those between crossed polarizers. (b) Retardation-based minima between crossed polarizers are superimposed onto those between parallel polarizers.

retardation-based minima can be observed and therefore the Brace-Köhler compensator technique applied are determined. This is shown in Figs. 3.17(a) and 3.17(b). In Fig. 3.17(a), the retardation-based minima magnitudes between parallel polarizers are superimposed onto the retardation-based minima magnitudes between crossed polarizers whereas in Fig. 3.17(b), the retardation-based minima magnitudes between crossed polarizers are superimposed onto the retardation-based minima magnitudes between parallel polarizers. Sample and compensator retardations for which retardation-based minima exist between crossed polarizers and parallel polarizers do not produce equal intensity. Although it is possible to observe retardation-based minima in both cases, the rotating waveplate is different and this produces a different intensity. The white region in Figs. 3.17(a) and 3.17(b) corresponds to sample and compensator retardations producing no retardation-based extrema regardless of which waveplate is rotated and regardless of the polarizers being crossed or parallel.

3.2.4 Resolvability

Experimentally, a commercial Brace-Köhler compensator is not rotatable over a full 360 *deg* revolution. Since all four retardation-based minima are analytically equivalent, only one needs to be found to determine the unknown retardation. The compensator manufactured by Olympus is rotatable from approximately -50 to $+50$ *deg*. Over this range,

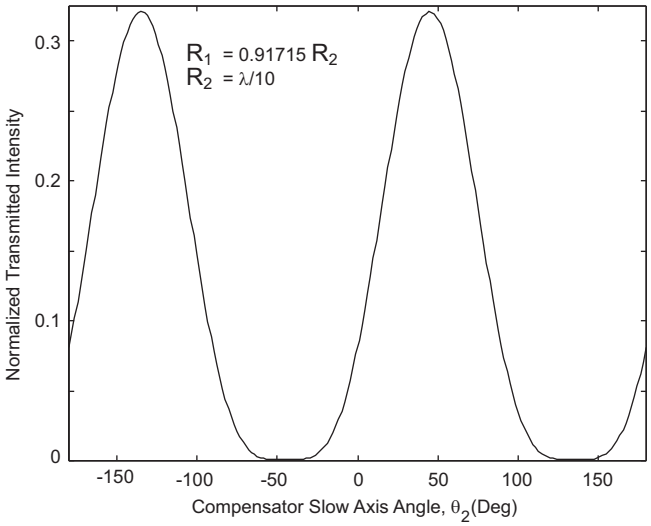

Figure 3.18: Normalized transmitted intensity for the limiting case of the existence of retardation-based minima. The compensator retardation is $R_2 = \lambda/10$. The retardation limit of the sample is calculated using Eq. (3.34) with θ_2 equal -45 *deg*. For this limiting case, the retardation-based intensity minimum merges with the non-retardation-based maximum at -45 *deg*.

three extrema are observed provided that the compensator and sample retardations satisfy Eq. (3.35): two non-retardation-based maxima (respectively minima) for θ_2 equal to -45 *deg* and $+45$ *deg*, and one retardation-based minimum (respectively maximum) for θ_2 given by Eq. (3.34). However, for a given phase-shift ϕ_2 there is a maximum phase-shift ϕ_1 beyond which Eq. (3.35) is not satisfied and the retardation-based extremum located between θ_2 equal -45 and $+45$ *deg* merges with one of these latter extrema. This maximum value ϕ_{L1} can be computed with Eq. (3.35) by substituting $\theta_2 = 45^o$

$$\phi_{L1} = \arctan\left\{2\frac{1-\cos\phi_2}{\sin\phi_2}\right\}. \tag{3.46}$$

For the retardation of the commercial Brace-Köhler compensator $R_2 = \lambda/10$, the maximum sample phase-shift ϕ_{L1} is approximately equal to $0.91715\phi_2$. The corresponding normalized transmitted intensity is calculated and represented as a function of the compensator orientation θ_2 in Fig. 3.18. The retardation-based minimum that occured for the previous value of ϕ_1 between $\theta_2 = -45^o$ and $\theta_2 = 45^o$ is not observed and a minimum is now observed for $\theta_2 = -45^o$ instead of a local non-retardation-based maximum previously.

The applicability range of the Brace-Köhler compensator technique can be judged based

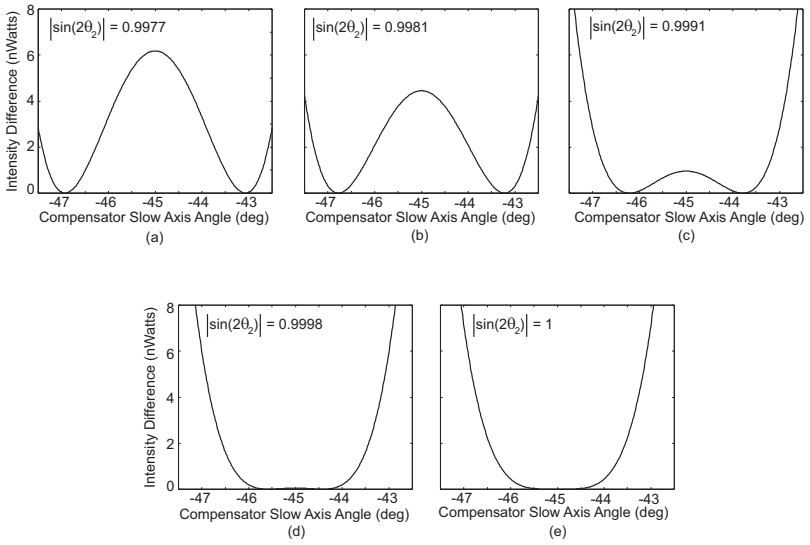

Figure 3.19: Resolvability of the Brace-Köhler compensator technique. (a)-(e) Transmitted intensity for various values of sample phase-shift ϕ_1. The compensator retardation is $R_2 = \lambda/10$. The input intensity is equal to 15 mW.

on its ability to resolve the retardation-based intensity minimum from the closest non-retardation-based intensity maximum that occurs at $\theta_2 = \pm 45^o$. This is illustrated in Fig. 3.19 where the transmitted intensity variations relative to the minimum intensity are plotted for various values of $|\sin 2\theta_2|$ as it approaches unity. The rotating waveplate phase-shift ϕ_2 corresponds to $\lambda/10$. The sample phase-shift is calculated for various values of $|\sin 2\theta_2|$ using Eq. (3.34). The successive values of $|\sin 2\theta_2|$ are indicated on each plot.

To determine the value of $|\sin 2\theta_2|$ for which the retardation-based intensity minimum cannot be resolved from the adjacent intensity maximum, the intensity variations relative to the intensity minimum are plotted as a function of the compensator orientation θ_2. To generate the plots in Fig. 3.19, it is assumed that the power of the light incident upon the first polarizer is 15 mW which corresponds to the power of the Spectra Physics Model 120S He-Ne laser that is used to test the different retardation measurement techniques. The resolution of the technique can be defined as the smallest intensity variation between a minimum and an adjacent maximum that can be detected by the photodetector. It is assumed that this smallest intensity variation is approximately 1 nW. The intensity minimum is resolvable for $|\sin 2\theta_2|$ equal to 0.9977, 0.9981 and 0.9991 respectively in Figs. 3.19(a), 3.19(b), and 3.19(c) as the intensity maximum is larger than the intensity minimum of at least 1 nW.

However, the minimum is not resolvable for $|\sin 2\theta_2|$ equal to 0.9998 in Fig. 3.19(d) as the intensity difference between the maximum and the minimum is much smaller than 1 nW. As a result, the condition of applicability of the Brace-Köhler compensator technique defined by the ability to resolve the minimum intensity from the adjacent maximum is mathematically given by

$$|\sin 2\theta_2| < 0.999, \tag{3.47}$$

$$\left| \frac{\sin\phi_1 \sin\phi_2}{2\cos\phi_1(\cos\phi_2 - 1)} \right| < 0.999. \tag{3.48}$$

3.2.5 Resolution

The resolution of the Brace-Köhler compensator technique also needs to be quantified. The resolution is defined as the smallest retardation change measurable. It depends on several parameters such as the angular resolution of the rotating mount in which the compensator is placed, the compensator retardation, and the sample retardation. For a given compensator retardation, the resolution can be calculated as a function of the angular resolution and the sample retardation. Considering a compensator and a sample with phase retardations ϕ_c and ϕ_{s1}, the compensator angle θ_c at which the intensity minimum is measured is given by Eq. (3.34) as

$$\sin(2\theta_c) = \frac{\sin\phi_{s1}\sin\phi_c}{2\cos\phi_{s1}(\cos\phi_c - 1)}. \tag{3.49}$$

Considering the angular resolution $\Delta\theta$, the nearest measurable sample phase retardation ϕ_{s2} is given by

$$\tan\phi_{s2} = \frac{2(\cos\phi_c - 1)\sin(2\theta_c + 2\Delta\theta)}{\sin\phi_c}. \tag{3.50}$$

The difference between ϕ_{s2} and ϕ_{s1} defines the resolution. The resolution is calculated and represented as a function of sample retardation and angular resolution in Figs. 3.20(a) and 3.20(b). Two different compensator retardations respectively $\lambda/10$ and $\lambda/30$ are considered that correspond to the two Brace-Köhler compensators (models U-CBR1 and U-CBR2 manufactured by Olympus). The maximum resolution is about 0.2 nm and 0.1 nm respectively for a 0.1 deg angular resolution. The resolution can be improved by decreasing

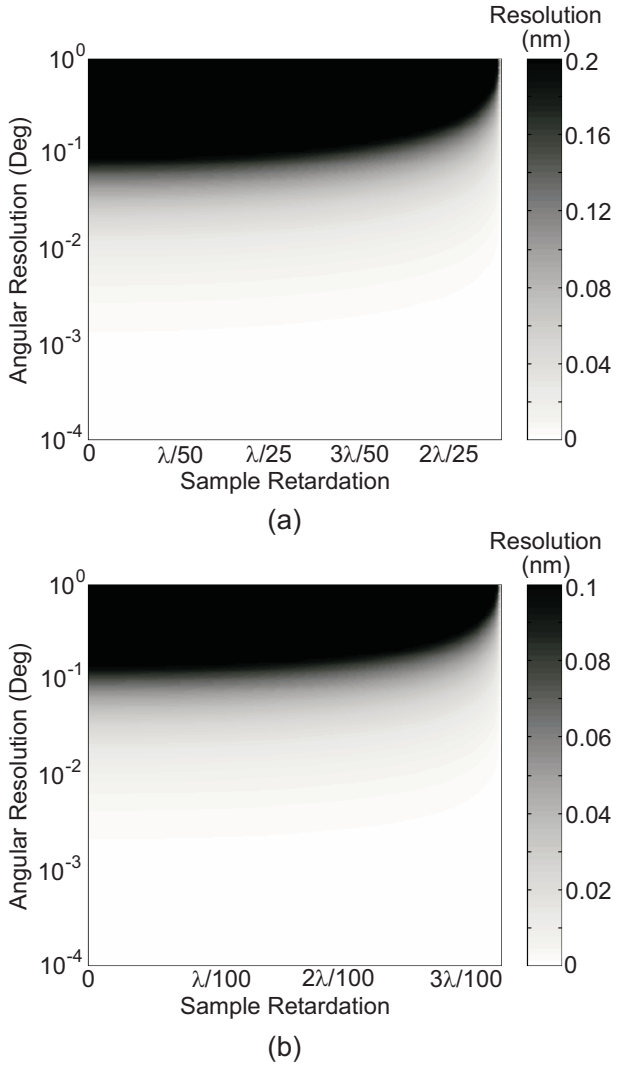

Figure 3.20: Resolution of the Brace-Köhler compensator technique as a function of sample retardation and angular resolution. (a) Compensator retardation equals $\lambda/10$. (b) Compensator retardation equals $\lambda/30$.

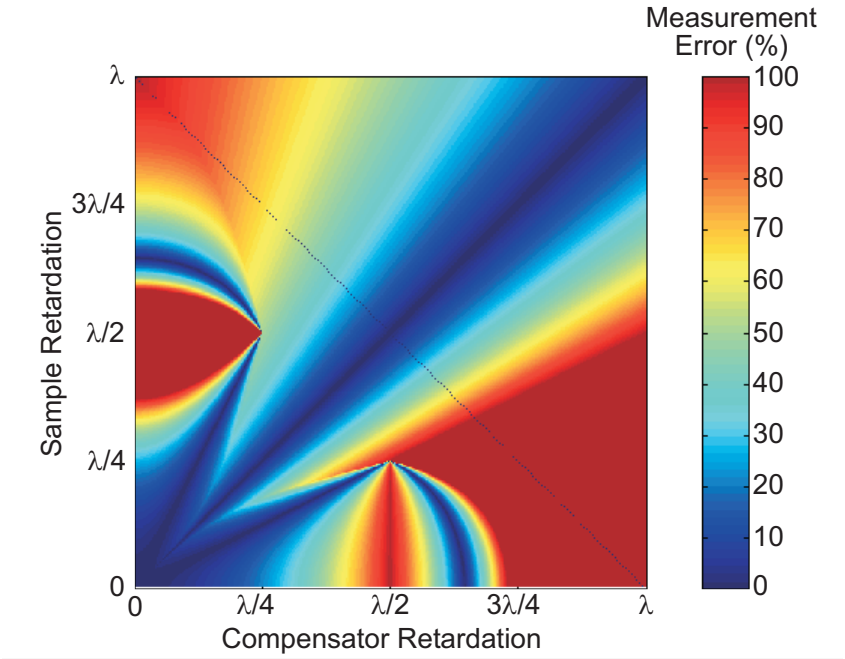

Figure 3.21: Error due to small retardation approximation in the Brace-Köhler compensator method.

the angular resolution of the rotating dial. An angular resolution of 0.01 *deg* allows resolutions of 0.04 *nm* and 0.02 *nm* to be obtained for compensator retardations $\lambda/10$ and $\lambda/30$ respectively. This is comparable to the resolution obtained with the commercially available photoelastic instrument (Exicor model 150AT manufactured by Hinds Instruments [35, 47, 49, 50]).

3.2.6 Accuracy

Having derived the expression of the intensity transmitted through a two-waveplate system placed between crossed polarizers, and the expression of the location and magnitude of the retardation-based extrema as Waveplate 2 is rotated (Fig. 3.1), the error due to the small retardation approximation in the Brace-Köhler compensator formula can be calculated. This error is represented in Fig. 3.21 for sample and compensator retardations ranging from 0 to λ. To generate this figure, it was first determined for each pair of sample and compensator which of the two waveplates needs to be rotated in the Brace-Köhler compensator sense, i.e. the rotating waveplate retardation must be greater than that of the fixed plate. The angles θ_2 producing global retardation-based intensity minima respectively maxima and the

angles θ_2 producing global and local non-retardation-based intensity maxima respectively minima are determined using Eqs. (3.32), (3.33), (3.34), (3.35), and (3.37). Having found the location of the intensity minimum and knowing the retardation of the compensator which is on the x-axis of Fig. 3.21, the sample retardation is calculated using Eq. (3.16) or (3.17). The calculated value is compared to the true value of the sample and the relative error is plotted as a percentage of the true value. The error remains low for relatively small retardations as expected. For compensator and sample retardations less than a quarter of a wavelength, the error remains lower than 20%. The error is zero for particular cases. When both waveplates have equal retardations, the intensity minimum occurs when the rotating waveplate slow axis is parallel to the fixed waveplate fast axis. Having the convention that the fixed waveplate slow axis is at 45 *deg* from the polarizer transmission direction, the rotating waveplate needs to be at -45 *deg* to obtain extinction. In this case, the Brace-Köhler compensator formula Eq. (3.16) calculates accurately the sample retardation.

Another particular case occurs when the rotating waveplate has twice the retardation than that of the fixed waveplate. By substituting $\phi_2 = 2\phi_1$ in the derivative of the intensity with respect to θ_2 Eq. (3.29), it can be shown that an extremum occurs for the following condition

$$\sin(2\theta_2) = \frac{\sin\phi_1 \sin(2\phi_1)}{2\cos\phi_1[\cos(2\phi_1) - 1]}, \tag{3.51}$$

$$= -\frac{1}{2}. \tag{3.52}$$

The angles θ_2 producing intensity minimum are given by the equation above and are equal to -75, -15, 105, and 165 degrees. Substituting these values of θ_2 in the Brace-Köhler formulas Eqs. (3.16) and (3.17) lead to $R_C = 2R_S$ or vice versa rendering the small retardation approximation formulas accurate.

The error peaks for either waveplate retardation equal to a half-wavelength. This can be understood with the aid of Fig. 3.22 which represents the ellipse traced by the electric field traveling through a two-waveplate system when the rotating waveplate is a half-waveplate. The different orientations of the rotating waveplate are indicated by θ_2 and the polarization ellipses are represented in the system defined by the polarization transmission directions of

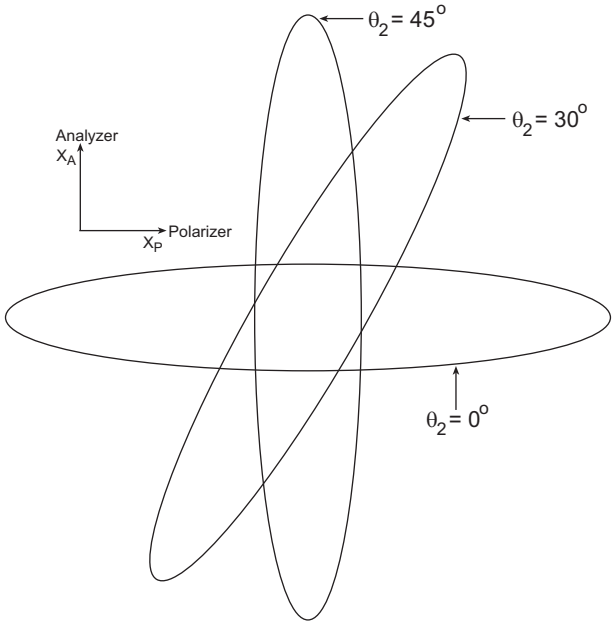

Figure 3.22: Polarizations resulting in a two-waveplate system with Waveplate 2 being a half-waveplate. θ_2 is the half-waveplate slow axis angle with respect to the polarizer transmission direction. The ellipses represent the polarization states of the light for various values of θ_2.

the crossed polarizers. The half-waveplate has the effect of rotating the ellipse of polarization produced after the first waveplate. As a matter of fact, for a given orientation ξ of the half-waveplate, the ellipse of polarization after the first waveplate is rotated by 2ξ. The first waveplate being oriented at 45 *deg* from extinction, the polarization transmission directions of the crossed polarizers are parallel to the principal axes of the ellipse of polarization traced by the electric field transmitted by the first waveplate. Consequently, the minimum of intensity is obtained when the ellipse minor axis of the light transmitted by the second waveplate is parallel to the analyzer polarization transmission direction. This is the case for θ_2 equal to zero as shown in Fig. 3.22. When $\theta_2 = 0$ is substituted in the Brace-Köhler compensator formulas Eqs. (3.16) and (3.17), it results to relative errors respectively equal to 100% and ∞.

CHAPTER 4

TWO-WAVEPLATE COMPENSATOR

4.1 Analysis and Development

The Brace-Köhler compensator technique has numerous shortcomings that limit its applicability range and its accuracy. It only minimizes the transmitted electric field component along the analyzer transmission direction as was shown in Fig. 3.12. Overall, it minimizes the phase-shift introduced between the input electric field component along the first polarizer transmission direction and the output electric field component along the analyzer transmission direction. It is therefore not a rigorous compensation method and does not produce extinction as is the case, for example, with the Sénarmont compensator technique.

Two extreme configurations may be considered when one waveplate is rotated and the other remains fixed: 1) the slow axis of the rotating waveplate may be parallel to the slow axis of the fixed waveplate in which case both retardations are added and 2) the slow axis of the rotating waveplate may be parallel to the fast axis of the fixed waveplate in which case the retardations are subtracted.

In between these two extremes, there exists a relative orientation of the waveplates resulting in a total retardation equal to 0 or λ producing a linearly polarized output. The retardation between the components along the slow and fast axis of the second waveplate in Fig. 3.10 is now considered as opposed to that between the components along the polarizers transmission direction. If this linearly polarized output exists, it is not parallel to the polarizers transmission directions and extinction can only be obtained if the analyzer is rotated so as to be perpendicular to the linear polarization direction of the electric field exiting the second waveplate. This is the basis for the development of a new retardation measurement technique, the Two-Waveplate-Compensator (TWC) technique. The remainder of this chapter deals with the thorough analysis of the relative orientation of both waveplates producing linearly polarized output and the development of an experimental procedure to

determine this orientation by rotating successively one waveplate and the analyzer.

4.1.1 Two-Waveplate System Analysis

An analytical expression for the rotating waveplate angle necessary to obtain a linearly polarized output is needed. The two-waveplate configuration used for the analysis is identical to that previously used with the Brace-Köhler technique and represented in Fig. 3.10. The analysis is done using Jones calculus as was done in Sec. 3.2 for the Brace-Köhler technique. Figure 3.3 can also be used to illustrate the various systems of axes in which the electric field is expressed. The Jones vector expressed in the system of axes associated with the second waveplate and characteristic of the electric field transmitted through the first fixed waveplate of phase retardation ϕ_1 and the second rotating waveplate of phase retardation ϕ_2 (Fig. 3.3) is given by

$$\vec{\mathcal{E}}_2 = T(\phi_2)R(\theta_2)\begin{pmatrix} a \\ be^{j\frac{\pi}{2}} \end{pmatrix}, \tag{4.1}$$

where $T(\phi_2)$ is the transmission matrix of phase retardation ϕ_2, $R(\theta_2)$ is the rotation matrix of angle θ_2, and a and b are the component magnitudes of the Jones vector characteristic of the electric field exiting the first waveplate expressed in the system of axes of the crossed polarizers. These last Jones vector components can be calculated as follows

$$\begin{aligned} \begin{pmatrix} a \\ be^{j\frac{\pi}{2}} \end{pmatrix} &= R(-\theta_1)T(\phi_1)R(\theta_1)\begin{pmatrix} 1 \\ 0 \end{pmatrix} \\ &= \begin{pmatrix} \cos\theta_1 & -\sin\theta_1 \\ \sin\theta_1 & \cos\theta_1 \end{pmatrix}\begin{pmatrix} 1 & 0 \\ 0 & e^{j\phi_1} \end{pmatrix}\begin{pmatrix} \cos\theta_1 & \sin\theta_1 \\ -\sin\theta_1 & \cos\theta_1 \end{pmatrix}\begin{pmatrix} 1 \\ 0 \end{pmatrix} \end{aligned} \tag{4.2}$$

The fixed waveplate slow axis being at 45 *deg* from the polarizer transmission direction, the components a and b can be computed as a function of ϕ_1 by substituting $\theta_1 = \pi/4$ into Eq. (4.2). It can be shown that the major and minor axes, respectively a and b, of the ellipse traced by the electric field exiting the first waveplate are given by

$$a = \cos\phi_1, \tag{4.3}$$

$$b = -\sin\phi_1. \tag{4.4}$$

Substituting Eq. (4.4) into Eq. (4.1) and carrying out the matrix multiplication, $\vec{\mathcal{E}}_2$ can be written in the form

$$\vec{\mathcal{E}}_2 = \begin{pmatrix} a_1 e^{j\delta_1} \\ a_2 e^{j(\delta_2+\phi_2)} \end{pmatrix}, \tag{4.5}$$

with

$$\begin{aligned} a &= \cos(\frac{\phi_1}{2}) && (4.6)\\ b &= -\sin(\frac{\phi_1}{2}) && (4.7)\\ a_1 &= (a^2\cos^2\theta_2 + b^2\sin^2\theta_2)^{\frac{1}{2}} && (4.8)\\ a_2 &= (a^2\sin^2\theta_2 + b^2\cos^2\theta_2)^{\frac{1}{2}} && (4.9)\\ \delta_1 &= \arctan(\frac{b\sin\theta_2}{a\cos\theta_2}) && (4.10)\\ \delta_2 &= \arctan(\frac{b\cos\theta_2}{-a\sin\theta_2}). && (4.11) \end{aligned}$$

The condition for the electric field to be linearly polarized after passing through the two waveplates is given by,

$$\delta_2 + \phi_2 = \delta_1 + k\pi, \qquad \text{with } k, \text{ an integer.} \tag{4.12}$$

Substituting the expressions of δ_1, δ_2 into Eq. (4.12),

$$\arctan[\tan(\frac{\phi_1}{2})\cot(\theta_2)] + \phi_2 = -\arctan[\tan(\frac{\phi_1}{2})\tan(\theta_2)]. \tag{4.13}$$

Using the trigonometric identity $\tan(r+t) = \dfrac{\tan(r)+\tan(t)}{1-\tan(r)\tan(t)}$ and simplifying gives

$$\cot(\theta_2) + \tan(\theta_2) = \frac{\tan(\phi_2)}{\tan(\phi_1/2)}(\tan^2(\frac{\phi_1}{2}) - 1). \tag{4.14}$$

Using trigonometric identities leads to the condition for linearly polarized light as

$$\sin 2\theta_2 = -\frac{\tan\phi_1}{\tan\phi_2}. \tag{4.15}$$

4.1.2 Applicability Range

In Eq. (4.15), the angle θ_2 is the angle of the rotating waveplate producing linearly polarized light. Similarly to the Brace-Köhler technique, the angle θ_2 depends upon the phase retardations ϕ_1 and ϕ_2. The condition of existence of the angle θ_2 is given by

$$\Big| -\frac{\tan\phi_1}{\tan\phi_2} \Big| \leq 1, \tag{4.16}$$

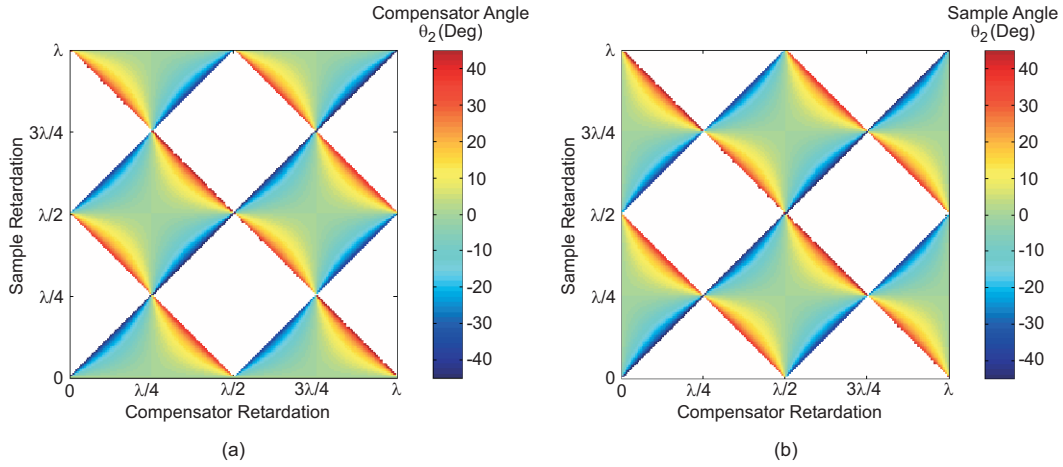

Figure 4.1: The magnitude of the angle θ_2 producing linearly polarized light is calculated for sample and compensator retardations ranging from 0 to λ. (a) The linearly polarizing angle is calculated when the compensator is rotated. The white region represents retardations for which no linearly polarized output is produced as the compensator is rotated. (b) The linearly polarizing angle is calculated when the sample is rotated. The white region represents retardations for which no linearly polarized output is produced as the sample is rotated.

For any given sample and compensator retardations, Eq. (4.16) allows one to determine which waveplate is to be rotated to obtain linearly polarized light. Contrary to the Brace-Köhler compensator technique whose retardation-based minima do not exist for all sample and compensator retardations (Fig. 3.17), the TWC technique is guaranteed to produce linearly polarized output provided that Eq. (4.16) is satisfied.

The applicability range of the TWC technique can be represented using Eq. (4.16) as a function of the sample and compensator retardations. Figure 4.1 represents the magnitude of the angle θ_2 in degrees for various sample and compensator retardations. For any given sample and compensator retardations, the angle θ_2 is calculated using Eq. (4.15). Depending on the retardation values, either the compensator needs to be rotated to obtain linearly polarized light which is represented in Fig. 4.1(a) or the sample needs to be rotated which is represented in Fig. 4.1(b). The fixed and rotating waveplates are chosen according to Eq. (4.16). For any given pair of sample and compensator retardations, a linearly polarized output can always be obtained provided that the fixed and rotating waveplate roles are assigned such that Eq. (4.16) is satisfied. If by rotating the compensator (or the sample) Eq. (4.16) is not satisfied, i.e., $|\sin 2\theta_2| > 1$, it is obvious that rotating the sample (or the

compensator) then satisfies Eq. (4.16) since inverting the roles of the two waveplates results in inverting the ratio $\tan\phi_1/\tan\phi_2$.

4.1.3 Experimental Procedures

Figure 4.1 allows one to determine which of the sample or compensator waveplate needs to be rotated to obtain linearly polarized light. However, with no prior knowledge of the sample retardation, it is important to develop an experimental procedure allowing the determination of the configuration that produces a linearly polarized output. The polarization state of the output light must be studied for given pairs of sample and compensator retardations for the two different configurations for which on one hand the compensator is rotated and on the other hand the sample is rotated. Depending on the retardation values of the sample and the compensator, one of these configurations is such that Eq. (4.16) is satisfied and linearly polarized light can be produced whereas the other configuration is such that Eq. (4.16) is not satisfied and linearly polarized light can not be produced.

Results of a detailed study of the output light polarization are shown in Figs. 4.2, 4.3, 4.4, and 4.5 for a sample of retardation equal to 0.15λ and a compensator of retardation equal to 0.45λ. The x-axis of the system in which the polarization states are plotted in Figs. 4.3 and 4.5 corresponds to the first polarizer transmission direction. In the TWC technique, this polarizer remains fixed. For the retardations used in this example, a linearly polarized output is produced when the sample of retardation 0.15λ is the rotating waveplate. By substituting the retardation values of the sample and compensator into Eq. (4.15), the sample orientation that produces a linearly polarized output is calculated and is equal to 6.83 *deg*. The lengths of the semi-axes and the ellipticity of the output light polarization ellipse as a function of the sample orientation are plotted in Fig. 4.2. The linearly polarized output is produced when the semi-minor axis of the polarization ellipse is equal to zero. Over a full 360 *deg* rotation of the sample, this occurs four times. Since these four angles are mathematically equivalent, only one is needed for the measurement. In Fig. 4.3, the output light polarization is represented when the sample of retardation 0.15λ is rotated from -45 to +45 *deg*. As calculated, the linearly polarized output is produced for θ_2 equal to 6.83

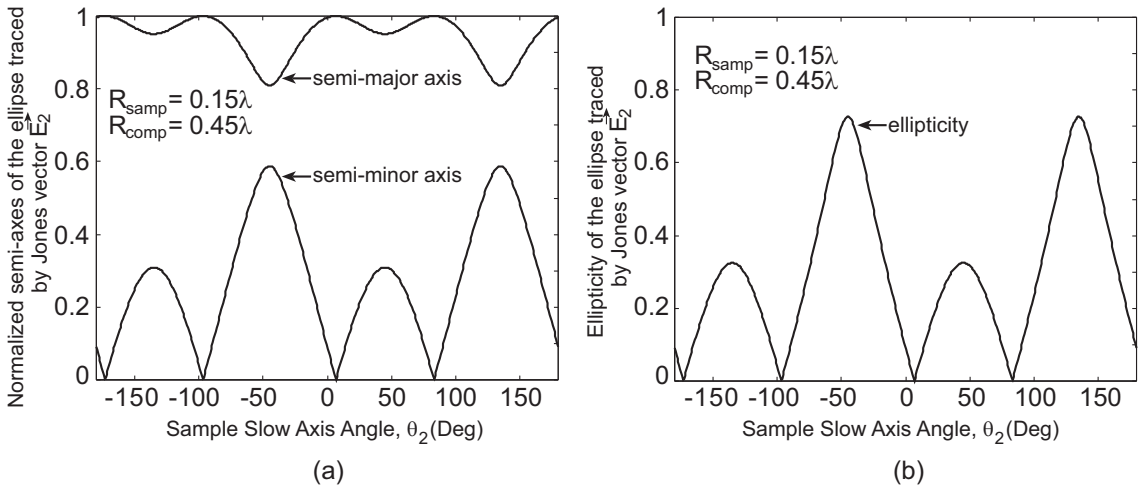

Figure 4.2: The semi-minor, semi-major axes, and the ellipticity of the output light are plotted as a function of the sample slow axis angle.

deg which is also seen in Fig. 4.2. When rotating the linearly polarizing waveplate from -45 to +45 *deg* the semi-minor axis of the output ellipse of polarization goes through zero. By incrementally rotating the analyzer so that its transmission direction is always parallel to the semi-minor axis of the polarization ellipse as the linearly polarizing waveplate is rotated, the intensity transmitted goes through extinction when the semi-minor axis goes through zero.

Figures 4.4 and 4.5 represent the semi-axes, ellipticity, and polarization states as the compensator is rotated. In this configuration the non-linearly polarizing waveplate is rotated and no linearly polarized output is produced between -45 *deg* and +45 *deg*. The semi-minor axis of the output polarization ellipse decreases monotonically as the compensator is rotated. The actual semi-axes lengths, minor semi-axis orientation, ellipticity of the polarization states represented in Figs. 4.3 and 4.5 are summarized in Tables 4.1 and 4.2.

The observation of the output polarization states as the linearly-polarizing or the non-linearly-polarizing waveplate is rotated allows the development of the experimental procedure needed to determine which of the sample or the compensator has to be rotated to use the TWC technique. The polarizers are first crossed. One of the waveplates, compensator or sample, is rotated at 45 *deg* from extinction and is chosen to be the fixed waveplate in this test experiment. The other waveplate, sample or compensator, is rotated so it is at

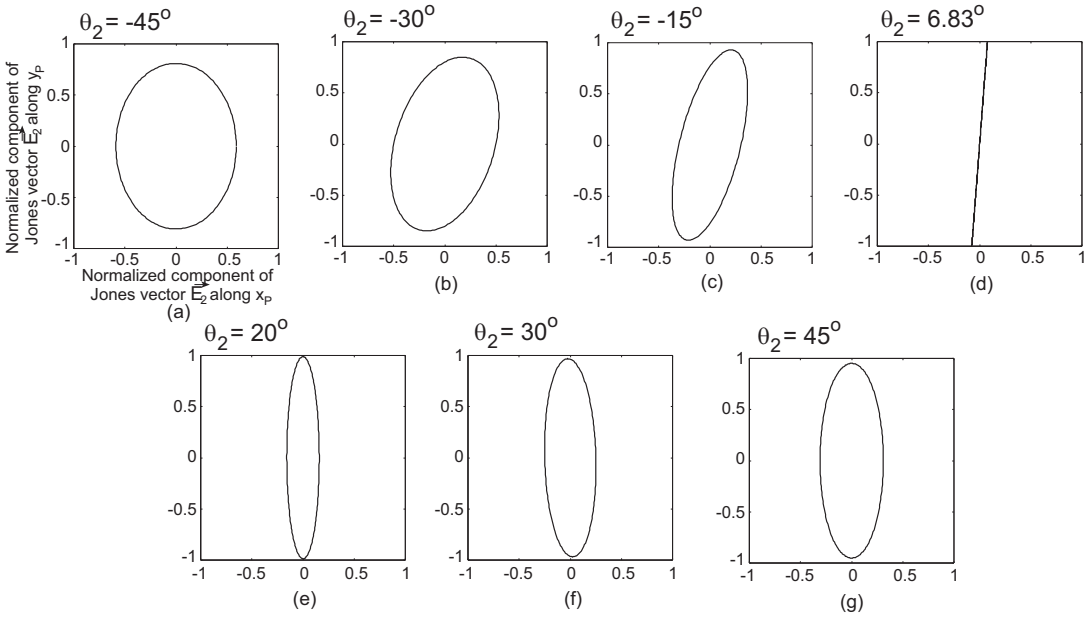

Figure 4.3: The output light polarization states are represented for various sample slow axes angles in the polarizer system of axes x_P and y_P (Fig. 3.3). The sample retardation $R_{samp} = 0.15\lambda$ and the compensator retardation $R_{comp} = 0.45\lambda$. Linearly polarized light is produced for a sample slow axis angle equal to 6.83 *deg*.

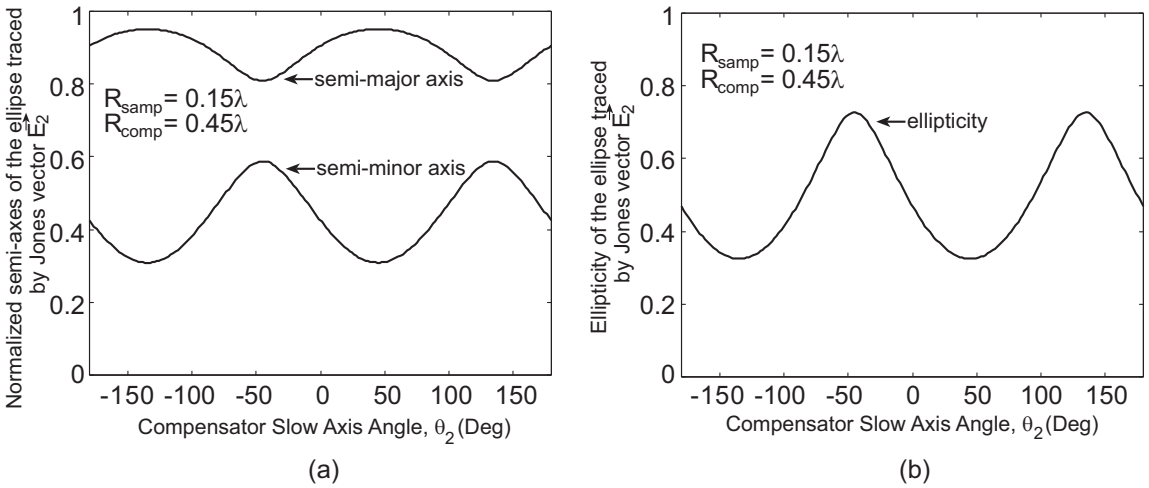

Figure 4.4: The semi-minor, semi-major axes, and the ellipticity of the output light are plotted as a function of the compensator slow axis angle.

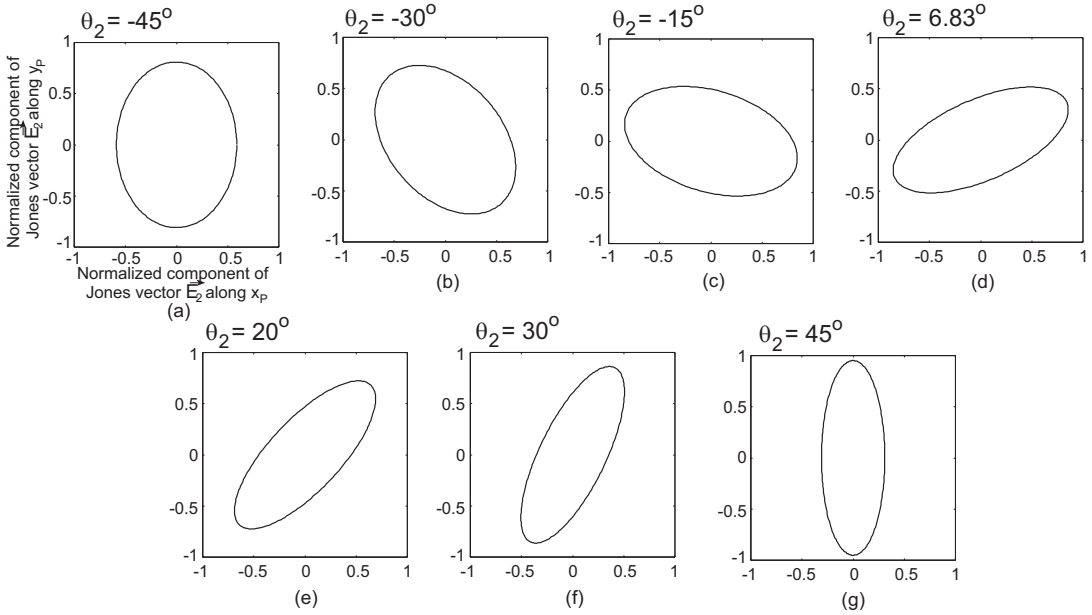

Figure 4.5: The output light polarization states are represented for various compensator slow axes angles in the polarizer system of axes x_P and y_P (Fig. 3.3). The sample retardation $R_{samp} = 0.15\lambda$ and the compensator retardation $R_{comp} = 0.45\lambda$. No linearly polarized light is produced when the compensator is rotated.

Table 4.1: Semi-axes lengths, ellipticity, semi-minor axis angle of the output light polarization ellipse as a function of the sample slow axis angle θ_2. $R_{samp} = 0.15\lambda$, $R_{comp} = 0.45\lambda$.

θ_2 (Deg)	Semi-Minor Axis Normalized	Semi-Minor Axis Angle (Deg)	Semi-Major Axis Normalized	Ellipticity
-45	0.5878	0	0.8090	0.7265
-30	0.4847	-16.89	0.8746	0.5542
-15	0.2965	-13.97	0.9550	0.3105
6.83	0	-4.40	1.0000	0
20	0.1585	0.05	0.9874	0.1605
30	0.2503	1.47	0.9682	0.2585
45	0.3090	0	0.9510	0.3249

Table 4.2: Semi-axes lengths, ellipticity, semi-minor axis angle of the output light polarization ellipse as a function of the compensator slow axis angle θ_2. $R_{samp} = 0.15\lambda$, $R_{comp} = 0.45\lambda$.

θ_2 (Deg)	Semi-Minor Axis Normalized	Semi-Minor Axis Angle (Deg)	Semi-Major Axis Normalized	Ellipticity
-45	0.5878	0	0.8090	0.7265
-30	0.5587	40.73	0.8294	0.6736
-15	0.4950	73.34	0.8687	0.5697
6.83	0.3955	113.71	0.9184	0.4306
20	0.3481	136.77	0.9374	0.3713
30	0.3234	154.09	0.9462	0.3418
45	0.3090	180	0.9510	0.3249

± 45 *deg* from extinction and is chosen to be the rotating waveplate. With the waveplates in their respective initial orientations the intensities transmitted between crossed and parallel polarizers are determined by rotating the analyzer accordingly. The analyzer must then be oriented to either of the positions that produced the minimum intensity ensuring that the analyzer transmission direction is parallel to the semi-minor axis of the output light polarization ellipse. The rotating waveplate is rotated in increments from ± 45 to ∓ 45 *deg*. For each rotating waveplate orientation, the analyzer is rotated so a minimum of intensity is transmitted ensuring that the analyzer transmission direction is locked on the semi-minor axis of the output polarization ellipse. The intensity transmitted through the analyzer is observed as it is rotated. If the intensity goes through extinction, the waveplate that was initially chosen as the rotating waveplate is the linearly-polarizing waveplate. Consequently, the measurement using the TWC technique is to be done by rotating the same waveplate. On the contrary, if the intensity decreased or increased monotonically during the test experiment, the waveplate that was initially chosen as the rotating waveplate is the non-linearly-polarizing waveplate. This waveplate must therefore be oriented at 45 *deg* from extinction and be fixed to use the TWC technique whereas the other waveplate is to be rotated.

This experimental procedure is illustrated in Fig. 4.6. With no prior knowledge of the sample retardation magnitude, the experimental procedure outlined in the flow chart

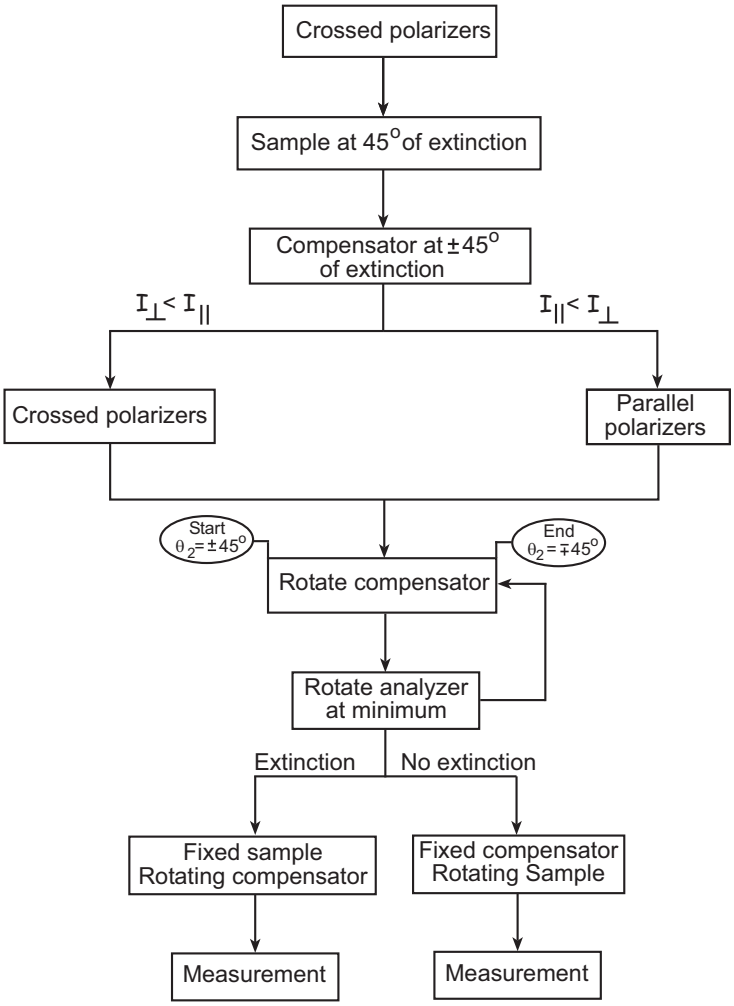

Figure 4.6: Flow chart representing the experimental procedure to determine which of the sample or compensator needs to be rotated to produce linearly polarized light. It is based on having the analyzer transmission direction parallel to the output ellipse semi-minor axis. Sample (compensator) and analyzer are successively rotated to observe the variations of the transmitted intensity.

of Fig. 4.6 can be followed to determine which of the sample or the compensator is the linearly-polarizing waveplate after which the measurement itself can be made.

The measurement using the TWC technique consists of following the steps in the procedure represented in the flow chart of Fig. 4.7. Once the test experiment has been done, the phase retardation values of the sample ϕ_{samp} and that of the compensator ϕ_{comp} are assigned to ϕ_1 or ϕ_2 depending upon which is the linearly-polarizing waveplate. According to the convention defined in our analysis, ϕ_1 is the phase retardation of the fixed waveplate and ϕ_2 is the phase retardation of the rotating waveplate. Following the determination of the waveplates roles, the analyzer transmission direction must be brought parallel to the semi-minor axis of the output polarization ellipse by placing the rotating waveplate at ± 45 *deg* and setting the analyzer to produce a minimum of intensity. This is similar to what is done in the test experiment. Having set the analyzer transmission direction parallel to the semi-minor axis of the polarization ellipse, the rotating waveplate is rotated by small increments and the analyzer is rotated at each increment so the intensity transmitted is minimum. When extinction is produced, the rotating waveplate angle θ_e is recorded and will be used to determine the unknown sample retardation. Equation (4.15) is used to calculate the unknown ϕ_{samp}. Two different expressions are derived to calculate the sample phase retardation depending if $\phi_1 = \phi_{samp}$ or $\phi_1 = \phi_{comp}$. These expressions are indicated at the end branches of the flow chart.

4.1.4 Resolvability

The applicability of the TWC technique for measuring retardation depends upon the capability of the optical system in resolving the point of extinction from the adjacent local maximum occuring for θ_2 equal to +45 *deg* (Fig. 4.2). For the sample and compensator retardation values of Figs. 4.3 and 4.5, the sample angle producing linearly polarized light is far enough from the adjacent maxima at +45 *deg* and -45 *deg* to be resolved. However, as the tangents of the sample and compensator phase retardations converge towards the same value, the angle producing linearly polarized light approaches +45 *deg* or -45 *deg* and the adjacent maximum intensity decreases which renders more difficult the distinction between

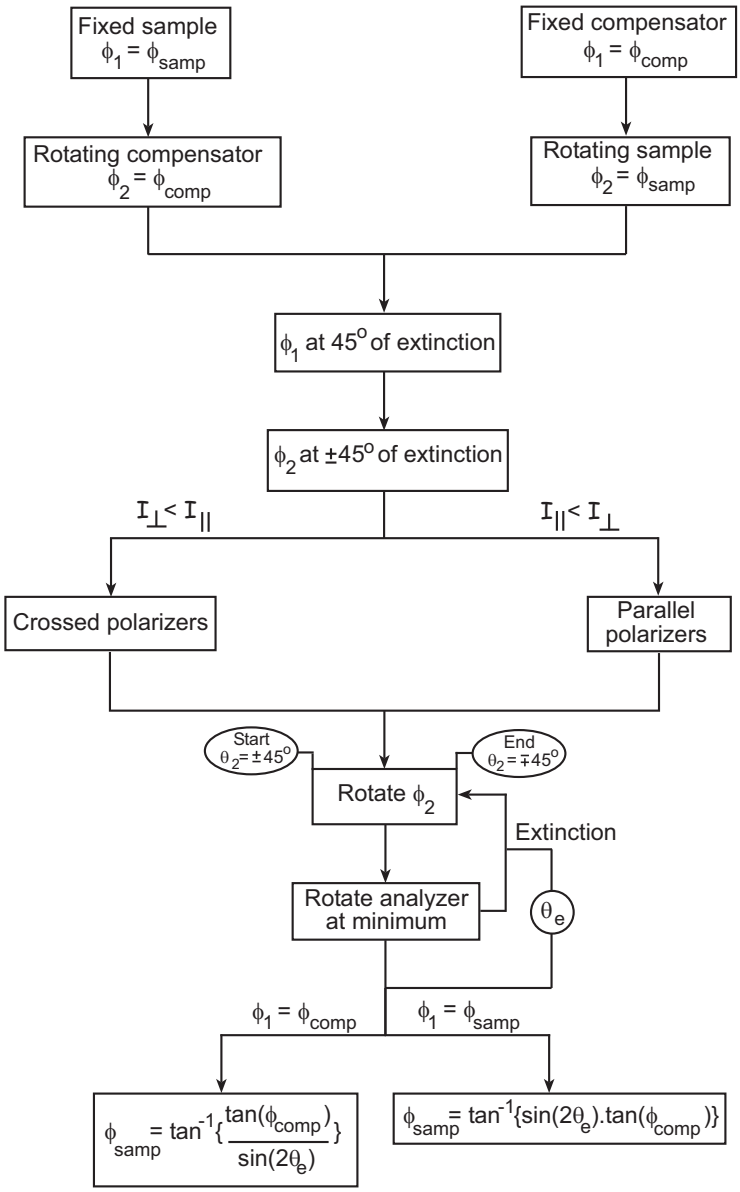

Figure 4.7: Flow chart representing the experimental procedure to measure retardation using the TWC method.

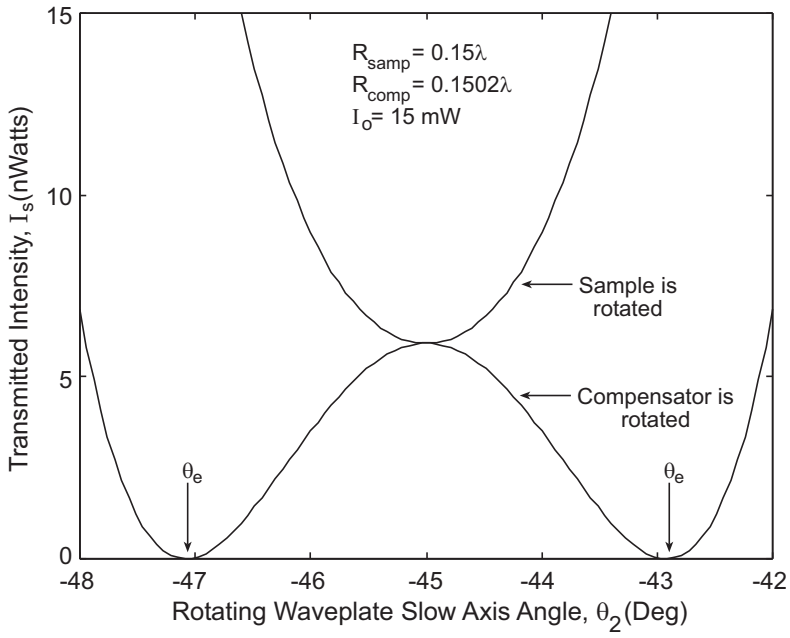

Figure 4.8: The intensity transmitted along the analyzer transmission direction is plotted for a sample retardation equal to 0.15λ and a compensator retardation equal to 0.1502λ. The input intensity is 15 mW. In one case, the sample is rotated and no extinction is obtained (upper curve with one global minimum). In the other case, the compensator is rotated and extinction is obtained (lower curve with two global minima and one local maximum).

the extinction and the adjacent maximum. This is illustrated in Fig. 4.8 where the intensity transmitted along the semi-minor axis of the output light polarization ellipse is plotted as a function of the rotating waveplate angle between -48 and -42 *deg* for a light source power I_o equal to 15 mW which corresponds to the power of a He-Ne laser used in experiments comparing Brace-Köhler and TWC techniques.

The retardations of the sample and compensator are respectively equal to 0.15λ and 0.1502λ. In the case where the compensator is the rotating waveplate, a linearly polarized output is produced for θ_2 equal to -47.08, -42.91, 132.92, and 137.08 *deg*. When the compensator is rotated between -48 and -42 *deg*, extinction is produced for two of these angles shown in Fig. 4.8. Also shown in Fig. 4.8 is the intensity transmitted as the sample is rotated over the same angular range. When the sample is rotated from -45 to +45 *deg*, no linearly polarized output is produced and the semi-minor axis of the output polarization ellipse increases monotonically similarly to that shown in Fig. 4.4. It will be shown later

analytically, that the intensity of the minimum produced at -45 *deg* when the sample is rotated is equal to that of the local maximum produced when the compensator is rotated. This is shown in Fig. 4.8. The capability of the system for measuring the intensity difference between the intensity of the global minimum reached at ±45 *deg* when the non-linearly-polarizing waveplate is rotated and the intensity of the global minimum reached when the linearly-polarizing waveplate is rotated defines the resolution of the TWC technique. This depends upon the sensitivity of the system in measuring and resolving low-level intensities. In the example of Fig. 4.8, the minimum measurable intensity must be less than 5 nW in order to resolve the global minimum when the compensator is rotated and the local maximum when the sample is rotated.

By deriving the exact expression for the intensity along the semi-axes of the output polarization ellipse occuring for θ_2 equal to ±45 *deg*, general criteria for the resolution range of the TWC can be developed in terms of the input power I_o and the minimum intensity I_{min} measurable by the experimental system. Using Jones calculus, an electric field is represented with the phasor $\vec{\mathcal{E}}$

$$\vec{\mathcal{E}} = \begin{pmatrix} c_1 e^{j\beta_1} \\ \\ c_2 e^{j\beta_2} \end{pmatrix}, \tag{4.17}$$

where c_1 and c_2 are the amplitudes of the vibrations along the two polarization directions of the birefringent medium, and β_1 and β_2 the phase-shifts introduced to the two vibrations upon traveling through the birefringent medium. Assuming two vibrations, respectively $u(t)$ and $v(t)$, along the slow and fast axes of the birefringent medium, the ellipse traced by the electric field can be represented by

$$u(t) = a_1 \cos \omega t \tag{4.18}$$

$$v(t) = a_2 \cos(\omega t + \beta_2 - \beta_1), \tag{4.19}$$

with ω the radian frequency. After transmission through the birefringent medium, it can be shown that the two semi-axes of the polarization ellipse traced by the electric field occur for the following parametric variables $t_1$and t_2,

$$t_1 = -\frac{1}{2} \arctan \frac{c_2^2 \sin\{2(\beta_2 - \beta_1)\}}{c_1^2 + c_2^2 \cos\{2(\beta_2 - \beta_1)\}} \tag{4.20}$$

$$t_2 = t_1 + 90^o. \tag{4.21}$$

By substituting Eqs. (4.20) and (4.21) into Eqs. (4.8) through (4.11), the length of the semi-axes S_1 and S_2 of the polarization ellipse can be derived for θ_2 equal to +45 and -45 *deg*

$$S_1(\theta_2 = 45^o) = \cos(\frac{\phi_1 + \phi_2}{2}) \tag{4.22}$$

$$S_2(\theta_2 = 45^o) = \sin(\frac{\phi_1 + \phi_2}{2}) \tag{4.23}$$

$$S_1(\theta_2 = -45^o) = \cos(\frac{\phi_1 - \phi_2}{2}) \tag{4.24}$$

$$S_2(\theta_2 = -45^o) = \sin(\frac{\phi_1 - \phi_2}{2}). \tag{4.25}$$

To calculate the actual intensity along the semi-axes of the polarization ellipse, we use the fact that the intensity of the electric field is given by $\vec{\mathcal{E}}.\vec{\mathcal{E}}^*$. Therefore, the intensity I_s along the semi axes of the polarization ellipse is

$$I_s(\theta_2 = \pm 45^o) = S_i(\pm 45^o)^2 I_o, \tag{4.26}$$

where i can have the value of 1 or 2 and I_o is the initial light source intensity. The intensity along the semi axes of the output polarization ellipse is derived using Eqs. (4.22) through (4.25)

$$I_1(\theta_2 = 45^o) = I_o \cos(\frac{\phi_1 + \phi_2}{2})^2 \tag{4.27}$$

$$I_2(\theta_2 = 45^o) = I_o \sin(\frac{\phi_1 + \phi_2}{2})^2 \tag{4.28}$$

$$I_1(\theta_2 = -45^o) = I_o \cos(\frac{\phi_1 - \phi_2}{2})^2 \tag{4.29}$$

$$I_2(\theta_2 = -45^o) = I_o \sin(\frac{\phi_1 - \phi_2}{2})^2. \tag{4.30}$$

In Fig. 4.8, in order for the local maximum occuring at θ_2 equal to -45 *deg* to be resolved, its intensity must be greater than the minimum intensity I_{min} measurable by the experimental system. This condition is expressed as follows in terms of the intensities above

$$I_o \cos(\frac{\phi_1 + \phi_2}{2})^2 > I_{min} \tag{4.31}$$

$$I_o \sin(\frac{\phi_1 + \phi_2}{2})^2 > I_{min} \tag{4.32}$$

$$I_o \cos(\frac{\phi_1 - \phi_2}{2})^2 > I_{min} \tag{4.33}$$

$$I_o \sin(\frac{\phi_1 - \phi_2}{2})^2 > I_{min}. \tag{4.34}$$

Using the four equations above, the resolvability condition can be expressed as a function of sample and compensator phase retardations, the input power and the minimum measurable power

$$2\arcsin(\sqrt{\frac{I_{min}}{I_o}}) < \phi_1 - \phi_2 < 2\arccos(\sqrt{\frac{I_{min}}{I_o}}) \tag{4.35}$$

$$2\arcsin(\sqrt{\frac{I_{min}}{I_o}}) < \phi_1 + \phi_2 < 2\arccos(\sqrt{\frac{I_{min}}{I_o}}). \tag{4.36}$$

4.1.5 Resolution

The resolution of the TWC technique can be quantified as a function of the sample retardation and angular resolution as was done with the Brace-Köhler compensator. The compensator angle θ_c necessary to produce linearly polarized light is given by Eq. (4.15) as $\sin(2\theta_c) = -\tan\phi_{s1}/\tan\phi_c$, with ϕ_{s1} and ϕ_c being the sample and compensator phase retardations. The nearest measurable retardation ϕ_{s2} is given by

$$\tan\phi_{s2} = -\tan\phi_c \sin(2\theta_c + 2\Delta\theta), \tag{4.37}$$

where $\Delta\theta$ is the angular resolution. The difference between ϕ_{s2} and ϕ_{s1} allows the resolution to be computed. The TWC resolution is calculated and represented as a function of the sample retardation and the angular resolution in Figs. 4.9(a) and 4.9(b) for compensator retardations $\lambda/10$ and $\lambda/30$ respectively. The TWC resolution is comparable to that of the Brace-Köhler compensator technique and is about 0.1 nm and 0.2 nm respectively for an angular resolution of 0.1 deg. Similarly to the Brace-Köhler compensator technique, the TWC resolution improves with angular resolution. For an angular resolution of 0.01 deg, resolutions of 0.04 nm and 0.02 nm are achieved respectively.

4.1.6 Accuracy

The measurement error using the TWC is calculated by determining the angular measurement uncertainty which is defined as the angular range over which the output light intensity decreases beyond the minimum measurable intensity. The corresponding measured retardations at either extreme of the angular range are calculated using the TWC formulas and

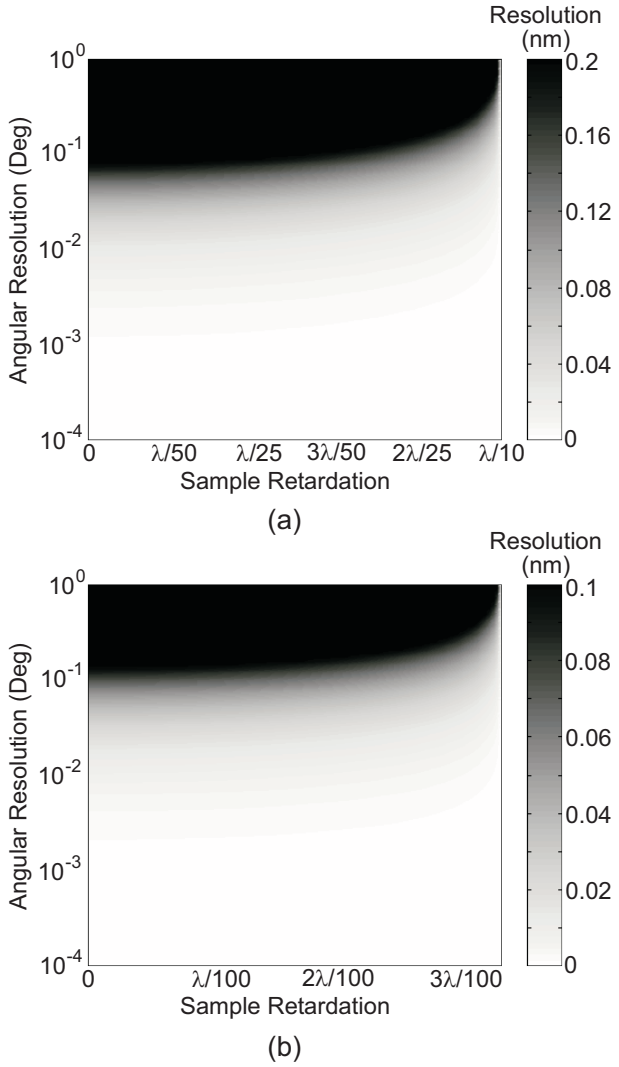

Figure 4.9: Resolution of the TWC technique as a function of sample retardation and angular resolution. (a) Compensator retardation equals $\lambda/10$. (b) Compensator retardation equals $\lambda/30$.

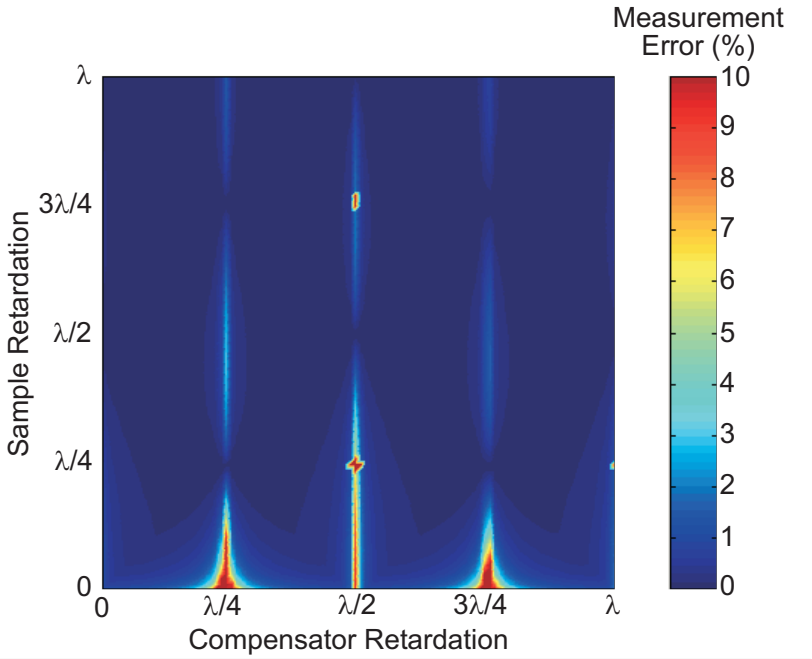

Figure 4.10: Measurement error in TWC for any given pair of sample and compensator retardations. The error is calculated based on the measurement angular uncertainty due to the sensitivity limit of the experiment.

compared to the true sample retardation. Figure 4.10 represents the relative measurement error for sample and compensator retardations ranging from 0 to λ. A minimum measurable intensity of 5 nW is considered to plot Fig. 4.10 which corresponds to the minimum measurable intensity of a UDT photodetector that is used at 632.8 nm to compare the accuracy of the Brace-Köhler compensator and the TWC. The relative error of the measurement remains below 2% over the entire range of sample and compensator retardations except when the compensator retardation is a multiple of a quarter-waveplate or a half-waveplate in which case the error increases beyond 10%. The error remains low however when the sample retardation is a multiple of a quarter-waveplate or a half-waveplate.

When either waveplate in the two-waveplate system is a quarter-waveplate, it needs to be the rotating waveplate to satisfy the condition stated in Eq. (4.16). Substituting $\phi_2 = \pi/4$ in Eq. (4.15), the angle θ_2 producing linearly polarized light is

$$\theta_2 = \frac{1}{2}\arcsin\left(\frac{\tan\phi_1}{\infty}\right) \tag{4.38}$$

$$= 0. \tag{4.39}$$

If the sample is the fixed waveplate and the compensator is the rotating quarter-waveplate, the sample unknown retardation is given by

$$\begin{aligned} \phi_{samp} &= \arctan\{\tan(90^o)\sin(2\theta_2)\}, && (4.40)\\ &= \arctan\{\infty \sin(2\theta_2)\}, && (4.41)\\ &= 90^o, && (4.42) \end{aligned}$$

considering the angular uncertainty of the measurement which results in not measuring accurately θ_2 equal to zero. When the compensator is a quarter-waveplate, the two-waveplate compensator technique determines erroneously the sample retardation as being equal to a quarter waveplate. This is the basis for the measurement error increasing in Fig. 4.10 when the compensator retardation approaches a multiple of a quarter-waveplate.

If the sample is the rotating quarter waveplate and the compensator the fixed waveplate, the sample unknown retardation is given by

$$\begin{aligned} \phi_{samp} &= \arctan\{\frac{\tan(90^o)}{\sin(2\theta_2)}\} && (4.43)\\ &= \arctan\{\frac{\infty}{\sin(2\theta_2)}\} && (4.44)\\ &= 90^o. && (4.45) \end{aligned}$$

When the sample is a quarter-waveplate, the TWC technique determines its retardation correctly. This is the basis for the measurement error remaining low in Fig. 4.10 when the sample retardation approaches a multiple of a quarter-waveplate.

A similar reasoning can be applied and can show that the TWC technique determines erroneously a sample retardation when the compensator is a half-waveplate and determines correctly the sample retardation when it is a half-waveplate.

4.2 Automated Two-Waveplate Compensator

In the previous sections, experimental procedures were presented using the TWC technique to measure a sample's retardation magnitude. In this section, the Automated Two-Waveplate Compensator (ATWC) is presented to also measure the sample's retardation orientation.

Previously, the sample slow axis orientation θ_1 was assumed to be known and the sample was oriented at 45 *deg* from extinction. For a sample whose slow axis orientation is not known, a rather simple preliminary experiment can be performed to determine its orientation. This gives therefore the ability to the TWC technique of locating a sample slow axis orientation. The sample can be placed between crossed polarizers. It can then be rotated until complete extinction is obtained. This orientation corresponds to the case where the sample slow and fast axes are parallel to the crossed polarizers transmission direction. The sample slow and fast axes are thus determined. Rotating the sample 45 *deg* from extinction, and following the TWC experimental procedure previously described allows one to measure the sample retardation magnitude.

However, the previous experimental procedure requires real-time reading of the intensity transmitted through the analyzer to determine the compensator angle producing linearly polarized light. This process can easily be automated. For single-point retardation measurement, the sample is oriented at 45 *deg* from extinction. The compensator waveplate is rotated by a small angular increment from its extinction position. Keeping the compensator waveplate in this position, the analyzer is rotated 180 *deg* in small angular increments and the transmitted intensity is recorded for each angle. After the analyzer has been rotated 180 *deg*, it is rotated back to its initial position. The compensator waveplate is rotated to a second angle and the analyzer is rotated again like it was for the previous compensator position. The procedure is repeated until the compensator has been rotated over a range of angles depending on the order of magnitude of the retardation to be measured. The recorded intensities are then inspected to determine which compensator angle produced extinction.

Both the angular ranges of the compensator and the analyzer can be reduced if the retardation order of magnitude is known. The ATWC technique will be particularly useful for full-field retardation measurements in which case numerous image pixels need to considered. The experimental procedure for the ATWC technique is represented in Fig. 4.11.

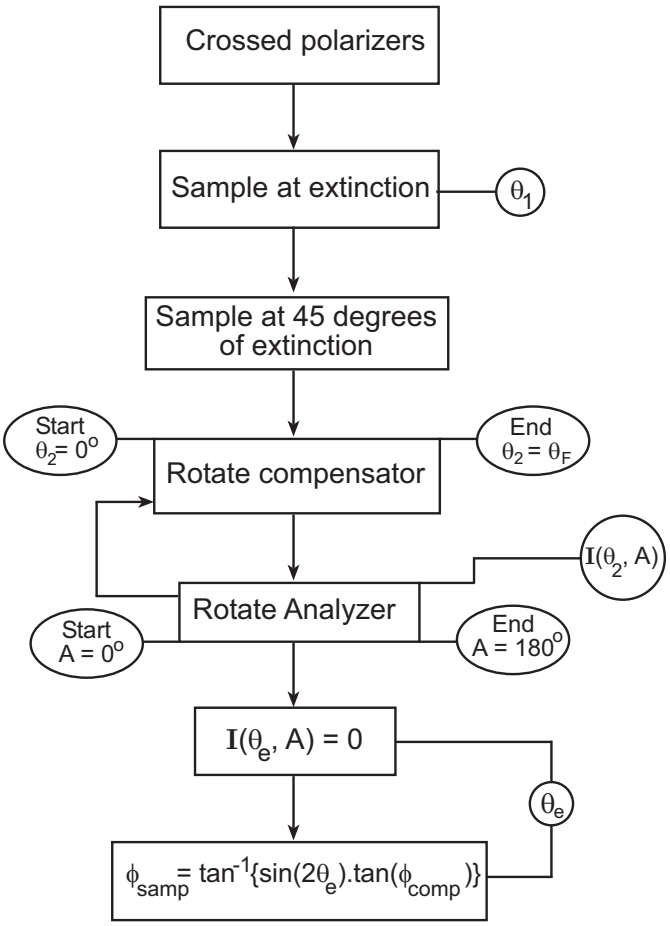

Figure 4.11: Flow chart for Automated TWC.

4.3 Phase-Stepping Two-Waveplate Retarder

The intensity expressions derived earlier can be used to construct systems of equations that may be helpful in retrieving the retardation magnitude and orientation of a sample.

4.3.1 2-Step PSTWR

The expression of the intensity transmitted through the analyzer has been derived and is given by Eq. (3.21)

$$\begin{aligned} I_A &= \mathcal{E}_{A_x}.\mathcal{E}^*_{A_x} \\ &= \sin^2\theta_2\{\cos^2\theta_2\cos^2\frac{\phi_1}{2} + \cos^2(2\theta_1-\theta_2)\sin^2\frac{\phi_1}{2}\} \\ &\quad + \cos^2\theta_2\{\sin^2\theta_2\cos^2\frac{\phi_1}{2} + \sin^2(2\theta_1-\theta_2)\sin^2\frac{\phi_1}{2}\} \\ &\quad -\frac{1}{2}\sin 2\theta_2\{\sin 2\theta_2\cos^2\frac{\phi_1}{2}\cos\phi_2 - \sin(4\theta_1-2\theta_2)\cos\phi_2\sin^2\frac{\phi_1}{2} \\ &\quad - \sin 2\theta_1\sin\phi_1\sin\phi_2\}. \quad (4.46) \end{aligned}$$

The Brace-Köhler compensator technique assumes that the sample slow axis orientation θ_1 is equal to 45 *deg*. This method therefore only allows the measurement of the sample retardation magnitude. Two intensity equations are needed to determine the sample retardation magnitude and orientation. In the above system, the intensity depends on four variables ϕ_1, ϕ_2, θ_1, and θ_2. The unknowns are ϕ_1 and θ_1. The retardation magnitude of the second waveplate ϕ_2 is fixed and known. By varying the compensator angle θ_2, enough intensity equations can be generated in order to determine the unknowns ϕ_1 and θ_1. Substituting θ_2 equal to 0, 45, and -45 *deg* in Eq. (3.21), three intensity equations are generated

$$I_1(\theta_2=0) = \sin^2(2\theta_1)\sin^2\frac{\phi_1}{2} \quad (4.47)$$

$$I_2(\theta_2=45^o) = \sin^2\frac{\phi_2}{2} + \sin^2(2\theta_1)\sin^2\frac{\phi_1}{2}\cos\theta_2 + \frac{1}{2}\sin(2\theta_1)\sin\phi_1\sin\phi_2 \quad (4.48)$$

$$I_3(\theta_2=-45^o) = \sin^2\frac{\phi_2}{2} + \sin^2(2\theta_1)\sin^2\frac{\phi_1}{2}\cos\theta_2 - \frac{1}{2}\sin(2\theta_1)\sin\phi_1\sin\phi_2. \quad (4.49)$$

The system of intensity equations above can be solved for ϕ_1 and θ_1 provided that the transmitted intensities I_1, I_2, and I_3 are known. Using I_1 and I_2, the sample retardation

magnitude and orientation are given by

$$\phi_1 = 2\arccos\left\{\frac{I_2 - \sin^2\frac{\phi_2}{2} - I_1\cos\phi_2}{\sin\phi_2\sqrt{I_1}}\right\}, \tag{4.50}$$

$$\theta_1 = \frac{1}{2}\arcsin\left\{\frac{\sqrt{I_1}}{\sin\frac{\phi_1}{2}}\right\}. \tag{4.51}$$

Using I_2 and I_3

$$\phi_1 = 2\arccos\left\{\frac{1}{\sqrt{2}}\frac{(I_2 - I_3)\sqrt{\cos\phi_2}}{\sin\phi_2\sqrt{I_2 + I_3 - 2\sin^2\frac{\phi_2}{2}}}\right\}, \tag{4.52}$$

$$\theta_1 = \frac{1}{2}\arcsin\left\{\frac{I_2 - I_3}{\sin\phi_1\sin\phi_2}\right\}. \tag{4.53}$$

This constitutes the basis for a new retardation measurement technique, the Phase-Stepping Two-Waveplate Retarder (PSTWR). Different retardation biases are generated by rotating the compensator at different angles. Measuring the intensities allows to solve systems of intensity equations for the sample retardation magnitude and orientation ϕ_1 and θ_1. This method can be implemented for single-point or full-field retardation measurements.

4.3.2 3-Step PSTWR

Equation (3.21) can also be further developed so the PSTWR can be applied for any bias angles θ_2. Using trigonometric relationships, the variables θ_1 and θ_2 are decoupled as

$$\begin{aligned} I_A = {} & \frac{1}{2}A(\theta_2) + \frac{1}{2}A(\theta_2)\cos\phi_1 - \frac{1}{2}\sin 4\theta_2\sin^2\frac{\phi_2}{2}\sin 2\theta_1\cos 2\theta_1 + \frac{1}{2}A(\theta_2) \\ & - A(\theta_2)\sin^2 2\theta_1 + \frac{1}{2}\sin 4\theta_2\sin^2\frac{\phi_2}{2}\sin 2\theta_1\cos 2\theta_1\cos\phi_1 - \frac{1}{2}A(\theta_2)\cos\phi_1 \\ & + A(\theta_2)\sin^2 2\theta_1\cos\phi_1 + \frac{1}{2}\sin^2 2\theta_1 - \frac{1}{2}\cos\phi_1\sin^2 2\theta_1 \\ & + \frac{1}{2}\sin 2\theta_2\sin\phi_2\sin 2\theta_1\sin\phi_1, \end{aligned} \tag{4.54}$$

with

$$A(\theta_2) = \sin^2 2\theta_2\sin^2\frac{\phi_2}{2}. \tag{4.55}$$

Successively factoring out $A(\theta_2) - 1/2$ and $(\cos\phi_1 - 1)$ leads to

$$I_A = A(\theta_2) - \frac{1}{2}\sin 4\theta_2\sin^2\frac{\phi_2}{2}\sin 2\theta_1\cos 2\theta_1(\cos\phi_1 - 1)$$

$$+ \quad \{A(\theta_2) - \frac{1}{2}\} \sin^2 2\theta_1 (\cos\phi_1 - 1)$$
$$+ \quad \frac{1}{2} \sin 2\theta_2 \sin\phi_2 \sin 2\theta_1 \sin\phi_1. \tag{4.56}$$

Subtracting $A(\theta_2)$ from both sides of the equation,

$$\begin{aligned} I_A - A(\theta_2) &= -\sin 4\theta_2 \sin^2 \frac{\phi_2}{2} \sin 2\theta_1 \cos 2\theta_1 \sin^2 \frac{\phi_1}{2} \\ &- 2\{A(\theta_2) - \frac{1}{2}\} \sin^2 2\theta_1 \sin^2 \frac{\phi_1}{2} \\ &+ \frac{1}{2} \sin 2\theta_2 \sin\phi_2 \sin 2\theta_1 \sin\phi_1. \end{aligned} \tag{4.57}$$

The unknowns in the above equation are

$$X_1 = \sin 2\theta_1 \cos 2\theta_1 \sin^2 \frac{\phi_1}{2} \tag{4.58}$$
$$X_2 = \sin^2 2\theta_1 \sin^2 \frac{\phi_1}{2} \tag{4.59}$$
$$X_3 = \sin 2\theta_1 \sin\phi_1. \tag{4.60}$$

Assuming

$$a(\theta_{2,i}) = -\sin 4\theta_{2,i} \sin^2 \frac{\phi_2}{2} \tag{4.61}$$
$$b(\theta_{2,i}) = 1 - 2A(\theta_{2,i}) \tag{4.62}$$
$$c(\theta_{2,i}) = \frac{1}{2} \sin 2\theta_{2,i} \sin\phi_2, \tag{4.63}$$

where i denotes the ith bias angle, the following matrix equation is obtained,

$$\begin{pmatrix} a(\theta_{2,1}) & b(\theta_{2,1}) & c(\theta_{2,1}) \\ a(\theta_{2,2}) & b(\theta_{2,2}) & c(\theta_{2,2}) \\ a(\theta_{2,3}) & b(\theta_{2,3}) & c(\theta_{2,3}) \end{pmatrix} \begin{pmatrix} X_1 \\ X_2 \\ X_3 \end{pmatrix} = \begin{pmatrix} I_{A,1} - A(\theta_{2,1}) \\ I_{A,2} - A(\theta_{2,2}) \\ I_{A,3} - A(\theta_{2,3}) \end{pmatrix} \tag{4.64}$$
$$BX = C, \tag{4.65}$$

where the matrix B is obtained by calculating $a(\theta_{2,i})$, $b(\theta_{2,i})$, and $c(\theta_{2,i})$ for the various bias angles $\theta_{2,i}$, and the matrix C is obtained by measuring the transmitted intensities at each bias angle and calculating $A(\theta_{2,i})$. Solving the matrix equation for X leads to

$$X = B^{-1}C. \tag{4.66}$$

Using the expressions for X_1, X_2, and X_3

$$\tan 2\theta_1 = \frac{X_2}{X_1} \tag{4.67}$$

$$\cos \phi_1 = \frac{X_3^2}{2X_2} - 1. \tag{4.68}$$

This constitutes the basis for the 3-step PSTWR method. Three intensity measurements for 3 bias angles θ_2 are needed to solve the system of equations for X_1, X_2, and X_3.

4.3.3 N-Step PSTWR

Equation (4.64) is a system of 3 intensity equations with 3 unknowns X_1, X_2, and X_3 which are functions of ϕ_1 and θ_1. Solving the system requires at least 3 intensities to be measured for 3 bias angles θ_2. However, intensities might not be measured accurately and more measurements might be needed to minimize the measurement error. This is the basis for the N-Step PSTWR method. When N intensity measurements are made for N different bias angles, the system will have N equations with 3 unknowns. The system is overspecified and the best solution is found by minimizing the squared error e defined as

$$e = BX - C, \tag{4.69}$$

where the matrix B is obtained by calculating $a(\theta_{2,i})$, $b(\theta_{2,i})$, and $c(\theta_{2,i})$ for the various bias angles $\theta_{2,i}$, and the matrix C is obtained by measuring the transmitted intensities at each bias angle and calculating $A(\theta_{2,i})$.

The solutions minimizing the squared error defined in Eq. (4.69) can be expressed in terms of the Moore-Penrose inverse of the matrix B [92]. Multiplying both sides of Eq. (4.65) by the matrix transpose of B leads to

$$B^T BX = B^T C. \tag{4.70}$$

If the inverse of the square matrix $(B^T B)$ exists, the least square solutions of Eq. (4.69) are given by

$$X = (B^T B)^{-1} B^T C, \tag{4.71}$$

$$X = B^+ C, \tag{4.72}$$

where the matrix B^+ is the generalized Moore-Penrose inverse or pseudoinverse of the matrix B [92]. The solutions derived in Eq. (4.72) are the least square solutions minimizing the error defined in Eq. (4.69). This is the basis for the N-step PSTWR method consisting of performing N intensity measurements, with $N > 3$, for N bias angles θ_2 and solving Eq. (4.72) for X_1, X_2, and X_3.

CHAPTER 5

COLORIMETRY-BASED RETARDATION MEASUREMENTS

5.1 White-Light Interference Colors

5.1.1 Color Formation

White-light interference colors are seen when a quartz wedge, depicted in Fig. 5.1, is viewed between crossed polarizers. The quartz wedge is composed of two pieces of quartz with their optic axes perpendicular to each other and both lying in a plane perpendicular to the light propagation. One of the pieces has a linearly increasing thickness as shown in Fig. 5.1. This causes the retardation between the two wavefronts formed in the wedge to increase linearly along the wavefront. The retardation affects the transmittance of each wavelength differently. Between crossed polarizers, the transmittance is given by [40]

$$T(R,\lambda) = I_o \sin^2(\frac{\pi R}{\lambda}), \tag{5.1}$$

where R is the retardation, I_o the incident intensity, and λ the freespace wavelength. In the quartz wedge, the retardation R increases as the thickness of the wedge increases.

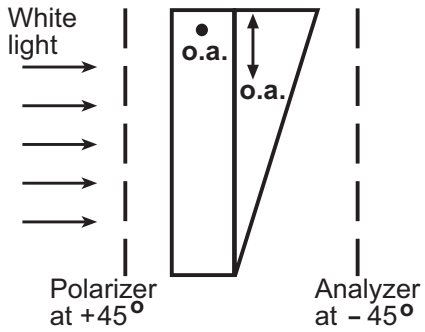

Figure 5.1: Quartz wedge made of two pieces of quartz with their optic axes perpendicular to one another. Placed between crossed polarizers and illuminated with white light, white-light interference colors are produced. o.a., optic axis.

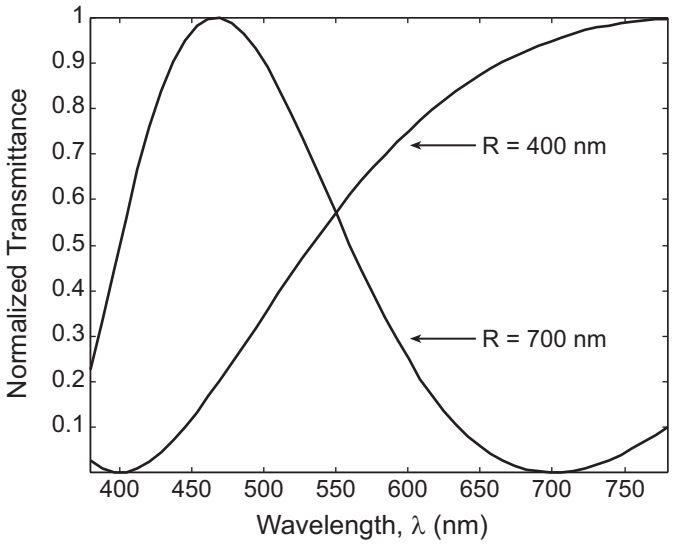

Figure 5.2: Normalized light intensity transmitted by a quartz wedge between crossed polarizers for retardations $R = 400$ nm and $R = 700$ nm.

Consequently, the spectrum of the transmitted light differs from the spectrum of the white-light illuminating the wedge as can be seen in Fig. 5.2 where the normalized transmittance has been plotted for two retardations, $R = 400$ nm and $R = 700$ nm. These two transmitted spectra can be seen in Fig. 5.3 which shows a quartz wedge observed with a transmission polarization microscope. The quartz wedge is placed on the microscope stage and observed with a $5\times$ objective. Its image is projected on a CCD camera connected to the frame-grabber of a computer. The image is then recorded using an image processing software. The field-of-view of the CCD camera is rectangular therefore truncating the circular field-of-view of the microsope. This picture shows the white-light interference colors as the retardation increases along the quartz wedge. At $R = 400$ nm, the transmitted spectrum appears bluish whereas it appears reddish/orangish at $R = 700$ nm. Both of these colors are consistent with the transmission curves in Fig. 5.2.

5.1.2 Chromaticity Diagram

Each color can be quantified and represented on a chromaticity diagram. Each color is uniquely defined by its chromaticity coordinates, x, y, and z which are derived from the

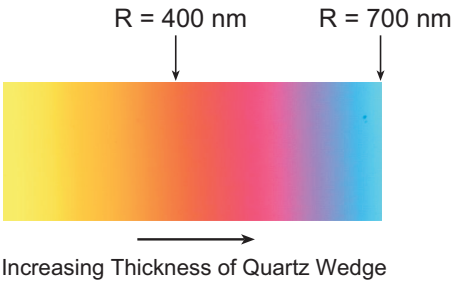

Figure 5.3: Quartz wedge observed between crossed polarizers with a transmitted polarization microscope at magnification 5×. The two colors corresponding to the transmitted spectra plotted in Fig. 5.2 are indicated.

tristimulus values, X, Y and Z as follows [93]

$$\mathrm{x} = \frac{X}{X+Y+Z},\ \mathrm{y} = \frac{Y}{X+Y+Z},\ \mathrm{z} = \frac{Z}{X+Y+Z}. \tag{5.2}$$

The tristimulus values represent the amount of light that must be sent from three imaginary primary colors to the eye to produce the same color sensation as that induced by the observed sample [93]. These tristimulus values are a function of the spectral distribution of the light source, $S(\lambda)$, the spectral reflectance $R(\lambda)$ or transmittance $T(\lambda)$ of the observed sample, the spectral transmittance $T_{optics}(\lambda)$ of the optical components of the system, and the color-matching functions $\overline{x}(\lambda)$, $\overline{y}(\lambda)$ and $\overline{z}(\lambda)$. The color-matching functions used here are those recommended by the Comité International de L'Eclairage (CIE) in 1931. The tristimulus values X, Y and Z are computed as follows [93]

$$X = \sum_{\lambda} S(\lambda)T(\lambda)T_{optics}(\lambda)\overline{x}(\lambda),\ Y = \sum_{\lambda} S(\lambda)T(\lambda)T_{optics}(\lambda)\overline{y}(\lambda), \tag{5.3}$$

$$Z = \sum_{\lambda} S(\lambda)T(\lambda)T_{optics}(\lambda)\overline{z}(\lambda), \tag{5.4}$$

where, in the case of the quartz wedge, $T(\lambda)$ is given by Eq. (5.1). The white-light interference colors formed by the quartz wedge (see Fig. 5.3) can therefore be represented on a chromaticity diagram using the above equations to calculate the chromaticity coordinates x and y corresponding to the spectrum of transmitted light as the retardation increases linearly along the wedge. The results of such calculations are shown in Fig. 5.4. The

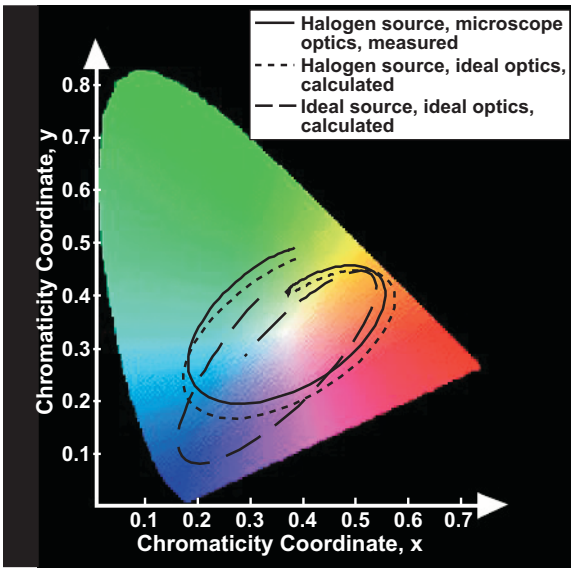

Figure 5.4: Chromaticity curves of the white-light interference colors as the retardation of the quartz wedge linearly increases. The long-dashed line represents the chromaticity coordinates calculated for an ideal white-light source and ideal optics of the microscope. The short-dashed line represents the chromaticity coordinates calculated for the spectral distribution of the halogen source used and ideal microscope optics. The solid line represents the measurements of the white-light interference colors generated when a quartz wedge is observed between crossed polarizers with a transmission polarization microscope.

long-dashed line represents the calculated chromaticity coordinates x and y of the white-light interference colors as the quartz wedge retardation increases when an ideal white-light source is used, i.e. $S(\lambda) = 1$ for all wavelengths, and ideal transmission through the optics is considered, i.e. $T_{optics}(\lambda) = 1$. The short-dashed line represents the calculated chromaticity coordinates x and y of the white-light interference colors when the actual spectral distribution of the halogen source used in the transmission polarization microscope is substituted into the above equations. The transmission through the optics is again considered ideal. Finally, the solid line represents the actual measurements made with a spectrophotometer. The measured values are slightly displaced from the calculations made with the halogen source and ideal optics, due to the fact that the optics of the microscope are not ideal.

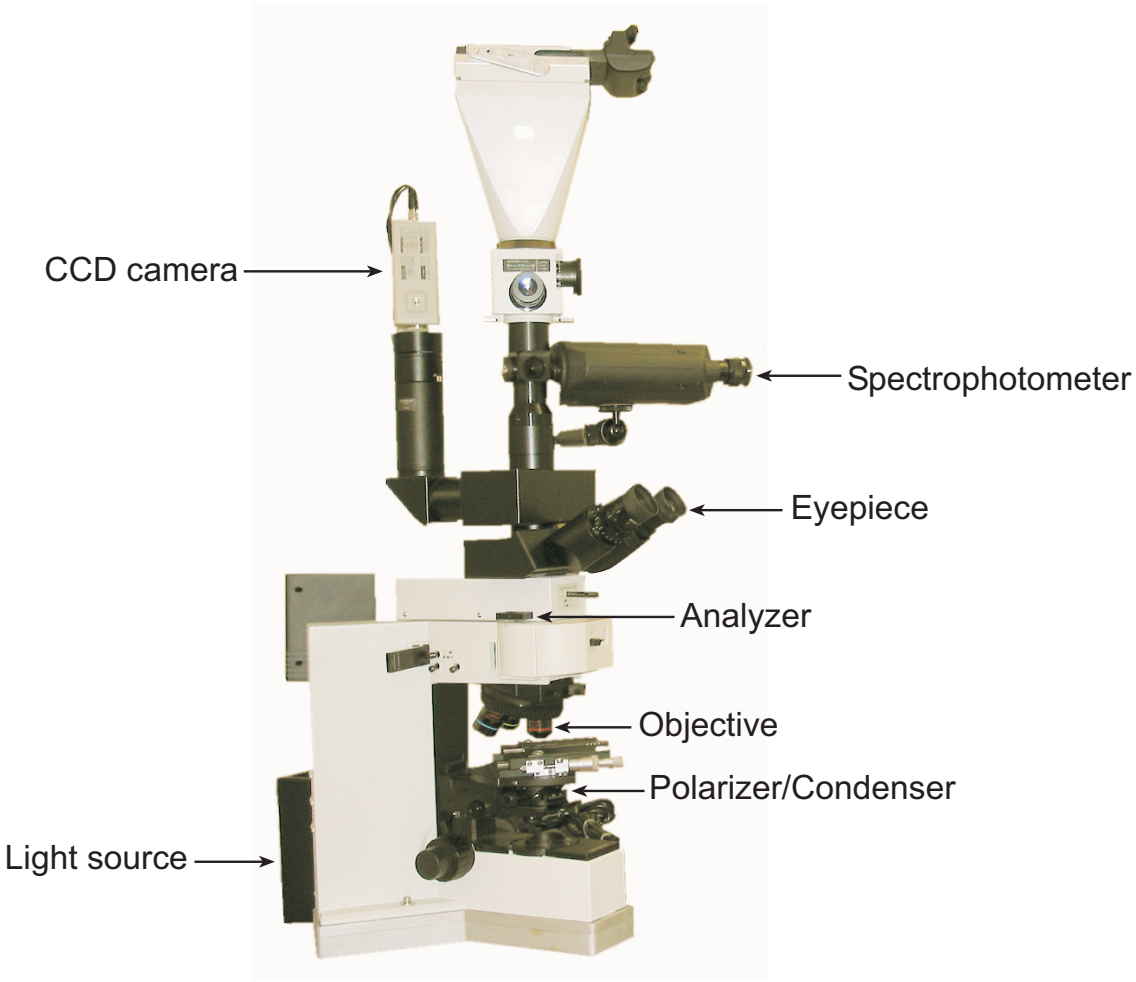

Figure 5.5: Polarization microscope.

5.2 Experiments

5.2.1 Calibration Retardation Measurements

The goal of these experiments is to determine the chromaticity coordinates of the white-light interference colors that correspond to retardations along the length of a quartz wedge, therefore creating a retardation-x,y calibration table. First, the quartz wedge is positioned on the microscope stage of a transmission polarization microscope. An Olympus microscope model BX-P is used in all these experiments (Fig. 5.5). The quartz wedge is accurately translated with a micrometer. The retardation as a function of the quartz wedge micrometer position is then determined. The quartz wedge is observed between crossed polarizers at a magnification of 50×. The retardation is accurately measured for various positions along

the wedge using the Sénarmont compensator technique. It consists of having a monochromatic linearly polarized beam of light incident upon the sample of unknown retardation. After transmission through the birefringent sample, the beam is elliptically polarized and is then incident upon a quarter-waveplate oriented so that its fast and slow axes coincide with the principal axes of the polarization ellipse. Consequently, the elliptically polarized light is converted to linear polarization. The direction of polarization is found by rotating the analyzer until extinction is obtained. The analyzer angle so determined allows the computation of the retardation [39]. The measurement configuration incorporates a 546 nm interference filter at the light source. For each measurement, the analyzer position that minimizes the intensity is read typically five times. These five readings are then averaged to calculate the retardation using

$$R = (m - \frac{\theta}{180^o})\ 546\ nm, \tag{5.5}$$

where R is the retardation in nm, m is the fringe order and θ is the average analyzer position in degrees. The fringe order m is determined with the white-light interference colors chart shown in Fig. 3.6.

These retardation measurements are plotted in Fig. 5.6 as a function of the quartz wedge micrometer translation. The inhomogeneous spacing between the measurement points is due to the fact that some measurements were added later to increase the number of points where the white-light interference colors vary rapidly which is the case for retardations between 400 nm and 600 nm. A polynomial fit is determined that relates the retardation to the micrometer position. This is used later to calculate the retardations at the micrometer positions where the colors are measured, eliminating the need for using the Sénarmont compensator. The degree of the polynomial fit is chosen using the deviation information shown in Fig. 5.7. The polynomial fit of degree six is chosen to give a small mean deviation between measured and calculated retardations and will be used throughout the remainder of this work to compute the retardation at a given micrometer position. The polynomial fit is also shown as a solid line in Fig. 5.6.

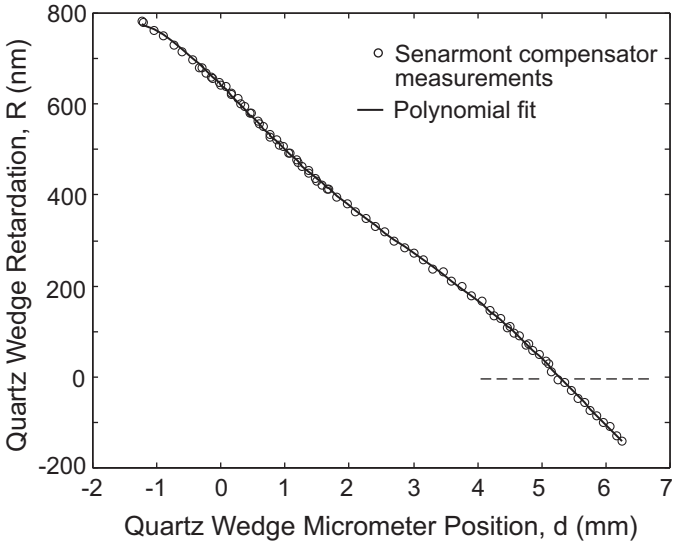

Figure 5.6: Quartz-wedge retardation as a function of the micrometer position. The dots correspond to the Senarmont compensator measurements. The solid line is the polynomial fit used to calculate the retardation as a function of the position along the quartz wedge. The measurements are conducted at a wavelength of 546 nm.

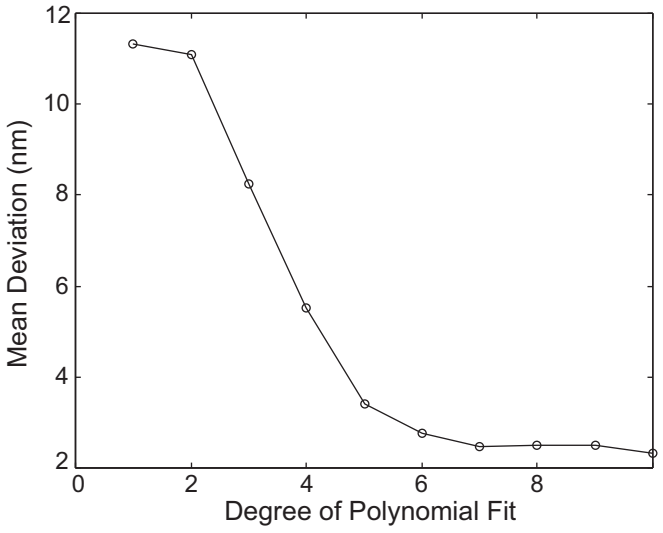

Figure 5.7: Mean deviation between calculated and measured retardations using polynomials of various degrees.

5.2.2 Calibration Color Measurements

The goal of these color measurements is to find polynomial fits that relate the chromaticity coordinates of the white-light interference colors to the retardations along the quartz wedge. To do so, the colors are measured using a spectrophotometer at positions along the quartz wedge. A Photo Research spectrophotometer model PR-650 is used for all experiments (Fig. 5.5). The retardations corresponding to these positions are calculated using the polynomial fit determined above. The color measurements are plotted in Fig. 5.8 in which Fig. 5.8(a) represents the chromaticity coordinate x as a function of retardation and Fig. 5.8(b) represents the chromaticity coordinate y as a function of retardation. Polynomials are used to relate the chromaticity coordinates to the retardation. The polynomial fit of degree 19 is chosen for the chromaticity coordinate x and the polynomial fit of degree 20 is chosen for the chromaticity coordinate y. These two polynomial fits are then used to compute the chromaticity coordinates x and y as a function of the retardation. Figure 5.9 shows the measured chromaticity coordinates x and y that were used to determine the two polynomial fits (black dots), and the chromaticity coordinates calculated using the polynomial fits (solid line). This constitutes a retardation-color calibration database associating a color with a retardation and a reference curve of the white-light interference colors that can be used to verify that a color measurement belongs to the white-light interference colors.

5.2.3 Method

Using the results from the above calibration experiments, a Colorimetry-Based Retardation Measurement (CBRM) method is presented. The polynomial fits determined in Sec. 5.2.2 are used to generate a fine grid in which the chromaticity coordinates x and y, i.e. the white-light interference colors, of each point are known as well as the corresponding retardation. To proceed to the measurement of an unknown retardation, the specimen color is measured, and the measurement is projected to the closest point on the white-light interference colors curve as shown in Fig. 5.10.

Knowing the retardation of the neighboring points in the grid and assuming a linear

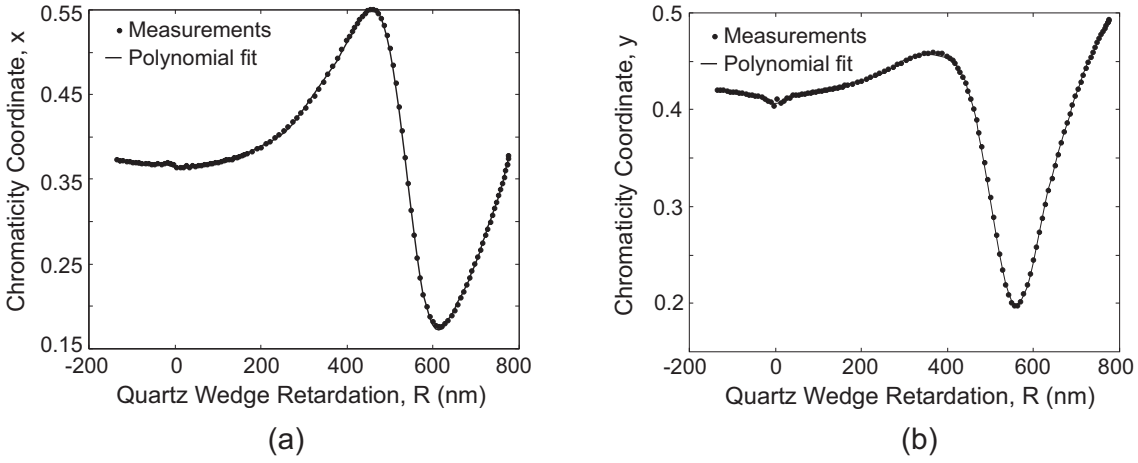

Figure 5.8: (a) Chromaticity coordinate x of the white-light interference colors as a function of the quartz wedge retardation. (b) Chromaticity coordinate y of the white-light interference colors as a function of the quartz wedge retardation. The dots represent the measurements made with a spectrophotometer when the quartz wedge is observed between crossed polarizers at a magnification of 50×. The solid line represents the polynomial fit used to calculate x and y as a function of the retardation.

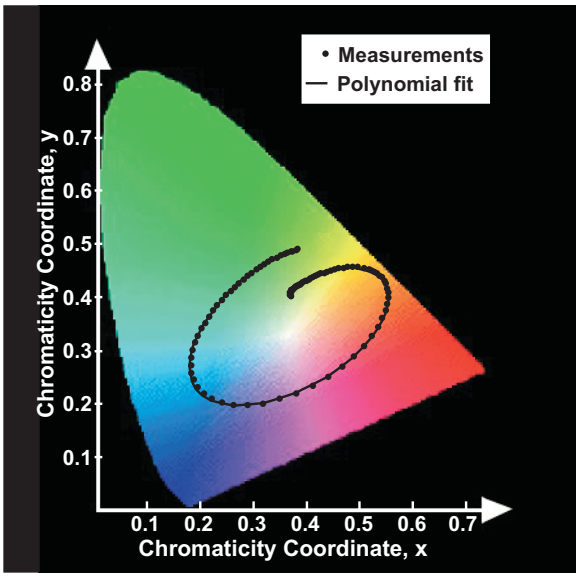

Figure 5.9: White-light interference colors curve plotted on a chromaticity diagram according to the conventions defined by the Comité International de l'Eclairage (CIE) in 1931. The dots represent the color measurements along a quartz wedge observed between crossed polarizers. The solid line represents the calculated chromaticity coordinates using the polynomial fits for chromaticity coordinates x and y as a function of the retardation.

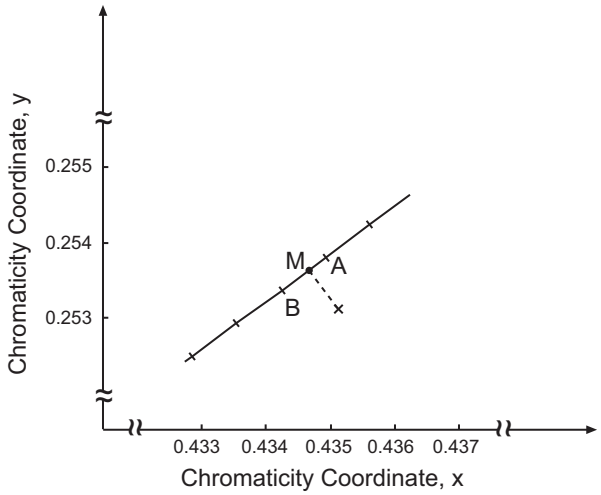

Figure 5.10: Retardation measurement using the CBRM method. The color is measured and plotted (×) in a chromaticity diagram. The measurement is projected onto the closest point M on the white-light interference colors curve defined using the polynomial fits determined in preliminary experiments. This curve is a fine grid in which the chromaticity coordinates x and y of each point, i.e. the color, are known as well as the corresponding retardation. The unknown retardation is then calculated at point M by assuming linear variation of the retardation in the grid between points A and B.

variation, the unknown retardation, R_M, can be computed as

$$R_M = R_B + \frac{D_{AM}}{D_{AB}}(R_A - R_B), \tag{5.6}$$

where R_A and R_B are respectively the retardations of points A and B in the calibration grid, D_{AB} is the distance between points A and B on the white-light interference colors curve, and D_{AM} is the distance between points A and M, the latter being the projection of the measurement point onto the white-light interference colors curve.

5.2.4 Results

The CBRM method was first applied to the quartz wedge. The results of these measurements are shown in Fig. 5.11. Table 5.1 summarizes numerical comparisons between the Sénarmont compensator method and the CBRM method. In Fig. 5.11, both sets of measurements can be fit to linear functions of the form

$$R = \frac{dR}{dd}d + R_o, \tag{5.7}$$

where R is the retardation along the quartz wedge in nm, d the position along the quartz wedge in mm, dR/dd the slope of the linear fit in nm/mm, and R_o the intercept of the

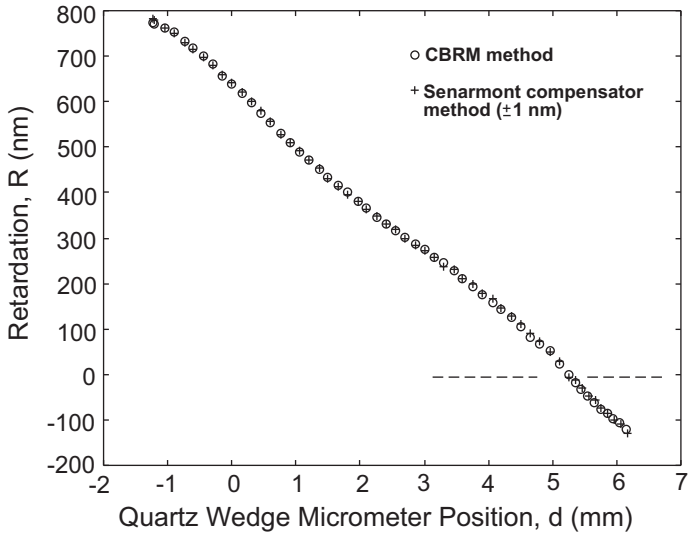

Figure 5.11: Quartz-wedge retardation measurements by CBRM method and by Sénarmont compensator method. Notice how both methods resolve the slight nonlinearity in the quartz wedge surface.

linear fit in nm. The slopes of the linear functions fit to the data of Fig. 5.11 for the CBRM method and the Sénarmont compensator method are respectively $-120.71\ nm/mm$ and $-120.59\ nm/mm$. The intercepts of these linear fits are respectively $632.22\ nm$ and $632.87\ nm$.

The quartz wedge is not completely flat and therefore small variations in the retardation as a function of position exist and, in this case, have somewhat the shape of a sinusoid. Figure 5.12 shows the quartz wedge retardation deviation from linear retardation for both sets of measurements. Figure 5.12 has been plotted by subtracting the two linear fits from the measurements made respectively with the CBRM and the Sénarmont compensator method (Fig. 5.11). The CBRM method was able to detect a deviation from flatness as small as $\lambda/40$ and is in very good agreement with the Sénarmont compensator method.

The Sénarmont compensator method consists of rotating the analyzer until minimum intensity is obtained. In practice, each measurement requires typically five readings whereas the CBRM method only requires a single color measurement. The CBRM method is about twelve times faster than the Sénarmont compensator. The mean deviation between the CBRM measurements and the Sénarmont compensator measurements is $3.59\ nm$, as indicated in Table 5.1, which corresponds to a mean error of 0.006 fringe order. This is

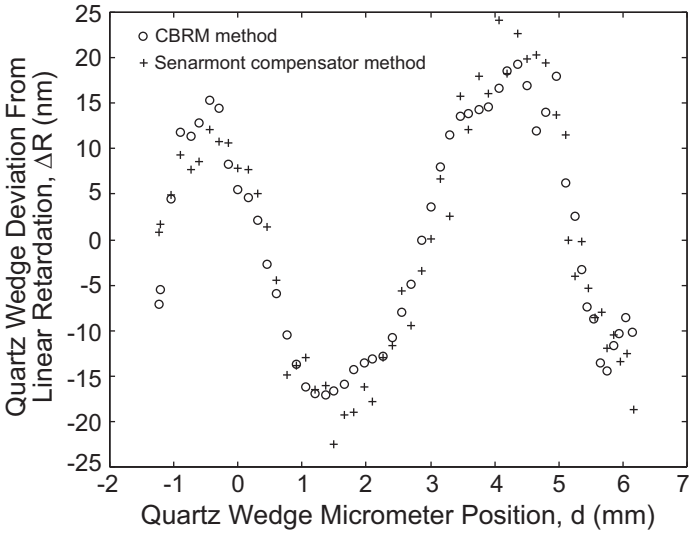

Figure 5.12: Quartz wedge retardation deviation from linear retardation for the CBRM method and the Sénarmont compensator method. This deviation from linearity has been determined by subtracting the two linear functions fit to the retardation measurements made respectively with the CBRM method and the Sénarmont compensator method and shown in Fig. 5.11.

Table 5.1: Comparison of retardation measurements of quartz wedge by Sénarmont compensator method and CBRM method.

Retardation mean deviation	3.59 nm
Retardation root mean square deviation	5.35 nm
Retardation displacement	0.12 nm

better than the 0.02 fringe order maximum error achieved with the RGB photoelasticity method [45]. In Table 5.1, retardation displacement indicates the displacement between the two linear fits to the Sénarmont compensator measurements and the CBRM measurements.

In quantifying the performance of the CBRM method, it was found that the smallest measurable retardation is about 5 nm. Indeed, between retardations of -5 nm and $+5$ nm, which in the white-light interference colors chart correspond to the zeroth-order fringe, the light level is very low and renders the color measurement uncertain. The accuracy has been defined previously by comparing the CBRM method measurements to Sénarmont compensator method measurements. It was found that the maximum deviation was 0.006 fringe order which is an improvement compared to the RGB photoelasticity method [45].

The resolution of the CBRM method was also determined. To obtained the minimum

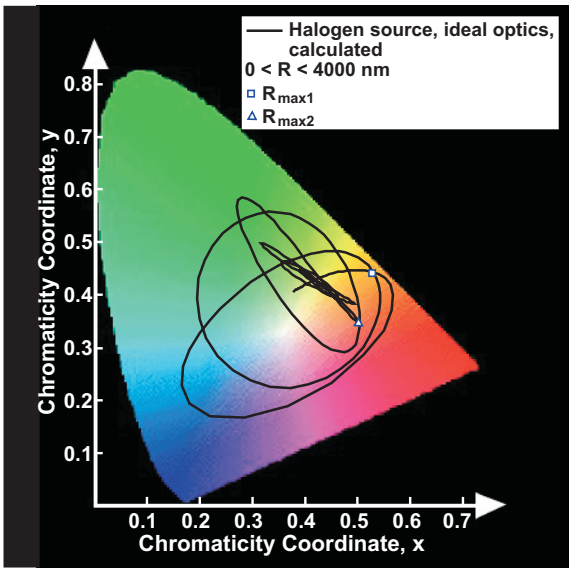

Figure 5.13: White-light interference colors curve calculated using the spectral distribution of the halogen source of the transmission polarization microscope and ideal optics. The colors are plotted for retardations from 0 to 4000 nm.

measurable retardation difference, the minimum measurable color difference was determined. The quartz wedge was translated in 5 μm increments. The color was measured and plotted as a function of the position. This measurement was done near a retardation of 500 nm. At this retardation, the chromaticity coordinate y varies slower than does the chromaticity coordinate x. Therefore, the minimum measurable color difference was determined according to the variations of the chromaticity coordinate y. To determine the minimum measurable y difference that corresponds to the minimum measurable color difference, 10 measurements were made at the same position over a period of 15 minutes so that the noise was quantified in terms of y. It was found that the largest noise deviation of y measured at the same position was 0.0004. Therefore, it was assumed that the measured color was different when the value of y changed by the noise value of 0.0004.

Using the measurement of the color as a function of the position, two values of y were found which had a difference of at least 0.0004. The corresponding values of x were also determined, and the corresponding retardations were computed using the CBRM method. Using this methodology, the resolution of the CBRM method was found to be ± 0.2 nm.

The range of measurable retardations can be found with the aid of Fig. 5.13 which represents the chromaticity coordinates, i.e. the white-light interference colors, as the retardation increases from 0 to 4000 nm. The spectral distribution of the halogen source of the transmitted polarization microscope was used to perform these calculations. The retardation can be determined without ambiguity in the range $0 < R < R_{max1}$ where R_{max1} is defined by the first intersection in Fig. 5.13 which occurs at retardation equal to 940 nm (x= 0.5282 and y= 0.4478). Retardations above R_{max1} can also be determined if one knows the range in which they fall. The upper limit of the measurement range of the CBRM method is determined by the coalescence of the white-light interference colors curve near the center of the chromaticity diagram, which occurs at retardation $R_{max2} = 2160$ nm (x= 0.5036 and y= 0.3499). Therefore the total range of the CBRM method is close to 0 - 4 fringe orders which is also an improvement compared to previous methods such as RGB photoelasticity method [45] whose range was found to be 0 - 3 fringe orders.

CHAPTER 6

COMPARATIVE ANALYSIS

6.1 Retardation Measurement Error

6.1.1 Error Analysis

The Brace-Köhler, Sénarmont, and TWC techniques have been investigated in terms of their applicability range, resolution, and accuracy in Chapters 3 and 4. In this chapter, the accuracies with which very small retardations can be measured with the three techniques are compared theoretically and experimentally. The techniques most suitable for measuring stress-induced birefringence in optical devices are therefore identified.

The measurement error is calculated using a similar approach to that used previously to calculate the error of the TWC in Chapter 4. In the case of the TWC, the exact angle necessary to produce linearly polarized light is calculated for a given pair of sample and compensator retardations. The transmitted intensity along the semi-minor axis of the output ellipse is calculated for angles near the extinction angle. The angular range over which the intensity is lower than the minimum measurable intensity is thus determined. The sample retardation is computed at both ends of the angular range corresponding to the angles for which the output intensity increases beyond the minimum measurable intensity. The maximum relative deviation from the exact retardation is defined as the relative measurement error.

In the case of the Brace-Köhler compensator however, this approach had to be slightly modified since the intensity minimum measured is greater than the minimum measurable intensity. Therefore, the angular uncertainty is defined as the angular range over which the intensity variation around the minimum of intensity is lower than the minimum measurable intensity change. The relative measurement error is then computed by calculating the maximum retardation deviation from the exact sample retardation similarly to what is done in the TWC case.

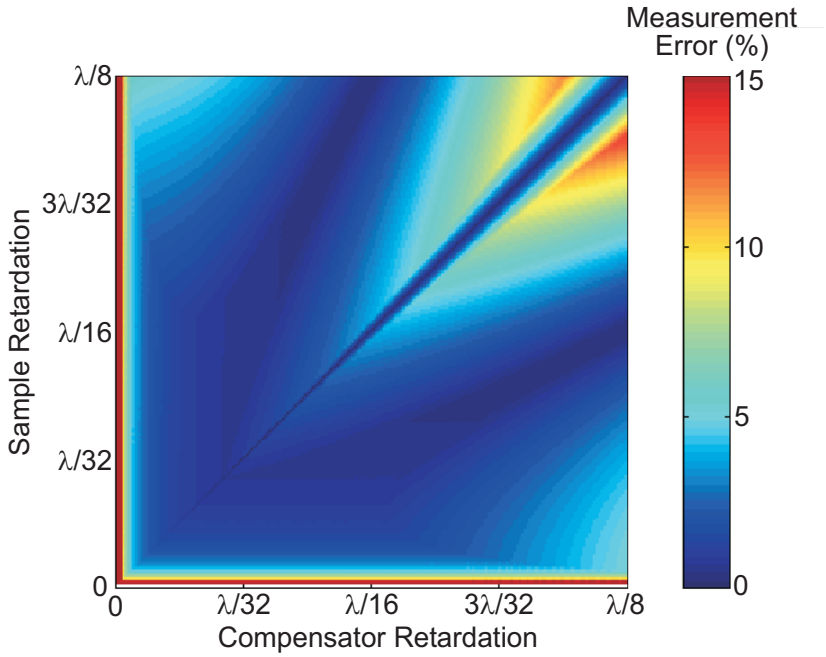

Figure 6.1: Error in Brace-Köhler compensator method for sample and compensator retardations ranging from 0 to $\lambda/8$. The error is determined taking into account the measurement angular uncertainty due to the sensitivity of the detector and taking into account the small retardation approximation. Only 22.125% of the total number of error data in the plot are below 1%.

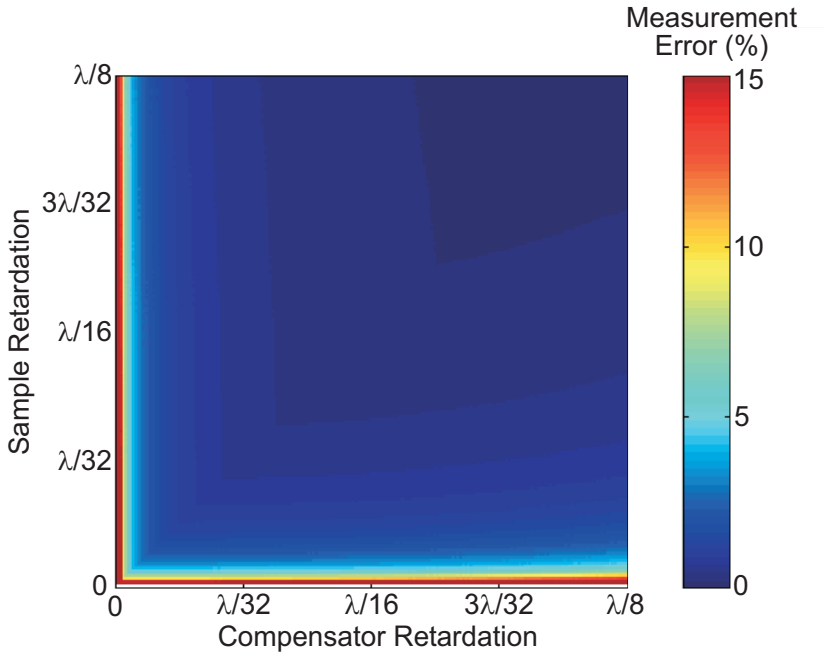

Figure 6.2: Error in TWC method for sample and compensator retardations ranging from 0 to $\lambda/8$. The error is determined taking into account the measurement angular uncertainty due to the sensitivity of the detector. 71.41% of the total number of error data in the plot are below 1%.

The measurement error is calculated for the Brace-Köhler compensator and the TWC in Figs. 6.1 and 6.2 for sample and compensator retardations between 0 and $\lambda/8$. Note that in the case of the Brace-Köhler compensator, the error calculated in Fig. 6.1 takes into account the measurement angular uncertainty and the error due to the small retardation approximation. Both plots were generated by considering 200 retardations between 0 and $\lambda/8$ for the sample and similarly 200 retardations for the compensator.

In the TWC case, 71.41% of the total number of calculated error data used to plot Fig. 6.2 are less than 1% whereas only 22.125% of the total number are less then 1% in Fig. 6.1 for the Brace-Köhler compensator. For the latter, the error increases as sample and compensator retardations increase due to the small retardation approximation. However, the main source of the error is the uncertainty in the measurement of the angle producing the intensity minimum. The intensities of the minima increase with retardations which render their detection less accurate than detecting complete extinction. The error also increases as sample and compensator retardations become very small due predominantly to the uncertainty of the angle measurement. More precisely, it increases beyond 10% for retardations less than $\lambda/500$. At that very low level of retardation, the absolute uncertainty of the measurement is not greater than that at larger retardations however, it becomes relatively larger compared to the retardation to be measured. The TWC error shown in Fig. 6.2 is entirely due to the angular uncertainty of the measurement. Therefore, as the retardations increase, the relative error decreases as there are no small retardation approximation. However, as retardations become very small, the relative error increases. Like in the case of the Brace-Köhler compensator, it increases beyond 10% for retardations less than $\lambda/500$ and this is also due to the fact that the error due to the angular uncertainty becomes relatively large.

6.1.2 Low-Level Retardation Measurements

The Brace-Köhler, Sénarmont, and TWC techniques are compared experimentally using the configuration shown in Fig. 6.3. A He-Ne laser of output power approximately equal to 15 mW is used as a light source. The polarizers P and A are Glan Thompson prisms. The

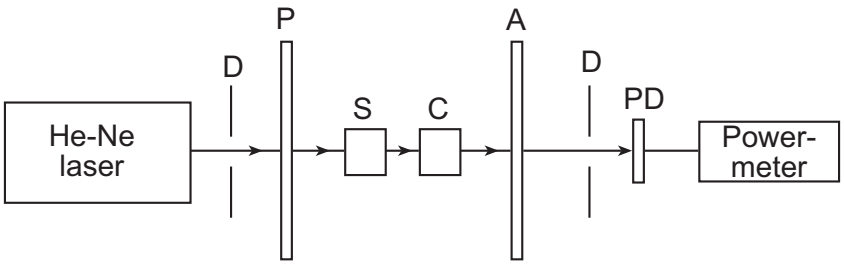

Figure 6.3: Experimental configuration used to measure small retardations with the Brace-Köhler, Sénarmont, and TWC techniques. The light source is a He-Ne laser. D, diaphragm; P, Glan-Thompson polarizer; S, sample; C, compensator; A, Glan-Thompson analyzer; PD, photodetector.

extinction ratio of the polarizers is measured prior to the retardation measurements and is equal to 6.6×10^{-8}.

Manufacturing accurately waveplates of small retardations is difficult. Consequently, various types of samples are used to produce very small retardations. The Brace-Köhler compensators provided with a Olympus polarization microscope are of known retardations. The models U-CBR1 and U-CBR2 are available with retardations equal to 59.66 nm and 21.78 nm respectively at a wavelength of 546 nm. Holders are designed so both of these waveplates can be easily inserted and rotated in the light path of the experiment in Fig. 6.3 and used as sample or compensator.

However, the retardations produced by stress-induced birefringence in optical devices are lower than that of the U-CBR2 waveplate. As a consequence, half-waveplates and quarter-waveplates are also used to produce exceedingly small retardations by crossing their fast and slow axes so their retardations are subtracted. For waveplates designed for closely spaced wavelengths, this allows retardations less than 10 nm to be produced.

6.1.2.1 Polarization Measurements

The polarization direction of the laser and the transmission directions of the two Glan-Thompson prisms polarizers used in the experiment of Fig. 6.3 are not known initially. The transmission directions of the polarizers are first determined using another experiment shown in Fig. 6.4. The polarization of the He-Ne laser in Fig. 6.4 is determined by measuring the height h_i of the beam incident on the window, and the height h_r of the reflected beam.

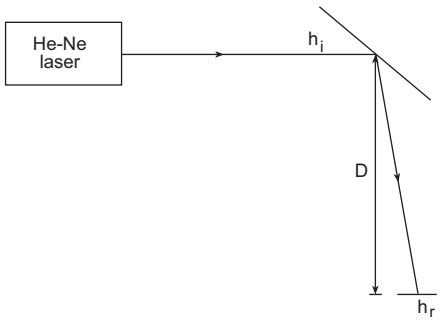

Figure 6.4: Experimental configuration used to measure the polarization direction of a He-Ne laser. The light is incident on a flat window at a height h_i from the optics table. It is reflected at the Brewster's angle. The height h_r of the reflected beam is measured.

The window is oriented so the light is incident at the Brewster's angle and a minimum of intensity is obtained on a screen placed in the path of the reflected beam. The screen is placed so the distance D is equal to 635 mm. At the Brewster's angle, the incident light is polarized along the projection of the reflected beam onto the vertical plane perpendicular to the incident beam and containing the intersection of the incident beam and the window. It can be shown that the polarization angle α of the incident beam is given by

$$\alpha = \arctan\Big(\frac{h_i - h_r}{D}\Big), \tag{6.1}$$

with h_i and h_r heights of the incident and reflected beams at the points indicated in Fig. 6.4. In this experiment, h_i and h_r are equal to 178.4 mm and 120.9 mm respectively which corresponds to an angle α equal to 5.17 deg. Consequently, the polarization direction of the He-Ne laser used in the experiment of Fig. 6.4 is at -5.17 deg (clockwise) from the horizontal looking parallel to the light propagation direction. The two Glan-Thompson prisms polarizers are placed individually in the light path of the laser and rotated to determine their transmission directions. Having determined the passing directions of the Glan-Thompson polarizers, the polarization direction of the He-Ne laser used in the experiment of Fig. 6.3 is also measured and is at -20.12 deg (clockwise) from the vertical looking parallel to the light propagation direction.

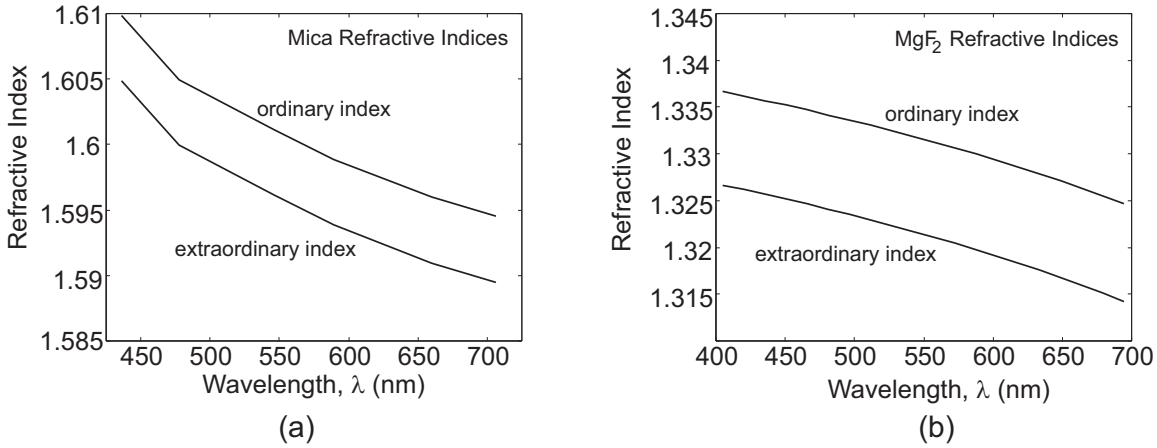

Figure 6.5: Ordinary and extraordinary refractive indices of mica and magnesium fluoride as a function of wavelength [94].

6.1.2.2 Retardation Dispersion

Pairs of half-waveplates and quarter-waveplates designed for closely spaced wavelengths are crossed so their fast and slow axes are parallel. In this configuration, their retardations are subtracted and small retardations can be produced. Waveplates made of mica and magnesium fluoride are purchased from Karl Lambrecht Corporation. The waveplates are manufactured with a retardation uncertainty of $\pm 5\ nm$. Consequently, the waveplates retardations are measured individually using the Sénarmont technique in the experimental configuration of Fig. 6.3 in which the sample S is a Karl Lambrecht waveplate oriented at 45 *deg* from extinction and the compensator C is a quarter-waveplate oriented at extinction, i.e., its slow axis is parallel to the polarizer P transmission direction.

The ordinary and extraordinary refractive indices of mica and magnesium fluoride as a function of wavelength are represented in Fig. 6.5. The Karl Lambrecht waveplates are designed for the wavelength specified by the manufacturer. Since the measurements are made using a He-Ne laser, the manufacturer's retardations values need to be calculated at this wavelength for an accurate comparison with the measured values. Considering a waveplate of retardation R_1 at wavelength λ_1, it is related to the birefringence and the thickness of the waveplate by

$$R_1 = \Delta n_1 t, \tag{6.2}$$

Table 6.1: Karl Lambrecht waveplates retardations calculated at the He-Ne laser wavelength λ of 632.8 nm.

Waveplate Material	Waveplate Type	Wavelength (nm)	Retardation ($\lambda = 632.8\ nm$) w/o Δn dispersion (nm)	Retardation ($\lambda = 632.8\ nm$) with Δn dispersion (nm)
mica	quarter-waveplate	650	162.5	161.41
mica	quarter-waveplate	660	165	163.26
mica	half-waveplate	645	322.5	320.96
mica	half-waveplate	650	325	322.82
mica	half-waveplate	660	330	326.51
mica	half-waveplate	780	390	392.81
mica	half-waveplate	800	400	402.88
MgF_2	half-waveplate	670	335	332.63
MgF_2	half-waveplate	675	337.5	334.77

Table 6.2: Olympus Brace-Köhler compensators retardations calculated at the He-Ne laser wavelength λ of 632.8 nm.

Waveplate Material	Retardation ($\lambda = 632.8\ nm$) w/o Δn dispersion (nm)	Retardation ($\lambda = 632.8\ nm$) with Δn dispersion (nm)
mica	21.54	21.78
mica	59.66	60.33

where Δn_1 is the birefringence of the waveplate material at wavelength λ_1 and t is the thickness of the waveplate. The retardation of the waveplate at wavelength λ_2 is R_2 and is thus given by

$$R_2 = R_1 \frac{\Delta n_2}{\Delta n_1}, \tag{6.3}$$

with Δn_2 the material birefringence at wavelength λ_2. Equation (6.3) is used to determine the Karl Lambrecht waveplates retardations at the wavelength of 632.8 nm. The corrected retardation values are shown in Table 6.1. The retardations of the two Brace-Köhler compensators U-CBR1 and U-CBR2 are also calculated at the wavelength of 632.8 nm in Table 6.2.

Table 6.3: Karl Lambrecht waveplates measured retardations using Sénarmont technique. $\lambda = 632.8\ nm$**.**

Waveplate Material	Waveplate Type	Manufacturer's Retardation ($\lambda = 632.8\ nm$) (nm)	Measured Retardation (nm)	Deviation (%)
mica	quarter-waveplate	161.41	164.53	1.93
mica	quarter-waveplate	163.26	163.49	0.14
mica	half-waveplate	320.96	320.37	0.18
mica	half-waveplate	322.82	323.47	0.20
mica	half-waveplate	326.51	328.49	0.61
mica	half-waveplate	392.81	389.87	0.75
mica	half-waveplate	402.88	406.82	0.98
MgF_2	half-waveplate	332.63	337.70	1.52
MgF_2	half-waveplate	334.77	341.99	2.15

6.1.2.3 Waveplates Retardation Measurements

The Karl Lambrecht waveplates retardations are measured using the Sénarmont method. The polarizers P and A in Fig. 6.3 are first oriented in crossed position to obtain the best extinction. The quarter-waveplate is placed into the light path and oriented at extinction so its slow and fast axes are parallel to the polarizers transmission directions. It is taken out of the light path so the sample S can be oriented at 45 *deg* from extinction between crossed polarizers. The quarter-waveplate is replaced into the light path and the analyzer A is rotated until extinction following the Sénarmont technique. For each sample, approximately 10 measurements are averaged. The measured retardations are shown in Table 6.3 and compared to the corrected manufacturer's retardations at $\lambda = 632.8\ nm$.

6.1.2.4 Low-Level Retardation Measurements

Having measured the retardations of the various quarter and half-waveplates individually, they are used in pairs to produce very small retardations. The resulting total retardations is calculated subtracting the individual measured retardations in Table 6.3. The Olympus Brace-Köhler compensators are also used to test the Brace-Köhler, TWC and, Sénarmont techniques. The polarizers P and A in Fig. 6.3 are first oriented in crossed position. When the sample is one of the Olympus waveplates, it is inserted in the light path and oriented

Table 6.4: Comparison between Brace-Köhler, TWC, and Sénarmont retardation measurements for a sample retardation equal to 60.33 nm.

Waveplate Type	Retardation (nm)	Technique	Measured Retardation (nm)	Error (nm)	Error (%)
U-CBR1	60.33	Brace-Köhler:	61.77	1.44	2.38
		TWC:	60.21	0.12	0.21
		Sénarmont:	60.12	0.21	0.36
U-CBR1	60.33	Brace-Köhler:	61.48	1.15	1.91
		TWC:	59.85	0.48	0.80
U-CBR1	60.33	Brace-Köhler:	59.18	1.15	1.90
		TWC:	59.00	1.33	2.20
		Sénarmont:	60.12	0.21	0.36

at 45 deg from extinction. When the sample is a pair of quarter or half-waveplates, a first waveplate is inserted in the light path and oriented at 45 deg from extinction. A second waveplate is inserted in the same rotary mount using a specially designed rotating insert. The rotating insert is rotated manually until a minimum of intensity is read on the photodetector corresponding to the case where both waveplates fast and slow axes are parallel and the waveplates retardations are subtracted.

A quarter-waveplate is inserted to measure the sample's retardation using the Sénarmont technique. The Olympus U-CBR2 waveplate is inserted to measure the sample's retardation using the Brace-Köhler and TWC techniques. For each sample, 5 angular measurements are averaged to compute the retardation. The measurements are repeated several times for each sample allowing a large number of measurements to be compared with the true sample's retardation value. The retardation measurements are shown in Tables 6.4, 6.5, 6.6, 6.7, 6.7, 6.8, and 6.9 for sample's retardations equal to 60.33, 21.78, 16.95, 8.12, 3.09, and 1.04 nm respectively. The measurement error is calculated in nm and in percentage of the true sample's retardation by computing the difference between the measured and true sample's retardation. The average measurement errors for each technique at each sample's retardation are shown in Table 6.10. The Brace-Köhler, TWC, and Sénarmont techniques are ranked according to measurement errors for each sample's retardation.

The TWC technique achieves the best measurement accuracy for sample's retardations

Table 6.5: Comparison between Brace-Köhler, TWC, and Sénarmont retardation measurements for a sample retardation equal to 21.78 nm.

Waveplate Type	Retardation (nm)	Technique	Measured Retardation (nm)	Error (nm)	Error (%)
U-CBR2	21.78	Brace-Köhler:	21.28	0.50	2.32
		TWC:	21.84	0.06	0.26
		Sénarmont:	22.15	0.37	1.68
U-CBR2	21.78	Brace-Köhler:	21.37	0.41	1.87
		TWC:	22.00	0.22	1.00
U-CBR2	21.78	Brace-Köhler:	21.37	0.41	1.87
		TWC:	21.77	0.01	0.03
U-CBR2	21.78	Brace-Köhler:	22.09	0.31	1.40
		TWC:	22.31	0.54	2.45
U-CBR2	21.78	Brace-Köhler:	21.62	0.16	0.74
		TWC:	21.81	0.03	0.13
		Sénarmont:	22.26	0.48	2.22
U-CBR2	21.78	Brace-Köhler:	22.20	0.42	1.94
		TWC:	22.39	0.61	2.79
		Sénarmont:	22.32	0.54	2.49

equal to 1.04, 8.12, 16.95, and 21.78 nm with measurement errors equal to 0.19, 0.30, 0.58, and 0.24 nm respectively. The Brace-Köhler technique achieves the best accuracy for only one sample's retardation equal to 3.09 nm with a measurement error equal to 0.81 nm. The Sénarmont technique also achieves the best accuracy for only one sample's retardation equal to 60.33 nm with a measurement error of 0.21 nm. For these two last sample's retardations, the TWC technique achieves the second best accuracy with measurement errors equal to 0.97 and 0.64 nm respectively rendering its accuracy close to that of the Brace-Köhler and Sénarmont techniques for these two samples.

The TWC technique also appears to be the most accurate of the three techniques when considering the total number of measurements in Tables 6.4 through 6.9. Over the 28 sets of measurements averaging a total number of approximately 450 measurements, the TWC technique achieves the best accuracy for 57.14% of the measurements while the Brace-Köhler achieves the best accuracy for only 32.14% of the measurements and the Sénarmont technique for only 10.72% of the measurements. This makes the TWC technique very suitable for measuring the stress-induced birefringence in optical devices.

Table 6.6: Comparison between Brace-Köhler, TWC, and Sénarmont retardation measurements for a sample retardation equal to 16.95 nm.

Waveplate Type	Retardation (nm)	Technique	Measured Retardation (nm)	Error (nm)	Error (%)
Crossed Mica 780nm $\lambda/2$	16.95[(1)]	Brace-Köhler:	17.05	0.10	0.61
Mica 800nm $\lambda/2$		TWC:	17.73	0.78	4.58
Crossed Mica 780nm $\lambda/2$	16.95	Brace-Köhler:	16.93	0.02	0.10
Mica 800nm $\lambda/2$		TWC:	17.33	0.38	2.26
Crossed Mica 780nm $\lambda/2$	16.95	Brace-Köhler:	17.02	0.07	0.43
Mica 800nm $\lambda/2$		TWC:	16.96	0.01	0.07
Crossed Mica 780nm $\lambda/2$	16.95	Brace-Köhler:	17.21	0.26	1.57
Mica 800nm $\lambda/2$		TWC:	16.97	0.02	0.10
		Sénarmont:	17.23	0.28	1.63
Crossed Mica 780nm $\lambda/2$	16.95	Brace-Köhler:	15.56	1.39	8.18
Mica 800nm $\lambda/2$		TWC:	16.26	0.69	4.08
		Sénarmont:	14.94	2.01	11.85
Crossed Mica 780nm $\lambda/2$	16.95	Brace-Köhler:	15.30	1.65	9.73
Mica 800nm $\lambda/2$		TWC:	15.31	1.64	9.69
Crossed Mica 780nm $\lambda/2$	16.95	Brace-Köhler:	17.78	0.83	4.88
Mica 800nm $\lambda/2$		TWC:	18.03	1.08	6.39
		Sénarmont:	18.02	1.07	6.30
Crossed Mica 780nm $\lambda/2$	16.95	Brace-Köhler:	15.92	1.03	6.08
Mica 800nm $\lambda/2$		TWC:	17.28	0.33	1.93
Crossed Mica 780nm $\lambda/2$	16.95	Brace-Köhler:	15.88	1.07	6.31
Mica 800nm $\lambda/2$		TWC:	17.27	0.32	1.89

[(1)]Difference of two Sénarmont measurements.

Table 6.7: Comparison between Brace-Köhler, TWC, and Sénarmont retardation measurements for a sample retardation equal to 8.12 nm.

Waveplate Type	Retardation (nm)	Technique	Measured Retardation (nm)	Error (nm)	Error (%)
Crossed Mica 645nm $\lambda/2$	8.12[(1)]	Brace-Köhler:	8.53	0.41	5.05
Mica 660nm $\lambda/2$		TWC:	8.26	0.14	1.66
		Sénarmont:	9.36	1.24	15.26
Crossed Mica 645nm $\lambda/2$	8.12	Brace-Köhler:	8.57	0.45	5.49
Mica 660nm $\lambda/2$		TWC:	8.69	0.57	7.00
		Sénarmont:	8.79	0.67	8.23
Crossed Mica 645nm $\lambda/2$	8.12	Brace-Köhler:	7.68	0.44	5.05
Mica 660nm $\lambda/2$		TWC:	7.90	0.22	2.66
		Sénarmont:	4.39	3.73	45.89

[(1)]Difference of two Sénarmont measurements.

Table 6.8: Comparison between Brace-Köhler, TWC, and Sénarmont retardation measurements for a sample retardation equal to 3.09 nm.

Waveplate Type	Retardation (nm)	Technique	Measured Retardation (nm)	Error (nm)	Error (%)
Crossed Mica 645nm $\lambda/2$ Mica 650nm $\lambda/2$	3.09[(1)]	Brace-Köhler:	2.56	0.53	17.28
		TWC:	2.51	0.58	18.87
		Sénarmont:	1.76	1.33	43.18
Crossed Mica 645nm $\lambda/2$ Mica 650nm $\lambda/2$	3.09	Brace-Köhler:	2.35	0.74	23.96
		TWC:	2.08	1.01	32.72
		Sénarmont:	2.11	0.98	31.82
Crossed Mica 645nm $\lambda/2$ Mica 650nm $\lambda/2$	3.09	Brace-Köhler:	2.10	0.99	31.95
		TWC:	1.90	1.19	38.58
		Sénarmont:	2.11	0.98	31.82
Crossed Mica 645nm $\lambda/2$ Mica 650nm $\lambda/2$	3.09	Brace-Köhler:	2.09	1.00	32.19
		TWC:	2.00	1.09	35.35
		Sénarmont:	2.11	0.98	31.82

[(1)]Difference of two Sénarmont measurements.

Table 6.9: Comparison between Brace-Köhler, TWC, and Sénarmont retardation measurements for a sample retardation equal to 1.04 nm.

Waveplate Type	Retardation (nm)	Technique	Measured Retardation (nm)	Error (nm)	Error (%)
Crossed Mica 650nm $\lambda/4$ Mica 660nm $\lambda/4$	1.04[(1)]	Brace-Köhler:	0.80	0.24	23.04
		TWC:	0.81	0.23	21.81
		Sénarmont:	0.70	0.31	32.20
Crossed Mica 650nm $\lambda/4$ Mica 660nm $\lambda/4$	1.04	Brace-Köhler:	0.84	0.20	18.88
		TWC:	0.85	0.19	17.60
		Sénarmont:	0.49	0.55	52.54
Crossed Mica 650nm $\lambda/4$ Mica 660nm $\lambda/4$	1.04	Brace-Köhler:	0.86	0.18	16.69
		TWC:	0.85	0.19	17.60
		Sénarmont:	0.42	0.62	59.32

[(1)]Difference of two Sénarmont measurements.

Table 6.10: Comparison between Brace-Köhler, TWC, and Sénarmont techniques accuracies.

Measured Sample's Retardation (nm)	Technique	Mean Error (nm)	Mean Error (%)	Rank
$60.33^{(1)}$	Sénarmont:	0.21	0.36	1
	Brace-Köhler:	1.24	2.06	3
	TWC:	0.64	1.07	2
$21.78^{(1)}$	Sénarmont:	0.46	2.13	3
	Brace-Köhler:	0.37	1.69	2
	TWC:	0.24	1.11	1
$16.95^{(2)}$	Sénarmont:	1.11	6.59	3
	Brace-Köhler:	0.71	4.21	2
	TWC:	0.58	3.44	1
$8.12^{(2)}$	Sénarmont:	1.88	23.12	3
	Brace-Köhler:	0.43	5.31	2
	TWC:	0.30	3.78	1
$3.09^{(2)}$	Sénarmont:	1.07	34.66	3
	Brace-Köhler:	0.81	26.34	1
	TWC:	0.97	31.37	2
$1.04^{(2)}$	Sénarmont:	0.50	48.02	3
	Brace-Köhler:	0.20	19.54	2
	TWC:	0.19	19.25	1

$^{(1)}$Manufacturer's value.

$^{(2)}$Difference of two Sénarmont measurements.

The Brace-Köhler technique accuracy remains low for sample's retardation less than 60.33 nm. For these retardations, it achieves accuracies of a fraction of a nm. The Brace-Köhler technique accuracy becomes very similar to that of the TWC for a retardation equal to 1.04 nm with a measurement error of 0.2 nm. Even though its accuracy is less than that of the TWC, the technique is still suitable for measuring small retardations such as those produced in optical devices.

The Sénarmont technique achieves the best accuracy for the largest sample's retardation which reinforces the fact that it is a very accurate technique for retardations larger than several tens of nm. However, its accuracy decreases for sample's retardations less than 10 nm. This makes the Sénarmont technique unsuitable for the characterization of stress-induced birefringence in optical devices.

6.1.3 CBRM Accuracy

The accuracy of the new CBRM method is assessed by measuring the retardations of various waveplates with the CBRM method and the Sénarmont compensator method using a polarization microscope and a photospectrometer.

Table 6.11 and Table 6.12 present comparative measurements of respectively antireflection-coated retardation plates and non-antireflection-coated retardation plates. The CBRM is in very good agreement with the Sénarmont compensator method for the retardation plates that had been antireflection coated. The deviation between both techniques is less than one percent and corresponds respectively for plate 1 and plate 2 to a deviation of 0.001 fringe order and 0.003 fringe order. This deviation increases for plates that had not been antireflection coated as can be seen in Table 6.12. This is due to the fact that the multiple reflections modify the color of the transmitted light and therefore adversely affect the measurement. A detailed study of the effect of multiple reflections on retardation-based electro-optic measurements can be found in [95].

Table 6.11: Retardation measurements of antireflection-coated retardation plates: comparison of Sénarmont compensator method and CBRM method.

Manufacturer's Description	Sénarmont Compensator Method	CBRM Method	Deviation
137 nm quarter-wave plate	161.1 nm	161.9 nm	0.53 %
530 nm full-wave tint plate	532.8 nm	534.9 nm	0.39 %

Table 6.12: Retardation measurements of non-antireflection-coated retardation plates: comparison of Sénarmont compensator method and CBRM method.

Type (Retardation)	Manufacturer's Description	Sénarmont Method	CBRM Method	Deviation Sénarmont/CBRM
Mica $\lambda/4$ plate	136.5 nm	132.1 nm	109.9 nm	16.80 %
Mica $\lambda/2$ plate	273 nm	263.1 nm	271.2 nm	3.06 %
Quartz $\lambda/4$ plate	136.5 nm	149.4 nm	206.7 nm	38.35 %
Quartz $\lambda/2$ plate	273 nm	278.6 nm	221.6 nm	20.46 %

CHAPTER 7

FULL-FIELD RETARDATION MEASUREMENTS

7.1 Brace-Köhler Method

7.1.1 Measurement Procedure

An Olympus polarization microscope model BX60 is used to implement the Brace-Köhler technique for full-field retardation measurements. The complete system used is shown in Fig. 7.1. For higher contrast and sensitivity, the halogen lamp provided with the microscope is replaced by a mercury arc lamp [36]. The measurements are made in green light by inserting an interference filter in front of the condenser. The sample is placed on the microscope stage and the compensator is inserted in the compensator slot. In single-point retardation measurements, the compensator angle producing an intensity minimum is determined between crossed polarizers with and without the sample. With only one measurement point, this is easily done by reading the light intensity with a photodetector as the compensator is rotated as is done in Sec. 6.1.2.4. Full-field retardation measurements consist of determining the intensity minima for each pixel or each group of pixels over the entire field-of-view. Images are recorded as the compensator is rotated using a CCD camera connected to a computer and the image processing software Image Pro Plus.

The retardation measurements procedure is composed of two stages. The first stage is experimental and consists of recording and storing images as the compensator is rotated with and without the sample. The procedure with a sample is represented in a flow chart in Fig. 7.2. The sample is first focused on and oriented at 45 *deg* from extinction between crossed polarizers. The compensator is inserted and an angular range producing intensity minima over the whole field-of-view is determined by viewing through the eyepiece. The angular range is defined by its start angle θ_1 and its end angle θ_N. A finer angular grid is defined between θ_1 and θ_N of N successive compensator angles. The compensator is then rotated from θ_1 to θ_N and N images are recorded corresponding to the N compensator

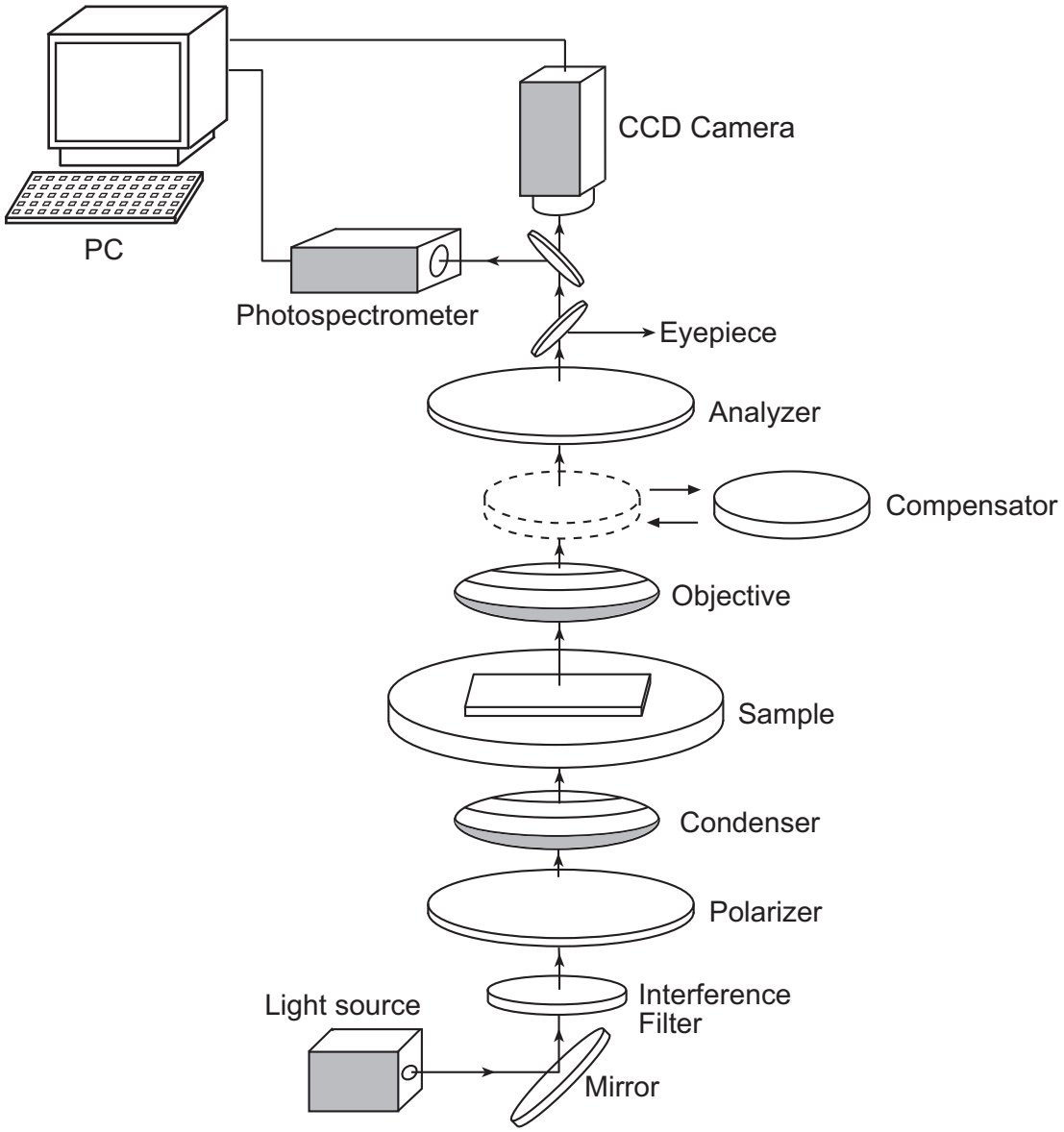

Figure 7.1: Polarization microscope system used for full-field retardation measurements.

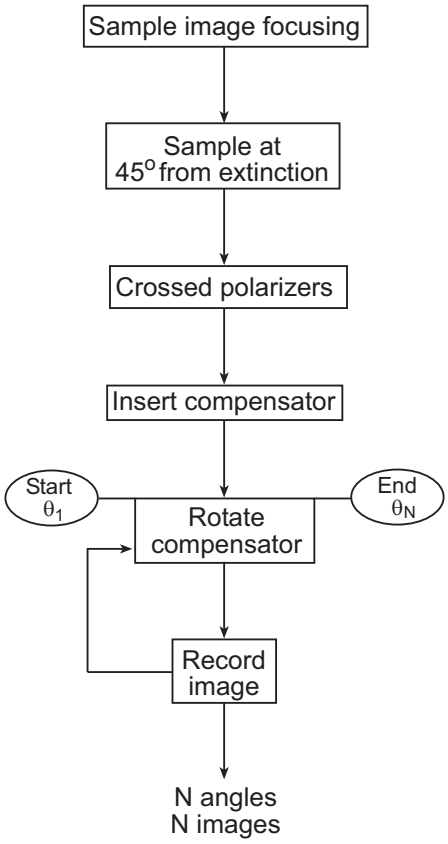

Figure 7.2: Flow chart of the experimental procedure for full-field retardation measurements using Brace-Köhler technique.

angles. This first experimental procedure is done with and without the sample.

This is applied, for example, to the full-field retardation measurement of the Olympus Brace-Köhler waveplate model U-CBR2 using the other model U-CBR1 as a compensator and an objective magnification of 10×. Viewing through the eyepiece and rotating the compensator U-CBR1, θ_1 and θ_N are determined and are equal to -15 and -1 *deg* respectively. The compensator is then rotated by increments of 0.5 *deg* from -15 to -1 *deg* with the sample U-CBR2 on the microscope stage corresponding to a total number of images N equal to 29. The sample U-CBR2 is taken out of the stage and the procedure is repeated. In this case, the compensator U-CBR1 is rotated from $\theta_1 = -5.5$ *deg* to $\theta_N = 11$ *deg* every 0.5 *deg* thereby recording 34 images without the sample.

The second stage consists of processing and analyzing the images to determine the compensator angles producing intensity minima over the entire field-of-view with and without the sample. Routines are coded in Matlab to accomplish these tasks. The algorithm of the image analysis is represented in Fig. 7.3. Considering again the full-field retardation measurement of the Olympus U-CBR2 waveplate, examples of the different subroutines and parameters used for the determination of the compensator angles producing intensity minima are shown in Fig. 7.3. The compensator angles are stored in the variable `BKangle.txt` during the experimental procedure. In this particular case, it contains 29 linearly-spaced values ranging from -15 to -1 *deg*. An image is recorded for each compensator angle. Each image is saved as a `imagekk.jpg` file with `kk` corresponding to the sequential number of the compensator angle. The images are 480 pixel high and 640 pixel long. The integer `kk` allows a direct determination of the corresponding compensator angle for each image by looking into the variable `BKangle.txt`.

The first part of the image processing consists of loading each image file and converting it to a binary file allowing the inspection of the color values of each pixel. This is accomplished by the first subroutine `pixelation.m`. Before the subroutine is run, the user defines several input variables as shown in Fig. 7.3. A string variable `y` or `n` indicates if there is a sample or not. This is used to name the output variables accordingly. In the example of Fig. 7.3, `y` indicates that the sample is on the microscope stage. The minima search can be conducted

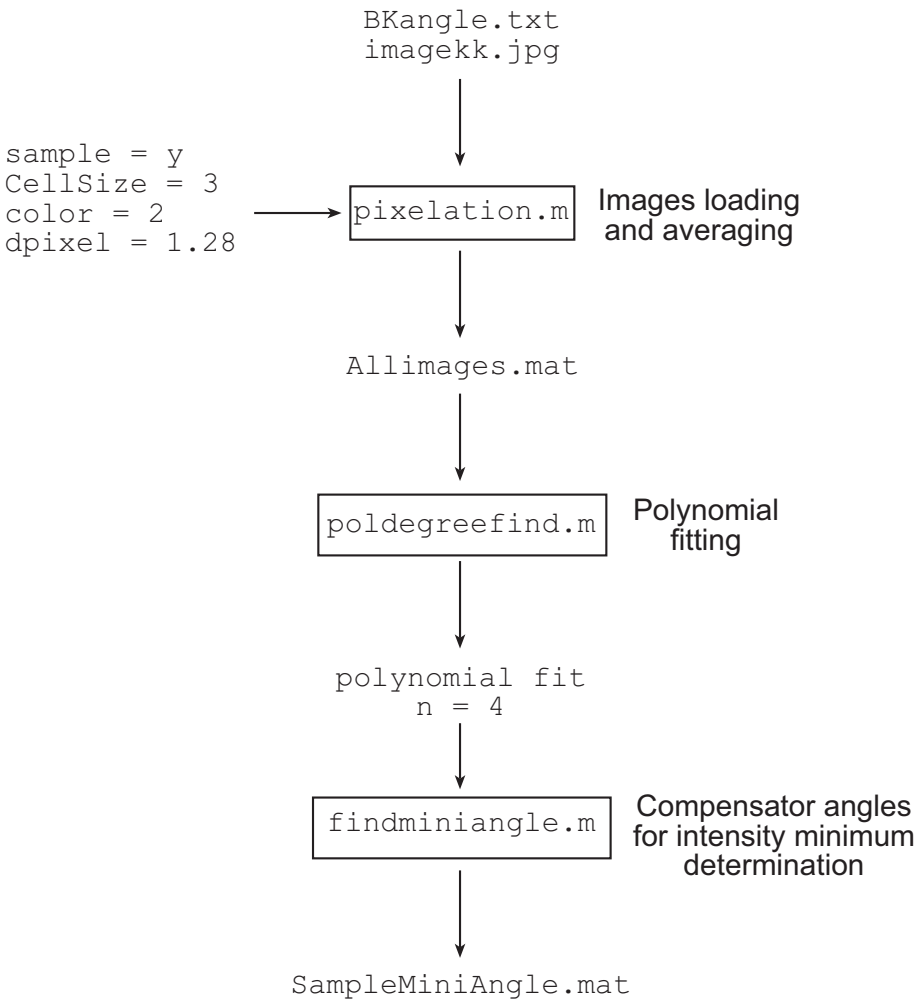

Figure 7.3: Flow chart of the algorithm used to process and analyze the images for full-field retardation measurements using the Brace-Köhler technique.

on each pixel or on each cell whose pixel-dimension is defined by the user. This is the input variable `CellSize` which in the example of Fig. 7.3 is equal to 3. In this case, each image is divided into cells of dimension 3×3 pixels and the color values RGB of each cell are the average color values RGB of the 9 pixels contained in each individual cell. This is done to reduce the noise in the measurements as will be shown in a later section and also because the pixel length may be less than the resolving power of the objective which results in undersampling if the analysis is done for each pixel. The color value on which the minima search is conducted is entered in the variable `color` which is equal to 2 in our example corresponding to the green color value. The insertion of the green interference filter allows this simplification. Finally, the variable `dpixel` indicates the length of one pixel in μm. This relationship is experimentally determined for each objective magnification used in these measurements. In the example of Fig. 7.3, the objective magnification used is 10× and each pixel in the image is 1.28 μm long. The images loading and averaging done with `pixelation.m` produces one single four-dimensional variable `Allimages.mat` containing all the color information for each image corresponding to each compensator angle. The first dimension corresponds to the number of images N equal to the number of compensator angles in `BKangle.txt`. In this example, N is equal to 29. The second and third dimension correspond to the number of cell rows and columns in each image which are equal to 160 and 213 respectively. The fourth dimension corresponds to the color values RGB of each cell.

The second subroutine `poldegreefind.m` allows the determination of a polynomial fit representing the variations of intensity as a function of compensator angles. The variations of the green value of the central cell as a function of compensator angles are fitted to polynomials whose coefficients are computed with a built-in function in Matlab. In a first time, `poldegreefind.m` produces a plot of the standard deviation between the measured data and the polynomial fit as a function of the polynomial degree as is shown in Fig. 7.4(a). The user can then test various polynomial fits to determine the polynomial degree which will be used for the intensity minima search. The polynomial fit of degree 4 is represented in Fig. 7.4(b) as a solid line and is chosen for the minima search in this example.

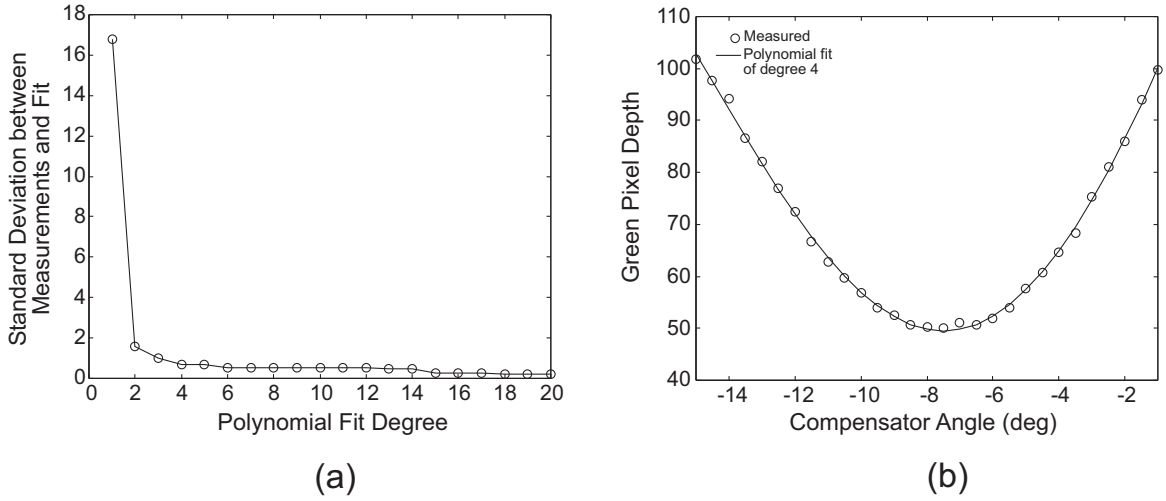

Figure 7.4: Polynomial fit of the intensity variations as a function of compensator angles in the Brace-Köhler technique. (a) Standard deviation between measurements and polynomial fit as a function of the polynomial degree. (b) Polynomial fit of degree 4.

The last subroutine `findminiangle.m` uses the polynomial degree previously determined to fit the variations of intensity of each individual cell. The angular resolution is chosen by the user and is in most of our examples 0.1 *deg*. This last subroutine computes the intensity minimum for each pixel-cell and the corresponding compensator angle. The output of this subroutine is a two-dimensional variable `SampleMiniAngle.mat` containing the values in *deg* of the compensator angles producing intensity minima for all pixel-cells over the whole field-of-view. This variable is named `NoSampleMiniAngle.mat` when the image analysis is done for the case without the sample. The angle differences between the two for all cells are substituted into Eq. (3.16) to compute the retardation over the whole field-of-view.

7.1.2 Measurements

The Brace-Köhler technique for full-field retardation measurements is first tested by using the two Brace-Köhler compensators models U-CBR1 and U-CBR2 provided with the Olympus microscope. They consist of mica waveplates placed into a holder and connected with a rotating dial. They can be inserted into the compensator slot of the microscope to measure the retardation of samples (Fig. 7.1). The retardations of U-CBR1 and U-CBR2 are given by the manufacturer and are equal to 59.66 *nm* and 21.54 *nm* respectively at the wavelength of 546 *nm*.

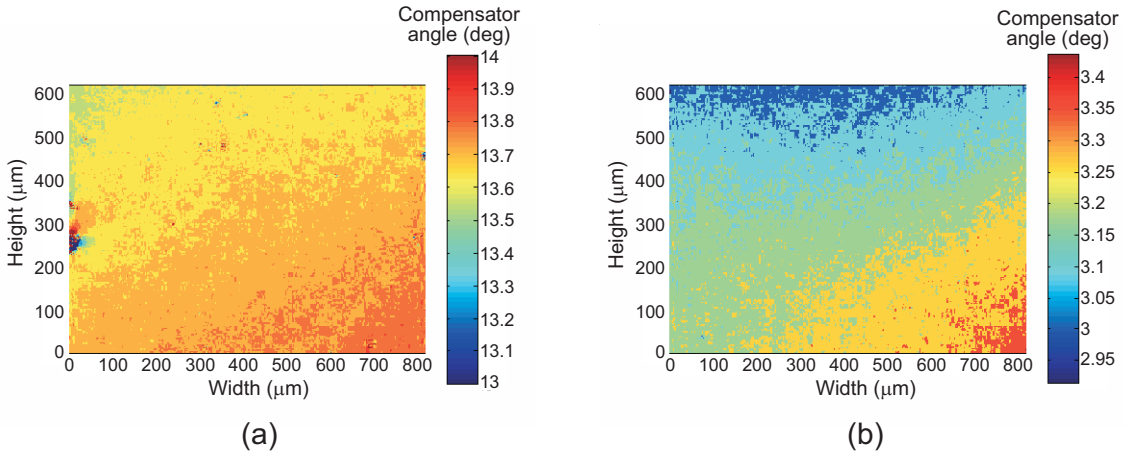

Figure 7.5: Compensator angles producing intensity minima in the entire field-of-view (a) with the sample U-CBR2 (b) without the sample.

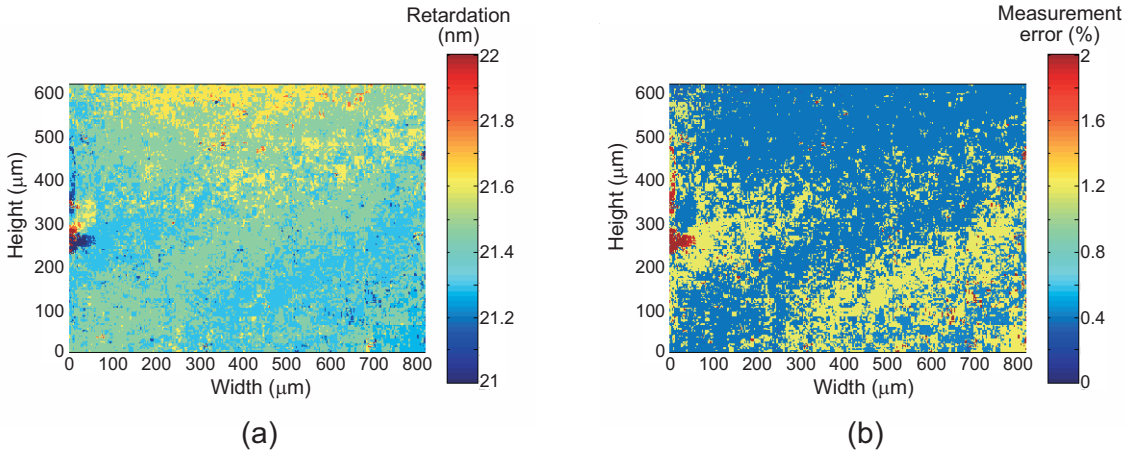

Figure 7.6: Full-field retardation measurements and error compared to the manufacturer's retardation value (a) Measured retardation in *nm* (b) Error in (%).

For this experiment, U-CBR2 is placed on the microscope stage and oriented at 45 *deg* from extinction while U-CBR1 is inserted in the compensator slot of the microscope. The objective magnification is 10×. The procedure outlined in the previous section is followed to determine the retardation of U-CBR2 over the entire field-of-view. The compensator angles producing intensity minima with and without the sample are shown in Fig. 7.5.

The retardation and the error compared to the manufacturer's value are shown in Fig. 7.6. The full-field retardation measurements are in very good agreement with the manufacturer's value. In fact, 99.63 % of the pixels in Fig. 7.6(b) are below 2 % error and 68.36 % are below 1 % error. A more detailed analysis of the error in the field-of-view

Table 7.1: Error analysis of the Brace-Köhler full-field retardation measurements represented in Fig. 7.6.

Error (%)	Proportion in FOV (%)
<5	99.83
<4	99.79
<3	99.73
<2	99.63
<1	68.36

is given in Table 7.1. The amounts of pixels below various error limits are expressed in percentage of the total number of pixels in the field-of-view.

7.2 Two-Waveplate Compensator

7.2.1 Measurement Procedure

The Two-Waveplate Compensator (TWC) is also implemented for full-field retardation measurements using the experimental configuration shown in Fig. 7.1. Similar to the Brace-Köhler technique, the TWC consists of an experimental stage and an image processing and analysis stage. The experimental procedure is presented as a flow chart in Fig. 7.7. The sample is first focused on and oriented at 45 *deg* from extinction between crossed polarizers. The compensator is inserted in the microscope tube. Viewing through the eyepiece, the compensator and analyzer are rotated to estimate the angular ranges for which an extinction is produced for all points over the whole field-of-view. Having determined the compensator and analyzer angular ranges, the compensator is rotated from θ_1 to θ_N in small increments. For each successive compensator angle, the analyzer is rotated from θ_1 to θ_K and an image is recorded. Rotating successively compensator and analyzer, $N.K$ images are recorded. Applying the procedure to the measurement of U-CBR2, the compensator U-CBR1 is rotated from -12 to -20 *deg* every 0.5 *deg* corresponding to $N = 21$. The analyzer is rotated from 0 to 5 *deg* every 0.5 *deg* for each compensator angle corresponding to $K = 11$. An image being recorded each time, a total of $N.K = 231$ images are recorded over the entire process. The compensator and analyzer angles are stored in two variables,

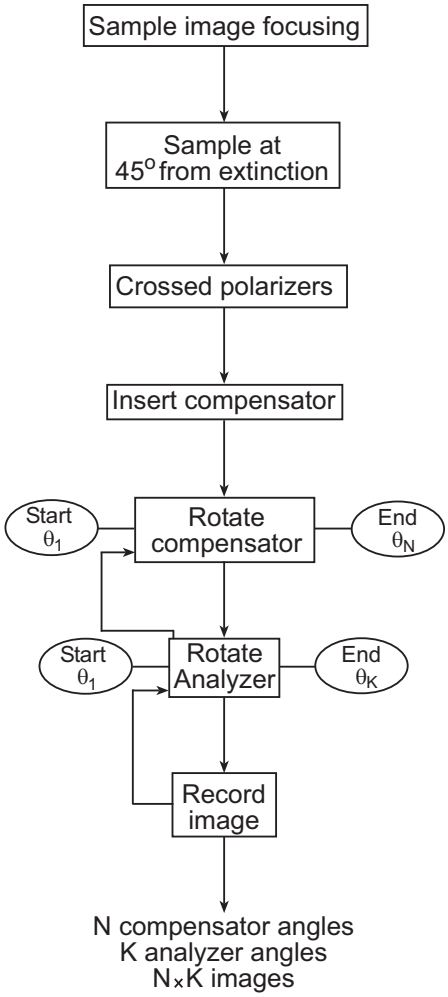

Figure 7.7: Flow chart of the experimental procedure for full-field retardation measurements using the TWC technique.

`BKangle.txt` and `Anaangle.txt` respectively. Each image is saved as a `imagekk.jpg` file where the integer kk corresponds to the sequential number of the total number of compensator and analyzer angles. For example, the integer `kk` for the image recorded at the compensator angle equal to -11 deg and the analyzer angle equal to 1.5 deg is $kk = 26$. The compensator angle sequential number is $l = 3$ and the analyzer angle sequential number is $m = 4$. The integer kk is thus given by

$$kk = (l-1)K + m. \tag{7.1}$$

The compensator and analyzer angles associated with each image are easily retrieved using the relationship in Eq. (7.1).

Following the experimental stage, the images are processed to determine the compensator and analyzer angles producing extinction over the entire field-of-view. The image analysis algorithm is represented in Fig. 7.8. The first part of the image analysis is identical to that presented in Sec. 7.1.1 for the Brace-Köhler technique and consists of the subroutine `pixelation.m` which converts and averages the images recorded during the experiments. A four-dimensional variable `Allimages.mat` is generated containing all the color information of all the images.

The analyzer angle producing an intensity minimum must first be determined for each compensator angle over the whole field-of-view. The subroutine `poldegreefind.m` allows the user to determine a polynomial fitting the variations of the green color of the central cell as a function of the analyzer angle at a given compensator angle which is usually chosen to be in the middle of the compensator angular range. A plot of the standard deviation as a function of the polynomial degree is generated and the user chooses the optimum fit (Fig. 7.4) similar to what was done in Sec. 7.1.1.

The polynomial degree is used to determine the analyzer angles producing intensity minima with the subroutine `findminiangle.m`. This generates a three-dimensional array `AnaMinimaInten.mat` containing the green value of the intensity minima produced by the analyzer over the whole field-of-view for each compensator angle. The first dimension corresponds to the number of compensator angles $N = 21$. The second and third dimension correspond to the number of cell rows and columns, 160 and 213 respectively when using a

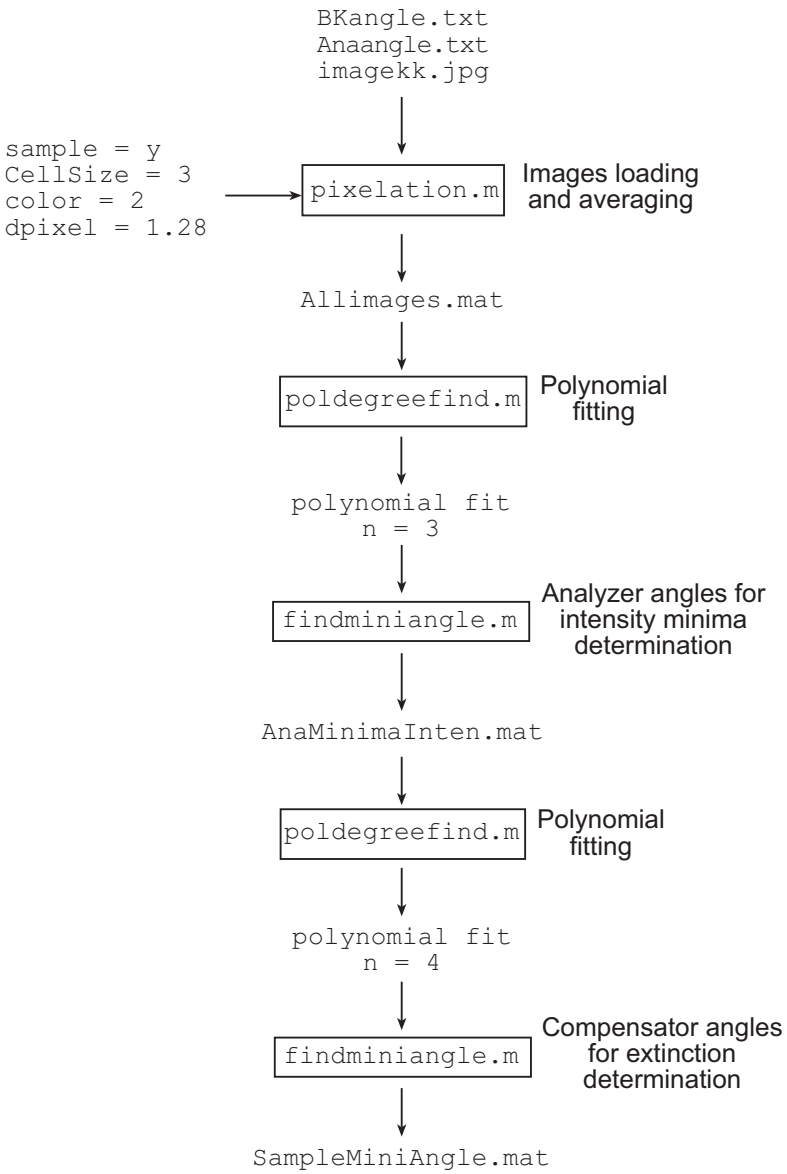

Figure 7.8: Flow chart of the algorithm used to process and analyze the images for full-field retardation measurements using the TWC technique.

cell dimension of 3×3 pixels for the initial `pixelation.m` subroutine.

The remaining problem consists of finding the compensator angles producing extinctions over the whole field-of-view. This is similar to what was presented with the Brace-Köhler technique in Sec. 7.1.1. However, the input to the `poldegreefind.m` and `findminiangle.m` subroutines is `AnaMinimaInten.mat` instead of `Allimages.mat`. The final output is the two-dimensional array `SampleMiniAngle.mat` containing the values in *deg* of the compensator angles producing extinctions over the entire field-of-view. The procedure is repeated without the sample to generate the output `NoSampleMiniAngle.mat`. The angle differences between the two are substituted into Eq. (4.15) to compute the retardation over the whole field-of-view.

7.2.2 Measurements

The Brace-Köhler waveplates U-CBR1 and U-CBR2 are used to test the TWC for full-field retardation measurements. U-CBR2 is placed on the microscope stage and U-CBR1 is inserted in the compensator slot of the microscope tube. The procedure outlined in the previous section is followed to record images while the compensator and analyzer are rotated. The sample is taken out of the microscope stage. The compensator is rotated and the analyzer remains fixed to determine the extinction angles without the sample. This is similar to what is done in the Brace-Köhler technique. The angles producing extinction with and without the sample as well as the measured retardation and the relative error are shown in Figs.7.9(a)-(d). For this experiment, the objective magnification is 10× and images are divided and averaged over cells of 3×3 pixels. A detailed error analysis of the retardation measurements is shown in Table 7.2 in which the amounts of pixels in the field-of-view that are below various error limits are calculated in percentage of the total number of pixels. The same sample is also measured using the Brace-Köhler technique. The compensator angles producing intensity minima with and without the sample, the measured retardation and the relative error are shown in Fig. 7.10. A detailed analysis of the error in Fig. 7.10 is shown in Table 7.3.

The TWC technique appears to be slightly less accurate over the whole FOV than the

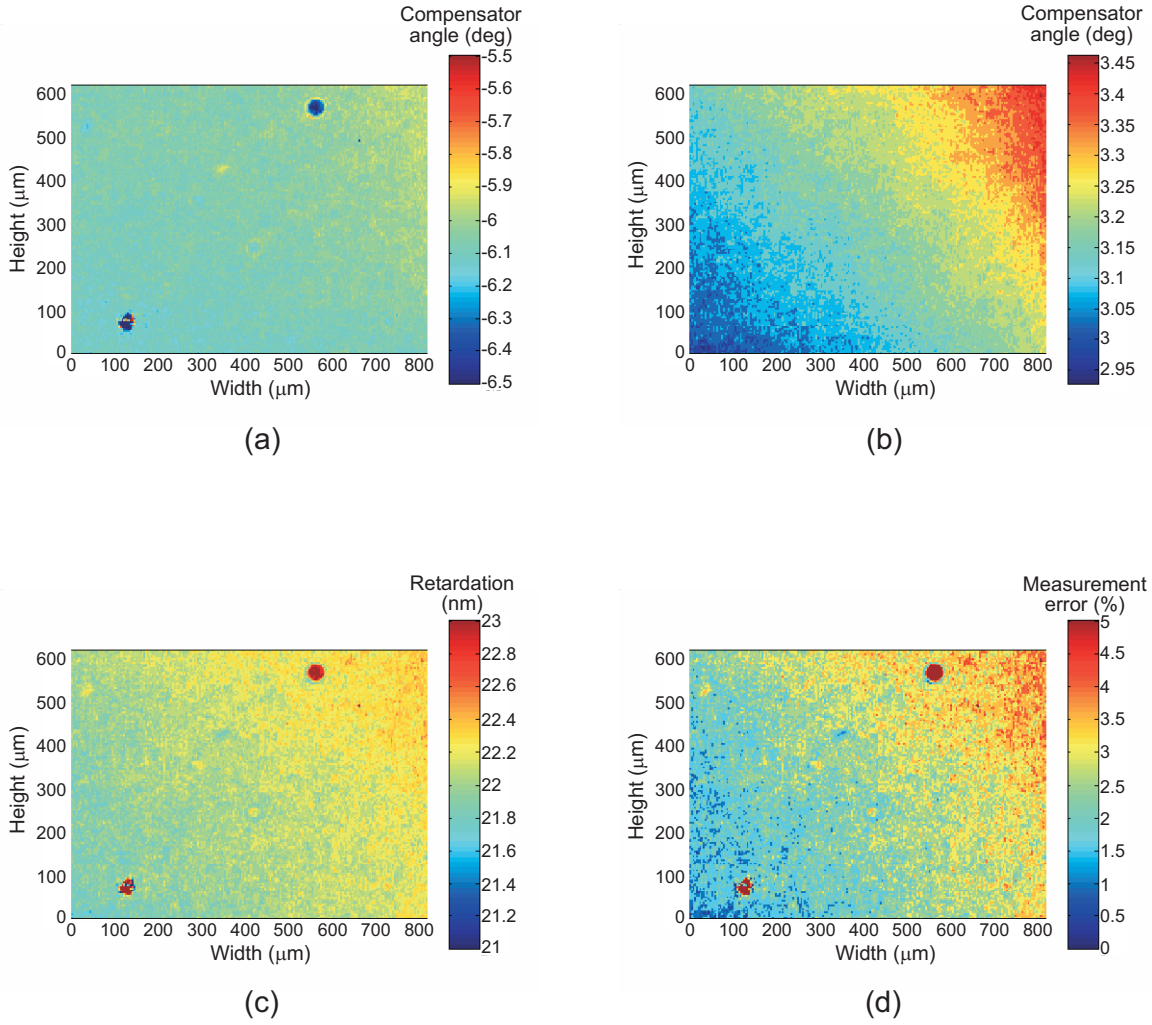

Figure 7.9: Full-field retardation measurements using the TWC technique (a) Compensator angles producing extinction with the sample in *deg*. (b) Compensator angles producing extinction without the sample in *deg*. (c) Measured retardation in *nm*. (d) Error compared to the manufacturer's retardation in (%).

Table 7.2: Error analysis of TWC full-field retardation measurements represented in Fig. 7.9.

Error (%)	Proportion of FOV (%)
<5	99.68
<4	97.88
<3	68.98
<2	20.34
<1	0.83

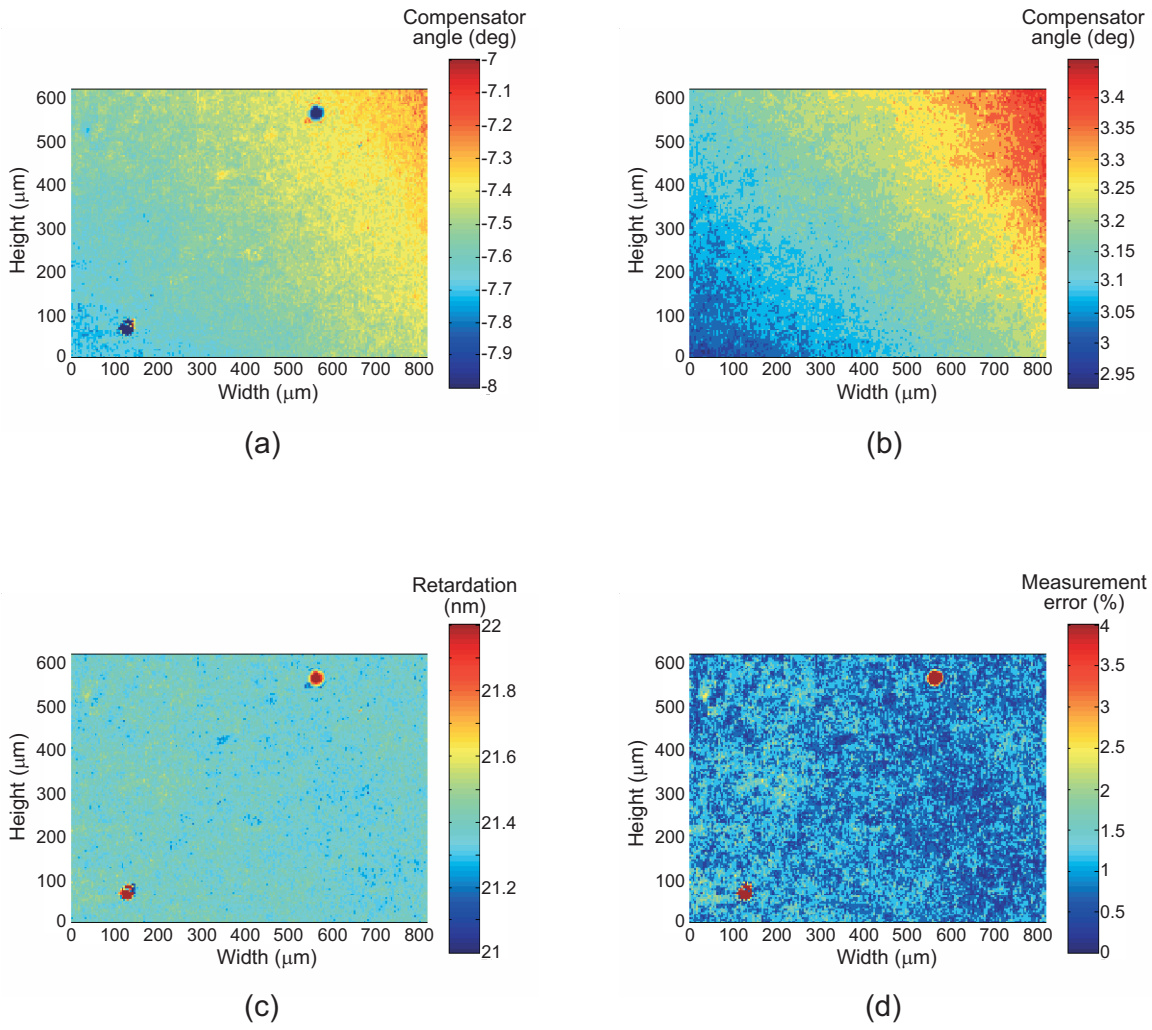

Figure 7.10: Full-field retardation measurements using the Brace-Köhler technique. The measured sample is the same as that of the TWC measurements in Fig. 7.9. (a) Compensator angles producing intensity minima with the sample in *deg*. (b) Compensator angles producing extinction without the sample in *deg*. (c) Measured retardation in *nm*. (d) Error compared to the manufacturer's retardation in (%).

Table 7.3: Error analysis of the Brace-Köhler full-field retardation measurements represented in Fig. 7.10.

Error (%)	Proportion of FOV (%)
<5	99.75
<4	99.69
<3	99.67
<2	98.53
<1	53.01

Brace-Köhler technique with only 68.98% of the measurements in Fig. 7.9(d) having less than 3% error compared to 99.67% for the Brace-Köhler technique in Fig. 7.10(d). The retardation measured with the TWC in Fig. 7.9(c) also exhibits a non-uniform distribution increasing along the diagonal of the FOV from the lower left-hand corner to the upper right-hand corner. On the other hand, the retardation measured with the Brace-Köhler technique appears more uniform in Fig. 7.10(c). The non-uniformity may be due to imperfections in the optics of the microscope arising when the different optical components are rotated in the tube of the microscope.

In the Brace-Köhler technique, the distribution of the compensator angles producing minima with and without the sample in Figs. 7.10(a) and 7.10(b) exhibit a similar non-uniformity. These non-uniformities partially cancel out when subtracting both sets of angles in order to calculate the retardation. In this case, however, the conditions to determine the minima angles with and without the sample are identical in the sense that only the compensator is rotated in the optical system giving rise to almost identical non-uniformities. Some additional non-uniformities arise due to the fact that the compensator waveplate U-CBR1 is not rotated over the same angular range illuminating the compensator in two different areas. The measured retardation is nonetheless uniform.

In the TWC technique, the non-uniformities arising in the distributions of the angles producing minima with and without the sample are not identical in Figs. 7.9(a) and 7.9(b). The angles in Fig. 7.9(a) are determined by rotating the compensator and the analyzer while in Fig. 7.9(b) they are determined by rotating the compensator only. The latter case does not take into account the non-uniformities arising from rotating the analyzer in the optical system. Consequently, when both sets of angles are subtracted in order to calculate the retardation with the TWC technique, the non-uniformities due to the rotation of the optical component do not cancel out and the measured retardation exhibits a similar distribution to that of the compensator angles producing minima without the sample in Figs. 7.10(b) and 7.9(b).

As a consequence, the compensator angles producing extinction without the sample are determined a second time in this TWC measurement by rotating both the compensator

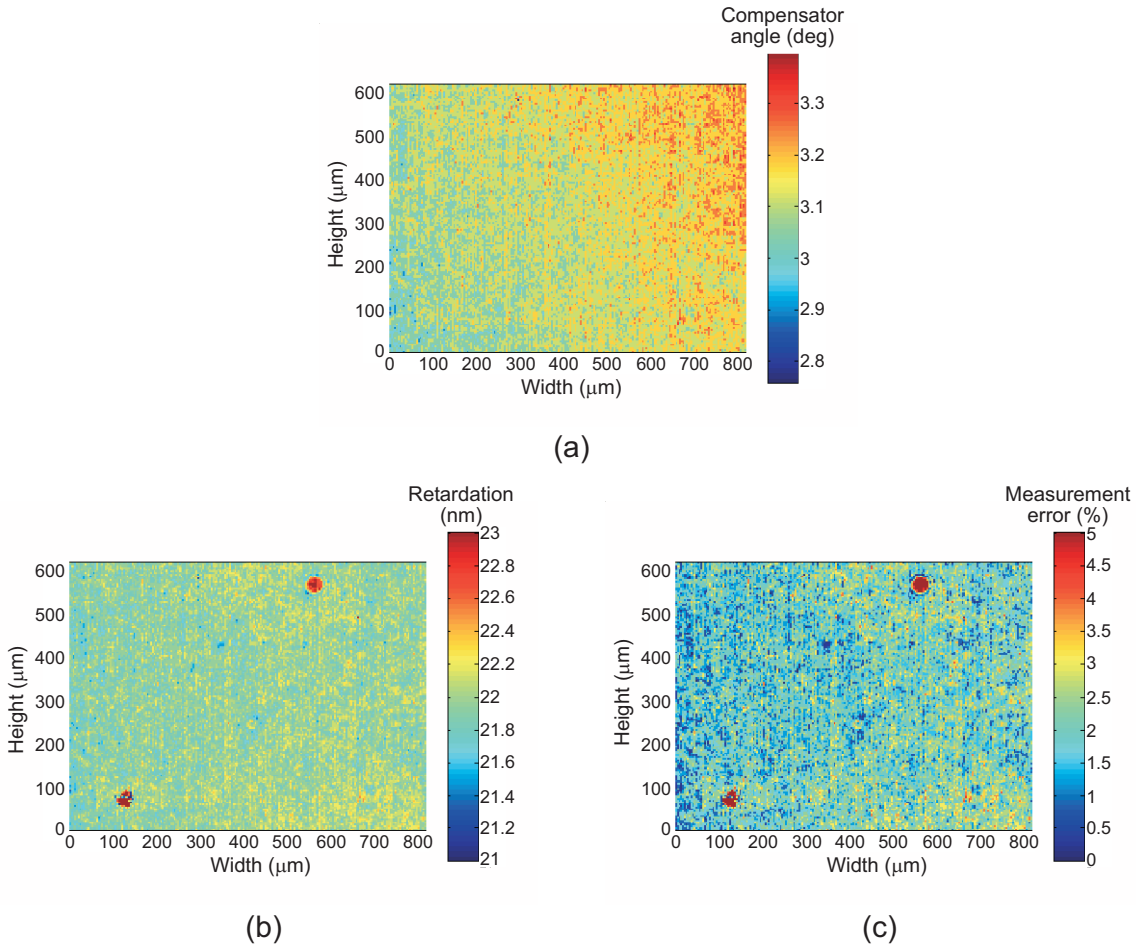

Figure 7.11: Full-field retardation measurements using the TWC technique. The compensator angles producing extinction without the sample are determined by rotating both the compensator and the analyzer (a) Compensator angles producing extinction without the sample in *deg*. (b) Measured retardation in *nm*. (c) Error compared to the manufacturer's retardation in (%).

and the analyzer. By doing so, the non-uniformities arising from the rotations of the compensator and the analyzer partially cancel out when subtracting the angles which produce extinction with and without the sample. There is not complete cancelation, however, due to the fact that the compensator and the analyzer are rotated over different angular ranges.

This can be seen in Fig. 7.11 where the compensator angles for extinction without the sample, the measured retardation, and the relative error are represented. The measured retardation in Fig. 7.11(b) is more uniform than the retardation measured previously represented in Fig. 7.9(c). In fact, a detailed analysis of the error distribution in the FOV in Table 7.4 confirms the improvement from the previous experiment. More particularly,

Table 7.4: Error analysis of TWC full-field retardation measurements in Fig. 7.11(c).

Error (%)	Proportion of FOV (%)
<5	99.69
<4	99.56
<3	94.33
<2	58.47
<1	6.86

the measurements producing a relative error less than 3% increased from 68.98% of the field-of-view to 94.33%.

The TWC proves to be very accurate for full-field measurements of small retardations. It is slightly less accurate than the Brace-Köhler technique with only 58.47% of the pixels in the FOV below 2% error compared to 98.53% of the pixels for the Brace-Köhler techniques. The TWC can be improved by optimizing the optics of the microscope such as the extinction ratio of the polarizers. This is critical to the TWC technique as the analyzer is rotated along with the compensator when searching for the intensity minima. In the current experimental configuration, the extinction ratio of the polarizers varies as the polarizer and analyzer are rotated in crossed position. These variations reveal that the light incident on the condenser polarizer is not randomly polarized. The light emerging from the light source becomes partially polarized while propagating through the different optical elements before the condenser in Fig. 7.1 probably because of stress-induced birefringence. Provided that the light incident on the first polarizer could be made randomly polarized, this would greatly improve the polarizers extinction ratio and further increase the TWC accuracy.

7.3 Sénarmont Method

7.3.1 Measurement Procedure

The Olympus polarization microscope model BX-60 is provided with a Sénarmont compensator plate that can be inserted into the compensator slot of the microscope tube (Fig. 7.1). It is recommanded for measuring retardations from 0 to λ. The measurement procedure

provided with the microscope consists of focusing on a sample placed at 45 *deg* from extinction between crossed polarizers. An interference filter with central wavelength equal to 546 *nm* is inserted after the light source to illuminate the sample with green light. With the quarter-waveplate in the compensator slot, the analyzer is rotated until extinction is produced in the middle of the field-of-view as seen through the eyepiece. The Sénarmont compensator formula, Eq. (3.12), is used to calculate the retardation. Although an image of the sample is formed, the latter procedure only allows single-point retardation measurements.

The Sénarmont technique needs to be implemented for full-field retardation measurements in a similar fashion to that done with the Brace-Köhler and TWC techniques in Secs. 7.1 and 7.2. The procedure for making full-field retardation measurements with the Sénarmont technique is identical to that of the Brace-Köhler technique with the exception being that the analyzer is rotated instead of the compensator. The experimental and image processing procedures outlined in Sec. 7.1.1 for the Brace-Köhler technique are thus identical for the Sénarmont technique.

7.3.2 Measurements

The Sénarmont technique is also tested by measuring the retardation of the Brace-Köhler compensator plate model U-CBR2 with retardation equal to 21.54 *nm*. Results are shown in Fig. 7.12. The measured retardation is not uniform over the field-of-view and fringes are clearly seen in the retardation distribution. Further, the relative measurement error is large over the entire field-of-view with only 0.18% of the pixels having less than 20% error. A detailed error analysis of the retardation measurements of Fig. 7.12 is summarized in Table 7.5. A total of 75% of the pixels have an error less than 25% and only 31.36% of the pixels have an error less than 24% making the Sénarmont technique far less accurate than the Brace-Köhler and TWC techniques for measuring small retardations.

A second measurement was made with the same sample to understand the fringes observed in Fig. 7.12. To vary the angle of incidence, the quarter-waveplate is tilted by inserting several sheets of paper under its holder in the compensator slot of the microscope.

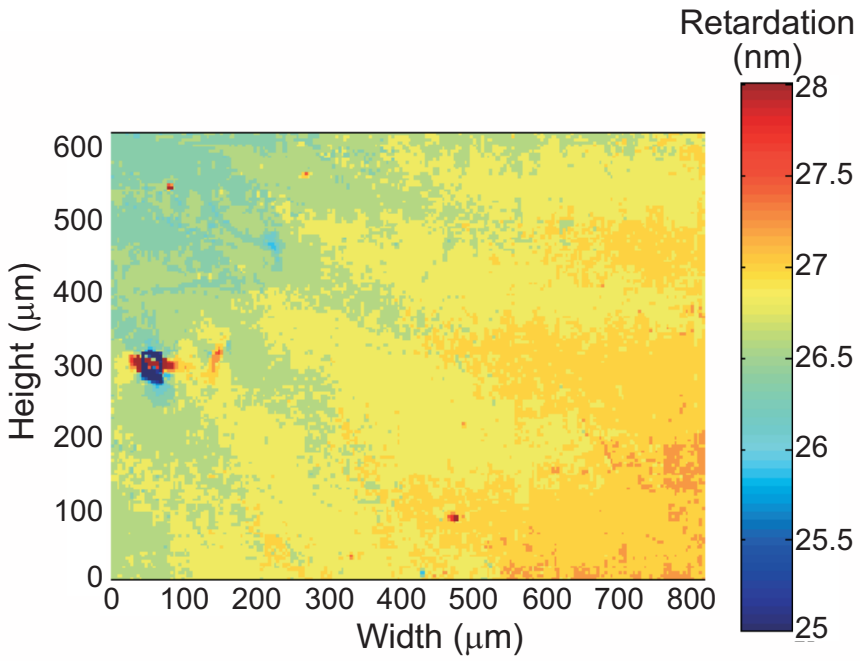

Figure 7.12: Full-field retardation measurements using Sénarmont technique.

Table 7.5: Error analysis of Sénarmont full-field retardation measurements in Fig. 7.12.

Error (%)	Proportion of FOV (%)
<30	99.89
<29	99.87
<28	99.85
<27	99.81
<26	98.07
<25	75
<24	31.36
<23	7.55
<22	0.54
<21	0.23
<20	0.18

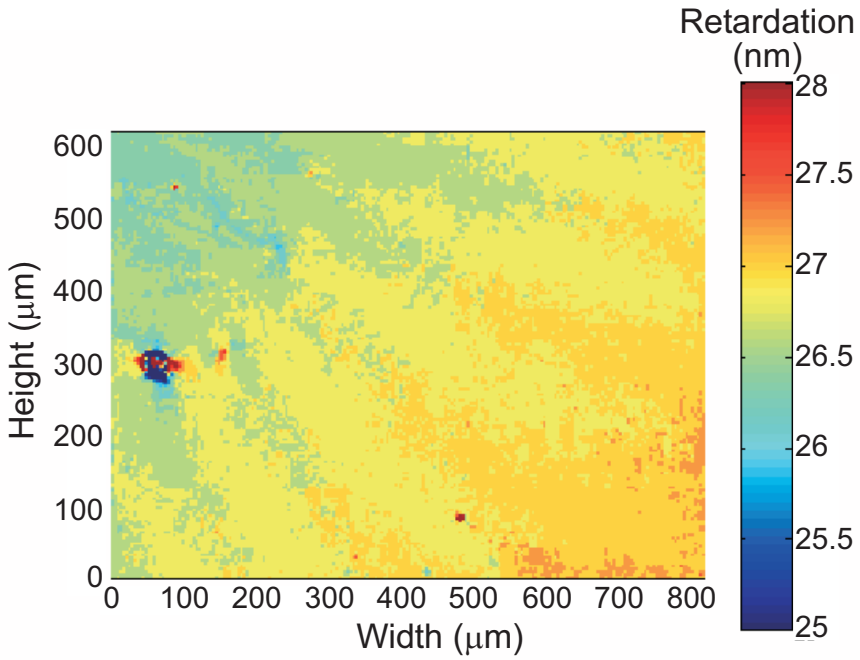

Figure 7.13: Full-field retardation measurements using Sénarmont technique. The quarter waveplate is tilted.

This tilts the waveplate by about 1 *deg*. The measured retardation in this configuration is shown in Fig. 7.13.

One more fringe appears in the retardation distribution compared to the previous measurement demonstrating the high sensitivity of the Sénarmont technique to variations of the angle of incidence on the quarter-waveplate. The error distribution is slightly worse than that of the previous measurement and is summarized in Table 7.6. Each of the various error limits defined in Table 7.6 contains approximately 1% fewer pixels in the second experiment when the quarter-waveplate is tilted.

The Sénarmont technique measures the retardation of the U-CBR2 plate much less accurately than the Brace-Köhler and the TWC techniques which both produced 95% of the measurements in the field-of-view below 3% error. The Sénarmont technique is therefore unsuitable for measuring accurately the small retardations present in optical devices. Further, a fringe-like pattern emerges in the measured retardation distribution due to small deviations from normal incidence. This also affects dramatically its accuracy as it wrongly

Table 7.6: Error analysis of Sénarmont full-field retardation measurements in Fig. 7.13. The quarter waveplate is tilted.

Error (%)	Proportion in FOV (%)
<30	99.90
<29	99.89
<28	99.85
<27	99.80
<26	98.12
<25	74.48
<24	29.32
<23	6.94
<22	0.63
<21	0.23
<20	0.19

produces a non-uniform retardation distribution of the U-CBR2 plate in Figs. 7.12 and 7.13 when in fact, the plate retardation is uniform.

CHAPTER 8

CHARACTERIZATION OF OPTICAL FIBERS AND INTERCONNECTS

The Brace-Köhler and TWC compensator techniques have proven to be very accurate for the measurement of low-level retardations for single-point and full-field measurements as was shown in Chapters 6 and 7. In this chapter, they are applied to the characterization of a variety of optical fibers and interconnects exhibiting stress-induced birefringence. Two-dimensional retardation measurements are performed with the Brace-Köhler and TWC techniques and compared to the intensity measured in the interference images of the samples.

8.1 Polarization-Maintaining Fiber

Polarization-maintaining fibers are used in optical fiber communication networks to preserve the state of polarization of the propagating light. There exists two types of polarization-maintaining fibers, namely, low-birefringent fibers and high-birefringent fibers. In low-birefringent fibers, a linearly polarized wave and a circularly polarized wave propagate with small polarization dispersion. In high-birefringent fibers, a linearly polarized wave propagates and remains in its state of polarization [96]. The image of a high-birefringent fiber fabricated by introducing stress-applying parts into the cladding is shown in Fig. 8.1.

8.1.1 Retardation Measurements

The polarization-maintaining fiber shown in Fig. 8.1 is placed on a microscope slide made of fused-silica whose stress-induced birefringence is negligible compared to that of the fiber. The optical fiber is immersed in index matching oil and covered by a cover slip also made of fused-silica. The optical fiber is oriented such that the two stress-applying parts axes are in the plane parallel to the microscope stage as is shown in Fig. 8.1.

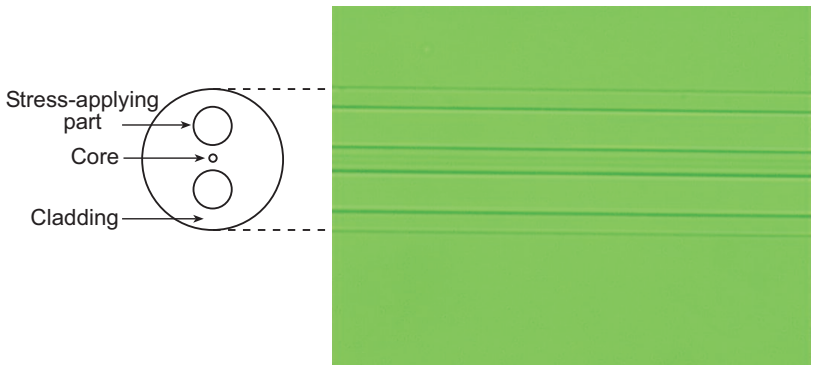

Figure 8.1: High-birefringence polarization-maintaining fiber image. The objective magnification is 20×.

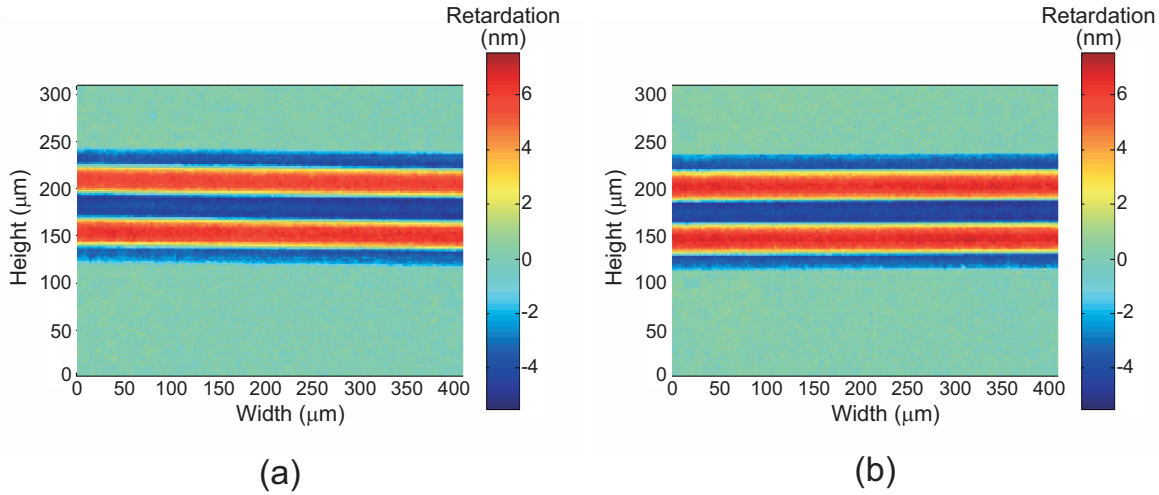

Figure 8.2: Polarization-maintaining fiber full-field retardation measurement. (a) Brace-Köhler technique. (b) TWC technique.

The retardation of the transversely illuminated polarization-maintaining fiber is measured with the Brace-Köhler and the TWC techniques using the procedures outlined in Secs. 7.1 and 7.2. The compensator used is the Olympus Brace-Köhler waveplate U-CBR2 of retardation 21.54 nm at $\lambda = 546$ nm. The resulting two-dimensional retardation distributions are shown in Figs. 8.2(a) and 8.2(b). The objective magnification is 20× and its numerical aperture is equal to 0.4. The pixel cells used during the image processing and averaging process introduced in Sec. 7.1.1 are square cells composed of 3×3 pixels. The two high-retardation regions in Figs. 8.2(a) and 8.2(b) correspond to the stress-applying parts shown in Fig. 8.1. The Brace-Köhler and TWC techniques are in good agreement and both resolve accurately the stress-applying parts exhibiting high birefringence.

8.1.2 Comparison with Interference Image

The retardation measurements of the high-birefringence polarization-maintaining fiber in Fig. 8.2 can be used to calculate the transmittance of the light transversely illuminating the fiber to compare with the intensity measured between crossed polarizers and to evaluate the accuracy of the retardation measurements. At such low level of retardations, a simple crossed-polarizers image results in intensities too weak to be resolved with sufficient dynamic range by the frame grabber. The transmittance comparison is thus done with an image of the optical fiber recorded when the compensator is at an angle thereby adding a bias retardation and resulting in larger intensities.

The transmittance of a system composed of two waveplates between crossed polarizers has been derived in Sec. 3.2.1 and is given by Eq. (3.23). Assuming that the phase-shifts ϕ_1 and ϕ_2 are small, the transverse transmittance $T_\perp$ becomes

$$T_\perp = (\frac{\phi_2}{2})^2 \sin^2 2\theta_2 + \frac{1}{2}\phi_1\phi_2 \sin 2\theta_2 + (\frac{\phi_1}{2})^2, \tag{8.1}$$

where ϕ_1 is the radian phase-shift produced by the optical fiber, ϕ_2 the radian phase-shift produced by the compensator, and θ_2 the compensator angle from extinction. The phase-shift along the fiber cross-section in the center of the retardation distribution measured with the Brace-Köhler technique in Fig. 8.2(a) is used to calculate the transmittance with Eq. (8.1). The phase-shift ϕ_2 corresponds to the compensator retardation equal to 21.54 nm in this experiment. The image was recorded for a compensator angle equal to 15 deg. The compensator angles for extinction without the sample are subtracted from this orientation all along the central cross-section of the fiber to determine the values of θ_2 for each pixel. The normalized calculated transmittance is plotted as a dashed line in Fig. 8.3. The normalized measured transmittance in the gray-scale image along the same cross-section of the optical fiber is plotted as a solid line in Fig. 8.3. A similar calculation is done for the retardation of the polarization-maintaining fiber measured with the TWC technique shown in Fig. 8.2(b). The comparison between the normalized measured transmittance and the normalized calculated transmittance is shown in Fig. 8.4. The transmittances calculated using the retardation profiles measured with the Brace-Köhler and TWC techniques are in

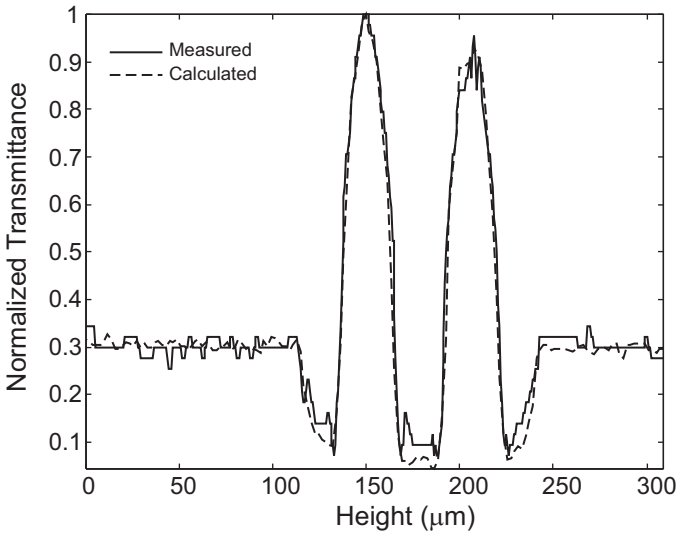

Figure 8.3: Comparison between the normalized measured transmittance between crossed polarizers (solid line) and the normalized transmittance calculated from the retardation of the polarization-maintaining fiber measured using the Brace-Köhler technique shown in Fig. 8.2(a) (dashed line).

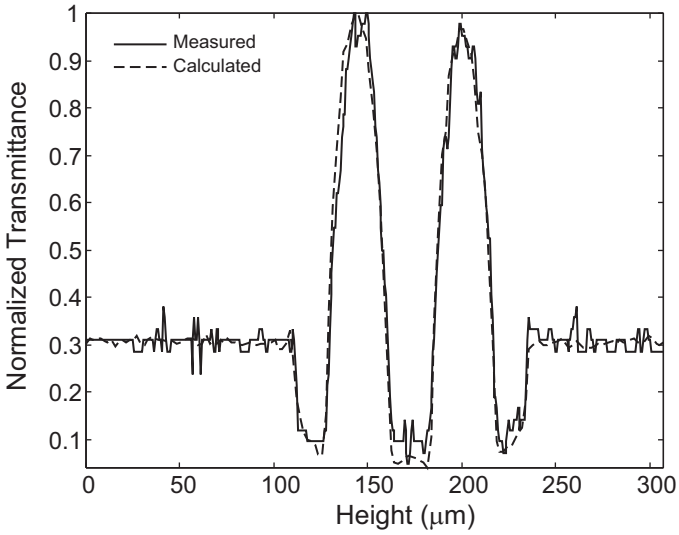

Figure 8.4: Comparison between the normalized measured transmittance between crossed polarizers (solid line) and the normalized transmittance calculated from the retardation of the polarization-maintaining fiber measured using the TWC technique shown in Fig. 8.2(b) (dashed line).

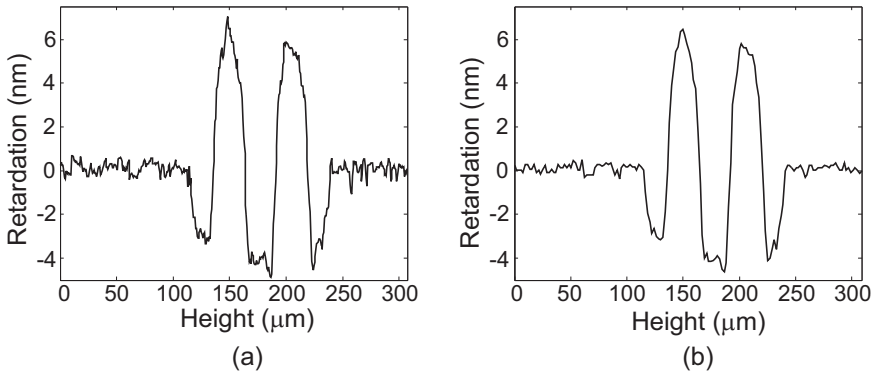

Figure 8.5: Image averaging effect on the noise in the retardation profile along the cross-section of a high-birefringence polarization-maintaining fiber measured with the Brace-Köhler technique. (a) Images are not averaged. The retardation is calculated at each pixel. (b) Images are averaged by computing the mean RGB values in cells of dimension 3×3 pixels. The retardation is calculated at each cell.

very good agreement with the measured transmittances in Figs. 8.3 and 8.4. The accuracy of the two techniques for measuring the low-level birefringence in samples such as optical fibers is thus verified.

8.1.3 Averaging Effect

The retardation profile along the cross-section of optical fibers needs to be extracted from the measured two-dimensional retardation distributions in order to calculate the residual stress. Noise arising in the retardation measurements affects the computation of the residual stress and needs to be reduced. In the full-field retardation measurement procedures presented in Chapter 7 for the Brace-Köhler and TWC techniques, noise is first reduced by recording images that are the averages of a large number of frames generated by the frame grabber over a certain period of time. In most of our experiments, each recorded image is the average of 16 to 20 frames.

The noise can be further reduced during the image processing stage of the retardation measurement procedures outlined in Chapter 7. As described in the flow charts of Figs. 7.3 and 7.8, before proceeding to the minima search the images can be reduced by averaging the RGB values of small pixel cells whose sizes are defined by the user. The effect on the noise in the retardation profile of this image averaging is shown in Fig. 8.5.

Table 8.1: Comparison between the objective resolution and the pixel length.

Objective Magnification	Resolution (μm)	Pixel Length (μm)
5×	2.24	2.56
10×	1.34	1.28
20×	0.84	0.64
40×	0.45	0.32

In Fig. 8.5, the retardation profiles are extracted from the two-dimensional retardation of the polarization-maintaining fiber measured with the Brace-Köhler technique. In Fig. 8.5(a), the retardation is computed by determining the intensity minima at each pixel without averaging the images. In Fig. 8.5(b), the retardation is calculated by determining the intensity minima in cells of dimension 3×3 pixels. The images are first averaged by computing the mean RGB values in each cell. The noise in the retardation profile can be significantly reduced as is shown in Fig. 8.5(b).

The averaging over several pixels is also necessary to avoid undersampling when the length of one pixel is less than the resolution of the microscope objective. For each objective magnification, one pixel in the image generated by the frame-grabber represents a specific length in the sample's space. This length is measured for each objective magnification using a micrometer scale provided with the Olympus microscope. A comparison between the objective magnification and the pixel length is presented in Table 8.1. For magnifications greater than 5×, the pixel length is less than the resolution of the objective. Computing the retardation of the sample pixel by pixel would therefore result in undersampling and would be inaccurate. Averaging the color information of the images over a few pixels allows the intensity minima search to be performed for distances greater than the objective resolution. In most of our experiments, the objectives with magnification 10×, 20×, and 40× are used and the color information of the images is averaged over square cells composed of 2×2 or 3×3 pixels.

8.2 Long-Period Fiber Grating

8.2.1 TWC Retardation Measurements

The retardation produced by a Long-Period Fiber Grating (LPFG) is measured with the TWC technique and is represented in Fig. 8.6(a). The LPFG has been fabricated by periodically exposing the axis of a single-mode optical fiber to pulses irradiation with CO_2 laser [76–78]. The spectral transmission and the characteristics of the grating are shown in Fig. 8.7. The grating is overmodulated exhibiting high resonances of 15 dB and 25 dB at wavelengths equal to 1335 nm and 1340 nm. The retardation is measured on a perturbed region of the LPFG, i.e., region that has been exposed to the CO_2 laser. The side of the fiber that has been exposed to the CO_2 laser is the upper edge of the optical fiber whose retardation is represented in Fig. 8.6(a).

As was shown in Sec. 8.1.2, the intensity of an interference image can be used to assess the retardation measurement accuracy. The gray scale intensity of the LPFG image recorded between crossed polarizers and with the compensator at an angle is represented in Fig. 8.6(b). It shows that the TWC retardation measurements are in very good agreement with the intensity of the crossed-polarizers image.

In fact, the retardation distribution of the LPFG in Fig. 8.6(a) can be substituted into Eq. (8.1) to calculate the transmittance and compare it to the intensity of the interference image. The calculated transmittance of the transversely illuminated LPFG is shown in Fig. 8.8. The calculated transmittance in Fig. 8.8 is in very good agreement with the interference image intensity represented in Fig. 8.6(b) confirming the high-accuracy and high-resolution of the full-field TWC technique. The details in the birefringence distribution are clearly resolved in the two-dimensional retardation measurements. The resolution of the technique will be quantified later in this chapter.

The retardation of another LPFG is measured and shown in Fig. 8.9(a). The spectral transmission and the characteristics of the grating are shown in Fig. 8.10. The grating is undermodulated exhibiting a low resonance of 6 dB at a wavelength of 1539 nm.

There are substantial differences in transmission characteristics between the two LPFG's of Figs. 8.7 and 8.10. The larger resonances in the overmodulated LPFG suggest that the

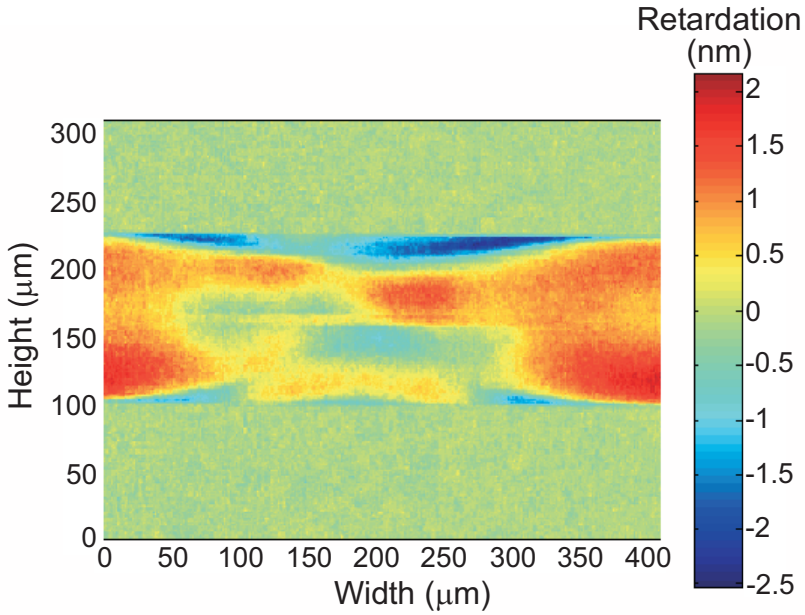

(a)

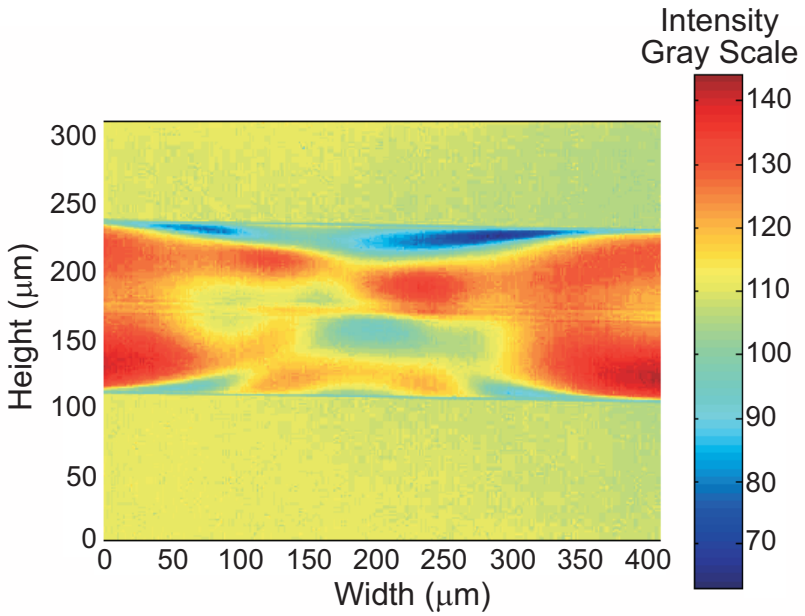

(b)

Figure 8.6: Comparison between the retardation measurement and the gray scale image intensity between crossed polarizers of a perturbed region of an overmodulated LPFG. The grating's characteristics are shown in Fig. 8.7. (a) Retardation measurements with the TWC technique. (b) Gray scale image intensity between crossed polarizers.

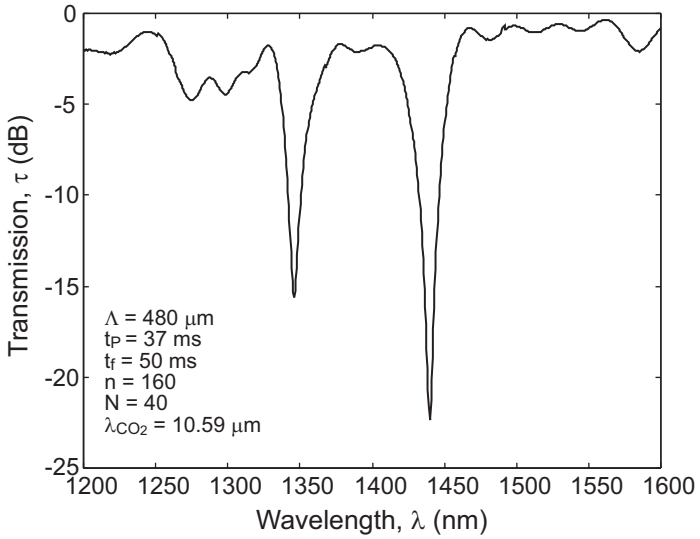

Figure 8.7: Spectral transmission and characteristics of an overmodulated LPFG.

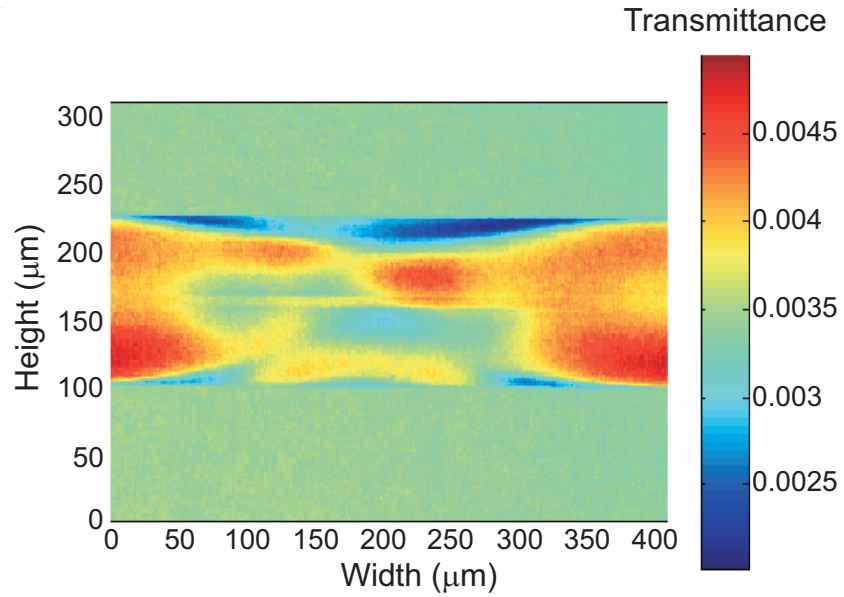

Figure 8.8: Transmittance of a transversely illuminated LPFG calculated using the retardation measured with the TWC technique in Fig. 8.6(a).

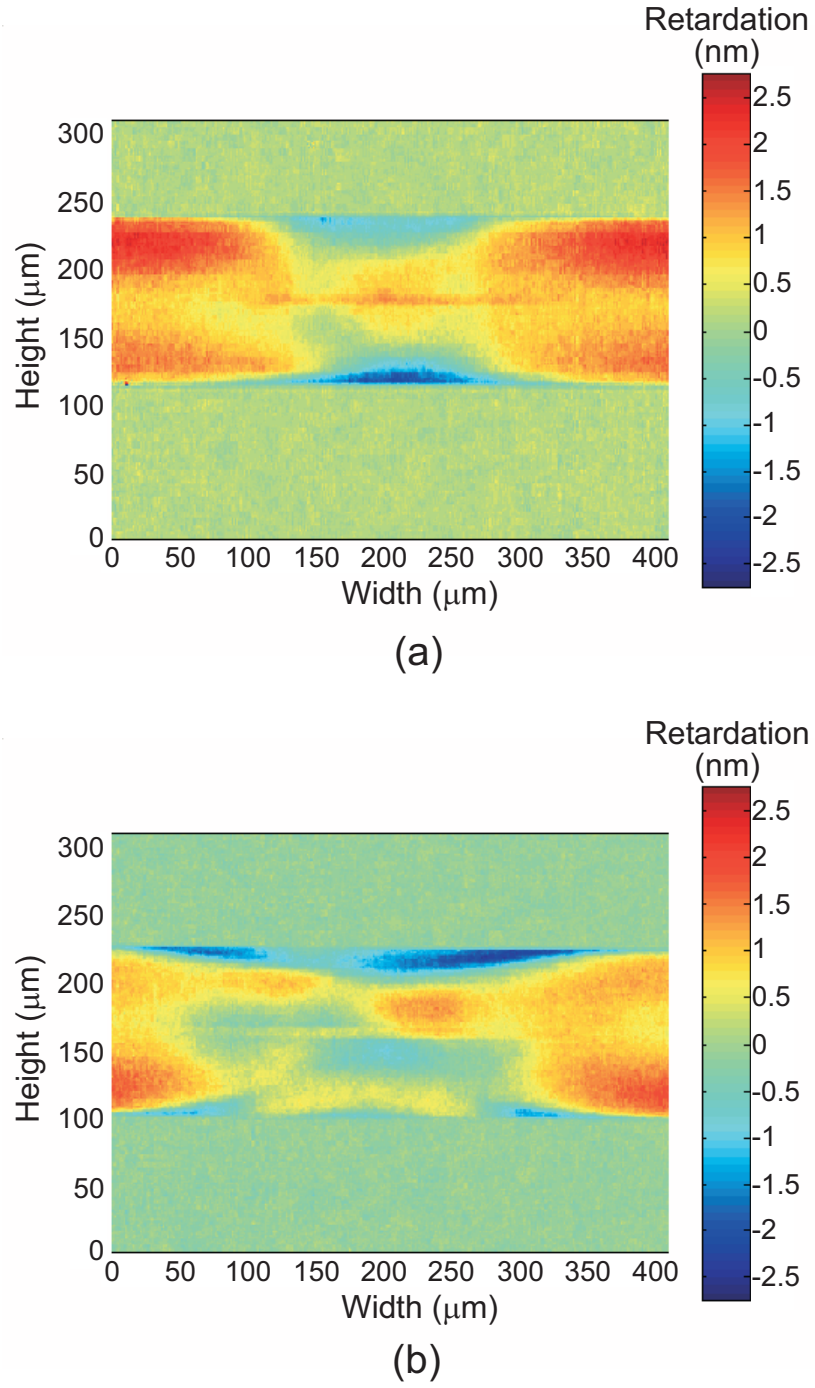

Figure 8.9: LPFG retardation measurements using the TWC technique. (a) Retardation of the perturbed region of an undermodulated LPFG. (b) Retardation of the perturbed region of an overmodulated LPFG.

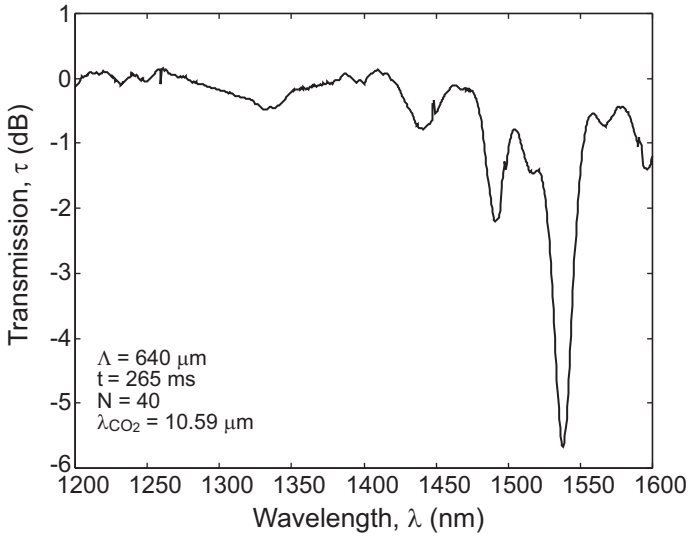

Figure 8.10: Spectral transmission and characteristics of an undermodulated LPFG.

exposure to the CO_2 laser during fabrication produced more changes to the refractive index and stress-induced birefringence than it did during the fabrication of the undermodulated LPFG.

This is confirmed by the two-dimensional retardation measurements shown in Fig. 8.9 illustrating the retardation changes of the perturbed regions in both gratings. With both gratings, one single period is imaged with the 20× objective. The unperturbed region of an LPFG is examined in the next section and its two-dimensional retardation distribution is shown in Fig. 8.11. In the case of the undermodulated LPFG (Fig. 8.9(a)), the area perturbed by the CO_2 laser radiations is much more confined, spanning over only 150 μm along the axis of the fiber, than it is in the case of the overmodulated LPFG whose perturbed area spans over 400 μm along the optical fiber axis (Fig. 8.9(b)).

Further, the retardation changes occur mostly in the outside of the cladding region of the slightly modulated grating with the retardation becoming negative at the edges. The region around the core conserves a retardation distribution similar to that of an unperturbed fiber. Axial symmetry is somewhat preserved. This is in complete contrast with the retardation changes occuring during the fabrication of the overmodulated grating whose entire cladding and core regions are affected by the CO_2 laser irradiations. Like previously, the largest changes are observed at the edges of the fiber with the retardation decreasing to less than

$-2\ nm$ (blue area). The retardation around the core is also greatly modified and decreases to approximately $0\ nm$ on either side of the fiber axis. The retardation distribution is not axially symmetric after fabrication of the overmodulated grating.

This demonstrates how full-field retardation measurements can be related to LPFG's performances characteristics and can be used to understand and monitor their fabrication reinforcing the importance of the development of techniques such as the Brace-Köhler and the TWC methods.

8.2.2 Brace-Köhler Retardation Measurements

The retardation of an unperturbed region of a LPFG, i.e., region that has not been exposed to the CO_2 laser, is measured using the Brace-Köhler technique. The measured two-dimensional retardation distribution is represented in Fig. 8.11(a). The gray scale intensity of the interference image is represented in Fig. 8.11(b).

The transmittance of the transversely illuminated LPFG is also calculated substituting the measured retardation into Eq. (8.1). The calculated transmittance is represented in Fig. 8.12. The very good agreement between the calculated transmittance in Fig. 8.12 and the measured intensity in Fig. 8.11(b) demonstrates the high accuracy and high resolution of the full-field Brace-Köhler technique. The resolution of the technique will be quantified later in this chapter.

8.2.3 Retardation Measurements versus Intensity Measurements

The normalized transmittances calculated using the retardation measurements presented in Secs. 8.1 and 8.2 are in excellent agreement with the transmittances of the interference images (Figs. 8.4, 8.3, 8.8, and 8.11). The full-field retardation measurements with the Brace-Köhler and TWC techniques resolve in great detail the stress-induced birefringence distribution in the optical fibers. This consistency between the measured retardation and the measured transmittance suggests that the retardation measurements could be used in order to calibrate the intensity of the interference image. The calibration could be done once with a sample of known retardation. The calibration measurements could then be used with other samples of unknown retardations avoiding the more lengthy process of the

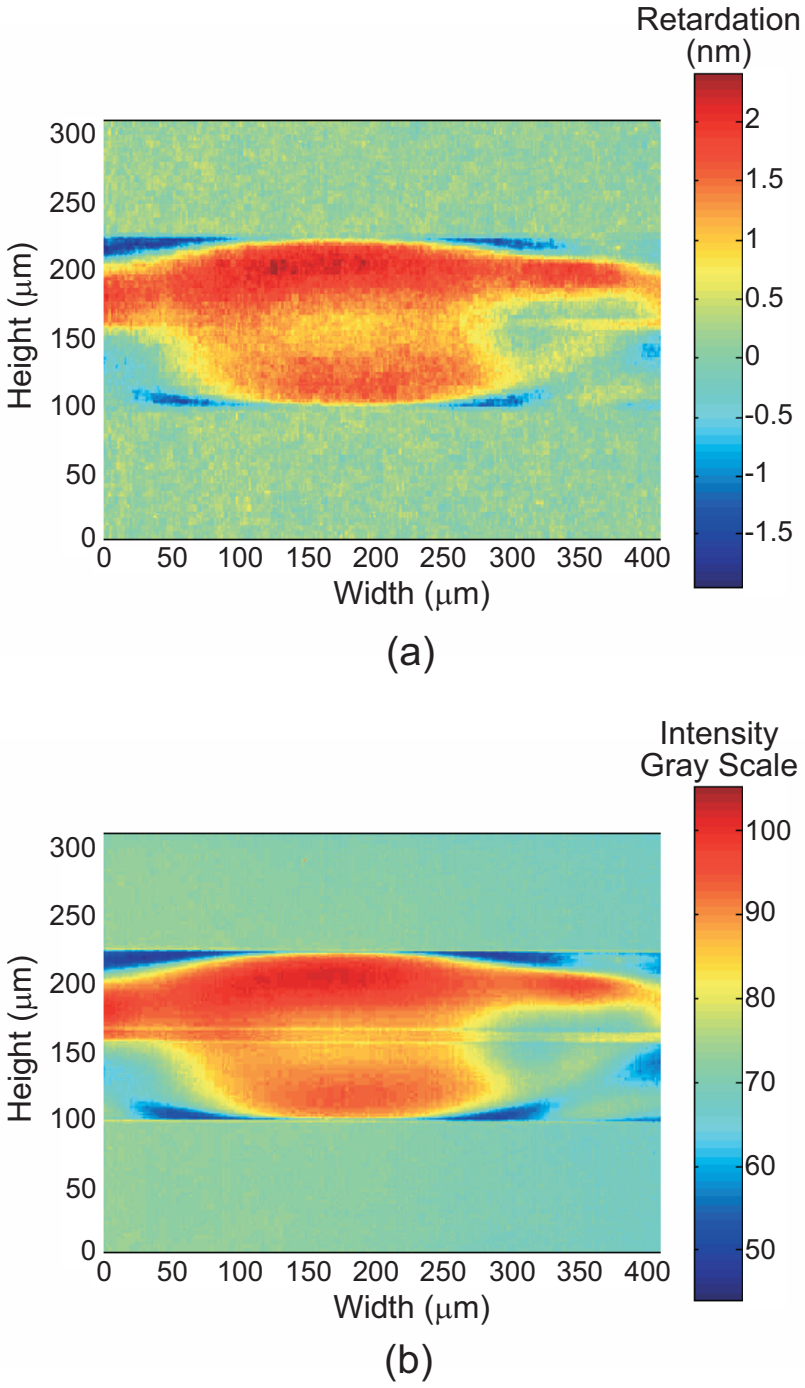

Figure 8.11: LPFG retardation measurements and gray scale intensity of the crossed-polarizers image. (a) Retardation measurements with the Brace-Köhler technique (b) Gray scale intensity of LPFG image between crossed polarizers.

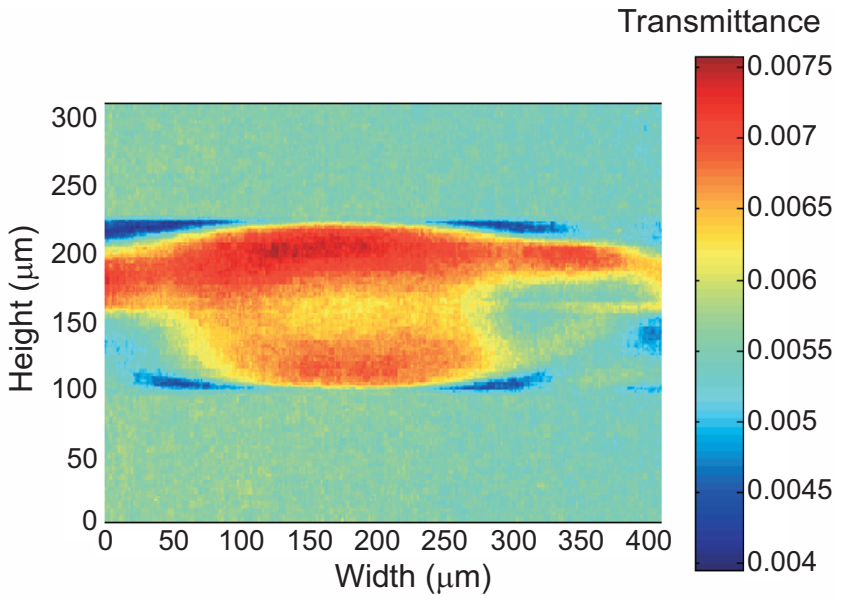

Figure 8.12: Transmittance of a transversely illuminated LPFG calculated using the retardation measured with the Brace-Köhler technique in Fig. 8.11(a).

full-field measurements using the Brace-Köhler and TWC techniques. Such a calibration process, however, may be more challenging and less accurate.

Depending on the magnitude of the sample's retardation, different bias retardations are necessary to generate the interference image. Consequently, the calibrations intensity/retardation would have to be done for different biases corresponding to different retardations magnitudes. Further, the retardation of the unknown sample must be necessarily less than that of the sample used during the calibration so the measured intensities fall into the calibrated range. This means that the unknown retardation cannot be measured with the calibrated intensities when the sample's retardation is greater than that used for the calibration. The range of retardations that can be measured with the calibrated intensities is therefore limited and constrained to samples whose retardations are less than that used for the calibration.

Most importantly, it is difficult to calibrate the intensities to the retardations due to the non-uniformities arising from the imperfections in the source or the optical components of the microscope. Residual stress in the objective lenses, for example, affects the formation of

the interference image whose intensity depends not only on the birefringence of the sample but also on that of the optical components of the microscope, however small this birefringence can be. This can be better understood looking at the retardation measurement of the overmodulated LPFG and the measured transmittance in Fig. 8.6. The retardation distribution measured with the TWC technique shows a uniform background color corresponding to 0 nm retardation in Fig. 8.6(a). This is not the case with the intensity of the interference image whose background intensity color varies from yellow to green from the left to the right side of the field-of-view in Fig. 8.6(b). This non-uniformity is eliminated with the retardation measurement using the TWC technique.

This can be explained by the fact that the effects due to the optical components of the system are canceled out with the Brace-Köhler and TWC techniques because the retardation measurements are based on subtracting intensity minima angles with and without the sample. When subtracting the two over the whole field-of-view to compute the retardation, the instrumentation effects are eliminated and the sample's birefringence only is calculated. This renders the Brace-Köhler and the TWC techniques more accurate than the intensity measurement technique because of the instrumentation compensation.

8.3 Optical Interconnects

Optical interconnects have emerged as a promising technology to overcome the limitations of electrical interconnects in clock distribution, system synchronization, cross-talk, and power dissipation. Recently, chip to board optical interconnection has been demonstrated using polymer pillar waveguides such as that represented in Fig. 8.13 [80–82].

Because of their recent development, very little is known about the mechanical and optical properties of these new polymer optical interconnects. The birefringence measurements of these waveguides may lead to important information about the residual stress and the uniformity in the waveguide. This ultimately may lead to a better understanding of their performance and their fabrication process. Retardation measurement techniques are thus crucial to assess and monitor the optical characteristics during and after the fabrication process.

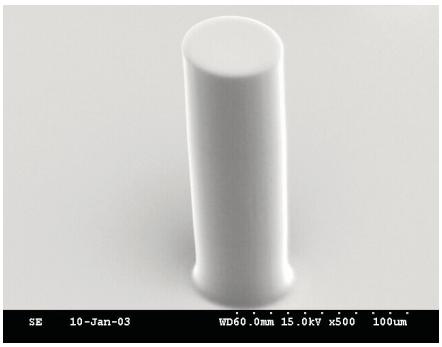

Figure 8.13: Polymer pillar waveguide for I/O chip to board optical interconnection [80–82].

Further, the polymer pillars may be used for connections between the board and the chip. As temperature varies, the difference in coefficient of thermal expansion between the board and the chip causes the materials to expand in different directions and magnitudes which bends the polymer pillars. Consequently, there is also a need to measure the birefringence of the polymer pillars when they are bent to assess their reliability as temperature varies.

Polymer pillars have been fabricated on Si substrates using the process outlined in References 81 and 82. The retardation of one transversely illuminated polymer pillar is measured with the Brace-Köhler technique. Two full-field retardation measurements are presented in Figs. 8.14 and 8.15. Interference images are also recorded corresponding to the two measurements and are shown in Figs. 8.16(a) and 8.16(b).

The main difference between the two measurements in Figs. 8.14 and 8.15 is the amount of index matching oil in which the pillar is immersed. The polymer pillars are usually fabricated in large arrays. They are oriented vertically on the substrate. The pillar used in this experiment was extracted from an array of pillars with diameters equal to 70 μm and heights equal to 170 μm. The distance between pillars was 325 μm.

Due to its small dimensions, the process of isolating one single pillar and placing it parallel to the microscope slide is very delicate. The Si substrate is first cleaved to obtain a small surface containing a row composed of just a few pillars. This small piece is then rotated so the axes of the pillars are horizontal. The Si substrate lays vertically while the pillars' axes are approximately parallel to the microscope slide. The surface of the Si substrate surrounding the pillars being evidently larger than the pillars' diameters, a cover

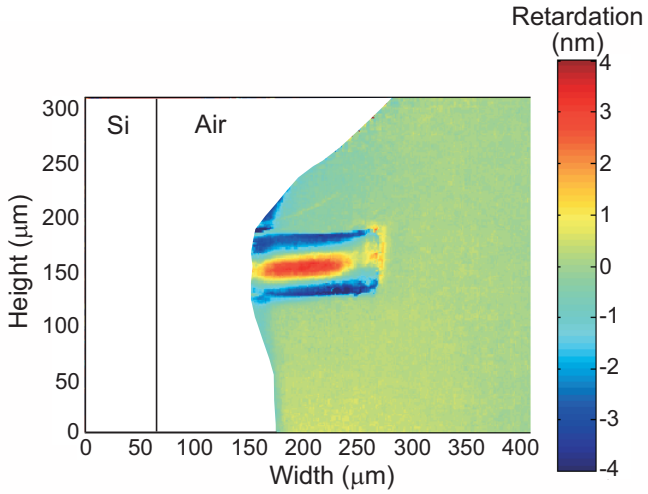

Figure 8.14: Polymer pillar retardation measurement with the full-field Brace-Köhler technique.

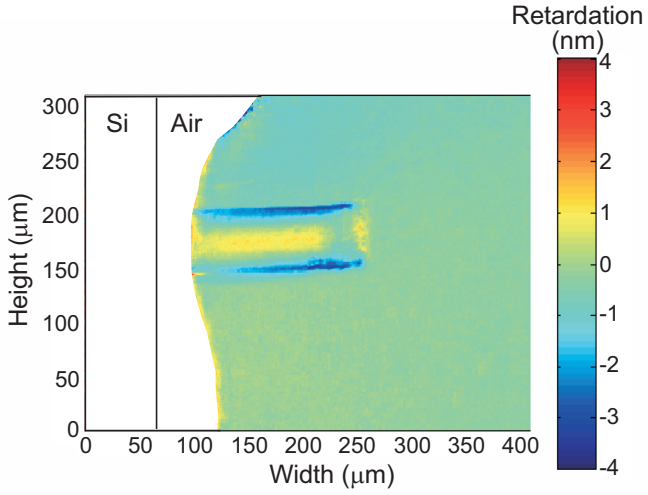

Figure 8.15: Polymer pillar retardation measurement with the full-field Brace-Köhler technique.

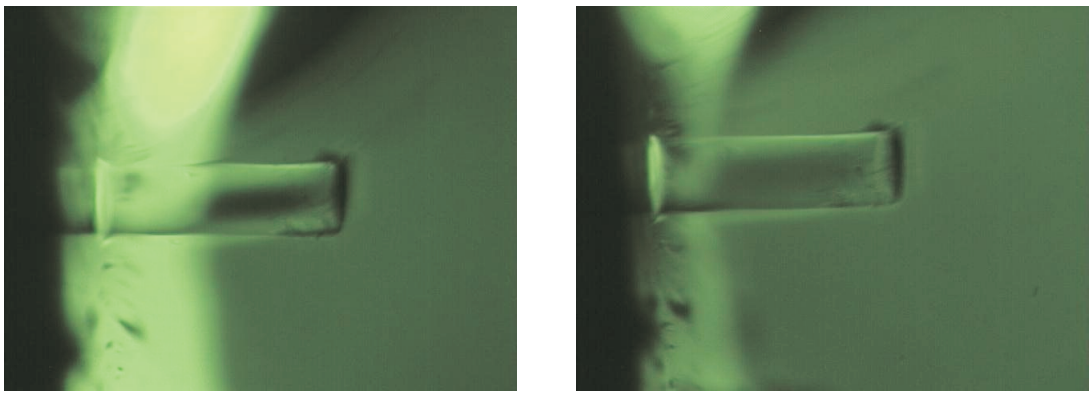

Figure 8.16: Polymer pillar interference images. (a) The pillar is immersed in index matching oil that does not completely cover the pillar all the way to the Si substrate. (b) More index matching oil is added to reduce the air-gap between the oil and the Si substrate.

slip cannot be placed on the sample without causing the Si substrate to fall back in its horizontal position. The pillar can only be delicately immersed in index matching oil. This must be done very carefully so the sample's orientation is not disturbed.

During the first measurement in Fig. 8.14, the quantity of index matching oil is not enough to cover the pillar entirely to the base attached to the Si substrate as can be seen in Fig. 8.16(a). An air-gap is clearly visible between the Si substrate and the surface of the index matching cell. The air-gap appears as a brighter region in the interference image while the envelope of the index matching oil appears darker. No birefringence can be measured in the Si substrate and the air-gap regions. Note that in the full-field retardation measurements shown in Figs. 8.14 and 8.15, the regions corresponding to the Si substrate and any remaining air-gap at the base of the pillar are white. This is seen to the left side of the retardation map. The measured retardations in the part of the pillar immersed in index matching oil are assigned colors within the range inside the colorbar reprensenting the measured retardations. More index matching oil is added during the second measurement in Fig. 8.15 so the air-gap is filled or almost filled. The interference image in Fig. 8.16(b) shows that the pillar is immersed closer to its base attached to the Si substrate. However, a small air-gap remains between the substrate and the oil. The retardation measured in the part of the pillar immersed in index matching oil is more uniform in Fig. 8.15.

In the first measurement, the index matching oil covers only 100 μm of the total length of the pillar. The weight of the upper layer of index matching oil and the lack of an underlying layer supporting the pillar all along its length result therefore in the pillar being bent. This can be seen in the interference image in Fig. 8.16(a) and the retardation measurement in Fig. 8.14. Retardations with higher magnitudes appear in large areas in the center and at the edges of the pillar. This corresponds to strain that the oil weight applies to the tip of the pillar resulting in an increased birefringence. On the other hand, the index matching oil covers approximately 150 μm of the total length of the pillar in the second measurement. The interference image in Fig. 8.16(b) and the retardation measurement in Fig. 8.15 show more uniformities and symmetry than previously. Retardations of high magnitudes comprise smaller areas in the center and at the edges of the pillar. The index matching oil applies less strain to the pillar in this second measurement. The additional matching oil infiltrates not only closer to the Si substrate but also fills any air-gap between the pillar and the microscope slide. Consequently, the weight of the pillar is evenly supported by the underlying matching oil layer preventing the upper layer weight to bend the pillar. No significant birefringence change is observed in the center and at the edges like was the case in the first measurement. Only the stress-induced birefringence of the pillar is measured. A detail analysis of the stress in the polymer pillar will be presented in the next chapter.

8.4 Retardation Measurement Resolution

The measurements presented in Secs. 8.2 and 8.3 illustrate how the full-field retardation measurements can be used to assess the uniformities and stress-induced birefringence in LPFGs and polymer pillar interconnects. The measurements prove to be very sensitive as they resolve the details in the retardation variations due to the stress-induced birefringence in the perturbed regions of LPFGs and in the polymer pillars. In fact, the minimum measurable retardation change can be determined by considering the noise in the background of the retardation images.

The mean retardation is calculated in the background of various retardation images generated with the Brace-Köhler and TWC techniques for microscope objectives having

Table 8.2: Sensitivity of TWC and Brace-Köhler techniques.

Objective Magnification	Objective NA	Measurement Technique	Sensitivity (nm)
20×	0.40	Brace-Köhler	0.10
20×	0.40	TWC	0.09
40×	0.75	Brace-Köhler	0.09
40×	0.75	TWC	0.07

magnifications of 20× and 40×. These two objectives are used in most of these experiments to achieve high spatial resolutions of 0.84 and 0.45 μm respectively (Table 8.1). The standard deviation of the background retardation is then calculated to evaluate the sensitivity of the two-dimensional retardation measurements. Any retardation change greater than the standard deviation in the background is detected by the optical system. These standard deviations calculations are summarized in Table 8.2 for the Brace-Köhler and the TWC techniques.

Both the Brace-Köhler and the TWC techniques achieve very good resolutions. The retardation resolution increases with the objective magnification and numerical aperture. The TWC has a better resolution than the Brace-Köhler technique for the two objectives magnifications used. The TWC measurements result in a resolution of 0.07 nm with the 40× objective while the Brace-Köhler measurements result in a resolution of 0.09 nm. The TWC has also a better resolution with the 20× objective. These resolutions are very good espcially given the fact that to find the intensity minima, the compensators are rotated every 0.5 deg. This angular increment can be decerased to 0.1 deg which would increase the accuracy of the minima search and reduce the noise floor in the retardation images background. The measurement resolution can therefore be improved even further.

CHAPTER 9

RESIDUAL STRESS

The two-dimensional retardation measurements of the various optical fibers and interconnects in Chapter 8 can be used to compute the residual stress profile in these structures. The built-in stress profile in optical devices governs the refractive index profile and thereby their waveguiding properties. Stress measurements are of primary importance to understand the refractive index changes that occured during the fabrication of devices such as fiber gratings or to monitor the quality and performance of optical devices during their fabrication process. The goal of this chapter is the development of efficient numerical and experimental procedures to retrieve accurately the residual stress profile from two-dimensional retardation measurements.

9.1 Automatic Gain Control Effect

The accuracy of the two-dimensional retardation measurements using the Brace-Köhler and TWC techniques depends on the ability of the system to resolve intensity minima and intensity extinctions. The optical elements are rotated over angular ranges containing the intensity minima and extinctions. The level of retardation being very low, the intensity transmitted between crossed polarizers is also low and produces very dim images. The camera settings must thus be adjusted so the intensity curve can be resolved.

The CCD camera used in these experiments is a Sony DXC-107A. Automatic Gain Control (AGC) is available to adjust the gain of the video circuit according to the lighting conditions. The intensity level along the cross-section of a Corning SMF-28 optical fiber observed between crossed polarizers is presented in Fig. 9.1. A retardation bias is introduced by rotating the compensator U-CBR2 at a small angle from extinction. The image intensity is converted to gray scale. The automatic gain control of the CCD camera is switched off in Fig. 9.1(a) and is switched on in Fig. 9.1(b). The overall level of intensity is higher in

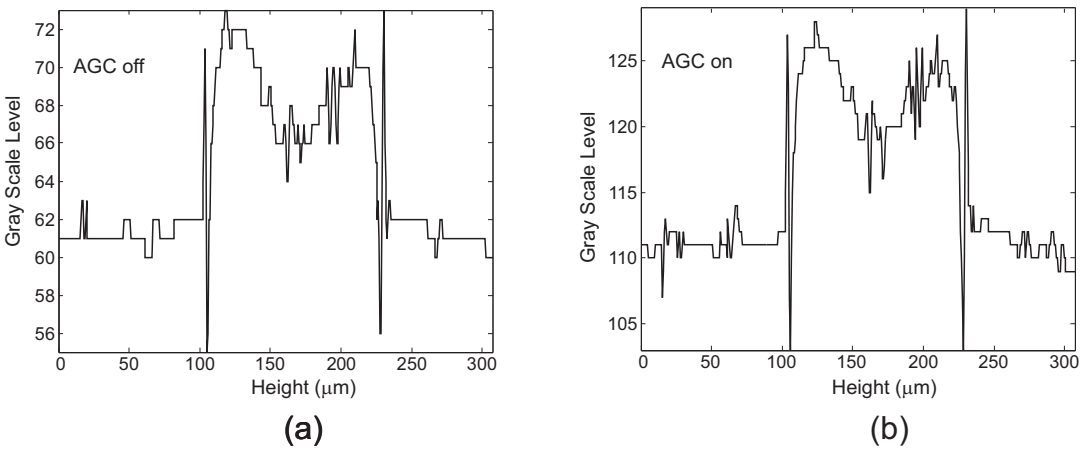

Figure 9.1: Gray scale level of the intensity along the cross-section of a Corning SMF-28 optical fiber observed between crossed polarizers with a bias retardation. (a) The AGC of the CCD camera is off. (b) The AGC of the CCD camera is on.

Fig. 9.1(b) due to the AGC with a background level of approximately 110 in gray scale while the background level is approximately 61 without the AGC in Fig. 9.1(a). The intensity variations and the noise are very similar in both cases. The AGC does not distort or affect the intensity variations in the image.

The other aspect that needs to be considered is the variation of intensity as the optical elements are rotated. This is illustrated in Fig. 9.2 where the variations of the green level of the central pixel are plotted as a function of the compensator angles. The solid line corresponds to the case where the AGC is on and the dashed line to the case where the AGC if off. For this experiment, a green filter is inserted in front of the light source as is usually done during the retardation measurements. The compensator is the Olympus U-CBR2 waveplate. Images are recorded for each angle according to the procedure described in Sec. 7.1.1. Only the variations of the green level of the pixel in the center of the field-of-view are represented in Fig. 9.2. When the AGC is turned off, the dynamic range of the green level of the pixel is extremely small, ranging in this case from 30 to 32. This makes it very difficult to resolve the minimum of the intensity curve. Thus the angle producing this minimum cannot be accurately determined. Switching on the AGC of the CCD camera increases the dynamic range of the green level which in this case ranges from 31 to 46 as can be seen in Fig. 9.2. It resolves the intensity curve near the minimum and renders a

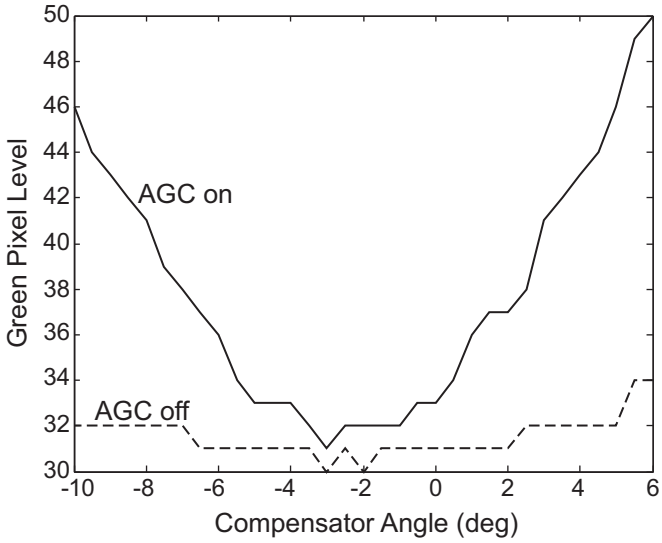

Figure 9.2: Green level of the central pixel as a function of compensator angles with the AGC on (solid line) and with the AGC off (dashed line).

more accurate determination of the compensator angle producing it.

Throughout the retardation measurements conducted in this research, the AGC of the CCD camera is switched on so the intensity curve can be represented more accurately by the frame grabber in terms of pixel color level as is shown in Fig. 9.2.

9.2 Noise Filtering

9.2.1 Wiener Filter

The two-dimensional retardation measurements are used to calculate the axial residual stress in optical fibers and interconnects. As is the case in most experiments, these measurements contain noise which needs to be filtered out to optimize the stress calculation. The noise filtering problem consists of estimating a given signal from noisy measurements or observations and has applications in speech transmission, radar signal detection, image processing, and communication. Classical filters such as lowpass, highpass, or bandpass can be designed to extract a signal from noisy measurements. However, these filters are not optimum. That is, they do not produce an accurate estimate of the signal. This has driven research to design optimum digital filters in the mean square error sense. In 1940, Norbert Wiener developed a filter enabling the determination of the minimum mean square error

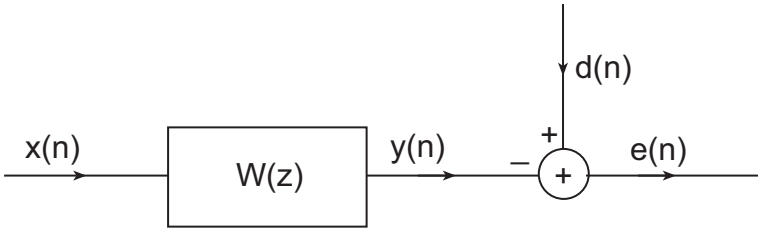

Figure 9.3: Principle of the general Wiener filtering problem. Considering two statistically related signals $x(n)$ and $d(n)$, $W(z)$ represents the Wiener filter producing the minimum mean-square error estimate $y(n)$ of $d(n)$ [97].

estimate of a noisy detected signal [97].

The general Wiener filtering problem is shown in Fig. 9.3. The best estimate $y(n)$ of the signal $d(n)$ is to be determined from noisy observations

$$x(n) = d(n) + v(n), \tag{9.1}$$

where $v(n)$ represents noise. The Wiener filter $W(z)$ minimizes the mean-square error ξ given by

$$\xi = E\{|e(n)^2|\}, \tag{9.2}$$

with

$$e(n) = d(n) - y(n), \tag{9.3}$$

and where E represents the statistical mean. It can be shown that it is equivalent to solving the Wiener-Hopf equations which in matrix form are given by

$$R_x w = r_{dx}, \tag{9.4}$$

where R_x is a $p \times p$ Hermitian Toeptlitz matrix of autocorrelations, w is a vector containing the Wiener filter coefficients, and r_{dx} is the vector of cross-correlations between the undistorted signal $d(n)$ and the measured signal $x(n)$ [97]. This allows the determination of the best estimate of a signal $d(n)$ by statistically analyzing the observed signal $x(n)$ and minimizing the mean-square error between the estimate $y(n)$ and the desired signal $d(n)$. In that sense, the Wiener filter is an optimum digital filter that can be used to recover signals from noisy observations such as the two-dimensional retardation measurements done in this research.

9.2.2 Noise Filtering of Retardation Measurements

As described in Sec. 9.2.1, the Wiener optimum digital filter can be used to filter out the noise in two-dimensional retardation measurements. A two-dimensional adaptative Wiener filter function is available from the Matlab images toolbox. This function filters out the noise in images or matrices by applying the Wiener filter principle pixelwise considering the statistical data from the local neighboring pixels. The number of pixels used to obtain the statistical data around each pixel is defined by the user.

The retardation of the perturbed region of a LPFG is measured with the TWC technique and the retardation along a cross-section is represented in Fig. 9.4(a) without filtering the noise. The objective magnification used is 20×. The Wiener filtering technique is applied to the two-dimensional retardation distribution in Figs. 9.4(b) and 9.4(c). The best estimate of the retardation is found at each pixel by minimizing the mean-square error in cells composed of 3 by 3 and 5 by 5 pixels in Figs. 9.4(b) and 9.4(c) respectively. The Wiener filter decreases the measurement noise efficiently without distorting the overall retardation function. It is also clear that the more pixels are used in the statistical optimization, the better the estimate of the retardation will be as can be seen in Fig. 9.4(c).

9.3 Residual-Stress Computation

9.3.1 Abel Transform

The retardation of the light transversely illuminating a birefringent cylinder is related to the axial residual stress by Eq. (2.2) introduced in Sec. 2.1.3.3,

$$R(y) = 2C \int_y^{r_o} \sigma_z(r) \frac{r dr}{\sqrt{r^2 - y^2}}, \tag{9.5}$$

where C is the stress-optic coefficient of the material, r_o is the outer radius of the cylinder, y is the height of the beam incident on the cylinder and the projected retardation $R(y)$, r is the radial coordinate, and $\sigma_z(r)$ is the axial residual stress. Equation (9.5) is the well-known forward Abel transform. The residual stress is in turn computed by using the inverse Abel transform,

$$\sigma_z(r) = -\frac{1}{\pi C} \int_r^{r_o} \frac{dR(y)/dy}{\sqrt{y^2 - r^2}} dy, \tag{9.6}$$

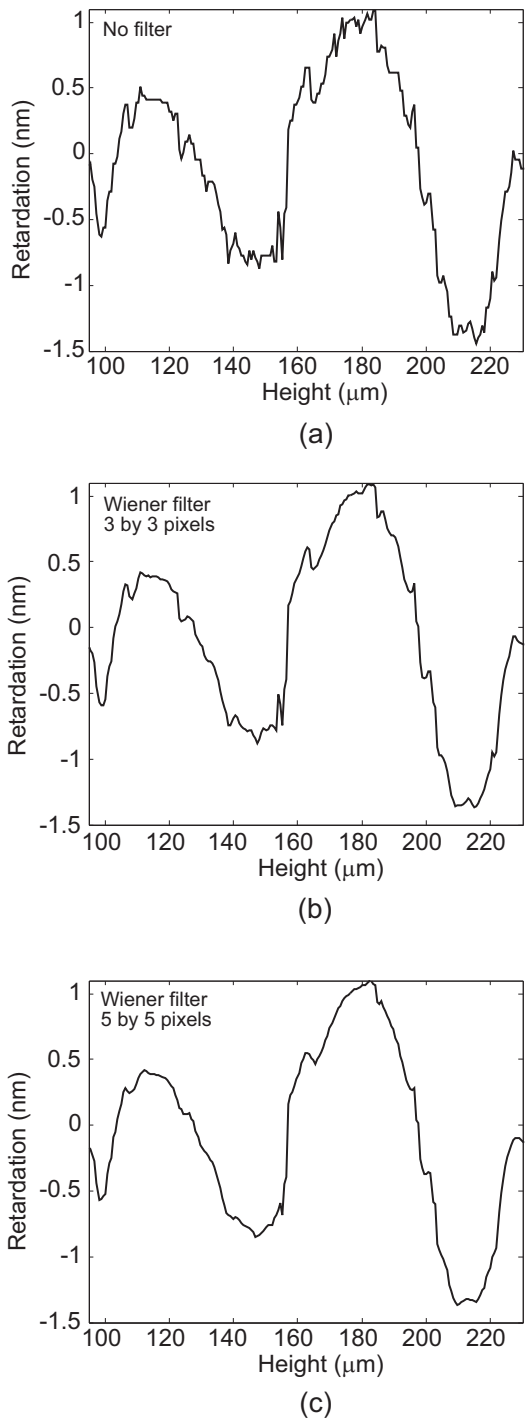

Figure 9.4: Wiener filter applied to the retardation of the perturbed region in a LPFG measured with the TWC technique. (a) No noise filter is applied. (b) The Wiener filter is applied to the two-dimensional retardation distribution using statistical data in cells of 3 by 3 pixels. (c) The Wiener filter is applied to the two-dimensional retardation distribution using statistical data in cells of 5 by 5 pixels.

which has also been introduced in Sec. 2.1.3.3. The axial residual stress profile in optical fibers is retrieved by computing Eq. (9.6) [16, 30, 31, 41, 65, 89, 90, 98, 99].

The inverse Abel transform is crucial in a plethora of applications. It is necessary for the determination of temperature profile in plasmas and flames, for the study of brightness/emission problems in astronomy, for the analysis of droplet distribution in axisymmetric spray, and for the retrieval of refractive index profile in plasmas and optical fibers [100]. The algorithms computing the inverse Abel transform Eq. (9.6) based on calculating the derivative of the measured data using finite-difference techniques have proved to be numerically very unstable [100, 101]. Further, the presence of a singular point at the origin results in an increased error and lack of resolution near the fiber axis [102]. Much research has been concentrated on developing numerical techniques overcoming these issues in order to compute the inverse Abel transform [100].

More particularly, Fourier-based techniques have drawn great interest as they allow the development of analytic formulas for the forward and inverse Abel transforms that avoid numerical differentiation and use no approximations [102, 103].

9.3.2 Fourier Expansion Method

Considering two functions $S(y)$, the observed data, and $f(r)$ the radial function to be determined, the Abel transform is written as

$$S(y) = 2\int_y^R f(r)(r^2 - y^2)^{-1/2} r dr, \tag{9.7}$$

and the inverse Abel transform as

$$f(r) = -\frac{1}{\pi}\int_r^R \frac{dS(y)}{dy}(y^2 - r^2)^{-1/2} dy, \tag{9.8}$$

where R is the maximum radius. The expansion of $S(y)$ as a Fourier series allows a relationship between the Fourier coefficients of $S(y)$ and its inverse Abel transform to be derived [103]. Assuming $S(y)$ is continuous, symmetric around zero, and has zero values outside the boundaries, the cosine expansion of $S(y)$ is

$$S(y) = \sum_{k=0}^{k=+\infty} a_k \cos(\frac{k\pi y}{R}), \tag{9.9}$$

with the Fourier coefficients a_k given by

$$a_0 = \frac{1}{R}\int_0^R S(y)dy, \tag{9.10}$$

$$a_k = \frac{2}{R}\int_0^R S(y)\cos(\frac{k\pi y}{R})dy. \tag{9.11}$$

Deriving $S(y)$ in its Fourier expansion form leads to

$$\frac{dS(y)}{dy} = -\sum_{k=1}^{k=+\infty} a_k \frac{k\pi}{R}\sin(\frac{k\pi y}{R}). \tag{9.12}$$

Substituting into Eq. (9.8), $f(r)$ becomes

$$f(r) = \sum_{k=1}^{k=+\infty} \frac{ka_k}{R}\int_r^R (y^2 - r^2)^{-1/2}\sin(\frac{k\pi y}{R})dy. \tag{9.13}$$

Proceeding to the change of variable [103]

$$t = \frac{(y^2 - r^2)^{1/2}}{R}, \tag{9.14}$$

the inverse Abel transform may be expressed as

$$f(r) = \sum_{k=1}^{k=+\infty} \frac{ka_k}{R}\int_0^{(1-\rho^2)^{1/2}} \sin\{k\pi(t^2+\rho^2)^{1/2})\}(t^2+\rho^2)^{-1/2}dt, \tag{9.15}$$

$$f(r) = \frac{\pi}{2R}\sum_{k=1}^{k=+\infty} ka_k g_k(\rho), \tag{9.16}$$

with

$$g_k(\rho) = \frac{2}{\pi}\int_0^{(1-\rho^2)^{1/2}} \sin\{k\pi(t^2+\rho^2)^{1/2})\}(t^2+\rho^2)^{-1/2}dt. \tag{9.17}$$

In a similar fashion, the forward Abel transform Eq. (9.7) can be calculated by expanding the function f(r) as a Fourier series given by

$$f(r) = \sum_{k=0}^{k=+\infty} b_k \cos(\frac{k\pi r}{R}), \tag{9.18}$$

with b_0 and b_k the Fourier coefficients given by,

$$b_0 = \frac{1}{R}\int_0^R f(r)dr, \tag{9.19}$$

$$b_k = \frac{2}{R}\int_0^R f(r)\cos(\frac{k\pi r}{R})dr. \tag{9.20}$$

Substituting Eq. (9.18) into Eq. (9.7), the forward Abel transform $S(y)$ is expressed as

$$S(y) = 2R \sum_{k=0}^{k=+\infty} b_k h_k(\rho), \tag{9.21}$$

with

$$h_k(\rho) = \int_0^{(1-\rho^2)^{1/2}} \cos\{k\pi(t^2+\rho^2)^{1/2})\}dt. \tag{9.22}$$

9.3.3 Example: Refractive Index Profile Reconstruction

The index profile of optical fibers can be determined using transverse interferometry and computing the inverse Abel transform of the fringe-shift measured in the transverse interferogram. The index profile $\Delta n(r)$ and the fringe-shift $s(y)$ are related by the inverse Abel transform

$$\Delta n(r) = -\frac{\lambda}{\pi d}\int_r^R \frac{ds(y)}{dy}(y^2-r^2)^{-1/2}dy, \tag{9.23}$$

where λ is the wavelength and d is the spacing of the fringe shift. In this section, the Fourier expansion technique outlined in Sec. 9.3.2 is applied to the reconstruction of the index profile from the transverse interferogram.

As an example, a parabolic index profile with a central dip is considered to test the technique. The general formula of the index profile is given by [102]

$$\Delta n(\rho) = \Delta n(1-\rho^2) - \Delta n D(\frac{1}{1+\rho^2/W^2} - \frac{1}{1+1/W^2}), \tag{9.24}$$

where D and W are the parameters governing the depth and the width of the central dip. The normalized fringe-shift of an index profile defined by $D = 0.09$ and $W = 0.05$ is calculated using the forward Abel transform Eq. (9.21) and is plotted in Fig. 9.5(a). The normalized refractive index profile is reconstructed using the inverse Abel transform in Eq. (9.16) with $k = 40$ and is plotted in Fig. 9.5(b). The solid line represents the true index profile and the circles represent the reconstructed index profile using the Fourier technique. The agreement between the two is excellent.

Measurements are not usually free of noise and the Fourier technique must be evaluated including noise in the fringe-shift. The Fourier technique also needs to be compared to the numerical differentiation technique that can be used to compute the inverse Abel

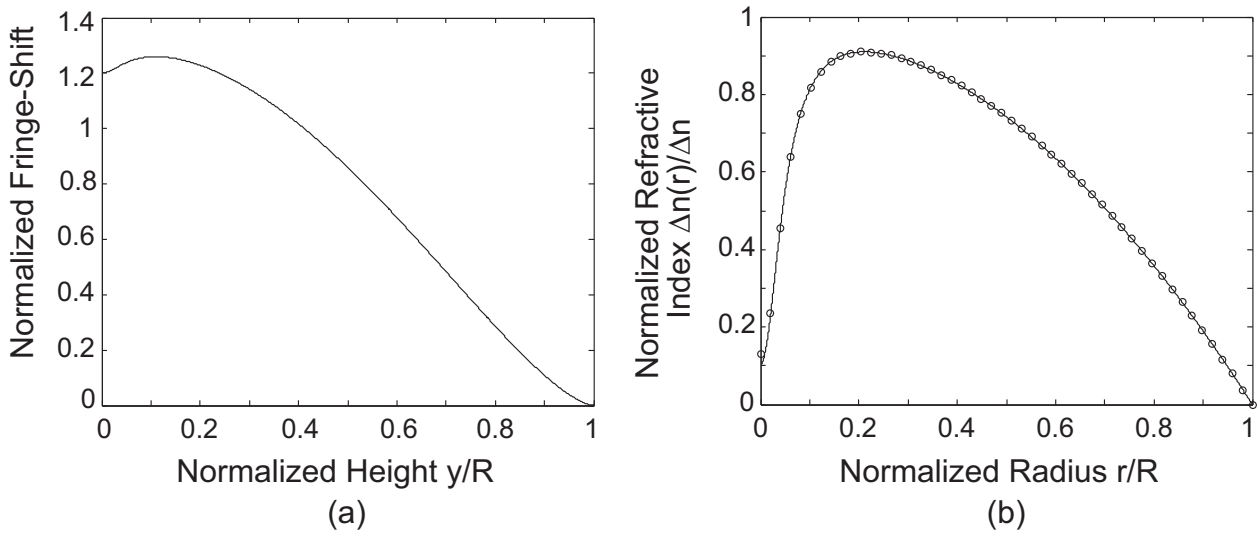

Figure 9.5: Refractive index profile reconstruction using an Abel inversion technique based on Fourier theory. (a) Normalized fringe-shift in the transverse interferogram calculated using the Abel transform. (b) Normalized refractive index profile. The solid line represents the true profile. The circles represent the reconstructed index profile using a Fourier technique.

transform. A comparison between the two techniques applied to noisy measurements is shown in Fig. 9.6. The same refractive index profile is considered. Noise is added to the fringe-shift calculated with the Abel transform (Fig. 9.6(a)). The refractive index profile is reconstructed with the Fourier technique using $k = 20$ and is shown in Fig. 9.6(b). A simple numerical differentiation technique is also used to compute the inverse Abel transform and the corresponding refractive index profile is shown in Fig. 9.6(c). This demonstrates how the Abel inversion computation based on Fourier theory reconstructs the refractive index profile more accurately than the technique based on numerical differentiation. The standard deviation between the true profile and the profile reconstructed using the Fourier technique is 0.004 while that between the true profile and the profile reconstructed using the numerical differentiation technique is 0.02. Further, the Fourier method maintains a very good accuracy and resolution for normalized radii near the axis ($r/R < 0.1$) which is a major disadvantage of the numerical differentiation technique. This will enable the determination of the axial residual stress in the core of the optical fibers. In the remainder of this chapter, the axial residual stress profile in optical fibers and interconnects will therefore be computed by using the inverse Abel transform technique based on Fourier theory.

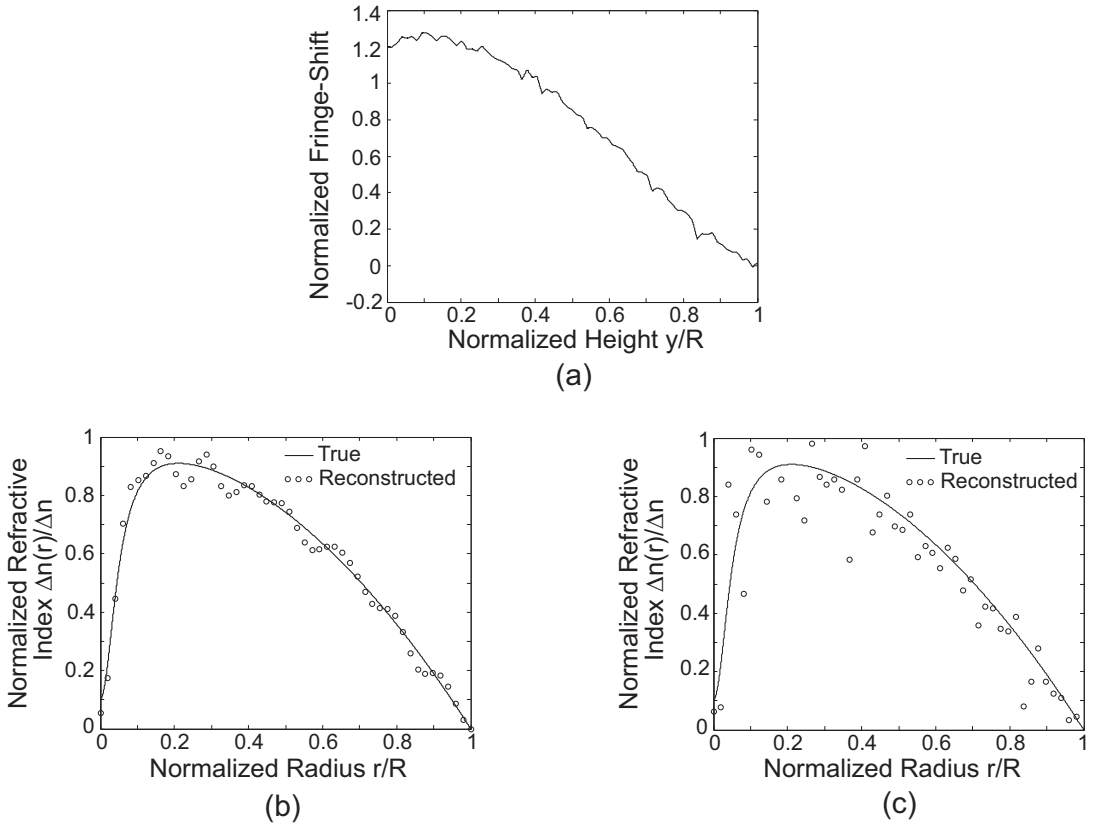

Figure 9.6: Comparison between refractive index profile reconstruction techniques. (a) Normalized fringe-shift measured in the transverse interferogram. Noise is added to the calculated fringe-shift. (b) The refractive index profile is reconstructed using the Abel inversion technique based on Fourier theory. The solid line represents the true profile and the circles represent the reconstructed profile. (c) The refractive index profile is reconstructed using the Abel inversion technique based on numerical differentiation of the fringe-shift. The solid line represents the true profile and the circles represent the reconstructed profile.

9.4 Residual-Stress Measurements

In this section, the full-field retardation measurement techniques are applied to a polymer pillar and a single-mode optical fiber. The retardation projection is then used to compute the axial residual stress profile following the Fourier method outlined previously.

9.4.1 Polymer Pillar

The axial residual stress in the polymer pillar whose two-dimensional retardation is measured and presented in Sec. 8.3 is computed using the inverse Abel transform algorithm presented in Sec. 9.3.2. The two-dimensional retardation is measured with the Brace-Köhler technique using a microscope objective with a magnification of 20× and a numerical aperture of 0.4 corresponding to a spatial resolution of 0.84 μm. The axial stress is plotted in Fig. 9.7. The dashed line represents the axial residual stress computed using the first retardation measurement of the polymer pillar (Fig. 8.14). The corresponding interference image is shown in Fig. 8.16(a). As discussed in Sec. 8.3, a second retardation measurement is done after adding more index matching oil (Fig. 8.15). The solid line in Fig. 9.7 corresponds to the axial residual stress computed using this second measurement. The interference image associated with this measurement is shown in Fig. 8.16(b). The stress-optic coefficient of the polymer material used to fabricate the pillar is not known by Promerus, the polymer manufacturer. Consequently, a value of $C = 1$ is assigned for the stress computation and the axial stress is then normalized to the maximum value of the computed stress. This allows a comparative analysis of the normalized stress between the two measurements as shown in Fig. 9.7.

The effects of the different quantities of the index matching oil between the two measurements were discussed in Sec. 8.3. This is confirmed by the stress computations. The first measurement is done without sufficient matching oil to immerse entirely the pillar which results in more stress as seen in Fig. 9.7. The maximum normalized stress decreases from 1 MPa in the first measurement to about 0.4 MPa in the second measurement near the pillar axis for $-10\ \mu m < r < 0\ \mu m$. It decreases from 0.9 MPa in the first measurement to about 0.3 MPa in the second measurement near the pillar axis for $0\ \mu m < r < 10\ \mu m$.

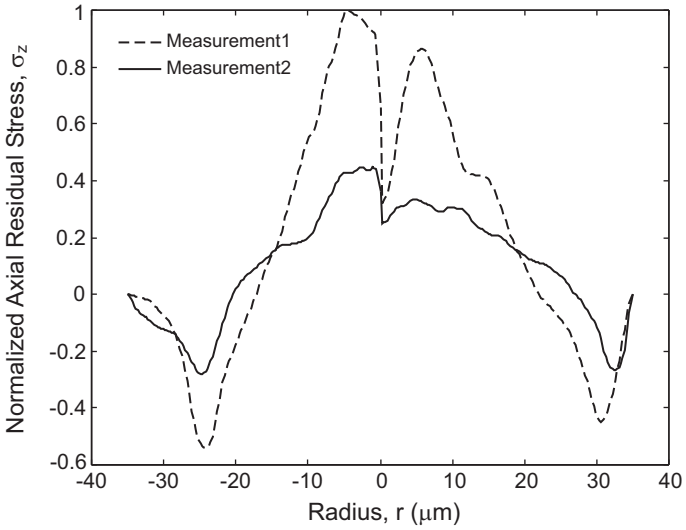

Figure 9.7: Measurement of the axial residual stress in a polymer pillar interconnect. The dashed line corresponds to the axial stress computed using the retardation measurements shown in Fig. 8.14. The solid line corresponds to the axial stress computed using the retardation measurements shown in Fig. 8.15.

Similarly, the maximum stress decreases in magnitude near the edges of the pillar from 0.5 MPa to 0.3 MPa.

The axial residual stress is also computed at various positions along the axis of the pillar. For these computations, the retardation measurements of the pillar almost entirely immersed in the index matching oil are considered (Figs. 8.15 and 8.16(b)). In this case, the stress effect of the index matching oil is minimal and only the residual-stress arising from the pillar fabrication is measured. The normalized residual stress is represented at three different axial positions in Figs. 9.8(a), 9.8(b), and 9.8(c). The distance w is measured from the left side of the field-of-view in Fig. 8.15 which corresponds to w = 0 μm. The stress profiles at w = 150 μm and w = 180 μm are almost identical. The maximum normalized residual stress near the pillar axis decreases slightly from 1 MPa to 0.9 MPa in Figs. 9.8(a) and 9.8(b). The stress profile at w = 235 μm corresponds to a cross-section very near the tip of the pillar. The maximum residual-stress near the axis at $-10\mu m < r < 0$ μm decreases significantly in Fig. 9.8(c) to 0.4 MPa. The residual-stress near the edges remains unchanged.

These axial stress variations can be better understood by considering the fabrication

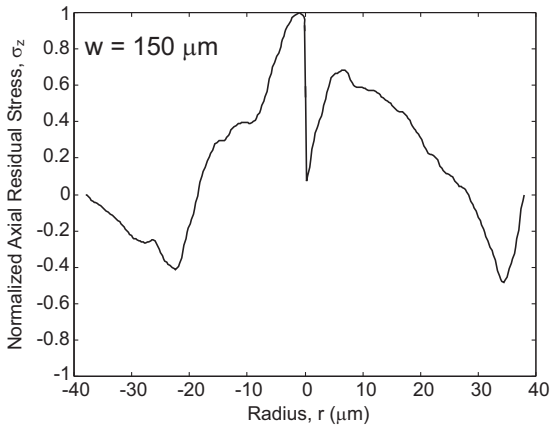

(a)

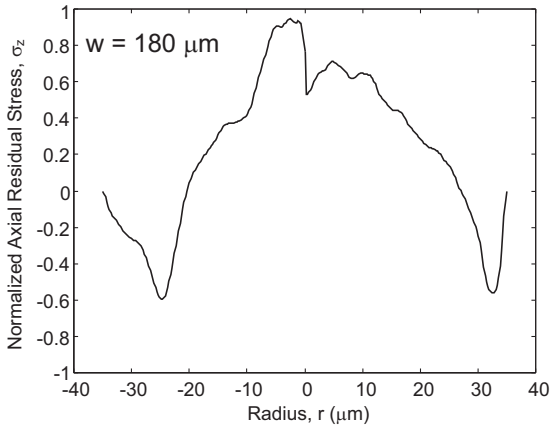

(b)

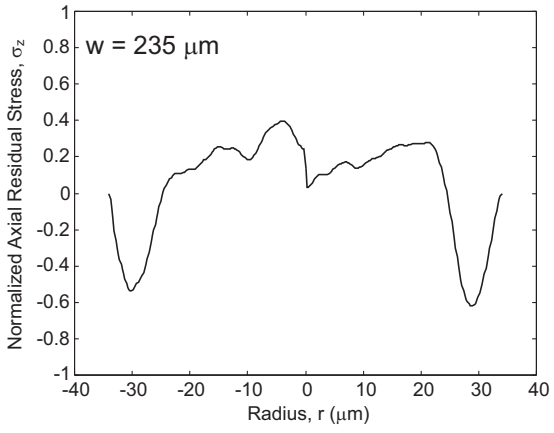

(c)

Figure 9.8: Measurement of the normalized axial residual stress along the axis of a polymer pillar. The residual stress profiles are computed using the two-dimensional retardation measurement of the polymer pillar shown in Fig. 8.15. The distance between the measured stress profile at a specific cross-section of the polymer pillar and the left side of the field-of-view is defined as w. (a) w = 150 μm. (b) w = 180 μm. (c) w = 235 μm.

process of the polymer pillars. Depending on the designed heights of the polymer pillars, several layers of polymer film are alternatively spun and soft-baked on the substrate [80–82]. The pillars are then fabricated by UV-exposure. The pillar height used in these experiments is 170 μm. It is fabricated by spinning three consecutive layers of polymer films. Each layer is first soft-baked and becomes solid before spinning the next layer. This causes a mismatch in visco-elastic properties between an already soft-baked layer and the newly applied liquid polymer film. Residual stress arises because of the thermal coefficient mismatch between the Si substrate and the polymer film, but also because of the visco-elastic mismatch between each polymer layer. The residual stress decreases in the third layer near the tip of the pillar since no extra cover layer is added. Consequently, the stress in the center of the pillar is relatively high for w = 150 and w = 180 μm as these axial positions are located in the second layer while the axial stress near the axis decreases for w = 235 μm as this axial position is located in the third layer close to the end of the pillar. The asymmetry in the stress profiles is produced by making the retardation measurements using the Brace-Köhler technique. It introduces a slowly varying retardation in the background which ultimately affects the residual stress computation. This will be discussed in more detail in the next section.

9.4.2 Single-Mode Fiber

The two-dimensional retardation of a single-mode optical fiber Corning SMF-28 is measured with the Brace-Köhler and TWC techniques using a microscope objective with a magnification of 40× and a numerical aperture of 0.75 corresponding to a spatial resolution of 0.45μm. A bare single-mode optical fiber is placed on a fused silica microscope slide and immersed in index matching oil. The retardation along a cross-section of the optical fiber is used to compute the axial residual-stress profile applying the inverse Abel transform algorithm introduced previously. The axial residual stress profiles computed using the TWC and the Brace-Köhler retardation measurements are shown in Figs. 9.9(a) and 9.9(b) respectively. The residual stress profile is also computed at another location along the axis of the optical fiber to verify the repeatability of the measurements. This is shown in Fig. 9.10.

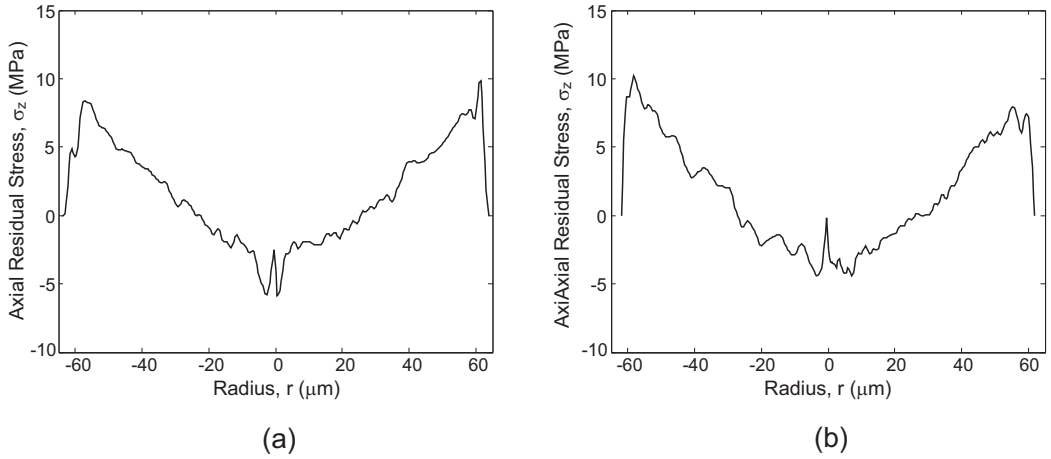

Figure 9.9: Measurement of the axial residual stress in a single-mode optical fiber Corning SMF-28. (a) The retardation is measured with the TWC technique. (b) The retardation is measured with the Brace-Köhler technique.

The stress-optic coefficient of fused silica $C = 35 \times 10^{-4}\ nm/\mu m/MPa$ is used for the stress computation. This stress-optic coefficient is known for the wavelength of 633 nm while the retardation measurements are done at 546 nm in these experiments. Consequently, the measured retardation is adjusted to obtain the corresponding retardation at 633 nm. This ensures an accurate computation of the residual-stress.

The positive values of stress correspond to tension and the negative values of stress correspond to compression. The axial residual stress profiles in Figs. 9.9 and 9.10 are in excellent agreement with single-mode fiber measurements previously reported by Raine *et al.* and Park *et al.* in References 89 and 98. These previously reported axial residual stress profiles are shown in Fig. 9.11. The TWC measurements resolve very well the details of the axial stress near the fiber axis. In particular, the sharp decrease in compressive stress in the center of the optical fiber is clearly visible in both measurements represented in Figs. 9.9(a) and 9.10(a).

The Brace-Köhler measurements are also in good agreement with previously reported measurements [89,98] but introduce asymmetry in the stress profile especially near the fiber axis as seen in Figs. 9.9(b) and 9.10(b). The axial stress computed for positive radii is also lower in magnitude than that computed for negative radii. This can be explained by a drawback arising with the Brace-Köhler technique. In all the two-dimensional retardation

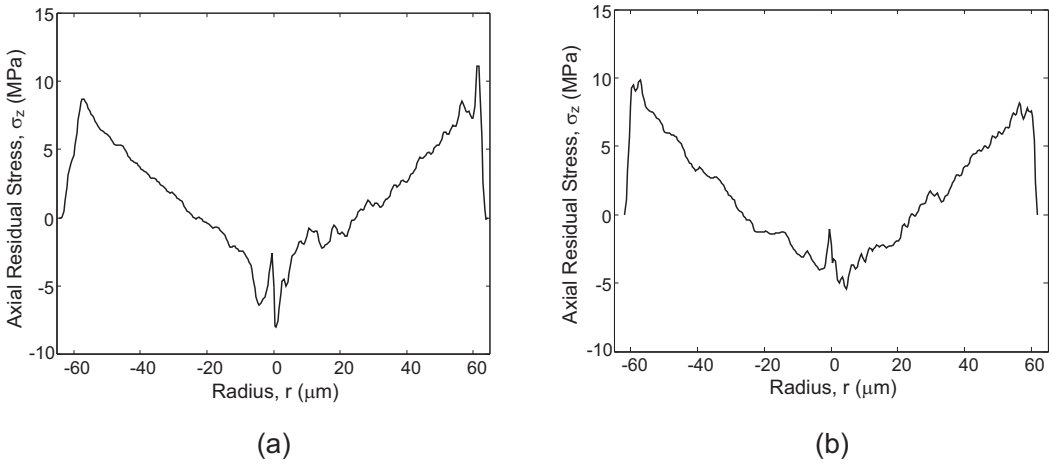

Figure 9.10: Measurement of the axial residual-stress in a single-mode optical fiber Corning SMF-28. The axial residual stress is calculated in a cross-section 10 μm away from that in Fig. 9.9. (a) The retardation is measured with the TWC technique. (b) The retardation is measured with the Brace-Köhler technique.

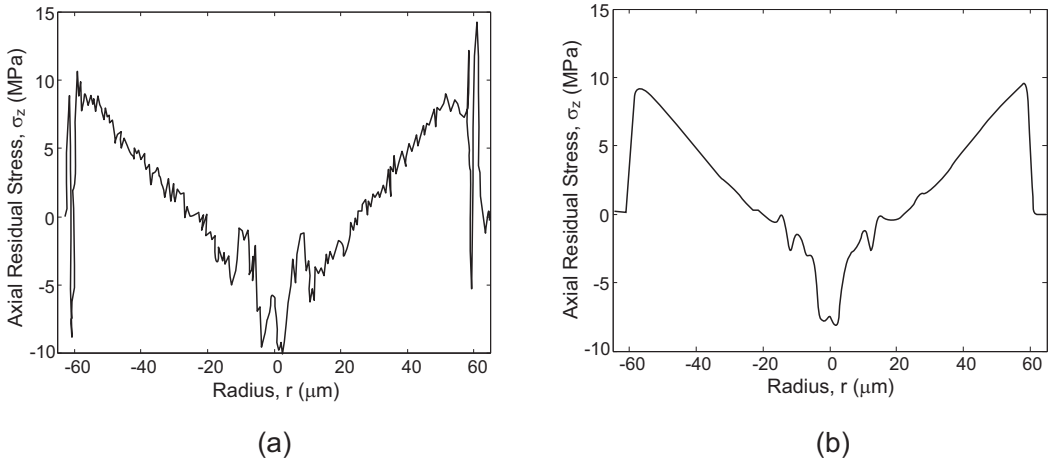

Figure 9.11: Measurement of the axial residual stress in a single-mode optical fiber Corning SMF-28. (a) Axial residual stress measured in Reference 89. (b) Axial residual stress measured in Reference 98.

measurements done with the Brace-Köhler technique, the background retardation is not constant. In fact, it slowly decreases from the bottom to the top of the field-of-view. The measured background retardation should ideally be constant and low since microscope slides and cover slips with low built-in stress are used in all these experiments. Searching for intensity minima rather than nulls makes the Brace-Köhler technique more sensitive to any non-uniformity in the illumination of the optical system which causes the slowly varying retardation of the background. This affects the retardation measurements of the single-mode fiber even more so when using a high-magnification objective because the fiber image fills most of the field-of-view. This in turn affects the residual stress computation as can be seen in Figs. 9.9(b) and 9.10(b). On the other hand, the background retardation measured with the TWC compensator is constant and allows for a more accurate computation of the axial residual stress profile at high-magnification. For smaller magnifications, in which case the sample image covers a smaller proportion of the field-of-view, the asymmetric effects in the Brace-Köhler technique can be considered negligible.

9.4.3 Long-Period Fiber Grating

The two-dimensional retardation measurements can be used to assess the effects of the CO_2 laser irradiations during the fabrication of Long-Period Fiber Gratings (LPFGs). It is first applied here to the case of the undermodulated LPFG whose retardation is measured with the TWC technique in Sec. 8.2.1. The residual stress is computed at various cross-sections along the optical fiber axis. As with the polymer pillars, the cross-sections locations are defined using the distance w between the left side of the field-of-view and the cross-section. The two-dimensional retardation of the perturbed region of the grating measured with the TWC is shown in Fig. 8.9(a). The residual stress is computed at cross-sections located in the unperturbed and perturbed regions of the LPFG. The residual stress profiles for w equal to 361.5, 349.9, 338.4, 325, 270 and 210 μm are represented in Figs. 9.12(a), 9.12(b), 9.12(c), 9.12(d), 9.12(e), and 9.12(f). The spatial resolution of the residual stress computations along the axis of the fiber is 0.84 μm corresponding to the resolution of the objective used to measure the retardation which had a magnification of 20× and a numerical aperture of

0.4. The LPFGs are fabricated by exposing periodically a single-mode fiber Corning SMF-28 to CO_2 laser irradiations. The two-dimensional retardation measurements allow the direct observation of the effects of the exposure on the stress profiles during the fabrication of LPFGs. The residual stress profile in the unperturbed region of the LPFG at w = 361.5 μm plotted in Fig. 9.12(a) is similar to that of a single-mode fiber shown in Figs. 9.9 and 9.10. The axial stress profile of the unperturbed single-mode fiber is represented as a dashed line in Fig. 9.12(a). There are differences, however, due to the fact that the residual stress of the unperturbed region in the LPFG is computed close to the exposed region and thus stress relaxations also occured near the region exposed. The stress profile of the unexposed single-mode fiber is nonetheless clearly recognizable.

The stress relaxations are of larger magnitudes in the exposed region of the LPFG as shown in Figs. 9.12(d), 9.12(e), and 9.12(f). The axial residual stress at the transition between the exposed and unexposed regions is represented in Figs. 9.12(b) and 9.12(c). The stress in the cladding is similar to that in the unexposed region. On the other hand, the residual stress in the core region varies from a compressive stress of $-10\ MPa$ at the center in the unexposed case to a tensile stress of 15 MPa in the exposed case (Fig. 9.12(d)). The tensile stress in the core increases in the center of the fiber towards the center of the exposed region as shown in Figs. 9.12(e) and 9.12(f). It reaches its maximum of 25 MPa at the center for w = 210 μm. The tensile stress in the cladding of the exposed region decreases to 3 MPa. These axial stress profiles after exposure to CO_2 laser irradiations are in very good agreement with the residual profiles previously reported by Kim *et al.* in References 28 and 29. This previously reported residual stress profile is represented in Fig. 9.13. The stress in the center of the core is 28 MPa and the stress in the cladding is 2 MPa.

The residual stress in the unexposed optical fibers is the superposition of the thermal stress and the mechanical stress. The thermal stress originates from the thermal expansion coefficient mismatch between the core and the cladding. It causes tension in the core due to an increase of the thermal expansion coefficient in the core that contains more dopants. However, this higher concentration of dopants results in a decrease of viscosity causing mechanical stress. For fibers drawn with high pulling tensions, the mechanical stress

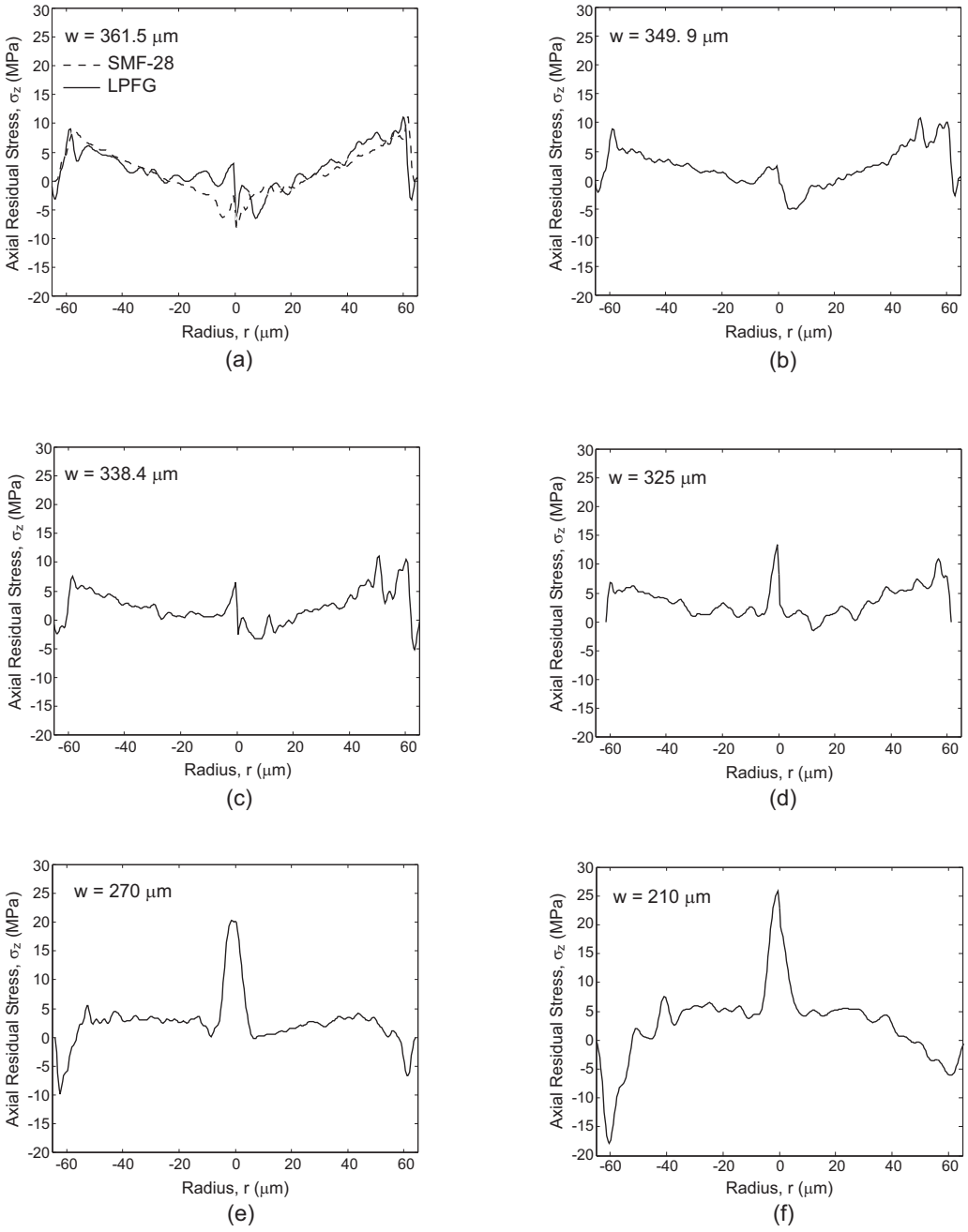

Figure 9.12: Measurement of the axial residual stress in the perturbed region of an undermodulated LPFG. The residual stress profiles are computed using the TWC two-dimensional retardation measurement shown in Fig. 8.9. (a) w = 361.5 μm. (b) w = 349.9 μm. (c) w = 338.4 μm. (d) w = 325 μm. (e) w = 270 μm. (f) w = 210 μm.

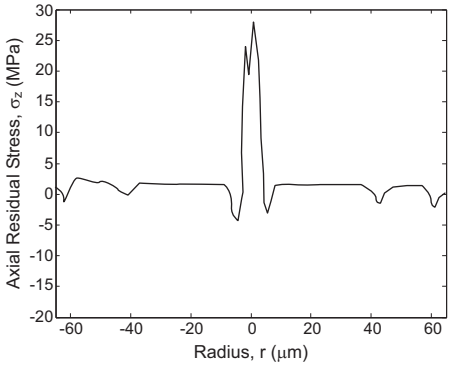

Figure 9.13: Measurement of the axial residual stress in a fiber exposed to CO_2 laser [29].

generates thus compression and its effect is more significant than the thermal stress. The core of the unperturbed fiber is therefore under a compression of $-5\ MPa$ (Fig. 9.9). The mechanical stress is relaxed after exposure to the CO_2 and only the thermal tensile stress remains in the core of the fiber [28, 29]. The core of the perturbed region of the LPFG is under a tension of 25 MPa (Fig. 9.12(f)).

The residual stress profiles in the perturbed region of an overmodulated LPFG are also computed using the TWC two-dimensional retardation measurement presented in Sec. 8.2.1 in Fig. 8.9. Stress profiles are calculated at different cross-sections located at w equal to 350, 300, 200, 165, 130, and 100 μm in Fig. 9.14. The stress profiles in Figs. 9.14(b), 9.14(c), and 9.14(d) are calculated within the perturbed region of the LPFG. They are very similar to the stress profiles computed in the perturbed region of the undermodulated LPFG. Tensile stresses are observed in the core of the exposed fiber with a maximum stress of 20 MPa in the center of the core for w = 165 μm and 10 MPa for w = 200 and w = 300 μm. The tensile stresses decrease in the cladding to 3 MPa as was also the case with the undermodulated LPFG. The variations of the stress profiles as a function of the axial position in the perturbed region of the overmodulated LPFG are larger than those within the perturbed region of the undermodulated LPFG. The stress profiles in the unperturbed region of the LPFG are shown in Figs. 9.14(a) and 9.14(f). The latter appears like a distorted axial stress profile of a single-mode fiber while the former is very similar to the stress profile of a single-mode fiber. The axial residual stress profile a an unexposed single-fiber is represented as a dashed line in Fig. 9.14(a). The transition between unperturbed

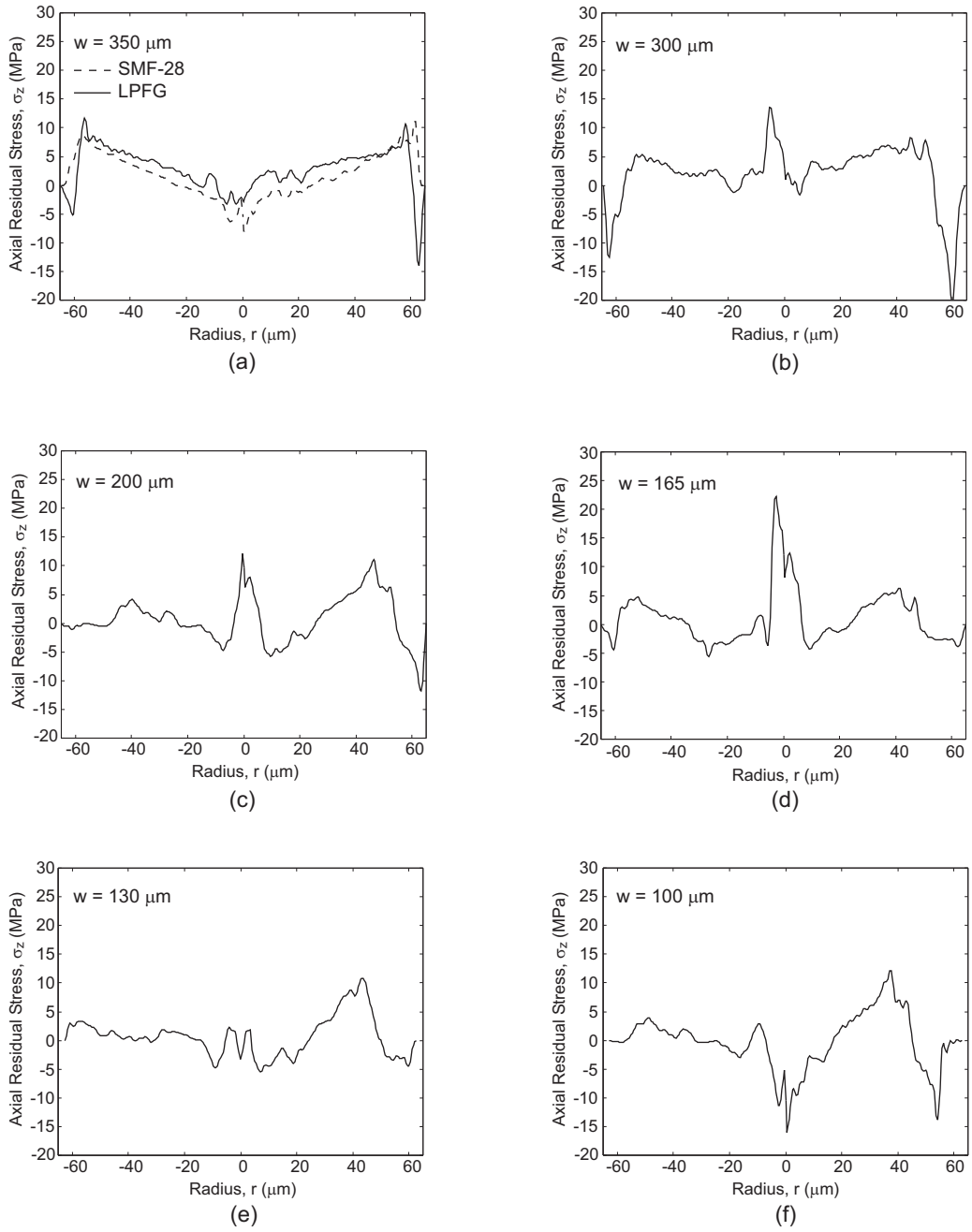

Figure 9.14: Measurement of the axial residual stress in the perturbed region of an over-modulated LPFG. The residual stress profiles are computed using the TWC two-dimensional retardation measurement shown in Fig. 8.9.(a) w = 350 μm. (b) w = 300 μm. (c) w = 200 μm. (d) w = 165 μm. (e) w = 130 μm. (f) w = 100 μm.

and perturbed regions can be seen in Fig. 9.14(e) for w = 130 μm. The stress in the cladding is similar to that in Fig. 9.14(f) while the stress in the center of the fiber becomes tensile with values ranging from 0 to 5 MPa. The stress in the center of the fiber is 0 MPa. As the stress is computed further in the perturbed region the tensile stress in the cladding decreases and the tensile stress in the center of the fiber increases as shown in Figs. 9.14(b), 9.14(c), and 9.14(d).

This consistency between the residual stress profiles computed in the perturbed region of the overmodulated LPFG and the perturbed region of the undermodulated LPFG suggests that the inverse Abel transform can also be applied to the overmodulated LPFG even though the retardation distribution exhibits less axial symmetry. This demonstrates the ability of the TWC two-dimensional retardation measurements and the inverse Abel transform algorithm in assessing the stress relaxations phenomena arising during the fabrication of LPFGs. This is essential to control and monitor the fabrication and performances of LPFGs.

9.5 Summary of Results

The sensitivity of the two-dimensional retardation measurements was shown to be better when using the automatic gain control of the camera. A Wiener filter approach was proposed to eliminate the noise in the measurements. An algorithm based on Fourier theory was presented to compute the inverse Abel transform relating the retardation to the axial residual stress profile.

The two-dimensional retardation measurements were applied to a polymer pillar and a single-mode optical fiber Corning SMF-28. Spatial resolutions of 0.84 μm and 0.45 μm were achieved using microscope objectives with numerical apertures of 0.4 and 0.75 respectively. The axial residual stress profiles of a single-mode fiber computed using the TWC retardation measurements were in excellent agreement with previously reported stress profiles. The axial profiles obtained from the Brace-Köhler retardation measurements were also in good agreement with previous results. However, the Brace-Köhler technique introduces an asymmetry in the retardation measurement which adversely impacts the stress profile computation. This could be made more accurate by normalizing the background retardation in

the Brace-Köhler two-dimensional retardation measurements.

The two-dimensional retardations measured with the TWC technique on the other hand exhibit a constant retardation in the background thereby making the measured retardation of the sample more accurate. This in turn results in a better stress profile reconstruction. This demonstrates the higher sensitivity and higher accuracy of this method to quantify stress-induced birefringence in optical devices.

The stress profiles computed using the two-dimensional TWC retardation measurements of LPFGs showed great consistency between an undermodulated LPFG and an overmodulated LPFG. The inverse Abel transform can therefore be applied to retardations measurements exhibiting less axial symmetry as is the case with the overmodulated LPFG. The TWC measurements along with the residual stress computation procedure presented in this research can thus be used to characterize devices such as the overmodulated LPFG which are not perfectly axially symmetric. Very good agreements were achieved with previously reported stress profiles of fibers exposed to CO_2 laser irradiations [28, 29].

CHAPTER 10

CONCLUSIONS

10.1 Summary of Results

The various retardation measurement techniques developed in this thesis represent major contributions to the birefringence and stress characterization of optical devices. These techniques are essential tools to evaluate and to understand the stress-induced birefringence effects on a device's performance and thus can be used to assess its status and usefulness during and after fabrication. This chapter summarizes the main contributions of the thesis and presents directions for future research.

10.1.1 Two-Waveplate Compensator

The Two-Waveplate-Compensator (TWC) has been developed to measure the retardation of a sample. It is based on rotating a compensator waveplate to produce a linearly polarized output when the sample is oriented at 45 deg from extinction between crossed polarizers. A null of intensity is measured by rotating the analyzer perpendicular to the polarization direction. A detailed analysis based on Jones calculus of the method has been presented. The relationship between the sample's retardation and the compensator's angle and retardation in order to produce a linearly polarized output has been derived using no approximations. The detection of a null of intensity makes the method more accurate than other techniques based on detecting a minimum of intensity or measuring the intensity of the light.

The TWC's accuracy for single-point retardation measurement has been compared theoretically and experimentally to the accuracies of the Sénarmont and the Brace-Köhler techniques. The TWC achieves the best accuracy for retardations from 1.09 nm to 60.33 nm with measurement errors of 0.19 nm to 0.64 nm respectively. The resolution of the TWC technique for single-point retardation measurement is 0.02 nm. The contributions of the TWC technique are summarized in a journal article [104]. The Automated-Two-Waveplate

Compensator (ATWC) has also been presented for full-field measurement of the retardation slow axis orientation and the retardation magnitude. The TWC and the ATWC have lead to two US patent applications [105, 106].

10.1.2 Phase-Stepping Two-Waveplate Retarder

The Phase-Stepping Two-Waveplate Retarder (PSTWR) was developed for high-accuracy measurement of the retardation slow axis orientation and the retardation magnitude. It is based on measuring the intensity transmitted by an optical system composed of a birefringent sample and a compensator waveplate placed between crossed polarizers. The transmitted intensities measured for various compensator angles are used to solve a system of equations whose solutions are related to the sample's slow axis orientation and retardation. Transmittance equations can be solved by measuring two transmitted intensities for two compensator angles (2-step PSTWR) or by measuring three transmitted intensities for three compensator angles (3-step PSTWR).

High-accuracy can be achieved with the N-step PSTWR consisting of measuring the transmitted intensities for N various compensator angles to solve the system of three intensity equations. The system of equations obtained is then overspecified and the solutions can be found using a Moore-Penrose inverse formulation and regularization methods [92]. This allows the retrieval of the sample's slow axis angle and retardation with high accuracy. The PSTWR has lead to one US patent application [107].

10.1.3 Colorimetry-Based Retardation Measurements

The Colorimetry-Based Retardation Measurements (CBRM) method was developed for single-point retardation measurements using white-light interference. A polarization microscope and a spectrophotometer were used to calibrate the retardations with the white-light interference colors which they produce. The retardation of a sample can then be determined immediately by measuring the sample's color and by reference to the calibration truth-table. The resolution of the CBRM is equal to 0.2 nm. The technique was tested on waveplates of known retardations and produced measurement errors of 0.53% and 0.39% for retardations of 161 nm and 533 nm respectively. The characteristics and performances of the CBRM

technique are summarized in a journal article [108].

10.1.4 Full-Field Retardation Measurements

The Brace-Köhler and the TWC techniques were implemented for full-field retardation measurements using a polarization microscope illuminated with a mercury arc lamp. Experimental and image processing procedures were presented to evaluate the retardation at every point of the sample. The two techniques were first tested with a waveplate of retardation of 21.54 nm and produced measurement errors of less than 0.4 nm over most of the field-of-view.

The Brace-Köhler and the TWC techniques were applied to the two-dimensional retardation measurements of transversely illuminated optical fibers and other interconnects. A comparison between the measured intensities of the interference images and the transmittances calculated with the retardation measurements showed very good agreement between the measured and the calculated transmittances, thus reinforcing the accuracy and sensitivity of the techniques. The Brace-Köhler and the TWC techniques have the advantage, however, to eliminate the birefringence present in the optical components of the microscopes by subtracting the angles measured with and without the sample. This instrumentation compensation renders these techniques superior to methods involving the calibration of intensities in the interference images with their corresponding retardations.

10.1.5 Characterization of Optical Devices

For the first time, full-field retardation measurements were used for the characterization of polymer pillar interconnects and Long-Period Fiber Gratings (LPFGs). The Brace-Köhler technique was applied to the two-dimensional retardation measurements of a transversely illuminated polymer pillar interconnect. The TWC technique was applied to the two-dimensional retardation measurements of the perturbed regions of LPFGs fabricated using CO_2 laser irradiation. A spatial resolution of 0.84 μm was achieved using a microscope objective with a magnification of 20$\times$ and a numerical aperture of 0.4. The retardation changes during the fabrication of an overmodulated LPFG are larger in magnitude and cover a longer region along the axis of the fiber than the changes in an undermodulated

LPFG. The Brace-Köhler and the TWC two-dimensional retardation measurements can therefore be used to monitor the fabrication of optical devices such as optical interconnects and LPFGs.

The Brace-Köhler and TWC techniques' resolutions are respectively 0.1 nm and 0.09 nm using a microscope objective with a magnification of 20× and a numerical aperture of 0.4. These resolutions improve to 0.09 nm for the Brace-Köhler technique and 0.07 nm for the TWC technique using a microscope objective with a magnification of 40× and a numerical aperture of 0.75. The TWC is therefore more sensitive to retardation changes.

10.1.6 Residual Stress Evaluation in Optical Devices

The two-dimensional retardation measurements with the Brace-Köhler and TWC techniques were used to compute the residual stress profiles in various optical fibers and optical interconnects. The experimental conditions and the noise filtering procedures were optimized to obtain the most accurate retardation measurements. An algorithm to compute the inverse Abel transform relating the retardation to the axial residual stress profile based on Fourier theory was implemented.

The stress profile retrieval of a single-mode optical fiber Corning SMF-28 obtained from the TWC and Brace-Köhler measurements showed very good agreement with previously reported results. An axial spatial resolution of 0.45 μm was achieved using a microscope objective with a magnification of 40× and a numerical of aperture 0.75. The stress profiles computed from the TWC measurements exhibit more axial symmetry than the profiles computed from the Brace-Köhler measurements demonstrating the superiority of the TWC technique.

The axial residual stress profile along the axis of a polymer pillar was computed for the first time to our knowledge. Also, the axial residual stress profiles in the unperturbed and perturbed regions of undermodulated and overmodulated LPFGs were computed at various axial positions along the fibers using the TWC retardation measurements. The resulting stress profiles showed very good agreement with previously reported profiles of optical fibers exposed to CO_2 laser irradiation. The stress profiles computed in the overmodulated LPFG

which possesses less axial symmetry than the undermodulated LPFG demonstrates that the inverse Abel transform can be applied to samples exhibiting a considerable degree of azimuthal variations.

10.2 Future Research

The single-point and full-field retardation measurement techniques developed in this thesis have already demonstrated excellent accuracies and sensitivities in the characterization of form and stress-induced birefringence in optical devices. Considering the novelty of the TWC, the ATWC, the PSTWR, and the CBRM methods, these preliminary results offer just an initial assessment of the far-reaching potential of these methods in quantifying and imaging birefringence. Further research is needed to expand the capabilities of these new techniques.

10.2.1 Full-Field Retardation Measurements

The detection of the intensity extinctions in the TWC technique is critical to measure the retardation at every point of the field-of-view. The measurement noise needs to be further reduced to enhance its accuracy and its sensitivity. The effects such as the polarization of the illuminating light, the extinction ratio of the polarizers, the sensitivity of the CCD camera, the angular resolution of the rotating compensator and analyzer, the numerical aperture of the objective must be investigated in order to optimize the experimental configuration. The rotation of the optical elements and the recording of the images must also be automated to increase the speed of the measurements.

The TWC technique proves very efficient for measuring the retardation magnitude with the sample oriented at 45 *deg* from extinction. This assumes that the retardation slow or fast axis direction is known. This is straightforwardly accomodated with optical devices such as optical fibers and polymer pillars since the birefringence axis is parallel to the axis of the cylindrical waveguides. The TWC must be expanded for arbitrarily oriented birefringent samples. Conditions for intensity minima must be understood. The relationships between these intensity minima, the slow axis orientation and the retardation magnitude must be derived.

The CBRM has also been proven accurate and efficient for single-point retardation measurements. It has the significant advantage that after calibration of the optical system, the retardation of a sample can be evaluated immediately by measuring its white-light interference color. However, the field-of-view of the spectrophotometer covers a large area of the image. This makes it difficult to take advantage of the high spatial resolutions available with microscopic imaging. Further research is needed to expand the CBRM for microscopic two-dimensional retardation imaging by measuring the color/retardation of each pixel.

The CBRM also requires white-light interference colors to be produced. This renders the method not easily applicable for small retardations which produce very dim transmitted light. However, the use of a bias retardations added to the sample's retardation can overcome this issue by increasing the value of the total retardation and generating a measurable white-light interference color. Further investigation is therefore needed in this domain to apply the CBRM technique to optical devices.

10.2.2 Optical Devices Characterization

The residual stress computation from the TWC measurements has proven very accurate in retrieving the axial residual stress profile in single-mode fibers and LPFGs. Further, a correlation was found between the transmission properties of undermodulated and overmodulated LPFGs and the retardation changes occuring during their fabrications. More measurements are needed to understand the variations of the retardations and the axial stress for various azimuthal angles around the fiber axis. The effects of the CO_2 laser on the exposed side of the fiber and on the unexposed side of the fiber could then be quantified. The radial and the azimuthal stresses can also be calculated from the axial stress computations.

Further, the two-dimensional retardation measurements and the axial stress computations must be applied systematically to LPFGs and polymer pillars for various fabrication conditions to understand the stress-induced birefringence effects on the devices performances. Quantifying the minimum levels of stress-induced birefringence allowed for these devices to perform as needed constitutes a major challenge and a necessary step to assess

their usability during and after the manufacturing process. Two-dimensional retardation techniques can therefore be used as diagnostic tools in the manufacturing of optical devices.

10.2.3 Birefringence Imaging of Biological Cells

The retardation measurements in this thesis concentrated on the characterization of optical devices. Polarization microscopy, however, had already been for some time of great interest to the biologist for imaging biological cells, which typically exhibit weak birefringence. From as early as 1950, Swann *et al.* had identified the refinements necessary in polarization microscopy to enhance the biological cells interference images [36]. Later publications have followed increasing the contrast and the resolution of polarization microscopy to within the scope of biological imaging. [37, 52].

Recently, birefringence measurements have emerged as a powerful non-invasive tool for the observation and diagnosis of living tissues. Birefringence measurement techniques based on polarization microscopy and optical coherence tomography have been presented for the dynamic observation of developing neurites [8, 9, 38, 53], for the visualization of cytoskeletal dynamics in living cells [109], and the characterization of the human retinal nerve fiber layer in order to detect glaucoma at an early stage [10, 110]. Birefringence imaging techniques do not necessitate any prior injection of the cells with chemical dyes as is the case with fluorescence microscopy. This chemical treatment eventually damages or kills the cell. Similarly, inserting electrodes also damages or kills the cell. Non-invasive polarization observation techniques thus have a crucial role to play in the characterization and diagnosis of biological samples.

The retardation measurement techniques presented in this thesis deal extensively with the accurate measurement and imaging of weak birefringence in optical devices. Considering the recent developments in using the weak birefringence present in biological cells as a mean towards imaging them, efforts must also be pursued to investigate the applicability of the TWC, ATWC, PSTWR, and CBRM retardation measurement techniques for the observation of living cells.

REFERENCES

[1] R. Wehner and S. Rossel, "The bee's celestial compass - a case study in behavioural neurobiology," in *Experimental Behavioral Ecology and Sociobiology* (B. Holldobler and M. Lindauer, eds.), 1985.

[2] H. J. Frier, E. Edwards, C. Smith, S. Neale, and T. Collet, "Magnetic compass cues and visual pattern learning in honeybees," *J. Exp. Biol.*, vol. 199, pp. 1353–1361, 1996.

[3] G. Smith, *An Introduction to Classical Electromagnetic Radiation*. New York: Cambridge University Press, 1997.

[4] K. Kitamura, S. Kimura, Y. Miyazawa, Y. Mori, and O. Kamada, "Stress-birefringence associated with facets of rare-earth garnets grown from the melt; a model and measurement of stress-birefringence observed in thin sections," *J. Crys. Growth*, vol. 62, pp. 351–359, 1983.

[5] K. Kitamura, Y. Miyazawa, Y. Mori, S. Kimura, and M. Higuchi, "Origin of difference in lattice spacings between on- and off-facet regions of rare-earth garnets grown from the melt," *J. Crys. Growth*, vol. 64, pp. 207–216, 1983.

[6] K. Kitamura, N. Lyi, and S. Kimura, "Growth-induced optical anisotropy of epitaxial garnet films grown on (110)-oriented substrates," *J. Appl. Phys.*, vol. 60, pp. 1486–1489, Aug. 1986.

[7] J. M. Desse, "Three-color differential interferometry," *Appl. Opt.*, vol. 36, pp. 7150–7156, Oct. 1, 1997.

[8] K. Katoh, K. Hammar, P. Smith, and R. Oldenbourg, "Birefringence imaging directly reveals architectural dynamics of filamentous actin in living growth cones," *Mol. Biol. Cell*, vol. 10, pp. 197–210, 1999.

[9] R. Oldenbourg, E. D. Salmon, and P. T. Tran, "Birefringence of single and bundled microtubules," *Biophys. J.*, vol. 74, pp. 645–654, 1998.

[10] B. Cense and T. C. Chen, "*In vivo* depth-resolved birefringence measurements of the human retinal nerve fiber layer by polarization-sensitive optical coherence tomography," *Opt. Lett.*, vol. 27, pp. 1610–1612, Sept. 15, 2002.

[11] I. Bloomer and R. Mirsky, "Broadband spectrophotometry: a fast, simple, accurate tool," *Phot. Spec.*, pp. 86–92, May 2002.

[12] A. Redner, "Photoelastic measurements by means of computer-assisted spectral-contents analysis," *Exp. Mech.*, vol. 25, no. 2, pp. 148–153, 1985.

[13] A. Redner, "Photoelastic measurements of residual stresses for NDE," in *Photomechanics and Speckle Metrology* (F.-P. Chiang, ed.), vol. 814 of *Proc. SPIE*, pp. 16–19, Aug. 1987.

[14] J. E. Houston, "The effect of stress on the nanomechanical properties of au surfaces," in *Structure and Evolution of Surfaces* (R. Cammarata, ed.), vol. 440 of *Proc. Mat. Res. Soc.*, pp. 177–187, 1997.

[15] E. D. Fabrizio, M. Baciocchi, M. Gentili, and L. Grella, "Microphotonic devices fabricated by silicon micromachining techniques," *J. Appl. Phys.*, vol. 36, pp. 7757–7762, Dec. 1997.

[16] P. L. Chu and T. Whitbread, "Measurement of stresses in optical fiber and preform," *Appl. Opt.*, vol. 21, pp. 4241–4245, Dec. 1, 1982.

[17] X. Zhao, C. Li, and Y. Z. Xu, "Stress-induced birefringence control in optical planar wave-guides," *Opt. Lett.*, vol. 28, pp. 564–566, Apr. 1, 2003.

[18] S. Y. Cheng, K. S. Chiang, and H. P. Chan, "Birefringence in benzocyclobutene strip optical wave-guides," *IEEE Phot. Tech. Lett.*, vol. 15, pp. 700–702, May 2003.

[19] D. J. Wissuchek, C. W. Ponader, and J. J. Price, "Analysis of residual stress in optical fiber," in *Optical Fiber Reliability and Testing*, vol. 3848 of *Proc. SPIE*, pp. 34–43, 1999.

[20] G. W. Scherer, "Thermal stress in a cylinder: application to optical wave-guide blanks," *J. Non-Crys. Sol.*, vol. 34, pp. 223–238, 1979.

[21] C. S. Kim, Y. Han, B. H. Lee, W. T. Han, U. C. Paek, and Y. Chung, "Induction of the refractive index change in B-doped optical fibers through relaxation of the mechanical stress," *Opt. Comm.*, vol. 185, pp. 337–342, Nov. 15, 2000.

[22] D. A. Krohn, "Determination of axial stress in clad glass fibers," *J. Amer. Cera. Soc.*, vol. 53, no. 9, pp. 505–507, 1970.

[23] U. C. Paek and C. R. Kurkjian, "Calculation of cooling rate and induced stresses in drawing of optical fibers," *J. Amer. Cera. Soc.*, vol. 58, no. 7-8, pp. 330–335, 1975.

[24] B. H. Kim, Y. Park, D. Y. Kim, U. C. Paek, and W. T. Han, "Observation and analysis of residual stress development resulting from OH impurity in optical fibers," *Opt. Lett.*, vol. 27, pp. 806–808, May 15, 2002.

[25] G. W. Scherer, "Stress-induced index profile distorsion in optical wave-guides," *Appl. Opt.*, vol. 19, pp. 2000–2006, June 1980.

[26] G. W. Scherer, "Stress-optical effects in optical wave-guides," *J. Non-Crys. Sol.*, vol. 38, no. 12, pp. 201–204, 1980.

[27] K. Dossou, S. LaRochelle, and M. Fontaine, "Numerical analysis of the contribution of the transverse asymmetry in the photo-induced index change profile to the birefringence of optical fiber," *J. Lightwave Tech.*, vol. 20, pp. 1463–1469, Aug. 2002.

[28] B. H. Kim, Y. Park, T. J. Ahan, D. Y. Kim, B. H. Lee, Y. Chung, U. C. Paek, and W. T. Han, "Residual stress relaxation in the core of optical fiber by CO_2 laser irradiation," *Opt. Lett.*, vol. 26, pp. 1657–1659, Nov. 1, 2001.

[29] B. H. Kim, T. J. Ahan, D. Y. Kim, B. H. Lee, Y. Chung, U. C. Paek, and W. T. Han, "Effect of CO_2 laser irradiation on the refractive-index change in optical fibers," *Appl. Opt.*, vol. 41, pp. 3809–3815, July 1, 2002.

[30] Y. Park, T. J. Ahn, Y. H. Kim, W. T. Han, U. C. Paek, and D. Y. Kim, "Measurement method for profiling the residual stress and the strain-optic coefficient of an optical fiber," *Appl. Opt.*, vol. 41, pp. 21–26, Jan. 1, 2001.

[31] Y. Park, U. C. Paek, and D. Y. Kim, "Complete determination of the stress tensor of a polarization-maintaining fiber by photoelastic tomography," *Opt. Lett.*, vol. 27, pp. 1217–1219, July 15, 2002.

[32] A. Ajovalasit, S. Baronne, and G. Petrucci, "A review of automated methods for the collection and analysis of photoelastic data," *J. Strain Analysis*, vol. 33, no. 2, pp. 75–91, 1998.

[33] A. Ajovalasit, S. Baronne, and G. Petrucci, "Automated photoelasticity in white light: influences of quarter-wave plates," *J. Strain Analysis*, vol. 30, no. 1, pp. 29–34, 1995.

[34] T. C. Oakberg, "Measurement of low-level strain birefringence in optical elements using a photoelastic modulator," in *Polarization Analysis and Applications to Device*, vol. 2873 of *Proc. SPIE*, pp. 17–20, June 1996.

[35] B. Wang and T. Oakberg, "A new instrument for measuring both magnitude and angle of low level linear birefringence," *Rev. Sci. Instr.*, vol. 70, pp. 3847–3854, Oct. 1999.

[36] M. M. Swann and J. M. Mitchison, "Refinements in polarized light microscopy," *J. Exp. Biol.*, vol. 27, pp. 226–237, 1950.

[37] R. D. Allen and L. I. Rebhun, "Photoelectric measurement of small fluctuating retardations in weakly birefringent, light-scattering biological objects," *Exp. Cell Res.*, vol. 29, pp. 583–592, 1963.

[38] R. Oldenbourg and G. Mei, "New polarized light microscope with precision universal compensator," *J. Micr.*, vol. 180, no. 2, pp. 140–147, 1995.

[39] N. H. Hartshorne and A. Stuart, *Crystals and the Polarizing Microscope, A Handbook for Chemists and Others.* London: Edward Arnold LTD, 1960.

[40] F. D. Bloss, *An Introduction to the Methods of Optical Crystallography.* Philadelphia: Holt, 1961.

[41] Y. Park, U. C. Paek, and D. Y. Kim, "Determination of stress-induced intrinsic birefringence in a single-mode fiber by measurement of the two-dimensional stress profile," *Opt. Lett.*, vol. 27, pp. 1291–1293, Aug. 1, 2002.

[42] A. Ajovalasit, S. Baronne, and G. Petrucci, "A method for reducing the influence of quarter-wave plate errors in phase-stepping photoelasticity," *J. Strain Analysis*, vol. 33, no. 3, pp. 207–216, 1998.

[43] A. S. Voloshin and A. S. Redner, "Automated measurement of birefringence: development and experimental evaluation," *Exp. Mech.*, vol. 29, no. 3, pp. 252–257, 1989.

[44] G. Petrucci, "Full-field automated evaluation of an isoclinic parameter in white light," *Exp. Mech.*, vol. 37, no. 4, pp. 420–426, 1997.

[45] A. Ajovalasit, S. Baronne, and G. Petrucci, "Towards RGB photoelasticity: full-field automated photoelasticity in white light," *Exp. Mech.*, vol. 35, no. 3, pp. 193–200, 1995.

[46] J. A. Quiroga, A. Garcia-Botella, and A. Gomez-Pedrero, "Improved method for isochromatic demodulation by RGB calibration," *Appl. Opt.*, vol. 41, pp. 3461–3468, June 10, 2002.

[47] B. Wang, "An improved method for measuring low-level linear birefringence in optical materials," in *Inorganic Optical Materials*, vol. 3424 of *Proc. SPIE*, pp. 120–124, July 1998.

[48] T. C. Oakberg and A. J. Bryan, "Use of detectors with photoelastic modulators," in *Polarization Measurement Analysis and Applications V* (D. H. Goldstein and D. B. Chenault, eds.), vol. 4819 of *Proc. SPIE*, pp. 1–8, 2002.

[49] B. Wang, "Accuracy assessment of a linear birefringence measurement system using a soleil-babinet compensator," *Rev. Sci. Instr.*, vol. 72, pp. 4066–4070, Nov. 2001.

[50] B. Wang, "Linear birefringence measurement instrument using two photoelastic modulators," *Opt. Eng.*, vol. 41, pp. 981–987, May 2002.

[51] B. Wang, J. List, and R. R. Rockwell, "A Stokes polarimeter using two photoelastic modulators," in *Polarization Measurement Analysis and Applications V* (D. H. Goldstein and D. B. Chenault, eds.), vol. 4819 of *Proc. SPIE*, pp. 1–8, 2002.

[52] E. D. Salmon and G. W. Ellis, "Compensator transducer increases ease, accuracy, and rapidity of measuring changes in specimen birefringence with polarization microscopy," *J. Micr.*, vol. 106, no. 1, pp. 63–69, 1975.

[53] M. Schribak and R. Oldenbourg, "Techniques for fast and sensitive measurements of two-dimensional birefringence distributions," *Appl. Opt.*, vol. 42, pp. 3009–3017, June 1, 2002.

[54] H. Aben and C. Guillemet, *Photoelasticity of Glass*. Berlin: Springer-Verlag, 1993.

[55] H. Scholze, *Glass. Nature, Structure, and Properties*. New-York: Springer-Verlag, 1991.

[56] D. G. Holloway, *The Physical Properties of Glass*. London: Wykeham Publications LTD, 1973.

[57] R. Priestley, "Birefringence dispersion in fused silica for DUV lithography," in *Optical Microlithography XIV*, vol. 4346 of *Proc. SPIE*, pp. 1300–1305, 2001.

[58] J. A. Buck, *Fundamentals of Optical Fibers*. New York: John Wiley & Sons, Inc., 1995.

[59] X. Zhao, Y. Z. Xu, and C. Li, "Birefringence control in optical planar wave-guides," *J. Lightwave Tech.*, vol. 21, pp. 2352–2357, Oct. 2003.

[60] R. Kasahra, M. Itoh, Y. Hida, T. Saida, Y. Inoue, and Y. Hibino, "Birefringence compensated silica-based wave-guide with undercladding ridge," *Electron. Lett.*, vol. 38, pp. 1178–1179, Sept. 26, 2002.

[61] M. Huang, "Thermal stresses in optical wave-guides," *Opt. Lett.*, vol. 28, pp. 2327–2329, Dec. 2003.

[62] L. G. Peralta, A. A. Bernussi, H. Temkin, M. M. Borhani, and D. E. Doucette, "Silicon-dioxide wave-guides with low birefringence," *IEEE J. Quantum Electron.*, vol. 39, pp. 874–878, July 2003.

[63] O. Watanabe, M. Tsuchimiro, A. Okada, and H. Ito, "Mode selective polymer channel wave-guide defined by the photoinduced change in birefringence," *Appl. Phys. Lett.*, vol. 71, pp. 750–752, Aug. 11, 1997.

[64] S. M. Garner, V. Chuyanov, S. S. Lee, and A. Chen, "Vertically integrated wave-guide polarization splitters using polymers," *IEEE Phot. Tech. Lett.*, vol. 11, pp. 842–844, July 1999.

[65] A. D. Yablon, "Optical and mechanical effects of frozen-in stresses and strains in optical fibers," *IEEE J. of Selected Topics in Quantum. Electron.*, vol. 10, pp. 300–311, Mar. 2004.

[66] K. Saitoh, M. Koshiba, and Y. Tsuji, "Stress-analysis method for optical wave-guides composed of elastically anisotropic materials and its application to strain-induced optical wave-guides," *Electron. Comm. in Japan*, vol. 81, pp. 16–22, Jan. 1998.

[67] S. T. Amimoto, D. J. Chang, and A. D. Birkitt, "Stress measurements in silicon microstructures," in *Laser Applications in Microelectronic and Optoelectronic Manufacturing V* (H. Helvajian, K. Sugioka, M. Gower, and J. Dubowski, eds.), vol. 3933 of *Proc. SPIE*, pp. 113–121, 2000.

[68] M. Huang, "Stress effects on the performance of optical wave-guides," *Int. J. Solids and Structures*, vol. 40, pp. 1615–1632, Apr. 2003.

[69] S. H. Baek and J. W. Kang, "Zero-birefringence photosensitivity polymides for optical wave-guides," *Opt. Lett.*, vol. 29, pp. 301–303, Feb. 1, 2004.

[70] A. Kilian, J. Kirchhof, B. Kuhlow, G. Przyrembel, and W. Wischmanm, "Birefringence free planar optical wave-guide made by flame hydrolisis deposition (FHD) through tailoring of the overcladding," *J. Lightwave Tech.*, vol. 18, pp. 193–198, Feb. 2000.

[71] D. Dai and S. He, "Analysis of the birefringence of a silicon-on-insulator rib wave-guide," *Appl. Opt.*, vol. 43, pp. 1156–1160, Feb. 10, 2004.

[72] Z. Zhu and T. G. Brown, "Stress-induced birefringence in microstructured optical fibers," *Opt. Lett.*, vol. 28, pp. 2306–2308, Dec. 1, 2003.

[73] S. H. Jeong, T. Mizumoto, K. Nakatsuhara, M. Takenaka, and Y. Nakano, "Deep-ridge distributed feedback wave-guide for polarisation independent all-optical switching," *Electron. Lett.*, vol. 37, pp. 498–499, Apr. 12, 2001.

[74] S. H. Jeong, H. C. Kim, T. Mizumoto, J. Wiedmann, S. Arai, M. Takenaka, and Y. Nakano, "Polarisation insensitive deep-ridge vertical-groove DFB wave-guide for all-optical swithcing," *Electron. Lett.*, vol. 37, pp. 1387–1389, Nov. 8, 2001.

[75] K. S. Lee and J. Y. Cho, "Polarization-mode coupling in birefringent fiber gratings," *J. Opt. Soc. Amer.*, vol. 19, pp. 1621–1631, Aug. 2002.

[76] D. D. Davis, T. K. Gaylord, E. N. Glytsis, S. G. Kosinski, S. C. Mettler, and A. M. Vengsarkar, "Long-period fibre grating fabrication with focused CO_2 laser pulses," *Electron. Lett.*, vol. 34, pp. 302–303, Feb. 5, 1998.

[77] D. D. Davis, T. K. Gaylord, E. N. Glytsis, and S. C. Mettler, "Very-high-temperature stable CO_2-laser-induced long-period fibre gratings," *Electron. Lett.*, vol. 35, pp. 740–742, Apr. 29, 1999.

[78] B. L. Bachim and T. K. Gaylord, "Polarization-dependent loss and birefringence in long-period fiber gratings," *Appl. Opt.*, vol. 42, pp. 6816–6823, Dec. 1, 2003.

[79] R. A. Villalaz, E. N. Glytsis, and T. K. Gaylord, "Volume grating couplers: polarization loss effects," *Appl. Opt.*, vol. 41, pp. 5223–5228, Sept. 1, 2002.

[80] M. S. Bakir, T. K. Gaylord, O. O. Ogunsola, E. N. Glytsis, and J. D. Meindl, "Optical transmission of polymer pillars for chip I/O optical interconnects," *IEEE Trans. Electron. Dev.*, vol. 16, pp. 117–119, Jan. 1, 2004.

[81] M. S. Bakir and J. D. Meindl, "Sea of polymer pillars electrical and optical chip I/O interconnections for gigascale integration," *IEEE Trans. Electron. Dev.*, vol. 51, pp. 1069–1077, July 7, 2004.

[82] M. S. Bakir, C. O. Chui, A. K. Okyay, K. C. Saraswat, and J. D. Meindl, "Integration of optical polymer pillars chip I/O interconnections with Si MSM photodetectors," *IEEE Trans. Electron. Dev.*, vol. 51, pp. 1084–1090, July 7, 2004.

[83] C. Dragone, "Optimum design of a planar array of tapered wave-guides," *J. Opt. Soc. Amer. A*, vol. 7, pp. 2081–2093, Nov. 1990.

[84] C. Dragone, "An $N \times N$ optical multiplexer using a planar arrangement of two star couplers," *IEEE Phot. Lett.*, vol. 3, pp. 812–815, Sept. 1991.

[85] M. Zirngibl, C. Dragone, and C. H. Joyner, "Demonstration of a 15×15 arrayed wave-guide multiplexer on InP," *IEEE Phot. Lett.*, vol. 4, pp. 1250–1253, Nov. 1992.

[86] M. Y. Park, S. C. Gwak, K. S. Choi, J. K. Oh, H. J. Lee, and G. H. Song, "Reduction in polarisation-dependent loss and birefringence of arrayed-wave-guide grating by adaptable thermal quenching," *Electron. Lett.*, vol. 39, pp. 54–55, Jan. 9, 2003.

[87] P. K. Bachmann, W. Hermann, H. Wehr, and D. U. Wiechert, "Stress in optical wave-guides. 1:Preforms," *Appl. Opt.*, vol. 25, pp. 1093–1098, Apr. 1, 1986.

[88] P. K. Bachmann, W. Hermann, H. Wehr, and D. U. Wiechert, "Stress in optical wave-guides. 2:Fibers," *Appl. Opt.*, vol. 26, pp. 1175–1182, Apr. 1, 1987.

[89] K. W. Raine, R. Feced, S. E. Kanellopoulos, and V. A. Handerek, "Measurement of axial stress at high spatial resolution in ultraviolet-exposed fibers," *Appl. Opt.*, vol. 38, pp. 1086–1095, Mar. 1, 1999.

[90] Y. Park, U. C. Paek, and D. Y. Kim, "Characterization of a stress-applied polarization-maitaining (PM) fiber through photoelastic tomography," *J. Lightwave Tech.*, vol. 21, pp. 997–1004, Apr. 2003.

[91] N. G. Theofanous, "Error analysis of circular polarizer-analyzer systems for phase retardation measurements," *J. Opt. Soc. Amer. A*, vol. 4, pp. 2191–2200, Dec. 1987.

[92] C. R. Rao and S. K. Mitra, *Generalized Inverse of Matrices and Its Applications*. New York: Wiley, 1971.

[93] A. Berger-Schunn, *Practical Color Measurement*. New York: John Wiley & Sons, Inc., 1994.

[94] M. Bass, *Handbook of Optics*. New York: McGraw-Hill, Inc., 1995.

[95] N. G. Theofanous and A. T. Arapoyianni, "Effect of multiple reflections on retardation-based electro-optic measurements," *J. Opt. Soc. Amer. A*, vol. 8, pp. 1746–1754, Nov. 1991.

[96] J. Noda, K. Okamoto, and Y. Sasaki, "Polarization-maintaining fibers and their applications," *J. Lightwave Tech.*, vol. 4, pp. 1071–1089, Aug. 1986.

[97] M. H. Hayes, *Statistical Digital Signal Processing and Modeling*. New York: John Wiley & Sons, Inc., 1996.

[98] Y. Park, U. C. Paek, S. Han, B. Y. Kim, C. S. Kim, and D. Y. Kim, "Inelastic frozen-in stress in optical fibers," *Opt. Comm.*, vol. 242, pp. 431–436, Dec. 2004.

[99] W. Urbanczyk, K. Pietraszkiewicz, and W. A. Wozniak, "Novel bifunctional systems for measuring the refractive index profile and residual stress birefringence in optical fibers and preforms," *Opt. Eng.*, vol. 31, pp. 491–499, Mar. 1992.

[100] E. W. Hansen and P. L. Law, "Recursive methods for computing the Abel transform and its inverse," *J. Opt. Soc. Amer. A*, vol. 2, pp. 510–520, Apr. 1985.

[101] P. A. Vicharelli and W. P. Lapatovich, "Iterative method for computing the inverse Abel transform," *Appl. Phys. Lett.*, vol. 50, pp. 557–559, Mar. 9, 1987.

[102] K. Tatekura, "Determination of the index profile of optical fibers from transverse interferograms using Fourier theory," *Appl. Opt.*, vol. 22, pp. 460–463, Feb. 1, 1983.

[103] M. Kalal and K. Nugent, "Abel inversion using fast Fourier transforms," *Appl. Opt.*, vol. 27, pp. 1956–1959, May 15, 1988.

[104] C. C. Montarou and T. K. Gaylord, "Two-waveplate compensator method for single-point retardation measurements," *Appl. Opt.*, vol. 43, pp. 6580–6595, Dec. 20, 2004.

[105] C. C. Montarou and T. K. Gaylord, "Performing retardation measurements: Single-point two-waveplate compensator for optical retardation, thickness, and refractive index measurement." U.S. Patent Application Number 10/949,602 (patent pending), Sept. 24, 2004.

[106] C. C. Montarou and T. K. Gaylord, "Performing retardation measurements: Full-field automated two-waveplate compensator for optical retardation magnitude, retardation orientation, thickness, and refractive index measurement." U.S. Patent Application Number 10/949,855 (patent pending), Sept. 24, 2004.

[107] C. C. Montarou and T. K. Gaylord, "Performing retardation measurements: High-accuracy single-point and full-field two-waveplate compensator for optical retardation magnitude, retardation orientation, thickness, and refractive index measurement." U.S. Patent Application Number 10/950,048 (patent pending), Sept. 24, 2004.

[108] C. C. Montarou and T. K. Gaylord, "Colorimetry-based retardation measurement method with white-light interference," *Appl. Opt.*, vol. 41, pp. 5290–5297, Sept. 1, 2002.

[109] J. F. Kuhn, Z. Wu, and M. Poenie, "Modulated polarization microscopy: a promising new approach to visualizing cytoskeletal dynamics in living cells," *Biophys. J.*, vol. 80, pp. 972–985, Feb. 2001.

[110] B. Cense, T. C. Chen, and B. H. Park, "*In vivo* birefringence and thickness measurements of the human retinal fiber nerve layer using polarization-sensitive optical coherence tomorgraphy," *J. Bio. Opt.*, vol. 9, pp. 121–125, Jan. 2004.

VITA

Carole C. Montarou was born on March 25, 1976 in Le Mans, France. She received a Licence de Physique in 1997 and a Maitrise de Physique in 1998, both from the University of Le Mans. She then attended the Georgia Institute of Technology where she obtained a Master of Science in 2000. During this time, she wrote a Master's thesis on the analysis and design of modified Wollaston prisms. She received the Sigma Xi M.S. thesis award for this work. Her Ph.D. research work involves the development of new high-accuracy retardation measurement methods for the characterization of optical devices. Carole is a member of the Optical Society of America and Eta Kappa Nu.